universität wien

DISSERTATION

Titel der Dissertation

Studies of atomic diffusion in binary alloys by X-ray Photon Correlation Spectroscopy with particular attention to B2 phases

Verfasser

Mag. Markus Stana

angestrebter akademischer Grad

Doktor der Naturwissenschaften (Dr. rer. nat.)

Wien, 2015

Studienkennzahl lt. Studienblatt:	A 796 605 411
Dissertationsgebiet lt. Studienblatt:	Physik
Betreuer:	Ao. Univ.-Prof. Mag. Dr. Bogdan Sepiol

Heraklit said “παντα ρει”. However, quite a bit of it actually hops.

Abstract

The way single atoms change places in a condensed system determines many of its properties. Insight into the mechanisms controlling such processes, therefore, yields a better understanding of matter which in turn allows for improving fabrication and tailoring of material properties. Intermetallic alloys have many attractive features for industrial applications, such as high specific strength, good corrosion and oxidation resistance and low raw material cost. Their application is, however, still strongly limited by properties such as high brittleness at low temperatures.

Methods capable of studying diffusion on an atomistic level have been restricted to high temperatures close to the melting point of intermetallics until now. The new method of atomic-scale X-ray Photon Correlation Spectroscopy provides a means of studying these materials at technically relevant working temperatures. This thesis demonstrates the application of this new technique to binary intermetallic alloys.

In the first part the theoretical concepts underlying atomic-scale X-ray Photon Correlation Spectroscopy such as correlation, rate equations, scattering and reciprocal space will be thoroughly discussed. As computer simulation techniques play an important role in data evaluation, a chapter is dedicated to this topic. The experimental preconditions are then treated. The last chapters are devoted to the presentation of experimental results. It is shown that a new diffusion mechanism is required to explain atomic hops at relatively low temperature in a B2 Fe-Al alloy with a few percent of excess Fe, while in a B2 Ag-Mg alloy with excess Ag commonly known mechanisms can explain the observed diffusion behavior.

Kurzfassung

Viele Eigenschaften kondensierter Materie sind durch die Bewegung einzelner Atome bestimmt. Gelingt es, die Mechanismen, die solchen Prozessen zugrunde liegen, nachzuvollziehen, so erlangt man ein tieferes Verständnis von Materie. Ein solches erlaubt es, Herstellungsprozesse und Eigenschaften von Werkstoffen zielgerichtet zu verbessern. Intermetallische Legierungen haben viele attraktive Merkmale für industrielle Anwendungen wie beispielsweise hohe Reißlänge, gute Korrosions- und Oxidationsbeständigkeit und geringe Rohstoffkosten. Ihre Anwendung ist jedoch aufgrund von Eigenschaften wie hoher Sprödigkeit bei niedrigen Temperaturen stark eingeschränkt.

Methoden zur Untersuchung von Diffusion auf atomarer Ebene waren bisher auf hohe Temperaturbereiche nahe dem Schmelzpunkt von intermetallischen Legierungen beschränkt. Eine neue Methode namens atomare Röntgen-Photonen-Korrelationsspektroskopie eröffnet die Möglichkeit, Materialien bei technologisch relevanten Arbeitstemperaturen zu untersuchen. In dieser Arbeit wird die Anwendung dieser neuen Methode auf binäre intermetallische Legierungen dargelegt.

Im ersten Teil werden theoretische Konzept wie Korrelation, Ratengleichung, Streuung und der reziproke Raum, die der atomaren Röntgen-Photonen-Korrelationsspektroskopie zugrunde liegen, eingehend diskutiert. Da Computersimulationen eine wichtige Rolle in der Datenauswertung spielen, beschäftigt sich ein Kapitel mit diesem Thema. Anschließend werden die experimentellen Voraussetzungen behandelt. In den letzten Kapiteln werden experimentelle Ergebnisse präsentiert. Es wird gezeigt, dass ein neuer Diffusionsmechanismus benötigt wird, um atomare Sprünge bei relativ niedriger Temperatur in einer B2 Eisen-Aluminium-Legierung mit einem Eisenüberschuss von ein paar Prozent zu erklären, während das Diffusionsverhalten in einer B2 Silber-Magnesium-Legierung mit Silberüberschuss durch bekannte Sprungmechanismen erklärt werden kann.

Acknowledgements

It is impossible to thank all the people who supported me during my time at the university and gave me vigor or helped me to clear my head when in danger of overload. Even so I would like to point out to the reader that this will get somewhat extensive.

First of all I would like to thank my supervisor Bogdan. I had full rein in following whichever approach I thought fit in our research but he always had an open ear and made time to discuss whatever was on my mind. The former led me to taking scientific detours from time to time, but I guess this was how I could learn the most. Whenever I felt depressed about my research he managed to tell me about new scientific findings he had just read about with such zest that I could not help getting carried along. Furthermore, he had the patience of a saint when it came to me and fine motor skills in the laboratory. As far as his personality goes, he is the most modest genius I have ever encountered.

The remarks and corrections Michael has contributed to this work have been indispensable, albeit sometimes devastating. He not only tirelessly proofread everything I sent to him, even when he was on holiday, he did it at a speed that often left me puzzled. I guess if I would owe him one cent for every sigh I caused him I would have to try my luck in the consulting business in order to ever be able to repay him. I genuinely thank him for his patience with a lesser mind.

I want to thank Herwig for having the time for academic discussions but also personal advice even though his schedule is bulging. It was very reassuring to know that he had my back. To Gero I would like to express my thanks not only for sharing his immersive experience but also for being a friend and a role model when showing juvenility in the mountains or pizzazz in the lecture hall. I would be most grateful if I was half as fit in body or mind as him when I am past seventy.

For all her help I would like to express my gratitude to Yvonne. She has always been the person to go to in our group. Whatever you need, she has it. From savvy in all bureaucratic things to life-advice and paper clips. I guess I would have given up on this work a few times if it was not for her. A big thank you for her help in administrative as well as linguistic matters goes also to Katharina.

I want to thank Johanna for her support with SAXS measurements and for having a genuinely good time even though I never made it to one of her birthday parties. For help with many technical matters I would like to thank Martina, Daniel, Peter and Gerry, Andi and everybody else at the technical workshop. For their supporting words at every chance encounter I would like to thank Wolfgang Pfeiler and Wolfgang Püschl. I would also like to thank Doris and Martijn for their support with VASP, even though my work trying to find displacement scattering parameters using ab initio methods did not find a place in this work as it was one of the detours mentioned above. At least it led to some interesting conversations during lunch. I would also like to thank all the other members of our group for making my days brighter.

Two of my colleagues became good friends over the years. I would like to thank Manuel for sitting in the same small boat as me for more than three years. Without him everyday life at the university, but also a number of beamtimes and the nights out that followed would not have been half of what they were. I also thank him for his precision and being nit-picking when

formulating scientific results. Without this German on my side, my work would have been even more chaotic. Stephan is about the best support unit there can be, even though he is a single person. But he compensates his lack in numbers by being one of the most expert, conscientious and hardworking people I have ever met. The only way he could be improved would probably be to make him care as much about himself as he cares about others.

I would like to thank all my other friends, who helped me through this time. Those who can be bothered to read this know that they are meant.

For supporting me through all my life and of course also through my studies and my process of writing this work I would like to thank my family. I would like to thank my mother Beatrix for always loving me unconditionally. I would like to thank my father Anton not only for making me immune to pretty much every form of harsh criticism, but for always deeply caring about me at the same time. And I would like to thank my sister Sarah who I know would walk through fire with me.

For sticking with me, especially in the last year, my sincere thanks goes to Teresa, who is probably the love of my life.

For proofreading I thank Michael, Stephan, Gero, my sister Sarah and of course Bogdan.

Contents

1. Introduction

Knowledge of diffusion rates and diffusion mechanisms is of great interest in material science. Therefore, the investigation of these phenomenons has a longstanding tradition. Important theoretical foundations were laid by Adolf Eugen Fick, Svante August Arrheinus and Albert Einstein and Marian Smoluchowski, while ground breaking experiments were performed by William Chandler Roberts-Austen, Georg Karl van Hevesy and Jean Baptist Perrin at the beginning of the previous century [Mehr 07].

During these more than one hundred years, the macroscopic methods for studying diffusion have very much improved, profiting from better tracers, higher microscopic resolution and discoveries like the Kirkendall effect. This lead to an abundance of scientific discoveries including much insight into microscopic processes. In most cases atomistic properties and the diffusion mechanisms have to be deduced from macroscopic properties. Not in all cases though. As microscopic methods operating in real space improved so much in the last decades that they can reach sub-atomic resolution, using techniques like high resolution transmission electron microscopy (HRTEM) nowadays even allows to follow particular processes like surface diffusion on the atomic scale [Surr 12]. There also exists a number of other methods, like Quasi-elastic Neutron Scattering (QNS), Quasi-elastic Mößbauer Spectroscopy (QMS) or Nuclear Magnetic Resonance (NMR), that allow to follow atomic motion directly. However, due to the restricted energy resolution of such methods, they can only be applied to relatively fast processes corresponding to diffusion proceeding at rather high temperatures near the melting point of most materials. At such temperatures atomic forces play a minor role, which means that extrapolating atomic jump mechanisms to lower temperatures, where such forces are important, is not straightforward. Furthermore these experimental techniques are often restricted to particular isotopes, which limits the number of accessible systems. The information on different systems investigated so far is therefore rather limited.

In order to gain direct access to jump processes of systems in the state of everyday applications, a new method had to be found. It was possible to advance the scattering method of X-ray Photon Correlation Spectroscopy (XPCS) [Brau 95], which is the X-ray equivalent of Dynamic Light Scattering (DLS), to the X-ray regime and show that it is capable of the determining atomic jump vectors [Leit 09, Leit 12a, Stan 13, Ross 14].

As distinct from "standard" XPCS in which dynamics of macroscopic objects are measured, atomic-scale X-ray Photon Correlation Spectroscopy (aXPCS) measures dynamics at the atomic-scale using wide-angle scattering. This presents new experimental challenges as in this regime the scattered intensity is much lower and higher longitudinal coherence is needed. Such a distinction is similar to the case of wide-angle X-ray scattering (WAXS) and small-angle X-ray scattering (SAXS). The applied technique is the same, but the area of reciprocal space, where the measurement takes place, differs.

aXPCS works in the time regime and is not restricted by any physical limits. In a nutshell, a

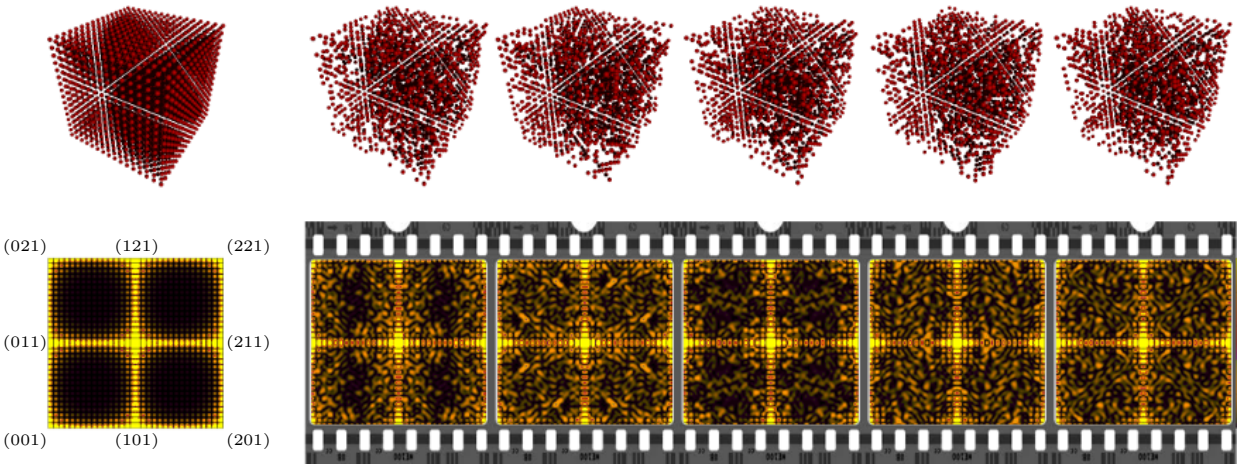

Figure 1.1.: Left: Completely filled bcc lattice and a plane in reciprocal space for a lattice of $16^3 \times 2$ atoms. The additional features between the peaks of Bragg reflection are due to finite size effects, which are strong for such a small lattice.
Right: The same lattices, only partially filled and corresponding reciprocal space images.

perfect, fully occupied lattice yields a scattering pattern featuring sharp Bragg reflection peaks. When the lattice is partially empty or occupied by different species with distinct scattering lengths, the scattering in the diffuse regime is strongly enhanced. Different configurations of real space, that is different arrangements of the scatterers, yield different scattering patterns, as schematically shown in Fig. 1.1. A temporal series of such scattering patterns is used to draw conclusions about atomic motion driven by diffusion. The time resolution depends only on the brilliance of the X-ray source and the readout speed of the X-ray detector. Furthermore, it is not restricted to selected isotopes and, as a large region of the sample is probed by the X-ray beam, no issues concerning localized sampling as in case of microscopic real space methods occur.

This work gives an introduction to the method of aXPCS and demonstrates how it can be applied to the interesting class of intermetallic alloys. The following three chapters set the scene. In Chapter 2 the theoretical concepts of aXPCS are introduced in a streamlined notation. Chapter 3 gives an overview over different atomic diffusion mechanisms. Some of the concepts discussed here have a long tradition, while others are relatively new. It is also shown how the different concepts can be tested against aXPCS experiments. As chemical short-range ordering has an influence on the stability of local configurations and therefore influences correlation times, it is an important factor when evaluating aXPCS data. Finding the appropriate short-range order parameters has presented itself as a very interesting and challenging problem over the last years. Thus, Chapter 4 is devoted to this topic. After these theoretical sections technical requirements for performing an aXPCS experiment will be discussed. In the following chapters a short treatment of aXPCS results for a solid solution and detailed discussions about results for two binary intermetallic alloys, namely $Fe_{0.54}Al_{0.46}$ and $Ag_{0.58}Mg_{0.42}$ (the subscripts indicates the fraction of atoms) will be presented. At last there will be a short outlook about what could be done in the future.

2. Theory of atomic-scale X-ray Photon Correlation Spectroscopy

In this chapter the theoretical keystones of atomic-scale X-ray Photon Correlation Spectroscopy (aXPCS) are introduced. As it is a scattering technique that operates in the Fraunhofer regime, the ground is laid by introducing scattering vectors and important concepts of reciprocal space. The framework of the method is based on correlation functions, which will be introduced in the second part.

2.1. Reciprocal space

For a three dimensional space spanned by a set of linear independent vectors $\vec{r}_1$, $\vec{r}_2$ and $\vec{r}_3$, there exists a set of vectors $\vec{q}_i$, such that $\vec{r}_i \cdot \vec{q}_j = 2\pi\delta_{ij}$. The latter set is called reciprocal space vectors. Historically this arises out of the Bragg condition, which is the reason why a vector in reciprocal space is often defined by the scattering planes orthogonal to it. On this basis a reciprocal lattice vector (hkl) can be written as $h\vec{q}_1 + k\vec{q}_2 + l\vec{q}_3$, which is very practical for crystallographic considerations. In a classical scattering experiment, however, the two dimensional section of q-space recorded by a detector does not coincide with a plane represented by such vectors, but coincides with the surface of a sphere. It is therefore sometimes useful, to represent a reciprocal space vector $\vec{q}$ by spherical coordinates rather than by means of a lattice vector (hkl).

2.1.1. Parameterization of reciprocal space

The reciprocal space vector $\vec{q}$ is defined as the difference between the incoming X-ray vector $\vec{k}_{\text{in}}$ and the scattered X-ray vector $\vec{k}_{\text{out}}$ as $\vec{q} = \vec{k}_{\text{out}} - \vec{k}_{\text{in}}$. A scattering triangle is shown in Fig. 2.1a. In the case of elastic scattering, where $\left|\vec{k}_{\text{out}}\right| = \left|\vec{k}_{\text{in}}\right| = k$, connecting the ends of the set of all possible scattering vectors forms a sphere in reciprocal space, called the Ewald sphere, as shown in Fig. 2.1b. A selection of these vectors fulfill the Bragg conditions. The rest stretches over the region of reciprocal space that is known in a scattering experiment as the regime of diffuse scattering. As in an aXPCS experiment quasi-elastic scattering is used, we will only treat the case of elastic scattering from here on.

The particular area of reciprocal space covered by a sphere formed by the set of possible $\vec{q}$-vectors is determined by the direction and length of $\vec{k}_{\text{in}}$. The length of the scattering vectors is determined by E, the energy of the electromagnetic wave

$$|\vec{k}_{\text{in}}| = \frac{2\pi}{\lambda} = \frac{E}{\hbar c}\,, \tag{2.1}$$

with λ being the wavelength and c the speed of light. Therefore, the length of the scattering vector $\vec{q}$ depends on the energy E and the angle between the initial and the outgoing scattering

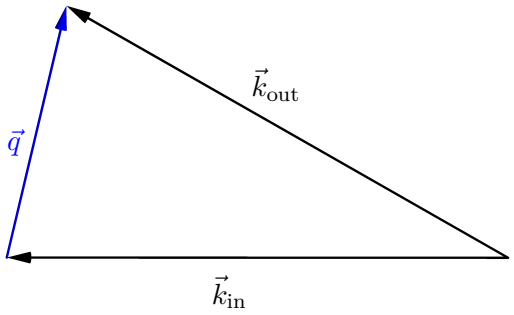

(a) Scattering triangle. The reciprocal space vector $\vec{q}$ is the difference between incoming and outgoing scattering vectors.

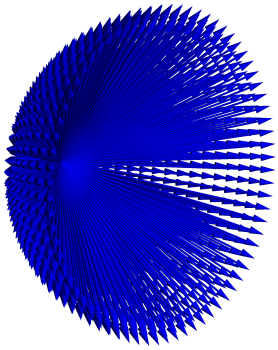

(b) The set of possible wavevector transfers for a fixed sample orientation in the case of elastic scattering form a sphere. Here half of the sphere is shown.

Figure 2.1.

vectors 2Θ:

$$|\vec{q}(2\Theta)| = 2k \sin\left(\frac{2\Theta}{2}\right) \tag{2.2}$$

In case of an amorphous scatterer, reciprocal space is rotationally symmetric with $\vec{k}_{\text{in}}$ being the symmetry axis. The direction of the scattering vector or the orientation of the scatterer respectively does not play a role. If the scatterer is of crystalline form, however, the direction of $\vec{k}_{\text{in}}$ is determined by the orientation of the scatterer in respect to the incoming or primary beam. The orientation can be chosen such that a certain crystallographic direction $\langle hkl \rangle$, e.g. $\langle 100 \rangle$, $\langle 110 \rangle$ or $\langle 111 \rangle$, is parallel to the incoming beam.

The reciprocal space vector can be split into two components $\vec{q} = \vec{q}_{\perp} + \vec{q}_{\parallel}$, where $\vec{q}_{\parallel} \parallel \vec{k}_{\text{in}}$. In order to introduce a parametrization of reciprocal space similar to spherical coordinates, the radial component of the coordinate system is chosen to be the length of the scattering vector $k = \left|\vec{k}_{\text{in}}\right|$. The polar angle coincides with the scattering angle 2Θ and the azimuthal angle shall be called φ. These are also the natural parameters in a scattering experiment as will be shown in Section 6.4. To interrelate these spherical coordinates with the Cartesian coordinates , an alignment vector $S(2\theta)$ and a rotation matrix $R(\varphi, u_x, u_y, u_z)$ are introduced. The alignment vector depends on the orientation of the sample and reorientates the coordination system with respect to the labor system. The rotation matrix is the standard rotation matrix (see (A.1)) and accounts for the free parameter, namely the azimuthal angle φ. In combination with (2.2) it is possible to define the scattering vector in dependence of the polar and the azimuthal angle as

$$\vec{q}(2\Theta, \varphi) := q(2\Theta) S(2\Theta) R(\varphi, \hat{h}, \hat{k}, \hat{l}). \tag{2.3}$$

Here $\left(\hat{h}, \hat{k}, \hat{l}\right)$ is a unit vector, giving the direction of orientation of the sample. For simplicity

$q(2\Theta) = |\vec{q}(2\Theta)|$ was introduced.

The alignment vectors for the main crystallographic orientations of a cubic system are given.

$\langle 100 \rangle$ **directions:** We choose one particular direction, namely $\vec{k}_{\text{in}} \parallel [100]$. The rotation axis of the rotation matrix is therefore $\left(\hat{h}, \hat{k}, \hat{l}\right) = (1, 0, 0)$. The components of the alignment vector for this case coincide with the natural choice of polar coordinates in a labor system, as can be seen in Fig. 2.2a.

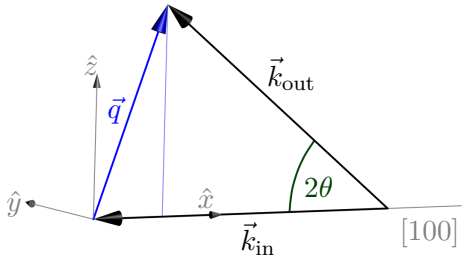

(a) Scattering triangle for a crystal oriented in the [100] direction. The components of the scattering vector are: $q_x = q\sin(2\Theta/2)$ and $q_z = q\cos(2\Theta/2)$.

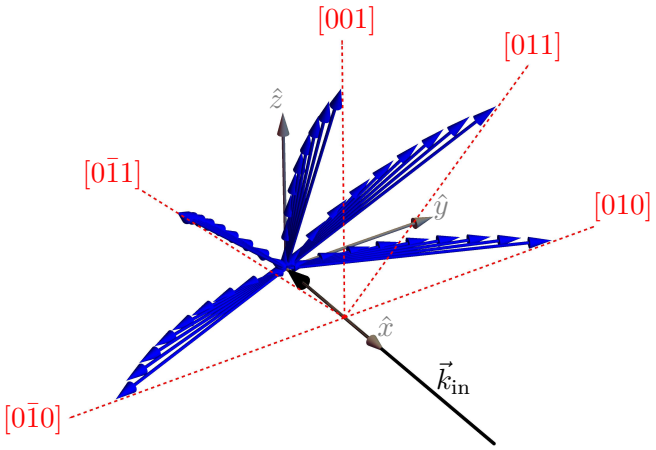

(b) Representation of subset of $\vec{q}$-vectors corresponding to $\vec{q}_\perp$ parallel to the main crystallographic directions for a crystal oriented in [100] direction.

Figure 2.2.

$$S(2\Theta) = \begin{pmatrix} \sin\left(\frac{2\Theta}{2}\right) \\ 0 \\ \cos\left(\frac{2\Theta}{2}\right) \end{pmatrix} \tag{2.4}$$

Multiplication of this alignment vector and the appropriate rotation matrix yields:

$$\begin{aligned} \vec{q}(2\Theta, \varphi) = 2k \sin\left(\frac{2\Theta}{2}\right) \Bigg(& \sin\left(\frac{2\Theta}{2}\right) \hat{x} \\ & + \cos\left(\frac{2\Theta}{2}\right) \sin(\varphi)\, \hat{y} \\ & + \cos\left(\frac{2\Theta}{2}\right) \cos(\varphi)\, \hat{z} \Bigg) \end{aligned} \tag{2.5}$$

Under certain azimuthal angles φ the perpendicular component of the reciprocal space vector $\vec{q}_\perp$ is parallel to certain crystallographic main directions as is visualized in Fig. 2.2b. With $n \in \mathbb{N}_0$ the following conditions hold:

$$\forall \varphi \in (n \times 90°) \quad : \quad \vec{q}_\perp \parallel \langle 100 \rangle \tag{2.6a}$$

$$\forall \varphi \in (n \times 90°) + 45° \quad : \quad \vec{q}_\perp \parallel \langle 110 \rangle \tag{2.6b}$$

The scattering image therefore has a fourfold symmetry.

$\langle 110 \rangle$ **direction:** We choose $\vec{k}_{\text{in}} \parallel [1\bar{1}0]$ as a representative for the set of $\langle 110 \rangle$ orientations. Again the rotation axis of the rotation matrix is chosen accordingly, $\left(\hat{h}, \hat{k}, \hat{l}\right) = \frac{1}{\sqrt{2}}(1, \bar{1}, 0)$.

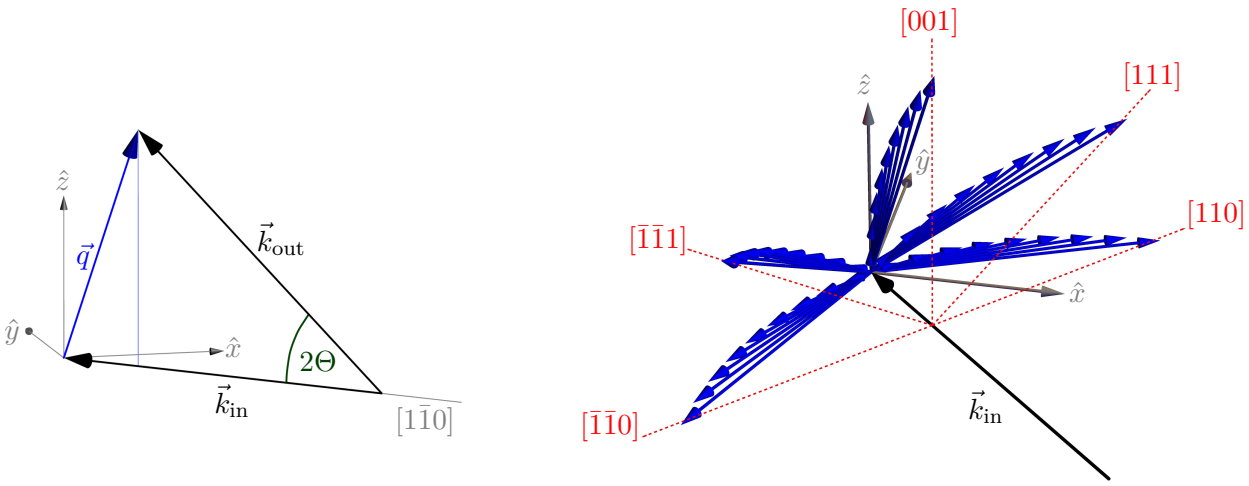

(a) Scattering triangle giving the alignment vector for $[1\bar{1}0]$ oriented crystal.

(b) Representation of subset of $\vec{q}$-vectors corresponding to $\vec{q}_\perp$ parallel to the main crystallographic directions for a crystal oriented in $[1\bar{1}0]$ direction.

Figure 2.3.

As can be seen from Fig. 2.3a, the alignment vector has the form

$$S(2\Theta) = \begin{pmatrix} \frac{\sin\left(\frac{2\Theta}{2}\right)}{\sqrt{2}} \\ \frac{-\sin\left(\frac{2\Theta}{2}\right)}{\sqrt{2}} \\ \cos\left(\frac{2\Theta}{2}\right) \end{pmatrix}. \tag{2.7}$$

Multiplying with the rotation matrix yields the reciprocal space vector depending on 2Θ and φ for this orientation:

$$\begin{aligned} \vec{q}(2\Theta, \varphi) = 2k \sin\left(\frac{2\Theta}{2}\right) \Bigg(& \frac{1}{\sqrt{2}} \left(\sin\left(\frac{2\Theta}{2}\right) + \cos\left(\frac{2\Theta}{2}\right) \sin(\varphi) \right) \hat{x} \\ & - \frac{1}{\sqrt{2}} \left(\sin\left(\frac{2\Theta}{2}\right) - \cos\left(\frac{2\Theta}{2}\right) \sin(\varphi) \right) \hat{y} \\ & + \cos\left(\frac{2\Theta}{2}\right) \cos(\varphi)\, \hat{z} \Bigg) \end{aligned} \tag{2.8}$$

The crystallographic main directions for the perpendicular component of the scattering vector $\vec{q}_\perp$ is parallel to are shown in Fig. 2.3b. They can be found at the following azimuthal angles:

$$\varphi \in \{0°, 180°\} \quad : \quad \vec{q}_\perp \parallel \langle 100 \rangle \tag{2.9a}$$

$$\varphi \in \{90°, 270°\} \quad : \quad \vec{q}_\perp \parallel \langle 110 \rangle \tag{2.9b}$$

$$\varphi \in \{54.74°, 125.26°, 234.74°, 305.26°\} \quad : \quad \vec{q}_\perp \parallel \langle 111 \rangle \tag{2.9c}$$

As can be seen from the symmetry of the main directions, the scattering image has a twofold symmetry.

⟨111⟩ **direction:** For the third main direction in cubic systems we chose $\vec{k}_{\text{in}} \parallel [111]$ and accordingly $\left(\hat{h}, \hat{k}, \hat{l}\right) = \frac{1}{\sqrt{3}}(1,1,1)$.

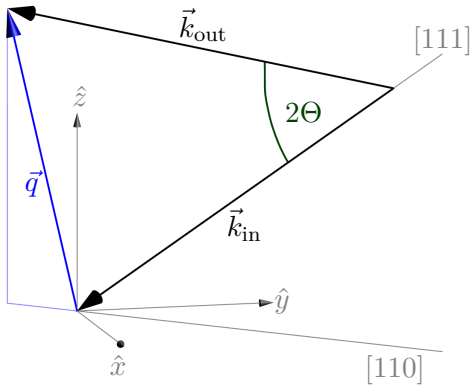

(a) Scattering triangle giving the alignment vector for [111] oriented crystal: $\sqrt{q_x^2 + q_y^2} = q\sin(\alpha)$ and $q_z = q\cos(\alpha)$ with $\alpha = 2\Theta/2 - 54.7356°$.

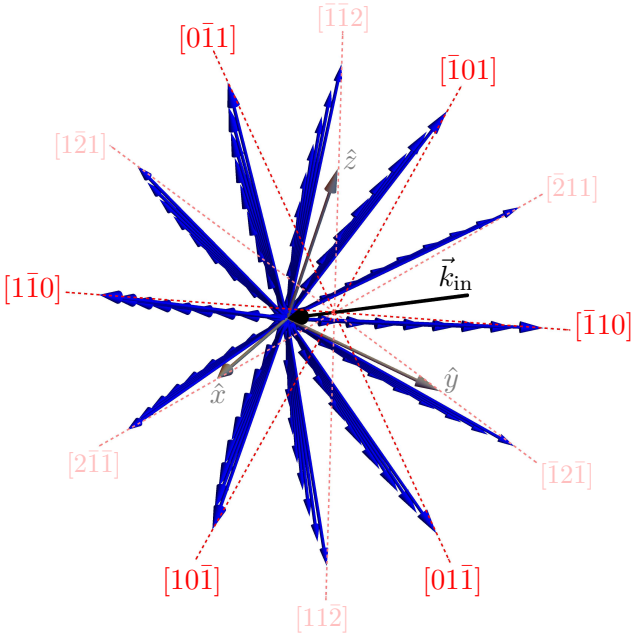

(b) Representation of subset of $\vec{q}$-vectors corresponding to $\vec{q}_\perp$ parallel to the main crystallographic directions for a crystal oriented in [111] direction.

Figure 2.4.

From Fig. 2.4a the alignment vector can be identified as:

$$S(2\Theta) = \begin{pmatrix} \frac{\sin\left(2\Theta/2 - \arcsin\left(1/\sqrt{3}\right)\right)}{\sqrt{2}} \\ \frac{\sin\left(2\Theta/2 - \arcsin\left(1/\sqrt{3}\right)\right)}{\sqrt{2}} \\ \cos\left(2\Theta/2 - \arcsin\left(1/\sqrt{3}\right)\right) \end{pmatrix} \tag{2.10}$$

Again, multiplying with the appropriate rotation matrix, the reciprocal space vector for this direction can be written as

$$\begin{aligned} \vec{q}(2\Theta,\varphi) = 2k\sin\left(\frac{2\Theta}{2}\right) \times \\ \left(\frac{\sin(2\Theta/2)}{\sqrt{3}} - \frac{\cos(2\Theta/2)}{6}\left(\sqrt{6}\cos(\varphi) + 3\sqrt{2}\sin(\varphi)\right)\hat{x}\right. \\ + \left(\frac{\sin(2\Theta/2)}{\sqrt{3}} + \frac{\cos(2\Theta/2)}{6}\left(-\sqrt{6}\cos(\varphi) + 3\sqrt{2}\sin(\varphi)\right)\right)\hat{y} \\ \left. + \frac{\sqrt{2}\cos(2\Theta/2)\cos(\varphi) + \sin(2\Theta/2)}{\sqrt{3}}\hat{z}\right). \end{aligned} \tag{2.11}$$

Comparing Fig. 2.2b, Fig. 2.3b and Fig. 2.4b one sees that for a crystal oriented in ⟨110⟩-direction, the rotation symmetry of the scattering image is lowest. Also $\vec{q}_{\parallel}$ can be chosen parallel to each of the three main crystallographic directions. Out of these three examples with high symmetry this is the orientation that yields the most information and is therefore a favored orientation in aXPCS measurements.

2.2. Correlations and diffusive motion

In this section some important concepts for describing diffusive motion are introduced. As the name states, X-ray Photon Correlation Spectroscopy is a method based on correlations, making it the first topic of discussion. Then a brief introduction to the idea of using master equations for treating jump probabilities will be given. Finally both concepts will be related to each other.

2.2.1. Correlations in real space

Using correlation to describe diffusive motion has a long standing tradition. The concept was introduced by extending the pair distribution function of space $\gamma(\Delta\vec{r})$ to a pair distribution function in space and time $G(\Delta\vec{r}, \Delta t)$ [Van 54]. These two functions can be defined as

$$\gamma(\Delta\vec{r}) = \langle \sigma(\vec{r})\, \sigma(\vec{r} + \Delta\vec{r}) \rangle_{\vec{r}} \tag{2.12}$$

$$G(\Delta\vec{r}, \Delta t) = \langle \langle \sigma(\vec{r}, t)\, \sigma(\vec{r} + \Delta\vec{r}, t + \Delta t) \rangle_{\vec{r}} \rangle_t \ , \tag{2.13}$$

where the brackets $\langle \ldots \rangle_{\vec{r}}$ and $\langle \ldots \rangle_{\vec{r}}$ denote the ensemble average over space and over time respectively. The state function $\sigma(...)$ indicates the state of occupation of space at a certain time.

Applying the Cauchy-Schwarz inequality$|\langle f(x)\, f(y) \rangle| \leq \sqrt{\langle f(x)\, f(x) \rangle \, \langle f(y)\, f(y) \rangle}$, taking care of preserving correlations shows that this function decreases with time:

$$|G(\Delta\vec{r}, \Delta t)| = \left| \langle \langle \sigma(\vec{r}, t)\, \sigma(\vec{r} + \Delta\vec{r}, t + \Delta t) \rangle_{\vec{r}} \rangle_t \right| \tag{2.14a}$$

$$\leq \sqrt{\langle \langle \sigma(\vec{r}, t)\, \sigma(\vec{r} + \Delta\vec{r}, t) \rangle_{\vec{r}} \rangle_t \, \langle \langle \sigma(\vec{r}, t + \Delta t)\, \sigma(\vec{r} + \Delta\vec{r}, t + \Delta t) \rangle_{\vec{r}} \rangle_t} \tag{2.14b}$$

$$= \sqrt{\langle \langle \sigma(\vec{r}, t)\, \sigma(\vec{r} + \Delta\vec{r}, t) \rangle_{\vec{r}} \rangle_t^2} \tag{2.14c}$$

$$|G(\Delta\vec{r}, \Delta t)| \leq |\gamma(\Delta\vec{r})| = |G(\Delta\vec{r}, 0)| \ . \tag{2.14d}$$

The state function σ is defined by the kind of particle occupying a certain position in space, or more specifically by the relevant properties of these particle. Let f_i be the measure of a certain property of a particle i. Then we can write the density of particles with this property as

$$\rho(\vec{r}, t) = \sum_i f_i \delta(\vec{r} - \vec{R}_i(t)) \tag{2.15}$$

where $\vec{R}_i(t)$ is the position vector of the ith particle at time t. Using the Wiener-Khinchin

theorem we can write the Van Hove correlation function as

$$G(\Delta\vec{r},\Delta t) = \int_{\mathbb{R}^3} \mathrm{d}\vec{r} \sum_i \sum_j \left\langle f_i \delta(\vec{r} - \vec{R}_i(t)) f_j \delta(\vec{r} + \Delta\vec{r} - \vec{R}_j(t+\Delta t)) \right\rangle_t \tag{2.16a}$$

$$= \int_{\mathbb{R}^3} \mathrm{d}\vec{r} \sum_i \left\langle f_i^2 \delta(\vec{r} - \vec{R}_i(t)) \delta(\vec{r} + \Delta\vec{r} - \vec{R}_i(t+\Delta t)) \right\rangle_t \tag{2.16b}$$

$$+ \int_{\mathbb{R}^3} \mathrm{d}\vec{r} \sum_{\substack{i,j \\ i\neq j}} \left\langle f_i f_j \delta(\vec{r} - \vec{R}_i(t)) \delta(\vec{r} + \Delta\vec{r} - \vec{R}_j(t+\Delta t)) \right\rangle_t \tag{2.16c}$$

$$= G_\mathrm{S}(\Delta\vec{r},\Delta t) + G_\mathrm{D}(\Delta\vec{r},\Delta t) \tag{2.16d}$$

Here $G_\mathrm{S}(\Delta\vec{r},\Delta t)$ represents the so called self-correlation function and $G_\mathrm{D}(\Delta\vec{r},\Delta t)$ the correlation function of different pairs. The self-correlation function describes the motion of one and the same particle through space as $G_\mathrm{S}(\Delta\vec{r},\Delta t)$ gives the probability for finding a particle at $\vec{r}+\Delta\vec{r}$ at time $t+\Delta t$, provided it was at a position $\vec{r}$ at time t. The distinct-pair-correlation function describes the probability to find another particle at $\vec{r}+\Delta\vec{r}$ and $t+\Delta t$ if a certain atom was at $\vec{r}$ at time t. The sum of both $G(\Delta\vec{r},\Delta t)$ therefore refers the probability of finding any particle (with the appropriate properties) at $\vec{r}+\Delta\vec{r}$ and $t+\Delta t$.

2.2.2. Correlation in reciprocal space

Fourier transforming (2.12) yields

$$\mathscr{F}_{\Delta\vec{r}\to\vec{q}}(\gamma)(\vec{q}) \propto \int \mathrm{d}\Delta\vec{r} \int_{-\infty}^{\infty} \mathrm{d}\vec{r}\, \sigma(\vec{r})\, \sigma(\vec{r}+\Delta\vec{r}) \exp(-\mathrm{i}\,\vec{q}\cdot\Delta\vec{r})\,. \tag{2.17}$$

As the pair distribution function is a representation of all inter-atomic distances, its Fourier transform is directly linked to the structure factor, $S(\vec{q}) \propto \mathscr{F}_{\Delta\vec{r}\to\vec{q}}(\gamma(\Delta\vec{r}))$.

We can write the Fourier transform of the Van Hove pair correlation function as:

$$\mathscr{F}_{\Delta\vec{r}\to\vec{q}}(G(\Delta\vec{r},\Delta t)) \propto$$

$$\int \mathrm{d}\Delta\vec{r} \exp(-\mathrm{i}\,\vec{q}\cdot\Delta\vec{r}) \int_{-\infty}^{\infty} \mathrm{d}\vec{r} \sum_i \sum_j \left\langle \delta(\vec{r} - \vec{R}_i(t)) \delta(\vec{r} + \Delta\vec{r} - \vec{R}_j(t+\Delta t)) \right\rangle_t \tag{2.18a}$$

$$= \sum_i \sum_j \int \mathrm{d}\Delta\vec{r} \left\langle \exp\left(-\mathrm{i}\,\vec{q}\cdot\vec{R}_i(t)\right) \exp\left(\mathrm{i}\,\vec{q}\cdot\vec{R}_j(t+\Delta t)\right) \right\rangle_t \exp(-\mathrm{i}\,\vec{q}\cdot\Delta\vec{r}) \tag{2.18b}$$

$$=: \mathscr{I}(\vec{q},\Delta t) \tag{2.18c}$$

$\mathscr{I}(\vec{q},\Delta t)$ is in the literature referred to as the intermediate scattering function [Hemp 00].

The Fourier transform of the density function for the experiment corresponds to the scattering amplitude of the electromagnetic field, $E(\vec{q}) = \int \mathrm{d}\vec{r}\,\sigma(\vec{r}) \exp(-\mathrm{i}\,\vec{q}\cdot\vec{r})$. This can be used to write the intermediate scattering function as

$$\mathscr{I}(\vec{q},\Delta t) = \langle E(\vec{q},t) E^*(\vec{q},t+\Delta t)\rangle_t\,. \tag{2.19}$$

It is useful to normalize this function by the time average of the scattering intensity and write

$$g^{(1)}\left(\vec{q},\Delta t\right)=\frac{\langle E(\vec{q},t)E^{*}(\vec{q},t+\Delta t)\rangle_{t}}{\langle E(\vec{q},t)E^{*}(\vec{q},t)\rangle_{t}}\,. \tag{2.20}$$

Because the amplitude of the electromagnetic field is the Fourier transform of the density distribution or the state function in real space, (2.20) holds exactly the same information as (2.13) and can therefore be used to characterize diffusive motion. Due to the so called phase problem, which describes the fact that no detector is currently fast enough to detect the modulation in an electromagnetic field, straight forward measurement of the amplitudes of the electromagnetic field is not possible. Even though phase retrieval techniques progress very fast, they can not cover time intervals small enough to be in the order of diffusive motion. It is, therefore, extremely difficult to measure (2.20) directly. It is, however, comparably easy to measure the scattering intensities $I(\vec{q})$. A so called intensity autocorrelation function can be defined in a similar fashion as (2.20) in the following way:

$$g^{(2)}(\vec{q},\Delta t)=\frac{\langle I(\vec{q},t)\,I(\vec{q},t+\Delta t)\rangle_{t}}{\langle I(\vec{q},t)\rangle_{t}^{2}} \tag{2.21}$$

In order to find a connection between (2.20) and (2.21) we use the fact that the intensity is the absolute square of the amplitude of the electromagnetic field $I(\vec{q},t)=E(\vec{q},t)\,E^{*}(\vec{q},t)$, rewriting (2.21) in the following way:

$$g^{(2)}(\vec{q},\Delta t)=\frac{\langle E(\vec{q},t)\,E^{*}(\vec{q},t)\,E(\vec{q},t+\Delta t)\,E^{*}(\vec{q},t+\Delta t)\rangle_{t}}{\langle E(\vec{q},t)\,E^{*}(\vec{q},t)\rangle_{t}^{2}} \tag{2.22}$$

When the statistics of the electromagnetic field are Gaussian of zero mean, which is the case if the fields of individual sources are not influencing each other (individual scatterers), only the second moments have to be considered. Therefore Isserlis' theorem (see e.g. [Mich 09]) is applicable and correlation functions of the right-hand side of (2.22) can be expressed as a sum of all the possible products of two-time field correlations:

$$\begin{aligned}
&\langle E(t)E^{*}(t)E(t+\Delta t)E^{*}(t+\Delta t)\rangle_{t}\\
&=\langle E(t)E^{*}(t)\rangle_{t}\langle E(t+\Delta t)E^{*}(t+\Delta t)\rangle_{t}+\langle E(t)E(t+\Delta t)\rangle_{t}\langle E^{*}(t+\Delta t)E^{*}(t)\rangle_{t}+\\
&\langle E(t)E^{*}(t+\Delta t)\rangle_{t}\langle E(t+\Delta t)E^{*}(t)\rangle_{t} &\text{(2.23a)}\\
&=\langle I(\vec{q},t)\rangle_{t}^{2}+\langle|E_{0}|\mathrm{e}^{\mathrm{i}\phi}|E_{0}|\mathrm{e}^{\mathrm{i}(\phi+\Delta\phi)}\rangle_{t}\langle|E_{0}|\mathrm{e}^{-\mathrm{i}(\phi+\Delta\phi)}|E_{0}|\mathrm{e}^{-\mathrm{i}\phi}\rangle_{t}+\\
&\langle E(t)E^{*}(t+\Delta t)\rangle_{t}\langle E(t+\Delta t)E^{*}(t)\rangle_{t} &\text{(2.23b)}
\end{aligned}$$

As the phase factor is not correlated with the modulus of the amplitude of the electromagnetic field, each factor of the middle part of (2.23b) can be rewritten as

$$\left\langle|E_{0}|\mathrm{e}^{\mathrm{i}\phi}|E_{0}|\mathrm{e}^{\mathrm{i}(\phi+\Delta\phi)}\right\rangle_{t}=\left\langle\mathrm{e}^{-\mathrm{i}\phi}\right\rangle_{t}\left\langle|E_{0}|^{2}\mathrm{e}^{\mathrm{i}\Delta\phi}\right\rangle_{t}\,. \tag{2.24}$$

The time average of the phase-factor is zero, $\left\langle \mathrm{e}^{-\mathrm{i}\phi} \right\rangle_t = 0$. Therefore

$$g^{(2)}(\vec{q}, \Delta t) = 1 + \left(\frac{\langle E(\vec{q}, t)\, E^*(\vec{q}, t + \Delta t) \rangle_t}{\langle E(\vec{q}, t)\, E^*(\vec{q}, t) \rangle_t^2} \right)^2 = 1 + \left| g^{(1)}(\vec{q}, \Delta t) \right|^2 . \tag{2.25}$$

This is known as the Siegert relation (see e.g. [Lemi 99]). It was proven that it is fulfilled even under harsh experimental conditions [Gitt 06]. (2.25) gives a direct relation between the intensity autocorrelation function and the amplitude autocorrelation function (2.20), which is in turn directly related to diffusive motion as shown above. In theory, $g^{(2)}(\vec{q}, \Delta t)$ can be measured over an unconfined dynamical range. In an experiment one is only limited by the number of coherent photons scattered by the sample and the readout time of the detector on the one hand, and by the stability of the setup on the other. Using optical light sources and common commercial correlators, Δt can range from nanoseconds to hours, covering a range of twelve orders of magnitude. This is the main reason why the method of dynamic light scattering found extensive use in colloid dynamics research [Peco 85, Cipe 10]. Even though huge progress has been made in the detection of X-rays in the last decades, the accessible time window is considerably smaller. A thorough discussion of this can be found in Chapter 6.

Two-times correlation function

Similar to (2.21), which is an intensity-correlation function of second order, it is possible to define a two-times correlation function. Such a function is an useful concept for checking the temporal evolution of a system. The two-times correlation function is defined as

$$\Gamma(\vec{q}, t_1, t_2) := \frac{\langle I(\vec{q}, t_1) I(\vec{q}, t_2) \rangle}{\langle I(\vec{q}, t_1) \rangle \langle I(\vec{q}, t_2) \rangle} . \tag{2.26}$$

In case where $\Gamma(\vec{q}, t_1, t_2)$ only depends on $\Delta t = t_2 - t_1$, the systems dynamics do not change over time, indicating equilibrium state dynamics. When interested in such processes, as is the case in this work, plotting a two dimensional map therefore gives a good indication whether the system under investigation is in equilibrium. It can, however, also indicate instabilities in the experimental setup.

It shall be mentioned that it is also possible to define correlation functions of higher order, which can be used for further investigations of non equilibrium dynamics. Such processes are, however, not the topic of this thesis.

2.2.3. Solving the rate equation

Dynamics can be formulated in terms of a rate equation for the probability distribution. Theories for diffusion in lattices, in light of probability distributions, are well developed [Haus 87]. Here a somewhat more simplistic approach will be followed.

The probability to find a particle of a certain type at a certain site $\vec{r}$ in a lattice at a certain time $t + \Delta t$, is given by the probability of the particle being at $\vec{r}$ at an earlier time t, reduced by the probability of performing a discrete jump of length $\Delta\vec{r}$ to a neighboring site, plus the probability of a particle having occupied a neighboring site $\vec{r} - \Delta\vec{r}$ and performing a jump to

$\vec{r}$. In a lattice (even in a one dimensional) there is more than one neighboring site at a distance $|\Delta\vec{r}|$. For a finite time interval Δt and a particular jump vector $\Delta\vec{r}$, the flux to and from all equivalent neighboring sites can be approximated by a difference equation:

$$P(\vec{r}, t+\Delta t) \approx \sum_{\Delta\vec{r}} P(\vec{r}, t) - P(\vec{r}, t)\Delta t\, \nu_{\vec{r}\to\vec{r}+\Delta\vec{r}} + P(\vec{r}-\Delta\vec{r}, t)\Delta t\, \nu_{\vec{r}-\Delta\vec{r}\to\vec{r}} \tag{2.27}$$

Jumps are considered to be independent. The appropriate jump rates are given by $\nu_{\vec{r}\to\vec{r}'}$. For $\lim_{\Delta t\to 0}$ this becomes exact and can be used to formulate a differential equation which is usually referred to as rate equation:

$$\frac{\partial}{\partial t}P(\vec{r}, t) = \sum_{\Delta\vec{r}} \left(P(\vec{r}-\Delta\vec{r}, t)\, \nu_{\vec{r}-\Delta\vec{r}\to\vec{r}} - P(\vec{r}, t)\, \nu_{\vec{r}\to\vec{r}+\Delta\vec{r}} \right). \tag{2.28}$$

It is also possible that jumps to neighboring sites at different distances take place. Considering a Bravais lattice let $\{\Delta\vec{r}_n\}$ be the set of jump vectors leading to sites in the neighboring shell of number n. With this, the rate equation in the general form becomes

$$\frac{\partial}{\partial t}P(\vec{r}, t) = \sum_{n}\sum_{\Delta\vec{r}_n} \left(P(\vec{r}-\Delta\vec{r}_n, t)\, \nu_{\vec{r}-\Delta\vec{r}_n\to\vec{r}} - P(\vec{r}, t)\, \nu_{\vec{r}\to\vec{r}+\Delta\vec{r}_n} \right). \tag{2.29}$$

Under the assumption that the jump frequency is only dependent on the jump distance $\nu_{\vec{r}\to\vec{r}+\Delta\vec{r}_n} = \nu_{\vec{r}-\Delta\vec{r}_n\to\vec{r}} = \nu_n = \tau_0^{-1} p_n$, where τ_0 is the average residence time of the particle and p_n the normalized probability for the particle to jump to any one particular neighboring site in neighbor shell n, (2.29) simplifies to

$$\frac{\partial}{\partial t}P(\vec{r}, t) = \frac{1}{\tau_0}\sum_{n} p_n \sum_{\Delta\vec{r}_n} \left(P(\vec{r}-\Delta\vec{r}_n, t) - P(\vec{r}, t) \right). \tag{2.30}$$

This can be solved using the standard Fourier transform method:

$$\begin{aligned}\frac{\partial}{\partial t}\mathscr{F}(P)(\vec{q}, t) &= \frac{1}{\tau_0}\sum_{n} p_n \sum_{\Delta\vec{r}_n} \left(\int \mathrm{d}\vec{r}\,' P(\vec{r}\,', t)\mathrm{e}^{-\mathrm{i}\vec{q}\cdot(\vec{r}\,'+\Delta\vec{r}_n)} - \int \mathrm{d}\vec{r}\, P(\vec{r}, t)\mathrm{e}^{-\mathrm{i}\vec{q}\cdot\vec{r}} \right) \\ &= \mathscr{F}(P)(\vec{q}, t)\, \tau_0^{-1} \sum_{n} p_n \sum_{\Delta\vec{r}_n} \left(\mathrm{e}^{-\mathrm{i}\vec{q}\cdot\Delta\vec{r}_n} - 1 \right)\end{aligned} \tag{2.31}$$

Let us consider the case where $P(\vec{r}, t)$ is the probability of finding a certain particle at $\vec{r}$ and t and $P(\vec{r}+\Delta\vec{r}, t+\Delta t)$ is the probability of finding the same particle at $\vec{r}+\Delta\vec{r}$ and $t+\Delta t$. Assuming that the particle started at the origin at time zero, $P(\Delta\vec{r}, 0) = \delta(\vec{r})$, and applying this as boundary condition to (2.31) the self correlation function [Chud 61] can be defined:

$$\mathscr{F}(G_\mathrm{S})(\vec{q}, t) = \exp\left(-\frac{1}{\tau_0}\sum_{n} p_n \sum_{\Delta\vec{r}_n} \left(1 - \mathrm{e}^{-\mathrm{i}\vec{q}\cdot\Delta\vec{r}_n} \right) t \right) \tag{2.32}$$

We define a $\vec{q}$-dependent self correlation time:

$$\tau_\mathrm{S}(\vec{q}) = \frac{\tau_0}{\sum_n p_n \sum_{\Delta\vec{r}_n} \left(1 - \mathrm{e}^{-\mathrm{i}\vec{q}\cdot\Delta\vec{r}_n} \right)}, \tag{2.33}$$

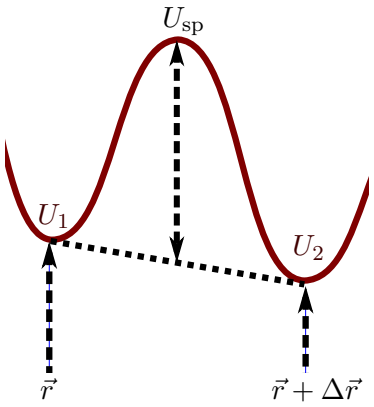

Figure 2.5.: Schematic representation of energy landscape determining jump rates of particles.

which can be written as

$$\tau_{\mathrm{S}}(\vec{q}) = \frac{\tau_0}{\sum_n \bar{p}_n \left(1 - Z_n^{-1} \sum_{\Delta\vec{r}_n} \cos(\vec{q}\cdot\Delta\vec{r}_n)\right)}, \tag{2.34}$$

if the lattice has inversion geometry where for every lattice $\Delta\vec{r}$ there exists a vector $\Delta\vec{r}\,'$ such that $\Delta\vec{r}\,' = -\Delta\vec{r}$, which is the case for Bravais lattices as considered here. Here $\bar{p}_n$ gives the probability of a particle to jump to any site in the neighboring shell ($\bar{p}_n = Z_n p_n$), where Z_n is the coordination number, thus the number of neighbors in shell n.

As this $\vec{q}$-dependent self correlation time is what is measured by incoherent scattering methods, it is also often referred to as the incoherent correlation time $\tau_{\mathrm{inc}}(\vec{q})$. Considering (2.18c) we get a model-dependent result for the amplitude self correlation function:

$$g_{\mathrm{S}}^{(1)}(\vec{q},t) = \mathscr{F}(G_{\mathrm{S}})(\vec{q},t) = \exp\left(-\frac{t}{\tau_{\mathrm{S}}(\vec{q})}\right) \tag{2.35}$$

Only the cornerstones of the ansatz by Leitner [Leit 11, Leit 12a], that is necessary to treat site-dependent jump rates, will be given. When considering pair correlations, whose underlying principle is particle interaction, the assumption that local jump frequencies vary in a negligible way does not hold anymore. Assessing all jumps by a constant jump frequency which led to (2.30) is therefore incorrect. For an individual jump, the jump probability is a function of temperature and the local energetic landscape, as shown in Fig. 2.5. According to transition state theory [Eyri 35, Evan 35, Vine 57] the jump rate is determined by the energy difference $U_{sp} - U_1$.

$$\nu_{\sigma_1\to\sigma_2} = \nu_{\Delta\vec{r}} \exp\left(-\frac{U_{sp}(\vec{r},\vec{r}+\Delta\vec{r};\sigma_1) - U(\sigma_1)}{k_{\mathrm{B}}T}\right) \tag{2.36}$$

Here $\nu_{\Delta\vec{r}}$ gives the average jump frequency of jumps of length $\vec{r}$ and a state function was introduced, giving the state of occupation of a certain position $\vec{r}$:

$$\sigma^X(\vec{r}) = \begin{cases} 1 & \text{if } X \text{ at } \vec{r} \\ 0 & \text{otherwise} \end{cases} \tag{2.37}$$

The difference between the states σ_1 and σ_2 is that a particle has been moved by $\Delta\vec{r}$. The energy U can be approximated by a cluster expansion [Sanc 84, Lerc 09] using interaction terms V_i, with i being the order of interaction (e.g. 2 for pairs):

$$U(\sigma) = V_0 + V_1 \sum_{X;\vec{r}} \sigma^X(\vec{r}) + \sum_{X,Y;\vec{r}} \sum_{\Delta\vec{r}} V_2^{XY}(\Delta\vec{r})\sigma^X(\vec{r})\sigma^Y(\vec{r}+\Delta\vec{r}) + \mathscr{O}(i \geq 3)\,, \tag{2.38}$$

For a binary system defining $V_2 := V_2^{AA} + V_2^{BB} - 2V_2^{AB}$ [Duca 91] is used to reduce the number of pair interaction parameters.

As was shown by Leitner [Leit 11, Leit 12a], solving the rate equation with these jump frequencies in the context of a linear theory yields the following expression of the rate equation:

$$\frac{\partial}{\partial t}\mathscr{F}(P)(\vec{q},t) = \frac{1}{\tau_0}\sum_n p_n \sum_{\Delta\vec{r}_n} \mathscr{F}(P)(\vec{q},t)\,\left(1 + \frac{\hat{V}(\vec{q})}{k_\mathrm{B}T}c(1-c)\right)\left(\mathrm{e}^{-\mathrm{i}\vec{q}\cdot\Delta\vec{r}_n} - 1\right) \tag{2.39}$$

which yields, applied to the pair correlation function

$$\mathscr{F}(G)(\vec{q},t) = \exp\left(\frac{1}{\tau_0}\sum_n p_n \sum_{\Delta\vec{r}_n}\left(\mathrm{e}^{-\mathrm{i}\,\vec{q}\cdot\Delta\vec{r}_n} - 1\right)\left(1 + \frac{\hat{V}_2(\vec{q})}{k_\mathrm{B}T}c(1-c)\right)t\right)\,. \tag{2.40}$$

The Fourier transform of a pair potentials $\hat{V}_2(\vec{q})$ is related to the short-range order intensity in Laue units (LUs) by the Clapp-Moss relation [Clap 66, Leit 12a]:

$$I_\mathrm{SRO}(\vec{q}) = \frac{1}{1 + \frac{\hat{V}_2(\vec{q})(c(1-c))}{k_\mathrm{B}T}} \tag{2.41}$$

This allows to write the correlation time as

$$\tau(\vec{q}) = \frac{\tau_0\, I_\mathrm{SRO}(\vec{q})}{\sum_n p_n \sum_{\Delta\vec{r}_n}\left(\mathrm{e}^{-\mathrm{i}\,\vec{q}\cdot\Delta\vec{r}_n} - 1\right)}\,, \tag{2.42}$$

and the amplitude-correlation function as

$$g^{(1)}(\vec{q}) = \mathscr{F}(G)(\vec{q},t) = \exp\left(\frac{t}{\tau(\vec{q})}\right)\,. \tag{2.43}$$

As can be seen from (2.33) and (2.42) a relation between the self correlation time and the correlation time including pair distributions is given by

$$\tau(\vec{q}) = \tau_\mathrm{S}(\vec{q})\, I_\mathrm{SRO}(\vec{q})\,. \tag{2.44}$$

This is the same result as found by Sinha and Ross [Sinh 88] and is also known as De Gennes narrowing [De G 59], which was first introduced for a qualitative description of coherent neutron scattering results in liquids.

Combining (2.18),(2.25) and (2.43) allows to connect the experimentally determinable intensity-correlation function to the Van Hove correlation function via the model dependent parameter

$\tau(\vec{q})$:

$$g^{(2)}(\vec{q},\Delta t) = 1 + \exp\left(\frac{-2\,\Delta t}{\tau(\vec{q})}\right) . \tag{2.45}$$

Non-Bravais lattice

For a non Bravais lattice, the rate equation becomes more general as jumps between the individual sublattices and within the superstructure have to be considered. An extension of the model by Chudley and Elliott [Chud 61], (2.32) was first discussed by Rowe [Rowe 71]. Let us consider a lattice consisting of m individual sites per primitive unit cell or Bravais sublattices. For simplicity only nearest-neighbor jumps $\Delta\vec{r}_1^{\,\lambda\mu}$ $(n = 1)$ between a lattice μ and a lattice λ will be considered at the beginning. Assuming equal occupation of the sublattices and an equal jump rate between the sublattices $(1/\tau_0)$ the rate equation can be written as

$$\frac{\partial}{\partial t}P^\lambda(\vec{r},t) = \frac{1}{\tau_0 Z^{\lambda\mu}}\sum_{\mu=1}^{m}\sum_{\Delta\vec{r}_1^{\,\lambda\mu}}\left(P^\mu(\vec{r}-\Delta\vec{r}_1^{\,\lambda\mu},t) - P^\lambda(\vec{r},t)\right) , \tag{2.46}$$

where $Z^{\lambda\mu} = Z^{\mu\lambda}$ is the coordination number, which gives the number of neighboring sites on sublattice μ for a site in sublattice λ. If the jump rates differ, this can be accounted for [Ande 84] by introducing individual residence times $\tau^{\lambda\mu}$:

$$\frac{\partial}{\partial t}P^\lambda(\vec{r},t) = \frac{1}{Z^{\lambda\mu}}\sum_{\mu=1}^{m}\sum_{\Delta\vec{r}_1^{\,\lambda\mu}}\left(\frac{1}{\tau^{\mu\lambda}}P^\mu(\vec{r}-\Delta\vec{r}_1^{\,\lambda\mu},t) - \frac{1}{\tau^{\lambda\mu}}P^\lambda(\vec{r},t)\right) , \tag{2.47}$$

For systems with a long-range order, the probability for a particle of a certain type to occupy a certain sublattice varies. The probability of finding a particle at sublattice μ shall be given by $W^\mu = c_X^\mu/c_X$, where c_X^μ is the partial concentration of particles of type X on sublattice μ and c^X is the overall concentration $(\sum_\mu^m W^\mu = 1)$. It shall be noted, that the probability of finding a particle on any sublattice at position $\vec{r}$ is given by $P(\vec{r},t) = \sum_\mu^m W^\mu P^\mu(\vec{r},t)$ and detailed balance demands $\frac{W^\lambda}{\tau^{\lambda\mu}Z^{\lambda\mu}} = \frac{W^\mu}{\tau^{\mu\lambda}Z^{\mu\lambda}}$.

Fourier transforming (2.47) yields

$$\frac{\partial}{\partial t}\mathscr{F}(P^\lambda)(\vec{q},t) = \frac{1}{Z^{\lambda\mu}}\sum_{\mu}\sum_{\Delta\vec{r}_1^{\,\lambda\mu}}\left(\frac{1}{\tau^{\mu\lambda}}\mathscr{F}(P^\mu)(\vec{q},t)\,\mathrm{e}^{-\mathrm{i}\,\vec{q}\cdot\Delta\vec{r}_1^{\,\lambda\mu}} - \frac{1}{\tau^{\lambda\mu}}\mathscr{F}(P^\lambda)(\vec{q},t)\right) . \tag{2.48}$$

Equation (2.48), defining the entry for the λth sublattice as $g_{\mathrm{S}}^{\lambda(1)}(\vec{q},t) := \mathscr{F}(P^\lambda)(\vec{q},t)$, can be written in matrix notation as:

$$\frac{\partial}{\partial t}\boldsymbol{g}_{\mathrm{S}}^{(1)}(\vec{q},t) = \tilde{\boldsymbol{A}}\,\boldsymbol{g}_{\mathrm{S}}^{(1)}(\vec{q},t)\,, \tag{2.49}$$

with the diffusion or jump matrix $\tilde{\boldsymbol{A}}$ of size $m \times m$. The elements of this matrix are defined [Ande 84, Rand 94] as

$$A^{\lambda\mu} = \frac{1}{\tau^{\mu\lambda}Z^{\mu\lambda}}\sum_{\Delta\vec{r}^{\,\mu\lambda}}\exp\left(-\mathrm{i}\,\vec{q}\cdot\Delta\vec{r}^{\,\mu\lambda}\right) - \delta_{\lambda\mu}\sum_{\mu}\frac{1}{\tau^{\lambda\mu}}\,. \tag{2.50}$$

As $\frac{1}{\tau^{\mu\lambda}}$ is the frequency of jumps from a particular site in the sublattice λ to a particular neighboring site in the sublattice μ, $\frac{Z^{\lambda\mu}}{\tau^{\mu\lambda}}$ is the frequency for jumps to any neighboring site in the sublattice μ.

In a case where $\tau^{\lambda\mu} \neq \tau^{\mu\lambda}$, the jump matrix $\tilde{\boldsymbol{A}}$ is non-Hermitian. It can, however be transformed into a Hermitian matrix [Kutn 77, Rand 94], due to detailed balance by similarity transformation

$$\tilde{\boldsymbol{B}} = \tilde{\boldsymbol{T}}\tilde{\boldsymbol{A}}\tilde{\boldsymbol{T}}^{-1}\,, \tag{2.51}$$

where

$$T^{\lambda\mu} = \frac{1}{\sqrt{W^{\lambda}}}\delta_{\lambda\mu}\,. \tag{2.52}$$

As the eigenvalues of a Hermitian matrix are always real and because the eigenvalues of $\tilde{\boldsymbol{B}}$ are also eigenvalues of $\tilde{\boldsymbol{A}}$ due to (2.51), the jump matrix has real eigenvalues which are called ϵ_j. The rate equation in matrix form (2.49) can be rewritten:

$$\frac{\partial}{\partial t}\tilde{\boldsymbol{T}}\boldsymbol{g}_{\mathrm{S}}^{(1)}(\vec{q},t) = \tilde{\boldsymbol{B}}\,\tilde{\boldsymbol{T}}\boldsymbol{g}_{\mathrm{S}}^{(1)}(\vec{q},t)\,, \tag{2.53}$$

which yields the solution

$$\tilde{\boldsymbol{T}}\boldsymbol{g}_{\mathrm{S}}^{(1)}(\vec{q},t) = \sum_j \exp(\epsilon_j t)\underline{K}_j \cdot \vec{b}_j^{\,*}\,. \tag{2.54}$$

Here $\vec{b}_j$ are the eigenvectors of $\tilde{\boldsymbol{B}}$ and $\underline{K}_j^{\lambda} = b_j^{\lambda *}\sqrt{1/W^{\lambda}}$ as shown by [Rand 94] .

After some algebra [Rand 94] this leads to a solution for the Fourier transform of the rate equation

$$g_{\mathrm{S}}^{(1)}(\vec{q},t) = \sum_j \underbrace{\left|\sum_{\lambda}\sqrt{W^{\lambda}}b_j^{\lambda}\right|^2}_{w_j}\exp(\epsilon_j t) \tag{2.55a}$$

$$=: \sum_j w_j \exp\left(\frac{t}{-\tau_{\mathrm{S}_j}(\vec{q})}\right)\,, \tag{2.55b}$$

where b_j^{λ} is the λ-th component of the j-th eigenvector. The self-intermediate scattering function is therefore a weighted sum of exponential functions. In order to find the amplitude-correlation function that includes pair distributions, short-range order information has to be included.

The intensity-correlation function is then given by

$$g^{(2)}(\vec{q},t) = 1 + \left(\sum_j w_j \exp\left(-\frac{t}{\tau_j(\vec{q})}\right)\right)^2\,. \tag{2.56}$$

2.2.4. The short-range order term I_{SRO}

According to (2.44) the $\vec{q}$-dependent self correlation time $\tau_{\mathrm{S}}(\vec{q})$ and the pair correlation time $\tau(\vec{q})$ are linked by a term accounting for the short-range order in the system, which is the short-range order intensity I_{SRO}. This $\vec{q}$-dependent term can be calculated using the so-called

Warren-Cowley parameters α_n [Cowl 60]. For a binary system these parameters are defined as

$$\alpha_n = 1 - \frac{\omega_n^{X,Y}}{c_Y}\,, \tag{2.57}$$

where $\omega_n^{X,Y}$ is the probability of finding an atom of type Y in the n-th neighbor shell of an atom of type X and c_Y is the concentration of atoms of type Y. The short-range order intensity can thus be calculated:

$$I_{\mathrm{SRO}}(\vec{q}) = \sum_{n,j} \alpha_n \cos\left(\vec{q}\cdot\Delta\vec{r}_{n_j}\right) \tag{2.58}$$

Finding the α_n-parameters is, however, not straightforward, as will be discussed in Chapter 4.

α_n-parameters in non-Bravais systems

In a system with strong long-range order, calculation of the short-range order parameters according to (2.57) will result in a series of non-converging parameters. For a B2 system with perfect order for example, (2.57) yields:

$$\omega_n = \begin{cases} 1 & \text{if } 2h, 2k \text{ and } 2l \text{ are all odd} \\ -1 & \text{if } 2h, 2k \text{ and } 2l \text{ are all even} \end{cases} \tag{2.59}$$

Calculating the intensity according to (2.58) and (2.59) produces an infinite sum yielding superstructure peaks. Small deviations from perfect order will only lead to small deviations from this. In order to calculate the local variations of chemical order, it is therefore advisable to split the superstructure into its sublattices and calculate the short-range order terms for each sublattice μ separately, using $\alpha_{\tilde{n}}^{\mu} = 1 - \frac{\omega_{\tilde{n}}^{X,Y}}{c_Y^{\mu}}$. Here $\tilde{n}$ indicates the number of the neighboring shell within the sublattice. Neglecting short-range order between sublattices, which is small compared to long-range order in ordered systems, the total short-range order intensity is given by

$$I_{\mathrm{SRO}}(\vec{q}) = \frac{1}{m}\frac{1}{c(1-c)}\sum_{\mu}^{m} c^{\mu}(1-c^{\mu}) I_{\mathrm{SRO}}^{\mu}(\vec{q})\,, \tag{2.60}$$

where c is the overall concentration of component X (the concentration of component Y is $(1-c)$, respectively) and c^{μ} the concentration of component X on sublattice μ.

A B2 system consists of two sublattices with a simple cubic structure. The relation between the neighboring shells in the B2 structure numbered by n and the neighbor shells within one of the sublattices μ_1 or μ_2 which are numbered by $\tilde{n}$, is given in Table 2.1. The set of vectors $\langle hkl\rangle$ points to the appropriate positions in the shell.

2.2.5. Explicit formula for diffusion in cubic Bravais lattices

In (2.34) as well as in (2.58) appears a sum over a number of cosine terms for the corresponding position vectors of atoms in a certain neighboring shell. In this thesis cubic Bravais lattices will

	neighboring shell B2 n	neighboring shell sublattice μ $\tilde{n}$
$\langle 100 \rangle$	2	1
$\langle 110 \rangle$	3	2
$\langle 111 \rangle$	5	3
$\langle 200 \rangle$	6	4
$\langle 210 \rangle$	8	5
$\langle 211 \rangle$	9	6

Table 2.1.: Relation of shell-numbering for lattice and sublattice in case of a B2 system

be treated, for which these terms can be analytically calculated. The sum

$$C_n(\vec{q}) := Z_n^{-1} \sum_{j=1}^{Z_n} \cos\left(\vec{q} \cdot \Delta\vec{r}_{n_j}\right) , \tag{2.61}$$

can be rewritten as

$$\begin{aligned} C_n(\vec{q}) = \frac{1}{6}\Big(& \cos(q_x h)\cos(q_y k)\cos(q_z l) + \cos(q_x h)\cos(q_y l)\cos(q_z k) \\ & + \cos(q_x k)\cos(q_y h)\cos(q_z l) + \cos(q_x k)\cos(q_y l)\cos(q_z h) \\ & + \cos(q_x l)\cos(q_y k)\cos(q_z h) + \cos(q_x l)\cos(q_y h)\cos(q_z k)\Big) \end{aligned} \tag{2.62}$$

There exist of course a number of special cases where this expression can be further simplified, as can be seen in Table 2.2. Z_n, the number of neighbors in the n-th shell is also given for the sake of completeness.

$\langle hkl \rangle$	Z_n	C_n
$\langle \xi 00 \rangle$	6	$\frac{1}{3}\Big(\cos(q_x\xi) + \cos(q_y\xi) + \cos(q_z\xi)\Big)$
$\langle \xi\xi\xi \rangle$	8	$\cos(q_x\xi)\cos(q_y\xi)\cos(q_z\xi)$
$\langle \xi\xi 0 \rangle$	12	$\frac{1}{3}\Big(\cos(q_x\xi)\cos(q_y\xi) + \cos(q_x\xi)\cos(q_z\xi) + \cos(q_y\xi)\cos(q_z\xi)\Big)$
$\langle \xi\xi\zeta \rangle$	24	$\frac{1}{3}\Big(\cos(q_x\zeta)\cos(q_y\xi)\cos(q_z\xi) + \cos(q_x\xi)\cos(q_y\zeta)\cos(q_z\xi) + \cos(q_x\xi)\cos(q_y\xi)\cos(q_z\zeta)\Big)$
$\langle \xi\zeta 0 \rangle$	24	$\frac{1}{6}\Big(\cos(q_x\xi)\cos(q_y\zeta) + \cos(q_x\zeta)\cos(q_y\xi) + \cos(q_x\xi)\cos(q_z\zeta) + \cos(q_x\zeta)\cos(q_z\xi) + \cos(q_y\xi)\cos(q_z\zeta) + \cos(q_y\zeta)\cos(q_z\xi)\Big)$

Table 2.2.: Special cases of cosine terms.

2.3. The contrast factor

2.3.1. Contrast and coherence

Only when all the electromagnetic waves have a constant phase relation and the same frequency, (2.25) holds. In this case one speaks of total coherence. If the waves are only partly coherent, the interference pattern is washed out, which leads to a decrease in contrast. This is reflected

in the normalized amplitude-correlation function (2.20) being compressed along the ordinate ($g_{\mathrm{m}}^{(1)}(\vec{q},0) < 1$). One accounts for this effect by introducing an experimental contrast factor, β_{exp}. With this, the relation between the measured intensity auto correlation function $g_{\mathrm{m}}^{(2)}(\vec{q},\Delta t)$ and the theoretical value of the Fourier transform of the Van Hove correlation function is given by

$$g_{\mathrm{m}}^{(2)}(\vec{q},\Delta t) = 1 + \beta_{\mathrm{exp}} \left| g^{(1)}(\vec{q},\Delta t) \right|^2 . \tag{2.63}$$

Coherence can be quantified by means of a complex cross correlation function [Laut 93]. Let us define a correlation function similar to (2.19), but for wavefronts propagating in a real space:

$$\mathscr{G}_{ij}(\Delta t) = \langle E(\vec{r}_i,t) E^*(\vec{r}_j,t+\Delta t)\rangle_t = \lim_{t_0\to\infty} \int_{-t_0/2}^{t_0/2} \mathrm{d}t\, E(\vec{r}_i,t) E^*(\vec{r}_j,t+\Delta t) \tag{2.64}$$

This is a measure for the temporal evolution of the electromagnetic waves at certain positions in space. The coherence dependent contrast can then be defined as

$$B_{ij}(\Delta t) = \left| \frac{2\,\mathscr{G}_{ij}(\Delta t)}{\mathscr{G}_{ii}(0) + \mathscr{G}_{jj}(0)} \right| . \tag{2.65}$$

Temporal coherence can be defined as the time window where $B_{ii}(t_{\mathrm{coh}}) > 1/\mathrm{e}$. This can be used to introduce a longitudinal coherence length $\xi_{\mathrm{l}} = t_{\mathrm{coh}} c$, where c is the speed of wave-propagation. The concept of a transversal coherence length can be introduced for two points $\vec{r}_i$ and $\vec{r}_i$ with $\xi_{\mathrm{tr}} = |\vec{r}_i - \vec{r}_j|$ and $B_{ij}(0) > 1/\mathrm{e}$.

The electromagnetic field resulting from the interference of two waves starting at different points $\vec{r}_1$ and $\vec{r}_2$ in space, can be written as $E = E_1 + E_2$. With this the intensity I can be written as:

$$I = \langle E E^* \rangle = \langle (E_1 + E_2)(E_1 + E_2)^* \rangle \tag{2.66a}$$

$$= \langle E_1 E_1^* \rangle + \langle E_2 E_2^* \rangle + \langle E_1 E_2^* \rangle + \langle E_2 E_1^* \rangle \tag{2.66b}$$

$$= I_1 + I_2 + 2\,\mathrm{Re}\Big(\langle E_1 E_2^* \rangle \Big) \tag{2.66c}$$

Assuming, that the amplitudes of the electromagnetic waves are equal for all point sources ($I_1 = I_2 = I_0$), the most and the least intense part of the scattering pattern can be identified as $I_{\max} = 2\,I_0 + 2\,|\mathscr{G}_{ii}(\Delta t)|$ and $I_{\min} = 2\,I_0 - |2\mathscr{G}_{ii}(\Delta t)|$.

The intensity contrast β resulting from two electromagnetic waves at two points in space, $\vec{r}_1$ and $\vec{r}_2$, can be defined as:

$$\beta(\Delta t) := \frac{I_{\max}(\Delta t_1) - I_{\min}(\Delta t_2)}{I_{\max}(\Delta t_1) + I_{\min}(\Delta t_2)} = 2\frac{\sqrt{\mathscr{G}_{11}(0)\mathscr{G}_{22}(0)}}{\mathscr{G}_{11}(0) + \mathscr{G}_{22}(0)} \, |B_{12}(\Delta t)| \tag{2.67}$$

$I_{\max}$ is the highest intensity in the interference pattern, $I_{\min}$ correspondingly the lowest and $\Delta t \in [\Delta t_1, \Delta t_2[$. Therefore, in case the amplitudes of the fields emitted at $\vec{r}_1$ and $\vec{r}_2$ are the same ($\mathscr{G}_{11}(0) = \mathscr{G}_{22}(0)$), the intensity contrast is the absolute value of the contrast of the electromagnetic field $\beta(\Delta t) = |B_{12}(\Delta t)|$.

2.3.2. Contrast and dynamics

It is possible that dynamical processes take place on more than one timescale. A very fast process, which is not detectable, could reduce the coherence of a system to a certain degree before a slower, detectable process, leads to an evident decrease of the intensity-correlation function. This can be accounted for by a systematic coherence factor, β_{sys}.

Summing up the relation between measured intensity-correlation function and theoretical model is given by

$$g_{\mathrm{m}}^{(2)}(\vec{q}, \Delta t) = 1 + \beta_{\mathrm{sys}}\, \beta_{\mathrm{exp}} \left| g^{(1)}(\vec{q}, \Delta t) \right|^2 = 1 + \beta \left| g^{(1)}(\vec{q}, \Delta t) \right|^2 . \tag{2.68}$$

The pre factor β is referred to as a contrast or Siegert factor in the literature [Shpy 14].

3. Models of diffusion in metals

This chapter gives a short and selective overview over some theoretical concepts of diffusion, which are important for aXPCS. For a more general and complete overview over the topic see e.g [Bocq 96, Murc 01, Mehr 07]. Particular attention will be given to different atomistic diffusion mechanisms, as this is the field where aXPCS presents itself as a powerful new method. As a model system a B2 system consisting of type A and type B atoms with atomic concentrations c_A and c_B is chosen to illustrate different mechanisms. Two sublattices are introduced (α and β) and the possible defects are a vacancy on each sublattice (V_α and V_β) and the appropriate antisites A_β and B_α. The results can be generalized for other systems, like $L1_2$, $D0_3$ or $L1_0$ etc. Dealing with all of them would, however, go beyond the scope of this work.

Diffusive motion is characterized by the diffusion constant D, which can be calculated according to the Einstein-Smoluchowski relation [Eins 05] as

$$D = \frac{\langle R^2 \rangle}{6\tau_0} \,. \tag{3.1}$$

Here $\langle R^2 \rangle$ is the mean squared displacement of the atom due to the diffusive motion. τ_0 is the average residence time of an atom at a position in the lattice, which is the inverse of the average jump frequency, $\nu_0 = \tau_0^{-1}$. For uncorrelated jumps that occur with a certain probability, p_n, and result in an effective jump to a position in shell n, the mean squared displacement can be written as the sum of mean squared displacements resulting from these jumps $\langle R^2 \rangle = \sum_n \bar{p}_n \langle \Delta r_n^2 \rangle$.

The following overview of diffusion mechanisms is restricted to diffusion on a lattice in the bulk. Boundary effects like surface diffusion or grain boundary diffusion will not be treated. In a system with lattice structure, the average jump frequency usually depends on the availability and mobility of vehicles mediating diffusion.

3.1. Classification of diffusion in solids

One of the established classifications divides diffusion into three types of vehicle mediated mechanisms. These are **the vacancy mechanism**, **the interstitial mechanism** and **the interstitialcy mechanism**. The vacancy mechanism describes a movement of vacancies through the lattice occupied by the diffusing atoms. This movement usually takes place by a nearest-neighbor exchange of the vacancy and an atom. In the interstitial mechanism, atoms sitting on interstices can jump directly to a neighboring, empty interstice. The interstitialcy mechanism describes a movement of an atom on the main lattice into an empty interstice, making space for another atom at the interstitial lattice to take its place. It is, however, possible to view the main lattice and the interstitial lattice as two different sub-lattices. In this picture, the vacancy migrating on one sub-lattice, which is filled with atoms, while the other sub-lattice is empty or

filled with another type of atoms, would coincide with the vacancy mechanism. In the interstitial mechanism picture, the second sub-lattice would be partly filled with atoms, meaning that the vacancy concentration is very high, giving the atoms many choices of exchanging there position with a vacancy. The interstitialcy mechanism can also be described by a vacancy, moving from one sub-lattice to the other and exchanging position with different types of atoms. Therefore, in all cases, empty lattice sites or vacancies can be seen as the vehicle of diffusion. This also explains, why diffusion via the interstitial mechanism is usually faster than via the vacancy mechanism, as there are simply more vehicles available.

Another possible classification is by the type of atom that diffuses in a certain environment.

Self diffusion describes the movement of an atom of type A on a lattice filled with atoms of the same type.

Tracer diffusion describes the movement of a particular atom of type A', which is an isotope of A, on a lattice filled with atoms of type A.

Impurity diffusion describes the movement of an atom of type B on a lattice of mainly filled with atoms of type A.

Inter-diffusion describes a concentration gradient driven motion of atoms of type B into a lattice occupied by atoms of type A and vice versa.

Chemical diffusion describes the exchange of atoms of types A and B on a lattice. This movement is due to thermal activation and is not gradient driven. It does, however, depend on the concentration of the components. This is the kind of diffusive motion that can be studied with aXPCS.

The above mentioned assignment is not unambiguous, as different definitions exist in literature. In the case of aXPCS chemical diffusion is studied. The motion of vacancies is usually not directly visible. On the one had their contribution to the scattering intensity is small due to their tiny number and on the other hand they move much faster than the atoms as will be discussed in the following. What can be observed is the exchange of two atoms of different species or the effective exchange of an atom and a vacancy in vacancy rich systems (e.g. Ni–Al with Al excess).

3.2. Time scales of atomic motion

There are five distinguishable timescales of atomic motion in a lattice. The first is the timescale of atomic vibrations, $\tau_{\text{phonon}} = \nu_{\text{phonon}}^{-1}$. It is of the same order as τ_{attempt}, the time an atom attempts a transition. The next timescale is determined by the time it takes for an atom to leave its initial position which is a local minimum in the energy landscape, overcome a local saddle point and settle into the next local minimum. This will be called transition time τ_{trans}. The time between jumps of an atom, τ_{inter}, is much longer than the time the atom requires

to execute such a transition. The fifth defining time is the average residence time of an atom τ_0. As an atom can sequentially execute a number of jumps when a vehicle of diffusion is in the surroundings, the average residence time is the time between the successive arrivals of such vehicles. To sum up, it is evident from this considerations, that

$$\tau_{\text{phonon}} \approx \tau_{\text{attempt}} \approx \tau_{\text{trans}} << \tau_{\text{inter}} << \tau_0 \,. \tag{3.2}$$

3.3. Vacancy mechanisms

For a vacancy mechanism, the average atomic jump frequency depends on the availability and mobility of vacancies. Following [Bocq 96, Mehr 07], the probability of having a vacancy in the vicinity of an atom so that it can act as a vehicle of diffusion for this atom, is given by $W_{\text{V}} = \exp\left(\frac{-\Delta H_{\text{f}} - T\Delta S_{\text{f}}}{k_{\text{B}}T}\right)$. ΔH_{f} is the formation enthalpy and ΔS_{f} the formation entropy of a vacancy, T the temperature and k_{B} the Boltzmann constant. Such a vacancy moves through the lattice by exchanging its position with different neighboring atoms. Therefore, the average vacancy jump frequency ν_{a} is much higher than the average atomic jump frequency ν_0 (the ratio between these jump frequencies is in the order of the vacancy concentration, which is typically not exceeding 10^{-4} in metals). The average vacancy jump frequency can be written as

$$\nu_{\text{V}} = \nu^* \exp\left(\frac{-\Delta H_{\text{m}} - T\Delta S_{\text{m}}}{k_{\text{B}}T}\right) , \tag{3.3}$$

where the migration enthalpy ΔH_{m} is the energy difference of the system between ground state and the saddle point energy, ΔS_{m} the corresponding migration entropy and ν^* can be approximated by the Debye frequency ($\nu_{\text{D}} \approx 10^{-13}\,\text{s}^{-1}$) representing lattice vibrations. More precise calculations of ν^* [Mant 08] can be made by applying first principle calculations and transition state theory [Vine 57]. While vacancies perform a random walk through the lattice, this is not true for the atoms. Considering one particular atom, the jump probability is high when a vacancy is close to the atom and zero when it is far away. This leads to a correlation effect, which is accounted for by the correlation factor $f \leq 1$. The ratio between average vacancy and average effective atomic jump frequency, which does not account for a sequence of jumps where an atom ends up at its starting site, can be written as $\nu_0/\nu_{\text{a}} = W_{\text{V}} f$. If the mean squared displacement $\langle R^2 \rangle$ is temperature-independent, (3.3) and (3.1) can be combined using $\Delta H = \Delta H_{\text{f}} + \Delta H_{\text{m}}$ and $\Delta S = \Delta S_{\text{f}} + \Delta S_{\text{m}}$ to:

$$D = \frac{\langle R^2 \rangle}{6}\nu_0 = \frac{\langle R^2 \rangle f \nu^*}{6} \exp\left(\frac{-\Delta H - T\Delta S}{k_{\text{B}}T}\right) \tag{3.4a}$$

$$D = D_0 \exp\left(\frac{-E_{\text{a}}}{k_{\text{B}}T}\right) \tag{3.4b}$$

This is known as the Arrhenius equation [Arrh 89], where E_{a} is the activation energy per atom and D_0 is referred to as the maximum diffusion coefficient or pre-exponential factor. The activation energy is therefore the sum of the Gibbs free formation energy and the Gibbs free migration energy of the vacancy $E_{\text{a}} = \Delta H_{\text{f}} + T\Delta S_{\text{f}} + \Delta H_{\text{m}} + T\Delta S_{\text{m}}$.

In pure metals the diffusion mechanism is well understood [Mehr 07]. The vacancy moves through the lattice performing nearest-neighbor jumps in an uncorrelated (Markovian) way, which leads to a random walk of the vacancy. For unordered systems, like solid solutions, the situation is very similar. When a vacancy diffuses in an ordered alloy, it must not destroy short- and long-range order of a system in equilibrium. Considering a B2 lattice carrying out random nearest neighbor (NN) jumps, the vacancy would destroy the order because A-atoms from the α-sublattice would end up on the β sublattice and B-atoms would do just the opposite. To avoid this, the vacancy would have to skip the NN position and carry out direct next-nearest-neighbor jumps, or perform a jump either correlated in a timely manner or with other defects. This leads to different diffusion mechanisms, which will be discussed in the following sections.

3.3.1. Vacancy random walk

	sc			bcc			fcc		
n	p_n	$\bar{p}_n$	$\lvert\Delta r_n\rvert$	p_n	$\bar{p}_n$	$\lvert\Delta r_n\rvert$	p_n	$\bar{p}_n$	$\lvert\Delta r_n\rvert$
0	0.16007	0.16007	0	0.12089	0.12089	0	0.08178	0.08178	0
1	0.12273	0.73638	1	0.09644	0.77152	$\sqrt{3/4}$	0.07083	0.84996	$\sqrt{1/2}$
2	0.00683	0.08196	$\sqrt{2}$	0.00900	0.05400	1	0.00365	0.02190	1
3	0.00057	0.00456	$\sqrt{3}$	0.00302	0.03624	$\sqrt{2}$	0.00149	0.03576	$\sqrt{3/2}$
4	0.00186	0.01116	2	0.00029	0.00696	$\sqrt{11/4}$	0.00062	0.00744	$\sqrt{2}$
5	0.00020	0.00480	$\sqrt{5}$	0.00104	0.00832	$\sqrt{3}$	0.00008	0.00192	$\sqrt{5/2}$
6	0.00002	0.00048	$\sqrt{6}$	0.00002	0.00012	2	0.00005	0.00040	$\sqrt{2}$
7	0.00001	0.00012	$\sqrt{8}$	0.00006	0.00144	$\sqrt{19/4}$	0.00002	0.00096	$\sqrt{7/2}$
8	0.00003	0.00072	3	0.00001	0.00024	$\sqrt{5}$	0.00001	0.00006	2
9	0.0	0.0	3	0.00001	0.00024	$\sqrt{6}$	0.0	0.0	$\sqrt{9/2}$
10	0.0	0.0	$\sqrt{10}$	0.00001	0.00008	$\sqrt{27/4}$	0.0	0.0	$\sqrt{9/2}$

Table 3.1.: Probabilities for an atom to end up in a particular position (p_n) or any position ($\bar{p}_n = Z_n p_n$) of neighbor shell n after an encounter as given in Table 2 in [Shol 81]. The displacement length $|\Delta r_n|$ is given in units of the lattice constant.

For a system where a vacancy mechanism takes place, the probability of jumps of a particular atom is enhanced when a vacancy stays in its vicinity. In a short time window several exchanges of the vacancy and one and the same atom are possible. As such a time window, which is given by the period of time between a vacancy reaching the neighborhood of a particular atom and leaving it again, is usually very small compared to the average residence time (the average time between two jumps) of an atom, all the individual jumps of one atom within such a window can be summed up to an effective jump. This time window is called encounter and the probability

for different effective jumps is calculated in the context of the encounter theory. For low vacancy concentrations the vacancies can be seen as individual random walkers while the atoms perform correlated jumps within one encounter, leading to effective jumps that can differ from nearest neighbor jumps. The correlation of such jumps can be accounted for by a correlation factor, originally introduced by Manning [Mann 59] as discussed in Section 3.3. The probability for jumps occurring to a certain neighbor shell n (where $n = 0$ indicates a jump back to or a stay at the original position, $n = 1$ indicates nearest-neighbor jumps, $n = 2$ next-nearest neighbor jumps and so on) have been calculated using computer simulations [Wolf 77], obtained from rate equation theory [Bend 79] or from well known functions of random walk theory [Shol 81]. The values according to [Shol 81] are given in Table 3.1.

Random walk on a sublattice - farther direct vacancy jumps

In order to preserve the order in a lattice, vacancies can move within one sublattice performing e.g. next-nearest or third-nearest neighbor jumps. Calculations [Wynb 67] and simulations [Fahn 99a] indicate, however, that such direct jumps lead to a rather high migration enthalpy of the vacancy for some systems. Additional defects like antisite atoms can lower the energy barrier for a direct next-nearest neighbor jump [Athe 97]. While direct next-nearest neighbor jumps could be possible for particular B2 systems (which corresponds to nearest-neighbor jumps on the sublattice), farther jumps can be ruled out. It shall be mentioned that for systems where computer simulations suggest next-nearest neighbor jumps, experimental evidence against it was found [Fran 01].

3.3.2. Percolation dependent mechanisms

This type of diffusion was recognized relatively late. It relies on the percolation of defects which are either anti-site atoms or vacancies. In the first case, the vacancy follows the mesh of nearest-neighbor atoms of the same species. This is known as the antistructure bridge mechanism. In the second case, an atom is passed on by exchanging its position with a net of vacancies. This case is termed vacancy bridge mechanism.

antistructure-bridge mechanism (ASB)

This percolation dependent mechanism was recognized by Kao and Chang in 1993 [Kao 93]. It relies on the availability of sufficient anti-site atoms building a closed network of bridges. In this way, the vacancy can diffuse performing nearest-neighbor jumps by exchanging position with only one type of atom. Even though some possible paths are blocked in comparison with the random walk of a vacancy, as the energy barriers which have to be overcome are comparably low, this mechanism leads to fast self diffusion of the peculating atomic species. This mechanism only takes place in off-stoichiometric composition, where the prevalent atomic species builds a network. This leads to a strong imbalance in the diffusivity of the constituents. The percolation threshold for the ASB to take place has been calculated using computer simulations and in frame of the percolation theory, see e.g. [Belo 98, Kurz 12]. For B2 systems it lies at 54.9(2)%

[Divi 97], which corresponds to approximately 10% of the β-sublattice sites being occupied by A-type atoms or vice versa.

As there is no exchange of atoms of different species required, the ASB does not lead to chemical diffusion and is therefore invisible to aXPCS.

Vacancy Bridge Mechanism (VB)

This was introduced under the term anti-structure bridge sequence for Al-atoms [Xu 10]. It was, however, pointed out, that a distinction form the ASB is sensible [Leit 15]. Systems, where an excess of A atoms leads to the introduction of structural β-vacancies rather than A_β antisites, can not form peculating clusters as discussed above. There is, however, a number of A_β antisites leading to A_α-A_β nearest-neighbor pairs, which can exchanging their position with a vacancy on the β-sublattice V_β either by jumping at the same time or with a very small time delay. Such a simultaneous pair-atom hop can lead to long ranging transport of A-atoms [Xu 10] in case of vacancy percolation on the β-sublattice with a threshold of 5% vacancy concentration for a B2 system [Leit 15].

3.3.3. Mono vacancy diffusion - correlated jump cycles

Effective atomic jumps further than the nearest-neighbor shell can be due to a correlated movement of a vacancy. The following mechanisms describe such a movement.

The six jump cycle (6JC)

The first effort to describe diffusion in ordered intermetallics was made by Huntington [Hunt, Hunt 61] and by McCombie and Elcock [Elco 58, Elco 59]. Therefore it is often referred to as Huntington-McCombie-Elcock (HME) mechanism. The underlying idea is that in a lattice with perfect order a progressive jump cycle is carried out, which in the first three steps decreases the oder in the system whereas in the last three steps the order is restored.

As such a cycle leads to migration of the dwellers of all sublattices involved, it was proposed [Elco 58] that for binary systems the ratio of the diffusivities for the constituents has to be within certain boundaries. Initially, this boundaries were taken to be $1/3 < D_A/D_B < 2$ for a B2 system [Elco 58]. Later calculations gave more prezise boundaries of $0.4917 < D_A/D_B < 2.034$ [Arit 89].

In a B2-system three different realizations of the 6JC exist. Two of them lead to an effective vacancy-atom exchange in form of an effective $\langle 100 \rangle$ jump while the third leads to an effective $\langle 110 \rangle$ jump (see e.g. [Arit 89] Fig.1). The probabilities for these families of particular jump cycles were also calculated in [Arit 89] as $0.5 < \bar{p}_{100} < 0.75$, $0.25 < \bar{p}_{110} < 0.5$ and $1/3 < \bar{p}_{110}/\bar{p}_{100} < 1$. This was used as an argument in [Sepi 93] to rule out the 6JC as the dominant mechanism in B2 Fe-Al. It was, however, shown [Drau 99] that no limits for the ratio of $\bar{p}_{100}$ and $\bar{p}_{110}$ can be established for a 6JC. Also calculations of the local energy barriers for diffusion in a Ni–Al system using embedded atom method show that the value $\bar{p}_{100}/\bar{p}_{110}$ cannot serve as an indicator for the occurrence of the 6JC [Divi 00]. For other B2 systems it was claimed that the 6JC is the dominant mechanism, e.g β-Ag-Mg [Domi 65] or Al-rich Ni-Al [Xu 10].

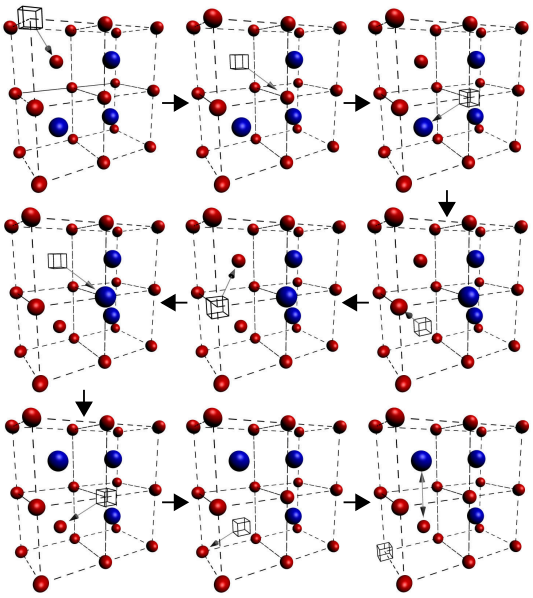

(a) 4+2 jump cycle bent leading to effective ⟨100⟩ jumps.

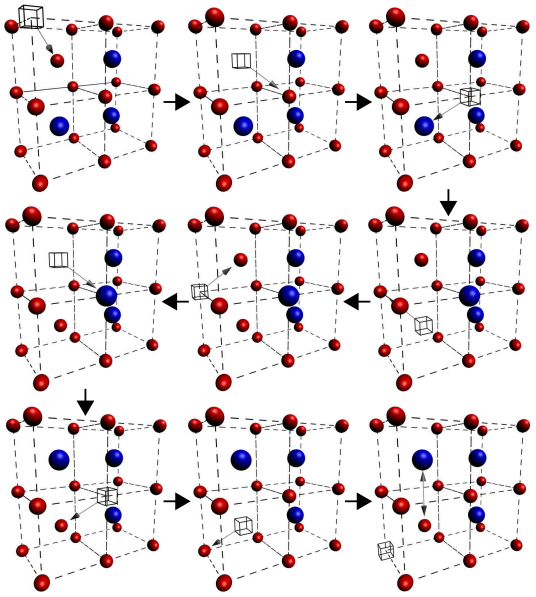

(b) 4+2 jump cycle straight leading to effective ⟨100⟩ jumps.

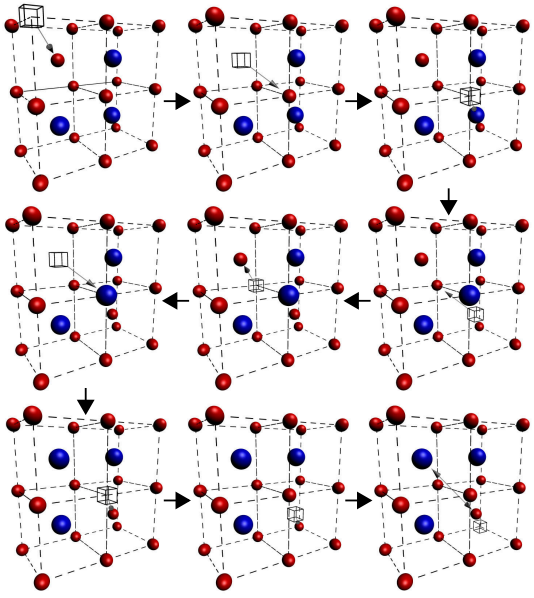

(c) 4+2 jump cycle leading to effective ⟨110⟩ jumps.

Figure 3.1.: The three possible 4+2 jump cycles for chemical diffusion in a B2 ordered, off-stoichiometric intermetallic alloy.

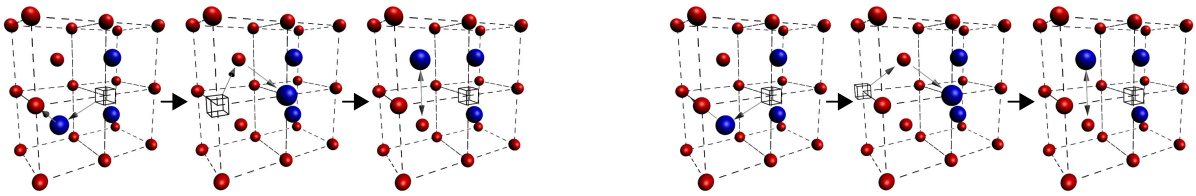

(a) Bent leading to ⟨100⟩ exchange.

(b) Straight leading to ⟨100⟩ exchange.

Figure 3.2.: Chemical diffusion via 2+2 jump cycle.

Six jump cycles can occur on different sublattices, depending from which sublattice the vacancy starts from. Sometimes this is used to distinguish between 6JCs and a cycle starting with a vacancy e.g. on the α-sublattice is termed α6JC. It was stated, that when an α6JC encounters an antisite (A_β), it anneals this antisite and continues as a cycle on a different sublattice (e.g. β6JC) "increasing the A_β concentration favors the annihilation process $V_\alpha + A_\beta \rightarrow V_\beta$ and therefore favors the β6JC over the α6JC" [Athe 97].

When a vacancy encounters an antisite on the same sublattice, the two defects tend to couple and the vacancy drags the antisite along [Athe 97]. This is due to the fact that the additional defect can lower the migration enthalpy, which was termed antisite assisted six jump cycle (A6JC). The same can be true for a second vacancy in the vicinity of one vacancy performing a 6JC [Ganc 00], which leads to a vacancy assisted six jump cycle (V6JC).

In case of a non-stoichiometric composition, the 6JC can lead to chemical diffusion, as can be seen in Fig. 3.1 for the case of a B2 system. The first two jumps are identical in all three cases. Also the last jump in the sequence, where the circle is closed does, not in any way influence the jump cycle, as long as it is not a backwards jump. Therefore, in case of chemical diffusion in a non-stoichiometric composition, the 6JC reduces to the so called 4+2 jump cycle [Leit 12a] in combination with ASB-like diffusion. It can be assumed that the 4+2 jump cycle has a lower total energy barrier to overcome than the 6JC in the same system with stoichiometric configuration [Leit 15].

The three jump cycle (3JC)

In B2 Fe-Al close to stoichiometry the concentration of Al-vacancies is very low due to an extremely high effective formation energy (see [Drau 99] section 3 and references cited therein). Therefore, configurations in a 6JC demanding an Al-vacancy are very expensive in terms of energy. This and the fact that the 6JC in Fe-Al is an unstable process [Drau 99] excludes the 6JC from taking place close to stoichiometry in this system. To take the similarity of the diffusion constants D_{Al} and D_{Fe} into account, a new correlated jump mechanism was proposed, called three jump cycle. It consists of symmetric cycles of three correlated double jumps where two sequential nearest-neighbor jumps of the vacancy are carried out as one collective two atom displacement, as was found by simulation studies for Ni–Al [Mish 03]. The same mechanism was published for Fe–Al by Fähnle et al. [Fahn 99b]. In other words, it is a 6JC where two jumps each are carried out simultaneously. For chemical diffusion starting with the vacancy on the A lattice, only two double jumps take place, again in combination with ASB-like jumps as shown

in Fig. 3.2. This is termed 2+2 jump cycle.

Jump cycles of higher order

In theory it is also possible that jump cycles of higher order (e.g. 10 jump cycle, see Fig. 3.3) take place [Koiw 92]. Such cycles can lead to farther effective jumps. However the longer the sequence, the lower the probability for it to be carried out. The probability of individual jumps depends on the local energy barrier as discussed above.

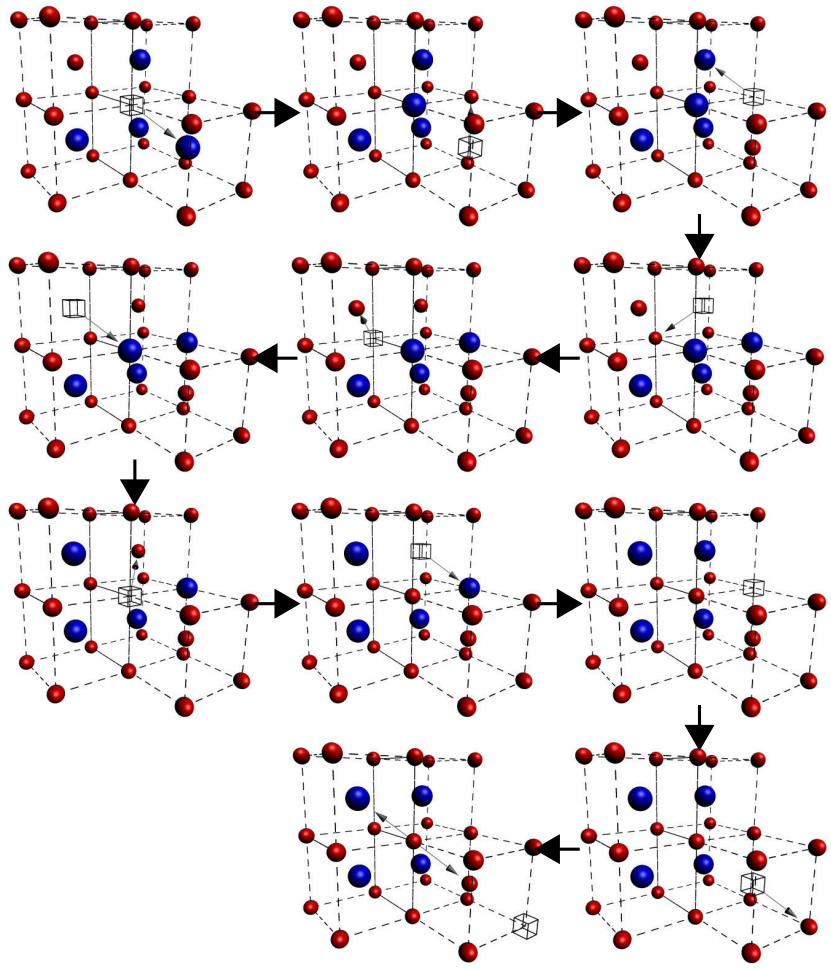

Figure 3.3.: One possible 10-jump cycle leading to effective ⟨111⟩ jumps.

3.3.4. Di-vacancy mechanisms

So far only monovacancy mechanisms have been discussed. It is, however, also possible, that two or more vacancies move through the lattice in a correlated manner. Effective attractive pair interaction of vacancies leads to a situation where for any relative starting position of two vacancies those jumps are preferred, which lead to a reduction of the distance between the two vacancies. Such mechanisms were considered for pure metals [Pete 78, Mund 78, Maie 79], and soon after also for alloys [Stol 80]. For the latter a distinction was established, depending on the ground state configuration of the defects participating in the process.

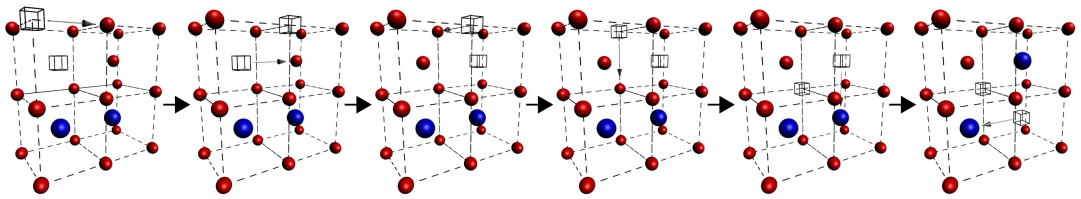

Figure 3.4.: Chemical diffusion in a B2 system by the leap frog mechanism (LF).

The leap frog mechanism (LF)

The basis of this mechanism, which was also referred to as dynamic pair mechanism (DP), is a strong attractive force between vacancies. The result is that the two vacancies are seeking each others nearest-neighbor position. This can lead to jumps as shown in Fig. 3.4. Such jumps can take place in two different ways.

The first possibility is that, in order not to leave the first coordination shell of the second vacancy the first vacancy performs a direct next-nearest-neighbor jump rather than a nearest-neighbor jump. Such jumps are facilitated as the presence of a second vacancy reduces the energy barrier for an atom to perform a next-nearest neighbor jump [Athe 97, Ganc 00].

The second possibility is for the first vacancy to perform a nearest-neighbor jump leaving the first coordination shell of the second vacancy, which immediately leads to a jump of the second vacancy, following the first one. This can lead to the intermediate configuration having the form of a classical triple defect.

Because the two vacancies occupy different sublattices in the ground state, it is possible that one defect is much more mobile than the other, which can lead to one of the vacancies idling at a certain position while the other performs several jumps in its first coordination shell, leading to a strong imbalance of self diffusion of the two constituents.

The triple-defect mechanism (TDM)

It is also possible that the ground state has the form of a classical triple defect [Wasi 68] consisting of two vacancies on the same sublattice, e.g. the α sublattice, and one antisite atom on the other (e.g. the β) sublattice. Therefore this form of the mechanism was originally termed TDM [Stol 80].

One possible migration mechanism for such a defect is very similar to the LF, with the difference that the intermediate configuration is the stable one and the configuration where the two vacancies are nearest-neighbors is unstable. The geometrical arrangement of vacancies and the antisite atom is not well defined for the triple defect. In case of the classical TDM, the vacancies are next-nearest neighbors (see e.g [Fran 01] Fig. 10). Therefore the anitisite atom and the vacancies form a triangle. This is the case for most arrangements of two vacancies and one antisite aotm. It is, however, also possible that the vacancies and the antisite are threaded along the $\langle 111 \rangle$ direction and the vacancies are fifth-nearest neighbors in case of a B2 structure. Such an arrangements shall be called linear triple-defect (lTD). When such a defect moves through the lattice, it leads to effective $\langle 111 \rangle$ jumps of atoms. Chemical diffusion by a linear triple-defect mechanism (lTDM) is shown in Fig. 3.5. If the jump frequency along the $\langle 111 \rangle$ axes is high,

this could be seen in farther jump along this axes in an aXPCS experiment (e.g. effective ⟨222⟩ jumps).

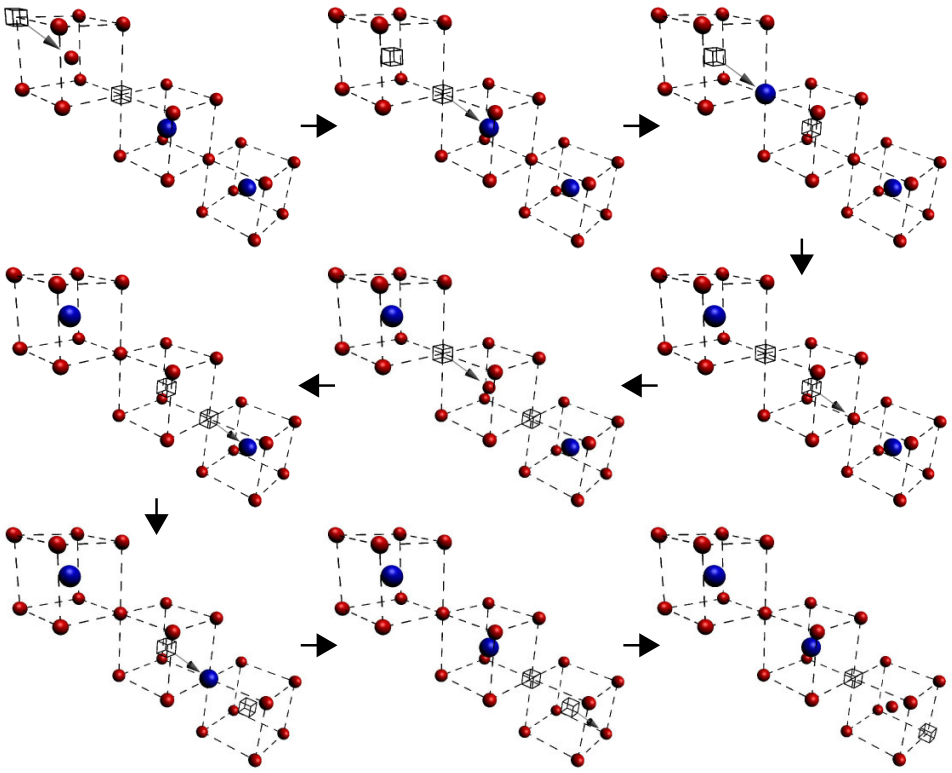

Figure 3.5.: The linear triple-defect mechanism (lTDM) leading to chemical diffusion along the ⟨111⟩ direction. The first 5 steps lead to effective ⟨111⟩ jumps, the additional steps show the possibility of effective ⟨222⟩ jumps.

It is possible that a triple defect or di-vacancy is formed by a vacancy diffusing in an isolated peculated region in an ASB-like manner until it reaches another vacancy. Once the di-vacancy complex is formed it can overcome the gap to another peculated region where the complex can be dissolved or move in an ASB-like manner again.

The waltzing-step mechanism (WS)

Starting with an initial V_α-pair, one of the vacancies exchanges position with an B_β atom. After this, a nearest neighbor A_α atom exchanges its position with both vacancies. The cycle is completed by the accrued B_α retaking its original position by an exchange with the second vacancy. This mechanism is called waltzing-step mechanism because the B atom stepping out of the way for the A atom to pass resembles the movement of two partners in a dance of waltz [Leit 15]. As one constituent (in this case the B atom) does not experience any net movement, this mechanism can never be exclusively active in a stoichiometric composition (otherwise one of the diffusion constants would be zero). When this mechanism reaches an antisite, it leads to chemical diffusion as depicted in Fig. 3.6.

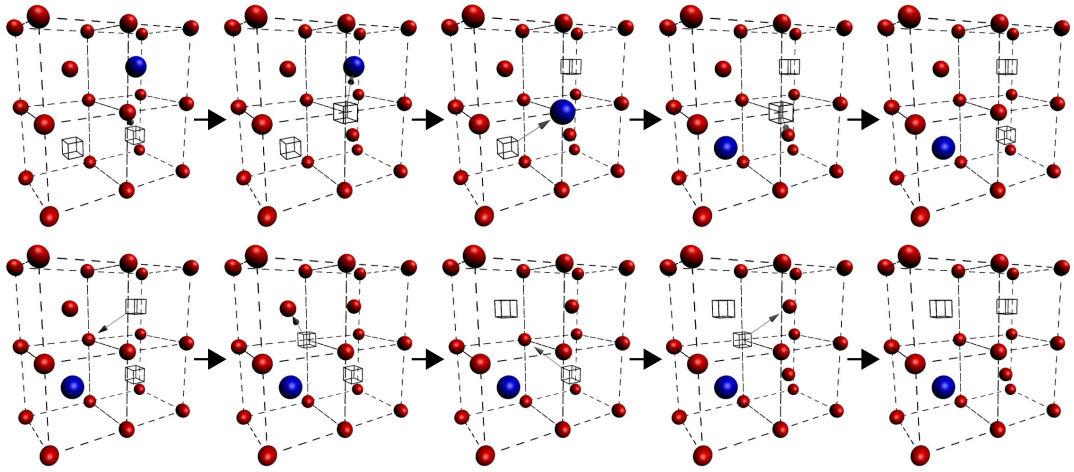

Figure 3.6.: A waltzing-step mechanism leading to diffusion of one constituent on its sublattice (lower part) and to chemical diffusion (upper part).

3.4. Distinguishing diffusion mechanisms

Different approaches can be undertaken to find out which diffusion mechanism is at work. One is a simulation approach. The migration enthalpy of the appropriate defect is calculated by comparing the energetic configurations of the system for each individual step in a mechanism using ab initio techniques (e.g. [Fu 93, Xu 09]). It is also possible to carry out MC (e.g [Youn 66, Athe 97]) and kinetic MC simulations [Xu 10] or Molecular Dynamic simulations (see [Bocq 96], section 1.5.1 and literature cited therein) and follow the paths of individual atoms. In case of kinetic MC also the jump frequencies depending on composition can be found [Xu 10].

Most experimental approaches, like tracer measurements, determine macroscopic quantities, usually the diffusion coefficient as a function of temperature. In a binary system for example the ratio of the diffusion coefficients of the constituents can yield information about the diffusion mechanism. For systems where the ASB is dominant one diffusivity strongly prevails. Systems where a correlated mechanism takes place on the other hand, feature diffusion coefficients of the same order. Also diffusion constants gained from simulations can be compared with macroscopic diffusion coefficients.

Microscopic methods, like quasielastic neutron scattering, quasielastic Mössbauer spectroscopy or aXPCS yield information about the effective jump length of diffusing atoms. This information is vital in deciphering diffusion mechanisms. Distinguishing the individual jump frequencies of one or more vacancies within one encounter or one correlated jump cycle is far from being experimentally resolvable. Such properties can only be gained from theoretical considerations (the five-frequency model for example) or simulation techniques.

3.5. Diffusion mechanisms studied by atomic-scale X-ray Photon Correlation Spectroscopy

Each set of effective jump vectors to a certain neighbor shell yields a corresponding correlation time, as can be seen from (2.42). Let us consider the first six neighbor shells of a bcc lattice. In Table 3.2 the values for the neighboring distance Δr in units of the lattice constant a, the set of neighboring vectors to the shell $\langle hkl \rangle$ in units of the lattice constant and the corresponding cosine terms (see Section 2.2.5) for reduced inverse correlation times are given.

n	Δr_n	$\langle hkl \rangle$	$1 - C_n(\vec{q}) = \tau_n(\vec{q})^{-1} \times \Big(\tau_0 I_{\mathrm{SRO}}(\vec{q})\Big)$
1	$\sqrt{3/4}$	$\langle \frac{1}{2}\frac{1}{2}\frac{1}{2} \rangle$	$1 - \cos(\frac{q_x a}{2})\cos(\frac{q_y a}{2})\cos(\frac{q_z a}{2})$
2	1	$\langle 100 \rangle$	$1 - \frac{1}{3}\Big(\cos(q_x a) + \cos(q_y a) + \cos(q_z a)\Big)$
3	$\sqrt{2}$	$\langle 110 \rangle$	$1 - \frac{1}{3}\Big(\cos(q_x a)\cos(q_y a) + \cos(q_x a)\cos(q_z a) + \cos(q_y a)\cos(q_z a)\Big)$
4	$\sqrt{11/4}$	$\langle \frac{3}{2}\frac{1}{2}\frac{1}{2} \rangle$	$1 - \frac{1}{3}\Big(\cos(\frac{3q_x a}{2})\cos(\frac{q_y a}{2})\cos(\frac{q_z a}{2}) + \cos(\frac{q_x a}{2})\cos(\frac{3q_y a}{2})\cos(\frac{q_z a}{2})$ $+ \cos(\frac{q_x a}{2})\cos(\frac{q_y a}{2})\cos(\frac{3q_z a}{2})\Big)$
5	$\sqrt{3}$	$\langle 111 \rangle$	$1 - \cos(q_x a)\cos(q_y a)\cos(q_z a)$
6	2	$\langle 200 \rangle$	$1 - \frac{1}{3}\Big(\cos(2q_x a) + \cos(2q_y a) + \cos(2q_z a)\Big)$

Table 3.2.: First six neighbor shells in a bcc lattice

These reduced inverse correlation times can be rewritten using a parametrization according to Section 2.1.1. This then yields the angle-dependent correlation time $\tau(2\Theta, \varphi)$ according to (2.42), which can be plotted on a sphere as shown in Fig. 3.7. When graphically illustrating the correlation time, it is advantageous to plot its inverse, $\tau(\vec{q})^{-1}$, as it approaches zero for 2Θ approaching zero. In Fig. 3.8 the different inverse correlation times for exclusive jumps to a certain neighbor shell in a bcc lattice as listed in Table 3.2 are shown. For convenience, the product of scattering vector and lattice constant (ka) was chosen to be 10.

3.5.1. Diffusion on a non-Bravais lattice

In case of a system consisting of sublattices, different processes can take place. Jumps within the individual sublattices can occur as well as jumps from one sublattice to another. As can be seen from (2.55a), this leads to a sum of exponential decays in the amplitude-correlation function. In order to find a model for the measured intensity-correlation functions, the eigenvalues and eigenvectors of the jump matrix have to be determined.

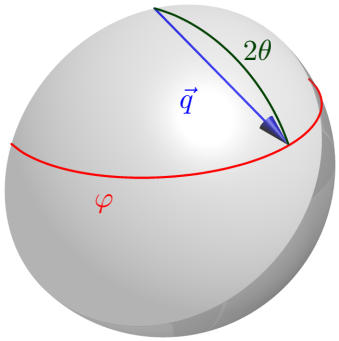

Figure 3.7.: Graphical representation of the sphere formed by a set of reciprocal space vectors $\vec{q}$. Here one representative is shown with its parameters, the polar angle 2θ and the azimuthal angle φ. The north pole was chosen as the origin.

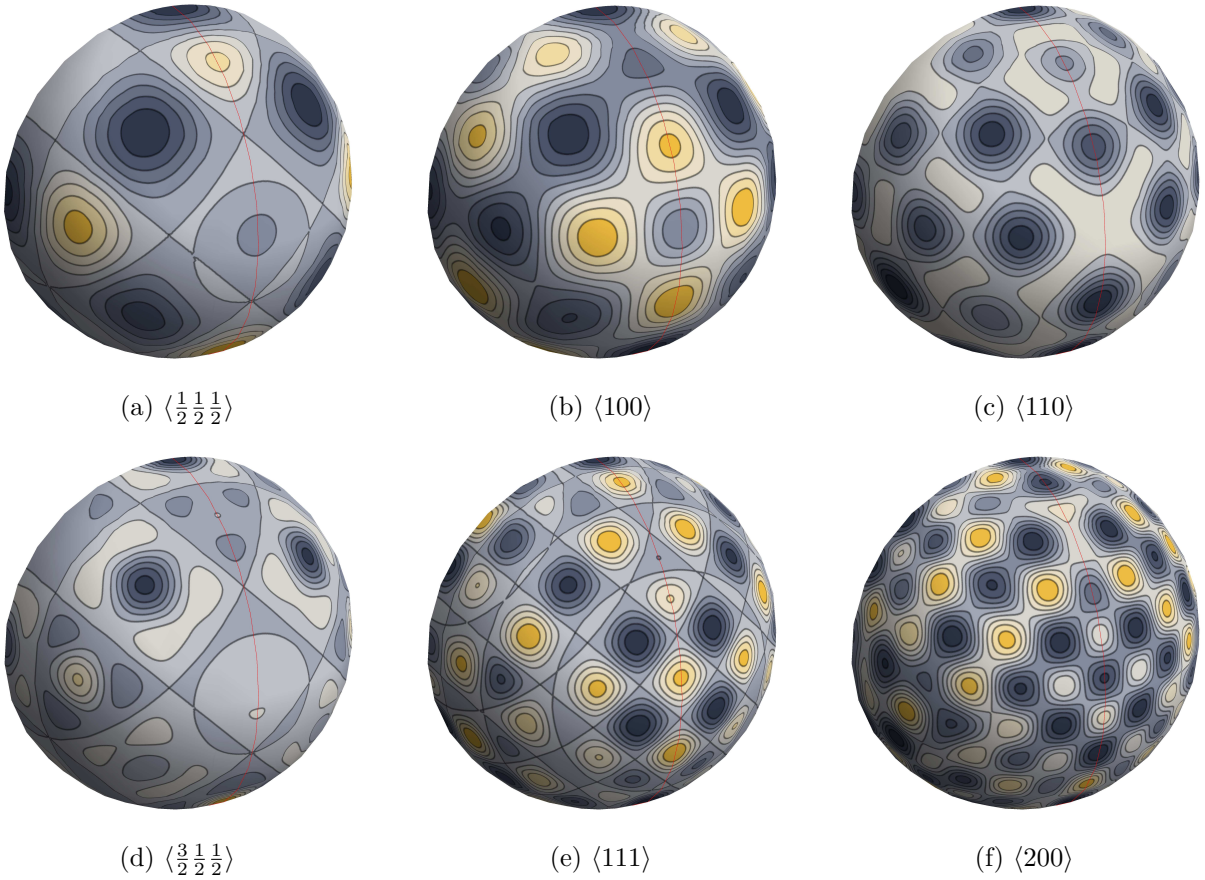

(a) $\langle \frac{1}{2}\frac{1}{2}\frac{1}{2} \rangle$ (b) $\langle 100 \rangle$ (c) $\langle 110 \rangle$

(d) $\langle \frac{3}{2}\frac{1}{2}\frac{1}{2} \rangle$ (e) $\langle 111 \rangle$ (f) $\langle 200 \rangle$

(g) Color code for $\tau(\vec{q})^{-1}$ in a.u.

Figure 3.8.: Reduced inverse correlation times as given in Table 3.2 as a function of polar angle 2θ and azimuthal angle φ for $ka = 10$. The point of origin is the north pole. The red line indicates $\varphi = 0°$.

B2-alloys

Considering a B2 system it can be assumed, that there will be nearest neighbor jumps between the α and β sublattice, $\Delta\vec{r}_1^{\alpha\beta} \in \langle \frac{a}{2}\frac{a}{2}\frac{a}{2}\rangle$. It is therefore possible, to define in consistency with Table 2.2

$$C_1^{\alpha\beta}(\vec{q}) = C_1^{\beta\alpha}(\vec{q}) := \cos\left(q_x\frac{a}{2}\right)\cos\left(q_y\frac{a}{2}\right)\cos\left(q_z\frac{a}{2}\right). \tag{3.5}$$

Within the individual sublattices there are different jump lengths possible from position μ to position μ', corresponding to different jump mechanisms. Therefore, a sum of jump terms weighted by the appropriate jump probability has to be considered. Denoting the sequence of shells within a sublattice by $\tilde{n}$, the jump matrix can be written, according to (2.50), as

$$\tilde{\mathbf{A}} = \begin{pmatrix} \frac{1}{\tau^{\alpha\alpha'}}\left(\sum_{\tilde{n}}\bar{p}_{\tilde{n}}^{\alpha\alpha'}C_{\tilde{n}}^{\alpha\alpha'}(\vec{q})-1\right) & \frac{1}{\tau^{\alpha\beta}}C_1^{\alpha\beta}(\vec{q}) \\ \frac{1}{\tau^{\beta\alpha}}C_1^{\alpha\beta}(\vec{q}) & \frac{1}{\tau^{\beta\beta'}}\left(\sum_{\tilde{n}}\bar{p}_{\tilde{n}}^{\beta\beta'}C_{\tilde{n}}^{\beta\beta'}(\vec{q})-1\right) \end{pmatrix}. \tag{3.6}$$

For the exchange between the sublattices, detailed balance demands that the jump frequencies times the probability of finding an atom on a particular sublattice are balanced,

$$\frac{1}{\tau^{\alpha\beta}}W^{\alpha} = \frac{1}{\tau^{\beta\alpha}}W^{\beta}. \tag{3.7}$$

Defining $\tau_0 = \tau^{\alpha\beta}$, $\kappa^{\mu} = \tau^{\mu\lambda}/\tau^{\mu\mu'}$ and $S^{\mu\mu'}(\vec{q}) = \sum_{\tilde{n}}\bar{p}_{\tilde{n}}^{\mu\mu'}C_{\tilde{n}}^{\mu\mu'}(\vec{q})$ with $\mu,\lambda \in \{\alpha,\beta\}$, the jump matrix is given by:

$$\tilde{\mathbf{A}} = \frac{1}{\tau_0}\begin{pmatrix} \kappa^{\alpha}(S^{\alpha\alpha'}(\vec{q})-1) & C_1^{\alpha\beta}(\vec{q}) \\ \frac{W^{\beta}}{W^{\alpha}}C_1^{\alpha\beta}(\vec{q}) & \kappa^{\beta}(S^{\beta\beta'}(\vec{q})-1) \end{pmatrix}. \tag{3.8}$$

The weights can be calculated according to (2.55a):

$$\omega_1 = \left|\sqrt{W^{\alpha}}b_1^{\alpha} + \sqrt{W^{\beta}}b_1^{\beta}\right|^2 \tag{3.9a}$$

$$\omega_2 = \left|\sqrt{W^{\alpha}}b_2^{\alpha} + \sqrt{W^{\beta}}b_2^{\beta}\right|^2 \tag{3.9b}$$

The eigenvectors are given by:

$$\vec{b}_{1,2}(\vec{q}) = \left(\frac{1}{\sqrt{W^{\alpha}}}\frac{1}{\sqrt{W^{\beta}}}\frac{W^{\alpha}\left(\kappa^{\alpha}(S^{\alpha\alpha'}(\vec{q})-1)-\kappa^{\beta}(S^{\beta\beta'}(\vec{q})-1)\right)\mp\Omega(\vec{q})}{2C_1^{\alpha\beta}(\vec{q})}, 1\right) \tag{3.10}$$

with

$$\Omega(\vec{q}) = \sqrt{4W^{\alpha}W^{\beta}C_1^{\alpha\beta}(\vec{q})^2 - (W^{\alpha})^2\left(\kappa^{\alpha}(1-S^{\alpha\alpha'}(\vec{q}))-\kappa^{\beta}(1-S^{\beta\beta'}(\vec{q}))\right)^2}. \tag{3.11}$$

In case of a B2 alloy with two sublattices, the intensity-correlation function, according to (2.56), is given by

$$g^{(2)}(\vec{q},t) = 1 + w_1^2\exp\left(-2\frac{t}{\tau_1(\vec{q})}\right) + 2w_1w_2\exp\left(-\frac{t(\tau_1(\vec{q})+\tau_2(\vec{q}))}{\tau_1(\vec{q})\tau_2(\vec{q})}\right) + w_2^2\exp\left(-2\frac{t}{\tau_2(\vec{q})}\right), \tag{3.12}$$

where

$$\tau_{1,2}(\vec{q}) = \frac{2W^\alpha \tau_0}{W^\alpha\Big(\kappa^\alpha(1 - S^{\alpha\alpha'}(\vec{q})) + \kappa^\beta(1 - S^{\beta\beta'}(\vec{q}))\Big) \mp \Omega(\vec{q})}\,. \tag{3.13}$$

Special case: solid solution

In case of a solid solution, both sublattices are occupied with equal probability, $W^\alpha = W^\beta = 0.25$. Furthermore, the residence time for a jump within a sublattice equals that of inter-sublattice jumps. Because $S^{\mu\mu'}(\vec{q}) = S^{\lambda\lambda'}(\vec{q})$ and $S^{\mu\lambda}(\vec{q}) = S^{\lambda\mu}(\vec{q})$, the jump matrix is of the form:

$$\tilde{\mathbf{A}} = \frac{1}{\tau_0}\begin{pmatrix} S^{\mu\mu'}(\vec{q}) - 1 & S^{\mu\lambda}(\vec{q}) \\ S^{\mu\lambda}(\vec{q}) & S^{\mu\mu'}(\vec{q}) - 1 \end{pmatrix} \tag{3.14}$$

For this matrix, the eigenvalues can be found

$$\epsilon_1 = \frac{1}{\tau_0}\big(-1 - S^{\mu\mu'}(\vec{q}) + S^{\mu\lambda}(\vec{q})\big) \tag{3.15a}$$

$$\epsilon_2 = \frac{1}{\tau_0}\big(-1 + S^{\mu\mu'}(\vec{q}) + S^{\mu\lambda}(\vec{q})\big)\,, \tag{3.15b}$$

and the eigenvectors are

$$\vec{b}_1 = \begin{pmatrix} -1 \\ 1 \end{pmatrix}, \quad \vec{b}_2 = \begin{pmatrix} 1 \\ 1 \end{pmatrix}\,. \tag{3.16a}$$

The amplitude-correlation function can be calculated, using (2.55a):

$$\begin{aligned} g_{\mathrm{S}}^{(1)}(\vec{q},t) =& \left|\sqrt{0.25}\times(-1) + \sqrt{0.25}\times 1\right|^2 \exp\left(\frac{1}{\tau_0}(-1 - S^{\mu\mu'}(\vec{q}) + S^{\mu\lambda}(\vec{q}))t\right) \\ &+ \left|\sqrt{0.25}\times 1 + \sqrt{0.25}\times 1\right|^2 \exp\left(\frac{1}{\tau_0}(-1 + S^{\mu\mu'}(\vec{q}) + S^{\mu\lambda}(\vec{q}))t\right) \qquad (3.17a) \\ =& \exp\left(-\frac{t}{\tau_{\mathrm{S}}(\vec{q})}\right)\,, \qquad (3.17b) \end{aligned}$$

with $\tau_{\mathrm{S}}(\vec{q})^{-1} = \tau_0^{-1}(1 - S^{\mu\mu'}(\vec{q}) - S^{\mu\lambda}(\vec{q}))$ in accordance with (2.34).

4. Chemical short-range order in metallic alloys

As shown in Section 2, information about the short-range order of a system is needed due to the so called De Gennes narrowing [De G 59]. Finding such information is not straightforward. Rather the opposite is true as it poses a formidable challenge which has been tackled by several different approaches. This section will give a brief overview of the theoretical concepts underlying some of these techniques. It will also show how different approaches can be applied to systems relevant for aXPCS measurements.

4.1. Diffuse scattering

The static diffuse scattering is the time average of the scattering patterns corresponding to different configurations in real space.

$$S(\vec{q}) = \langle S(\vec{q}, t) \rangle_t \tag{4.1}$$

A perfect crystal lattice can be reduced to a particular unit cell. This means that a small subset of lattice atoms forms a geometrical construct, which can be used to assemble the whole lattice using only translation symmetry operations. The scattering pattern corresponding to a perfect lattice is therefore determined by Fourier transform of such a unit cell, resulting in what is known as Bragg reflection. However, such a perfect lattice does not exist in reality. The atoms oscillate around their ideal positions and defects in the lattice lead to displacements, which means that the distance between neighboring atoms can vary locally. Furthermore, systems composed of more than one type of atom possess chemical order. Only for stoichiometric composites this order can in theory be described by a superstructure. Therefore, in order to thoroughly describe a crystal, the whole lattice must be treated as the unit cell. As the lattice is built of discrete scatterers, the structure factor, representing the scattering intensity, can be written as

$$S(\vec{q}) = \sum_i \sum_j f_i(\vec{q}) f_j(\vec{q}) \exp\left(\mathrm{i}\,(\vec{r}_i - \vec{r}_j) \cdot \vec{q}\right) , \tag{4.2}$$

where each sum runs over all the atoms in the lattice. The scattering length (or atomic scattering factor)

$$f_i(\vec{q}) = \int_V \mathrm{d}\vec{r} \rho_i(\vec{r}) \exp(\mathrm{i}\,\vec{q} \cdot \vec{r}) \tag{4.3}$$

generally depends on the scattering angle. In case where the wave length of the scattered radiation is larger than the diameter of the scatterer $\lambda >> \varnothing_{\mathrm{scatterer}}$, the scattering length is in good approximation constant (this is true for elastic neutron scattering). When an electromagnetic wave is scattered, it corresponds to the number of electrons the scatterer contains ($f_i = Z_i$) for a forward scattering.

The form of (4.2) does not include any parameters corresponding to any kind of chemical

order or displacements. In order to gain such information, different approaches have been developed. Here a short overview of some of them will be given. For a detailed overview see e.g. [Schw 77, Scho 03].

4.1.1. Serial expansion of intensity

This approach was introduced by Borie and Sparks [Bori 71]. In order to deal with local displacements, the real space vectors as used in (4.2) are split into an average position vector and a local variation $\vec{r}_i = \vec{R}_i + \vec{\delta}_i$. With this the scattering function can be written as

$$S(\vec{q}) = \sum_i \sum_j f_i \, f_j^* \, \mathrm{e}^{\left(\mathrm{i}\,\vec{q}\cdot(\vec{R}_i - \vec{R}_j)\right)} \, \mathrm{e}^{\left(\mathrm{i}\,\vec{q}\cdot(\vec{\delta}_i - \vec{\delta}_j)\right)} \,. \tag{4.4}$$

Now we apply a series expansion of $\mathrm{e}^{\left(\mathrm{i}\,\vec{q}\cdot(\vec{\delta}_i - \vec{\delta}_j)\right)}$:

$$\mathrm{e}^{\left(\mathrm{i}\,\vec{q}\cdot(\vec{\delta}_i - \vec{\delta}_j)\right)} = 1 + \mathrm{i}\,\vec{q}\cdot\left(\vec{\delta}_i - \vec{\delta}_j\right) - \frac{1}{2}\left(\vec{q}\cdot\left(\vec{\delta}_i - \vec{\delta}_j\right)\right)^2 - \frac{\mathrm{i}}{6}\left(\vec{q}\cdot\left(\vec{\delta}_i - \vec{\delta}_j\right)\right)^3 + O\left(|\vec{q}|^4\right) \tag{4.5}$$

Using (4.4) yields a expression for the scattering function where the individual summands depend on the order of local displacement, as indicated by $S_{\mathrm{order}}(\vec{q})$:

$$S(\vec{q}) = \underbrace{\sum_i \sum_j f_i \, f_j^* \, \mathrm{e}^{\left(\mathrm{i}\,\vec{q}\cdot(\vec{R}_i - \vec{R}_j)\right)}}_{S_0(\vec{q})} \tag{4.6}$$

$$+ \underbrace{\mathrm{i} \sum_i \sum_j f_i \, f_j^* \, \mathrm{e}^{\left(\mathrm{i}\,\vec{q}\cdot(\vec{R}_i - \vec{R}_j)\right)} \vec{q}\cdot\left(\vec{\delta}_i - \vec{\delta}_j\right)}_{S_1(\vec{q})} \tag{4.7}$$

$$- \underbrace{\frac{1}{2} \sum_i \sum_j f_i \, f_j^* \, \mathrm{e}^{\left(\mathrm{i}\,\vec{q}\cdot(\vec{R}_i - \vec{R}_j)\right)} \left(\vec{q}\cdot\left(\vec{\delta}_i - \vec{\delta}_j\right)\right)^2}_{S_2(\vec{q})} \tag{4.8}$$

$$- \underbrace{\frac{\mathrm{i}}{6} \sum_i \sum_j f_i \, f_j^* \, \mathrm{e}^{\left(\mathrm{i}\,\vec{q}\cdot(\vec{R}_i - \vec{R}_j)\right)} \left(\vec{q}\cdot\left(\vec{\delta}_i - \vec{\delta}_j\right)\right)^3}_{S_3(\vec{q})} \tag{4.9}$$

Before treating the individual terms let us introduce some useful concepts. We define an average scattering factor as $\bar{f} = \sum_i c_i f_i$, where c_i is the concentration of a certain type of scatterers and f_i its scattering length. For simplicity let us consider a binary system from here on. The number of atoms of type A shall be given by N_A and the number of atoms of type B by N_B. N is the total number of atoms. The concentration of atoms of those types will be given as c_A and c_B respectively. For an atom of type B that sits at i the probability to find an atom of type A at position j is given by ω_{ij}^{BA} and the probability to find an atom of type B at position j is given by ω_{ij}^{BB}. Therefore

$$\omega_{ij}^{BA} + \omega_{ij}^{BB} = 1 \tag{4.10a}$$

and

$$\omega_{ij}^{AA} + \omega_{ij}^{AB} = 1, \tag{4.10b}$$

if an atom of type A sits at i, respectively. Together with (4.10) the expectation value of the product of two scattering lengths can be written as

$$\begin{aligned}\langle f_i f_j\rangle &= c_A f_A \omega_{ij}^{AA} f_A + c_B f_B \omega_{ij}^{BB} f_B + c_A f_A \omega_{ij}^{AB} f_B + c_B f_B \omega_{ij}^{BA} f_A \\ &= c_A f_A^2 + c_B f_B^2 - c_A \omega_{ij}^{AB} (f_A - f_B)^2. \end{aligned} \tag{4.11}$$

This can be used to calculate the expectation value of the 0th order term in the expansion of the scattering function:

$$\langle S_0(\vec{q})\rangle = \sum_{i,j} \langle f_i f_j\rangle \, \mathrm{e}^{\mathrm{i}\,\vec{q}\cdot(\vec{R}_i - \vec{R}_j)} \tag{4.12a}$$

$$= \sum_{i,j} (\bar{f})^2 \, \mathrm{e}^{\mathrm{i}\,\vec{q}\cdot(\vec{R}_i - \vec{R}_j)} + \sum_{i,j} \left(\langle f_i f_j\rangle - (\bar{f})^2 \right) \mathrm{e}^{\mathrm{i}\,\vec{q}\cdot(\vec{R}_i - \vec{R}_j)} \tag{4.12b}$$

$$= \sum_{i,j} (\bar{f})^2 \, \mathrm{e}^{\mathrm{i}\,\vec{q}\cdot(\vec{R}_i - \vec{R}_j)} + \sum_{i,j} \left(c_A c_B (f_A - f_B)^2 - c_A \omega_{ij}^{AB} (f_A - f_B)^2 \right) \mathrm{e}^{\mathrm{i}\,\vec{q}\cdot(\vec{R}_i - \vec{R}_j)} \tag{4.12c}$$

$$= \sum_{i,j} (\bar{f})^2 \, \mathrm{e}^{\mathrm{i}\,\vec{q}\cdot(\vec{R}_i - \vec{R}_j)} - \sum_{i,j} c_A (c_B - \omega_{ij}^{AB}) (f_A - f_B)^2 \, \mathrm{e}^{\mathrm{i}\,\vec{q}\cdot(\vec{R}_i - \vec{R}_j)} \tag{4.12d}$$

$$= \underbrace{\sum_{i,j} (\bar{f})^2 \, \mathrm{e}^{\mathrm{i}\,\vec{q}\cdot(\vec{R}_i - \vec{R}_j)}}_{I_{\mathrm{Bragg}}(\vec{q})} + \underbrace{\sum_{i,j} c_A c_B (f_A - f_B)^2 \alpha_{ij} \, \mathrm{e}^{\mathrm{i}\,\vec{q}\cdot(\vec{R}_i - \vec{R}_j)}}_{I_{\mathrm{SRO}}(\vec{q})} \tag{4.12e}$$

Here the definition of the Warren Cowley short-range order parameters, as already introduced in (2.57) was used ($\alpha_{ij} = 1 - \frac{\omega_{ij}^{AB}}{c_B} = 1 - \frac{\omega_{ij}^{BA}}{c_A}$).

For a Bravais lattice, where $\vec{r}_{ij} = \vec{R}_i - \vec{R}_j$ it holds that $\vec{r}_{ij} = -\vec{r}_{ji}$ because of the symmetry. This allows the use of cosine terms instead of the exponential functions as $2\cos(x) = \exp(\mathrm{i}x) + \exp(-\mathrm{i}x)$. The ensemble average (or time average given ergodicity) of the 0th order term of the scattering function can be written as

$$\langle S_0(\vec{q})\rangle = \underbrace{(\bar{f})^2 \sum_{i,j} \mathrm{e}^{\mathrm{i}\,\vec{q}\cdot\vec{r}_{ij}}}_{I_{\mathrm{Bragg}}(\vec{q})} + \underbrace{c_A c_B (f_A - f_B)^2 \sum_{i,j} \alpha_{ij} \, \cos(\vec{q}\cdot\vec{r}_{ij})}_{I_{\mathrm{SRO}}(\vec{q})} . \tag{4.13}$$

The second summand is the short-range order intensity as already introduced in (2.58), where $\mathrm{LU} = c_A c_B (f_A - f_B)^2$ is called a Laue unit. Therefore, for a system with no chemical short-range order, the scattering pattern of 0th order features Bragg reflection and a constant background in the diffuse regime of one Laue unit.

The term of 1st order in the scattering function was termed atomic-size effect in the original work by Warren, Averbach and Roberts [Warr 51]. It is therefore also referred to as Warren size effect. Because of the symmetry argument given above, for a Bravais lattice this term can be

written as

$$S_1(\vec{q}) = \mathrm{i} \sum_i \sum_j f_i \, f_j^* \, \mathrm{e}^{\left(\mathrm{i}\,\vec{q}\cdot(\vec{R}_i - \vec{R}_j)\right)} \vec{q} \cdot \left(\vec{\delta}_i - \vec{\delta}_j\right) \tag{4.14a}$$

$$= \sum_i \sum_j f_i \, f_j^* \, \vec{q} \cdot \left(\vec{\delta}_i - \vec{\delta}_j\right) \sin\left(\vec{q} \cdot \vec{r}_{ij}\right) \tag{4.14b}$$

Now let us make the assumption that the displacements are solely due to a rescaling of the neighboring distances for different types of atoms:

$$\begin{aligned} \vec{\delta}_i^A - \vec{\delta}_j^A &= \Delta^{AA} \vec{r}_{ij} \\ \vec{\delta}_i^B - \vec{\delta}_j^B &= \Delta^{BB} \vec{r}_{ij} \\ \vec{\delta}_i^A - \vec{\delta}_j^B &= \vec{\delta}_i^B - \vec{\delta}_j^A = \Delta^{AB} \vec{r}_{ij} \end{aligned} \tag{4.15}$$

This assumption is, of course not exact, because for different local configurations (different number of neighboring atoms of type AA for example) different displacements result. Using (2.57) and (4.10) we get:

$$c_A \omega_{ij}^{AB} = c_B \omega_{ij}^{BA} = c_A c_B (1 - \alpha_{ij}) \tag{4.16}$$

With (4.15) and (4.16) we can write the average displacement scattering of first order as

$$\langle S_1(\vec{q}) \rangle = \sum_i \sum_j \left\langle f_i \, f_j^* \, \vec{q} \cdot \left(\vec{\delta}_i - \vec{\delta}_j\right) \right\rangle \sin\left(\vec{q} \cdot \vec{r}_{ij}\right) \tag{4.17a}$$

$$= \sum_i \sum_j \left(c_A \omega_{ij}^{AA} f_A^2 \langle \Delta_{ij}^{AA} \rangle + c_B \omega_{ij}^{BB} f_B^2 \langle \Delta_{ij}^{BB} \rangle + c_A \omega_{ij}^{AB} f_A f_B \langle \Delta_{ij}^{AB} \rangle + c_B \omega_{ij}^{BA} f_B f_A \langle \Delta_{ij}^{BA} \rangle \right) \times \vec{q} \cdot \vec{r}_{ij} \sin\left(\vec{q} \cdot \vec{r}_{ij}\right) \tag{4.17b}$$

$$= \sum_i \sum_j \Bigg((c_A - c_A \omega_{ij}^{AB}) f_A^2 \langle \Delta_{ij}^{AA} \rangle + (c_B + c_B \omega_{ij}^{BA}) f_B^2 \langle \Delta_{ij}^{BB} \rangle + c_A \omega_{ij}^{AB} f_A f_B \langle \Delta_{ij}^{AB} \rangle + c_B \omega_{ij}^{BA} f_A f_B \langle \Delta_{ij}^{BA} \rangle \Bigg) \times \vec{q} \cdot \vec{r}_{ij} \sin\left(\vec{q} \cdot \vec{r}_{ij}\right) \tag{4.17c}$$

$$= \sum_i \sum_j \Bigg((c_A - c_A c_B (1 - \alpha_{ij})) f_A^2 \langle \Delta_{ij}^{AA} \rangle + (c_B + c_A c_B (1 - \alpha_{ij})) f_B^2 \langle \Delta_{ij}^{BB} \rangle + 2 c_A c_B (1 - \alpha_{ij}) f_A f_B \langle \Delta_{ij}^{AB} \rangle \Bigg) \times \vec{q} \cdot \vec{r}_{ij} \sin\left(\vec{q} \cdot \vec{r}_{ij}\right) , \tag{4.17d}$$

because $\langle \Delta_{ij}^{AB} \rangle = \langle \Delta_{ij}^{BA} \rangle$.

For simplification the so called size effect parameter [Warr 51, Niel 00] is introduced

$$\beta_{ij} = \left(\frac{1}{f_B/f_A - 1} \right)^2 \left(\left(\frac{c_A}{c_B} + \alpha_{ij} \right) \langle \Delta_{ij}^{AA} \rangle + 2(1 - \alpha_{ij}) \frac{f_B}{f_A} \langle \Delta_{ij}^{AB} \rangle + \left(\frac{c_B}{c_A} + \alpha_{ij} \right) \frac{f_B^2}{f_A^2} \langle \Delta_{ij}^{BB} \rangle \right) . \tag{4.18}$$

Usually a fixed volume is taken as a boundary condition, thus the sum over all displacements

has to be zero. This is used to reduce the number of free parameters:

$$c_B\omega_{ij}^{AB}\langle\Delta_{ij}^{AB}\rangle + c_A\omega_{ij}^{BA}\langle\Delta_{ij}^{BA}\rangle = \omega_{ij}^{AB}\langle\Delta_{ij}^{AB}\rangle \underbrace{(c_B + c_A)}_{=1} = -c_A\omega_{ij}^{AA}\langle\Delta_{ij}^{AA}\rangle - c_B\omega_{ij}^{BB}\langle\Delta_{ij}^{BB}\rangle \quad (4.19)$$

This reduces the size effect parameter to [Niel 00, Scho 03]

$$\beta_{ij} = \frac{1}{f_B/f_A - 1}\left(\left(\frac{c_A}{c_B} + \alpha_{ij}\right)\langle\Delta_{ij}^{AA}\rangle + \left(\frac{c_B}{c_A} + \alpha_{ij}\right)\frac{f_B^2}{f_A^2}\langle\Delta_{ij}^{BB}\rangle\right). \quad (4.20)$$

The average displacement scattering of first order can be written as

$$\langle S_1(\vec{q})\rangle = \underbrace{c_A c_B (f_B - f_A)^2}_{\mathrm{LU}} \sum_{i,j} \beta_{ij}\, \vec{q}\cdot\vec{r}_{ij}\, \sin\left(\vec{q}\cdot\vec{r}_{ij}\right). \quad (4.21)$$

As already mentioned, (4.21) is only an approximation that does not hold when atomic displacement varies strongly with the local configuration in the lattice. In such a case information about displacement has to be sought by simulation techniques.

The term, of 2th order has a strong influence in the region of Bragg reflection. Here Huang scattering, which is due to defects in the lattice, plays a role. Also thermo-diffuse scattering (TDS) of first order is strong in this vicinity. Thermo-diffuse processes are inelastic scattering processes. The Debye-Waller factor can be calculated within the framework of the Debye approximation [Scho 99]:

$$2\mathrm{M_{th}} = \frac{3\hbar^2}{m k_\mathrm{B}\Theta_\mathrm{D}}\left(\frac{1}{4} + \frac{T}{\Theta_\mathrm{D}}\Phi\left(\frac{\Theta_\mathrm{D}}{T}\right)\right)|\vec{q}|^2, \quad (4.22)$$

where m is the average atomic mass, Θ_D the Debye temperature, and the Deby integral is given by

$$\Phi(x) = \frac{1}{x}\int_0^x \mathrm{d}t\, \frac{t}{\exp(t) - 1}. \quad (4.23)$$

This leads to a modulation of th structure factor [Welb 95, Scho 99] of

$$\langle S_0(\vec{q})\rangle^{\mathrm{TDS}} = \langle S_0(\vec{q})\rangle\left(1 - \mathrm{e}^{-2\mathrm{M_{th}}}\right). \quad (4.24)$$

Higher order terms also result in diffuse scattering close to the Bragg reflections. The relevant terms for aXPCS are therefore the term of 0th order, as it is needed for short-range order correction and the therm of 1st order, as it is present in the same regions of reciprocal space.

4.1.2. Modulation wave approach in reciprocal space

This approach was introduced by Krivoklaz [Kriv 69] and shall be mentioned here for the sake of completeness. In a binary system a state function σ_i is defined similar to Section 2.2.1, with $\sigma_i = 1$ if a certain particle sits at position $\vec{r}_i$ and $i = 1, ..., N$ with N the number of particles. This is used to introduce Fourier components calculated from the local deviation in

concentration:

$$\sigma_{\vec{q}} = \sum_{i=1}^{N} (\sigma_i - \langle \sigma_i \rangle) \exp(-\mathrm{i}\, \vec{q} \cdot \vec{r}_i) \tag{4.25}$$

In frame of this theory, displacements are treated by considering static displacement waves. Let the position vector again be the sum of the average position vector and a local displacement, $\vec{r}_i = \vec{R}_i + \vec{\delta}_i$. The Fourier component of statical displacement waves is then defined as:

$$\vec{\delta}_{\vec{q}} = \sum_{i} \vec{\delta}_i \exp(-\mathrm{i}\, \vec{q} \cdot \vec{r}_i) \tag{4.26}$$

The advantage compared to the formalism introduced in Section 4.1.1 is that long-range effects are included. A correlation term like $\epsilon_{ij} = \langle \sigma_i \sigma_j \rangle_{\Delta \vec{r}_{ij}}$ with $\Delta \vec{r}_{ij} = \vec{r}_j - \vec{r}_i$ can be introduced, which again is used to define a Fourier component:

$$\epsilon_{\vec{q}} = \sum_{\Delta \vec{r}_{ij}} \epsilon_{ij} \exp(-\mathrm{i}\, \vec{q} \cdot \Delta \vec{r}_{ij}) \tag{4.27}$$

The diffuse scattering intensity is then given by the Krivoglaz formula

$$I_{\text{diffuse}} = \epsilon_{\vec{q}} \left| \bar{f}\, \vec{q} \cdot \vec{A}_{\vec{q}} - \Delta f \right|^2 , \tag{4.28}$$

where $\bar{f}$ is the average scattering length, Δf the variation in scattering length and coupling parameter $\vec{A}_{\vec{q}}$ is linked to the Fourier component of the statical displacement wave $\vec{\delta}_{\vec{q}}$ via coupling forces. This method finds its application in measurements over a wide q-range [Kriv 96, Gyor 83, Scho 99, Scho 03]. As this approach was not applied to determine short-range order parameters in this work a detailed treatment of the matter would go beyond its scope.

4.1.3. Pair distribution function

Rather than extracting chemical order and displacement directly from the scattering intensity, the real-space pair correlation function, which directly reveals such information, can be calculated from the scattering pattern. This approach was introduced almost 90 years ago [Zern 27], but has undergone a surprising renaissance in the last two decades. A pair distribution function is basically a probability distribution of the number of atoms at all atomic distances. The underlying principal for measuring such a function is to use the powder diffraction data up to sufficiently high $|\vec{q}|$-values to calculate the pair distribution function via a Fourier transform. This can be used directly, or in comparison with a modeled system, to determine inter-atomic distances, chemical order, but also stacking faults, size of nano-particles, correlation length and many more parameters. Like in all powder diffraction techniques, crystallographic directions are averaged. Therefore, starting from (4.2) one acquires an expression for the intensity that is independent of the azimuthal angle and is therefore only a function of the length of the scattering

vector $q = |\vec{q}|$:

$$S(q) = \frac{1}{4\pi} \int_0^{2\pi} \mathrm{d}\varphi \int_0^{\pi} \mathrm{d}\theta \sin(\theta) \sum_i \sum_j f_i f_j \exp\left(\mathrm{i}\,(\vec{r}_i - \vec{r}_j) \cdot \vec{q}\right) \tag{4.29}$$

$$= \frac{1}{2} \sum_{i,j} f_i f_j \int_0^{\pi} \mathrm{d}\theta \sin(\theta) \exp\left(\mathrm{i}\,\Delta r_{ij}\, q\, \cos(\theta)\right) \tag{4.30}$$

$$= \sum_{i,j} f_i f_j \left(\frac{\sin(\Delta r_{ij}\, q)}{\Delta r_{ij}\, q} \right) \tag{4.31}$$

To obtain the reduced pair correlation function $\gamma^*(r)$ from the measured intensity three steps are taken:

$$I^{\exp}(q) \longrightarrow S(q) \longrightarrow \gamma(r) \longrightarrow \gamma^*(r)$$

The experimentally measured scattering intensity depends on a number of additional factors, like the self absorption of the sample depending on the sample geometry, the resolution of the detector, Compton scattering, thermo-diffuse background intensity and other instrumental specifics of the setup. There is quite a number of software packages which can be used to refine the measured data. A commonly used one is PDFgetX3.

There are different definitions of pair distribution functions (see e.g. [Keen 01]). One possible definition is given by:

$$\gamma(r) = \frac{2}{\pi} \int_0^{\infty} \mathrm{d}q\, q\, (S(q) - 1) \exp\left(\mathrm{i}qr\right) \tag{4.32}$$

As the number of surrounding atoms and therefore the number of scattering electrons increases, this function increases with increasing r. Therefore, one usually works with the reduced pair distribution function, whose limit is zero as r approaches infinity:

$$\gamma^*(r) = \frac{\gamma(r)}{4\pi n r}\,, \tag{4.33}$$

where n is the number of scatterers per $\mathrm{Å}^3$.

4.2. Experimental techniques

Different experimental techniques are based on the concepts introduced above. As all these techniques operate in reciprocal space, scattering experiments using neutrons, electrons or X-rays are performed to find the relevant parameters. As a thorough discussion of this topic would go way beyond the scope of this work, only a few comments and references are given.

4.2.1. Reciprocal space mapping

Early work in this field was done by [Cowl 50], [Warr 51], [Clap 66] and [Bori 71]. Many systems were also studied by B. Schönfeld and colleges (see e.g [Scho 99]).

Fig. 4.1 shows the diffuse intensities of single crystalline samples measured the Bruker AXS Nanostar of the Faculty Center for Nano Structure Research, Faculty of Physics, University

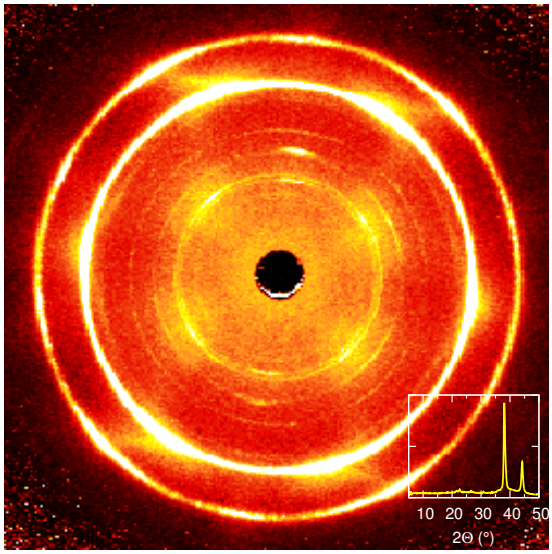

(a) $Ag_{58at.\%}Mg_{42at.\%}$ single crystalline sample.

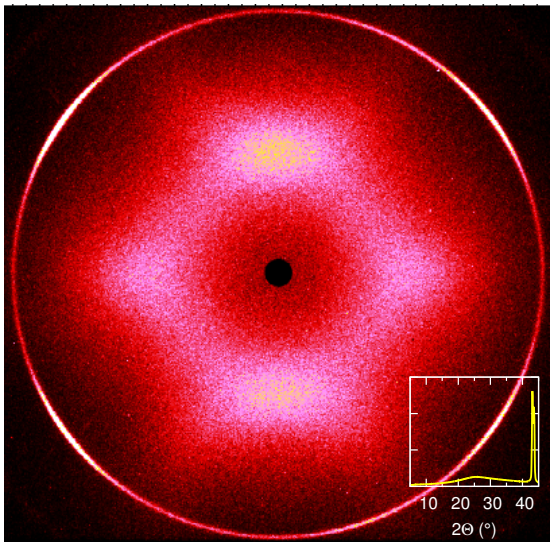

(b) $Ni_{90at.\%}Pt_{10at.\%}$ single crystalline sample.

Figure 4.1.: Diffuse intensity measured at Bruker AXS Nanostar using a flat Fuji Image Plate as detector and K-α radiation with a wavelength of 1.54189 Å. The small images give the calibrated φ integration of the intensity. Both samples were oriented in $\langle 110 \rangle$ direction.

of Vienna. In case of the Ni–Pt sample, one Debye-Scherer ring is visible, which corresponds to the fundamental (111) reflex of the fcc structure. This ring is due to arbitrarily misoriented crystallites on the surface. The Ag–Mg sample shows a number of such rings. At 26.8° the (100)-superstructure peak from the intended AgMg (B2) structure and at 38.2° and 55.4° (which is outside the section covered by the image) the fundamental (110) and (200) bcc peaks are visible. Additionally, there are a (100) superstructure peak at 21.2° and 22.2° (double line due to tetragonal phase at room temperature) and the (110)-peak at 30.4° as well as fundamental fcc peaks at 37.9° (111) and 44.1° (200) visible, corresponding to a $MgAg_3$ ($L1_2$) phase. Lines at 37.0° (111) and 43.0° (200) could, however, also correspond to MgO, which has NaCl structure and a lattice constant of 4.212 Å. It is likely, that the formation of MgO, by oxidation of Mg reduces the magnesium content of the alloy in the surface region, which initiates the formation of the $MgAg_3$. This, however, is limited only to the surface and therefore has no influence on bulk properties. Both samples are oriented in $\langle 110 \rangle$ direction, visible in the twofold symmetry of the diffuse scattering intensity.

It shall be mentioned, that using a detector with good energy resolution, the quasi-elastic scattering for the thermo diffuse term can be masked. Unfortunately, such 2D-detectors do not exist for X-rays. In order to distinguish between diffuse scattering of 0th and 1st order, a large fraction of reciprocal space (up to high $|\vec{q}|$-values) has to be mapped. It is also important to avoid areas around Bragg reflection, where additional effects play a role.

4.2.2. Pair distribution function analyzes

The key to success with this method is to get the correct real-space pair distribution function from the scattering data. Once this is achieved, finding information about local short-range

order and displacements is straightforward for binary intermetallic alloys. For more complex systems, simulation packages like DISCUS [Prof 97] are available. In order to get the pair distribution function, however, several corrections are necessary. Attempts to apply this method to intermetallics have proofed extremely difficult.

4.3. Numerical concepts for finding chemical short-range order properties

With ever growing computational power, simulation techniques have developed into an indispensable tool in solid state and material sciences. There is a manifold of different techniques for different purposes. In order to gain detailed information about local configurations, such as the local distances between atoms and configurational energies, ab initio codes, like for example the Vienna Ab initio Simulation Package (VASP) or ABINIT can be used. Due to the high computational demand, such methods are, however, limited to small unit cells. In order to gain information about large systems, information about configuration potentials gained from ab initio calculations can be used to find effective cluster expansion potentials, which in turn are used for MC simulations. A different approach is to use the embedded atom method (EAM). The parameters for both, cluster expansion and EAM can be gained by fitting to experimental data.

For a topical review, see e.g. [Schw 98, Mull 03]. The combination of experimental tools and simulation is a useful for finding information about disorder in systems [Welb 94].

In the following chapter an overview over some simulation techniques, which find application in this thesis, will be given.

5. Simulation techniques

Simulation techniques play an important role in aXPCS data evaluation. Here a short outline of the concepts used in this thesis is given.

5.1. The Monte Carlo (MC) method

Introduced at the beginning of the second half of the last century [Metr 53] the MC method has since developed into a indispensable tool in computational physics. Here only a very brief overview of the underlying idea is given.

When in thermal equilibrium, a system is found in a state σ which is a member of the canonical ensemble (CE). The probability to find a certain state σ is given by

$$P(\sigma) = \frac{\exp\left(\frac{-H(\sigma)}{k_\mathrm{B}T}\right)}{\sum_{\sigma\in\Omega}\exp\left(\frac{-H(\sigma)}{k_\mathrm{B}T}\right)} = \exp\left(\frac{F - H(\sigma)}{k_\mathrm{B}T}\right), \tag{5.1}$$

where F is the free energy, which is constant at thermal equilibrium, and $H(\sigma)$ the energy of the system in this state. The average property $\langle A\rangle$ of a system in equilibrium can then be determined from the weighed sum over this property of the individual states,

$$\langle A\rangle = \sum_{\sigma\in\Omega} P(\sigma)A(\sigma) = \sum_{\sigma\in\Omega}\exp\left(\frac{F - H(\sigma)}{k_\mathrm{B}T}\right)A(\sigma), \tag{5.2}$$

where Ω is the set of states within the CE. In order to find this probability analytically, F has to be known. For binary alloys, the energy of all states $\sigma \in \Omega$ is only known for special cases. Therefore, the sum over all states can also only be carried out in special cases. Alternatively, information about property A can be found by evaluating a subset of Ω and calculating an average value $\bar{A}$. Choosing any arbitrary subset for evaluation is unrewarding, as the contribution of states with low probability gives a wrong bias for $\bar{A}$. In order to find a value $\bar{A} \approx \langle A\rangle$, the states chosen for averaging have to be highly probable.

Let the probability for a transition from state σ to state σ' be given by $P(\sigma \to \sigma')$, The principle of detailed balance than states:

$$P(\sigma)\,\omega(\sigma \to \sigma') = P(\sigma')\,\omega(\sigma' \to \sigma) \tag{5.3}$$

Therefore, an improbable state is keen to transit, while a probable state rather stays the way it is. With this the ratio of transition probabilities can be written as

$$\frac{\omega(\sigma \to \sigma')}{\omega(\sigma' \to \sigma)} = \frac{P(\sigma')}{P(\sigma)} = \exp\left(\frac{H(\sigma') - H(\sigma)}{k_\mathrm{B}T}\right) = \exp\left(\frac{-\Delta H}{k_\mathrm{B}T}\right) \tag{5.4}$$

This allows to define

$$\omega(\sigma \to \sigma') = \frac{1}{\tau_0} \begin{cases} \exp\left(\frac{-\Delta H}{k_\mathrm{B}T}\right) & \text{if } \Delta H > 0 \\ 1 & \text{if } \Delta H \leq 0 \end{cases} \tag{5.5a}$$

or

$$\omega(\sigma \to \sigma') = \frac{1}{\tau_0} \frac{1}{1 + \exp\left(\frac{\Delta H}{2k_\mathrm{B}T}\right)}, \tag{5.5b}$$

where (5.5a) is according to [Metr 53] and (5.5b) an alternative definition according to [Glau 63]. Both yield the same result. The time scale is given by the average residence time τ_0. Starting at an arbitrary state, a probable state of the ensemble is chosen. This is done by comparing a random number $w \in [0, 1]$ with the transition probability. If $w \leq \omega$ the transition is performed, otherwise not.

For atomic properties in a bulk, a set of particles is chosen to occupy positions in a three-dimensional space. Either they occupy discrete positions on a lattice, which shall be termed an on-lattice approach, or the atoms can relax around the average positions. This is called off-lattice approach. The particles can be of different type and the interactions between them create a 3N-dimensional energy landscape. There exist different concepts for modeling such interactions, as will be discussed further below.

5.1.1. Kawasaki type diffusion

One way to switch between states is by a direct exchange of two particles. In the Kawasaki type simulation, two particles of the system are chosen at random and the exchange probability is given according to (5.5).

5.1.2. Vacancy driven walk

A vacancy in the lattice is chosen at random. A dice is rolled again to determine a number between 1 and Z, the number of possible neighbor atoms. A decision whether to exchange the vacancy and the respective atom is made based on (5.5).

5.2. Configurational functions and potentials

In order to apply a MC approach for changing states, for minimization as well as in equilibrium, the energy of the system has to be determined. This can be done following different approaches of which two will be briefly discussed in the following sections.

5.2.1. Pair potentials

A simple approach for building an energy landscape is to introduce a Hamiltonian that depends on effective pair interactions, similar to what was discussed in (2.38). With M being the number

of particles in the system, the total internal energy of the system can be written as

$$H = \underbrace{E_0 + \sum_{i}^{M} E(\sigma_i)}_{H_0} + \underbrace{\sum_{i,j}^{M} E_{ij}(\sigma_i, \sigma_j; \Delta r_{ij})}_{\tilde{H}} \; . \tag{5.6}$$

For closed systems where no particle exchange with the outside takes place, H_0 is a constant. Therefore the difference between $H(\sigma)$ and $H(\sigma')$ only depends on $\tilde{H}(\sigma) - \tilde{H}(\sigma')$. Let X and Y denote the type of particle. Systems composed of two types of atoms (A,B) and vacancies (V), $X, Y \in \{\text{A,B,V}\}$ are ternary systems. The relevant part of the Hamiltonian can be written as

$$\tilde{H}(\sigma) = \sum_{i=1}^{M}\sum_{j=1}^{M} E_{ij}(\sigma_i, \sigma_j; \Delta r_{ij}) = \sum_{i=1}^{M}\sum_{s=1}^{S}\sum_{i_s=1}^{Z_s} E_{ii_s}(\sigma_i, \sigma_{i_s}; \Delta r_s) \tag{5.7}$$

Here i_s is the index of a neighbor in shell s arround the atom at i, Z_s is the coordination number of shell s (e.g. $s = 1$ for first neighboring shell, $s = 2$ second neighboring shell and so on) and S is the coordination shell that marks the cutoff radius of interaction. This can be rewritten in a more compact form, using the number of pairs of a certain type, $n^{X,Y}$ for each shell as

$$\tilde{H} = \sum_{i=1}^{M}\sum_{s=1}^{S} \sum_{\substack{(X,Y) \\ \in\{\text{A,B,V}\}}} n_{i;s}^{X,Y} E_s^{X,Y} \tag{5.8}$$

As $E^{\text{X,Y}} = E^{\text{Y,X}}$, there are six independent parameters, $E^{\text{A,A}}$, $E^{\text{A,B}}$, $E^{\text{B,B}}$, $E^{\text{A,V}}$, $E^{\text{B,V}}$, $E^{\text{V,V}}$, which have to be determined for the simulation.

The ABV model

In order to reduce the number of free parameters, the so called ABV model was introduced [Yald 91, Vive 93, Wein 98]. A spin variable is introduced which is defined by

$$\varsigma(X) = \begin{cases} +1 & \text{if } X = \text{A} \\ -1 & \text{if } X = \text{B} \\ 0 & \text{if } X = \text{V} \end{cases} \; . \tag{5.9}$$

This makes it possible to formulate the interaction-dependent part of the Hamiltonian for interactions up to the first neighboring shell as [Wein 00]

$$\tilde{H} = \tilde{H}_0 + K\sum_{\langle ij\rangle} \varsigma_i^2\varsigma_j^2 + J\sum_{\langle ij\rangle} \varsigma_i\varsigma_j + U\sum_{\langle ij\rangle} (\varsigma_i^2\varsigma_j + \varsigma_i\varsigma_j^2) + M\sum_{\langle ij\rangle} \varsigma_i^2 + R\sum_{\langle ij\rangle} \varsigma_i \, . \tag{5.10}$$

Here Z is the coordination number of the first neighbor shell (the number of nearest-neighbor pairs) and $\langle ij\rangle$ indicates the corresponding atomic pairs.

The individual terms are defined as:

$$K = \frac{1}{4}(E^{\mathrm{A,A}} + E^{\mathrm{B,B}} + 2E^{\mathrm{A,B}}) + E^{\mathrm{V,V}} - E^{\mathrm{A,V}} - E^{\mathrm{B,V}} \tag{5.11a}$$

$$J = \frac{1}{4}(E^{\mathrm{A,A}} + E^{\mathrm{B,B}} - 2E^{\mathrm{A,B}}) \tag{5.11b}$$

$$U = \frac{1}{4}(E^{\mathrm{A,A}} - E^{\mathrm{B,B}}) - \frac{1}{2}(E^{\mathrm{A,V}} - E^{\mathrm{B,V}}) \tag{5.11c}$$

$$M = \frac{Z}{4}(E^{\mathrm{A,V}} + E^{\mathrm{B,V}} - 2E^{\mathrm{V,V}}) \tag{5.11d}$$

$$R = \frac{Z}{2}(E^{\mathrm{A,V}} - E^{\mathrm{B,V}}) \tag{5.11e}$$

$$\tilde{H}_0 = \frac{MZ}{2}E^{\mathrm{V,V}} \tag{5.11f}$$

It is obvious, that $\tilde{H}_0$ is a constant. With N_A the number of A atoms and N_B the number of B atoms for a CE $\sum_{\langle ij\rangle} \varsigma_i^2 = N_\mathrm{A} + N_\mathrm{B}$ and $\sum_{\langle ij\rangle} \varsigma_i = N_\mathrm{A} - N_\mathrm{B}$ are also constant. Therefore the configuration dependent term of the Hamiltonian is given by

$$\tilde{H}^{\mathrm{CE}} = K\sum_{\langle ij\rangle} \varsigma_i^2\varsigma_j^2 + J\sum_{\langle ij\rangle} \varsigma_i\varsigma_j + U\sum_{\langle ij\rangle}(\varsigma_i^2\varsigma_j + \varsigma_i\varsigma_j^2)\,. \tag{5.12}$$

Assuming that there is only one vacancy in the system, the parameter K can also be dropped, because in this case $\sum_{\langle ij\rangle}^{Z} \varsigma_i^2\varsigma_j^2 = Z\left(\frac{Z}{2} - 1\right)$. This can be used to define [Wein 98] similar to (5.8)

$$\tilde{H}^* = \sum_{s=1}^{S}\left(2J_s n_s^{\mathrm{A,B}} + U_s(n_s^{\mathrm{A,V}} - n_s^{\mathrm{B,V}})\right)\,. \tag{5.13}$$

In comparison to (5.8) the number of independent parameters per shell was reduced from six to two.

5.2.2. The embedded atom method (EAM)

The embedded atom method determines the energy of a system as the sum of electrostatic parameters and an embedding function. Assuming that the charge density ρ at a certain position can be a superposition of local atomic density functions, the embedding function accounts for the difference of energy when introducing a particle into this charge.

The total energy of the the system can be written as a sum of the individual energies per atom

$$H = \sum_{i=0}^{M} E_i^{(X)} \tag{5.14}$$

where the energy per atom is given as

$$E_i^{(X)} = F^{(X)}(\rho_i) + \frac{1}{2}\sum_{j=0(j\neq i)}^{M} \phi(r_{ij})^{(X,Y)}\,. \tag{5.15}$$

$F^{(X)}(\rho_i)$ is the embedding energy of an atom of type X in a charge density ρ_i at position i,

which is given by

$$\rho_i = \sum_{j=1(j\neq i)}^{M} f(r_{ij})^{(X)} \,. \tag{5.16}$$

Ouyang et al. [Ouya 12] proposed the following definitions, where the embedding energy can be calculated piecewise:

$$F^{(X)}(\rho_i) = \begin{cases} \sum_{k=0}^{4} F_{1k}^{(X)} \left(\rho_i - \rho_1^{(X)}\right)^k & , \quad \forall\ \rho_i \leq \rho_1^{(X)} \\ \sum_{k=0}^{4} F_{2k}^{(X)} \left(\rho_i - \rho_2^{(X)}\right)^k & , \ \forall\ \rho_1^{(X)} < \rho_i \leq \rho_2^{(X)} \\ \sum_{k=0}^{4} F_{3k}^{(X)} \left(\rho_i - \rho_2^{(X)}\right)^k & , \ \forall\ \rho_2^{(X)} < \rho_i \end{cases} \tag{5.17}$$

As mentioned in Section 4.3, the system parameters such as $F_{11}^{(X)}$ to $F_{34}^{(X)}$, $\rho_1^{(X)}$ and $\rho_2^{(X)}$ can be gained by fitting to experimental results or to results from ab initio calculations. The contribution of a neighboring atom j to the charge density at position i depends on its distance r_{ij} in the following way

$$f(r_{ij})^{(X)} = f_e^{(X)} {r_{ij}}^4 \exp\left(-\beta^{(X)}(r_{ij} - r_1^{(X)})\right) , \tag{5.18}$$

with $f_e^{(X)}$, $\beta^{(X)}$ and $r_1^{(X)}$ being fitting parameters. The electrostatic interaction is approximated by pair interaction potentials. The pair interaction of different types of atoms is the weighted average of interactions of particles of the same type

$$\phi(r_{ij})^{(X,Y)} = \frac{1}{2}\left(\left(\frac{r_1^{(X)}}{r_1^{(Y)}}\right)^4 \phi(r_{ij})^{(Y,Y)} + \left(\frac{r_1^{(Y)}}{r_1^{(X)}}\right)^4 \phi(r_{ij})^{(X,X)}\right) . \tag{5.19}$$

The pair potentials for same type particles are defined in segments:

$$\phi(r_{ij})^{(X,X)} = \begin{cases} -\phi_e^{(X)}\left(1 + \alpha^{(X)}\left(\frac{r_{ij}}{r_1^{(X)}} - 1\right)\right)\exp\left(-\delta^{(X)}\left(\frac{r_{ij}}{r_1^{(X)}} - 1\right)\right) & , \quad \forall\ r_{ij} \leq r_b^{(X)} \\ \sum_{k=0}^{6} \lambda_k^{(X)}\left(\frac{r_{ij}}{r_b^{(X)}} - 1\right)^k & , \ \forall\ r_b^{(X)} < r_{ij} \leq r_c^{(X)} \\ \sum_{k=0}^{5} \kappa_k^{(X)}\left(\frac{r_{ij}}{r_c^{(X)}} - 1\right)^k & , \ \forall\ r_c^{(X)} < r_{ij} \leq r_e^{(X)} \\ 0 & , \ \forall\ r_e^{(X)} < r_{ij} \end{cases} \tag{5.20}$$

Here again $\phi_e^{(X)}$, $\alpha^{(X)}$, $\delta^{(X)}$, $\lambda_k^{(X)}$, $\kappa_k^{(X)}$, $r_b^{(X)}$, $r_c^{(X)}$ and $r_e^{(X)}$ are fitting parameters. Some of the fitting parameters can be identified. $r_1^{(X)}$ is the nearest-neighbor distance, $r_e^{(X)}$ is obviously the cutoff radius. A list of fit parameters for the system Fe–Al according to [Ouya 12] is given in Section A.3.

5.3. Illustrative computer experiments

In this section the concepts introduced above will be used for some illustrative simulations. As a model system a solid solution with a low concentration of solute atoms is chosen. Such a

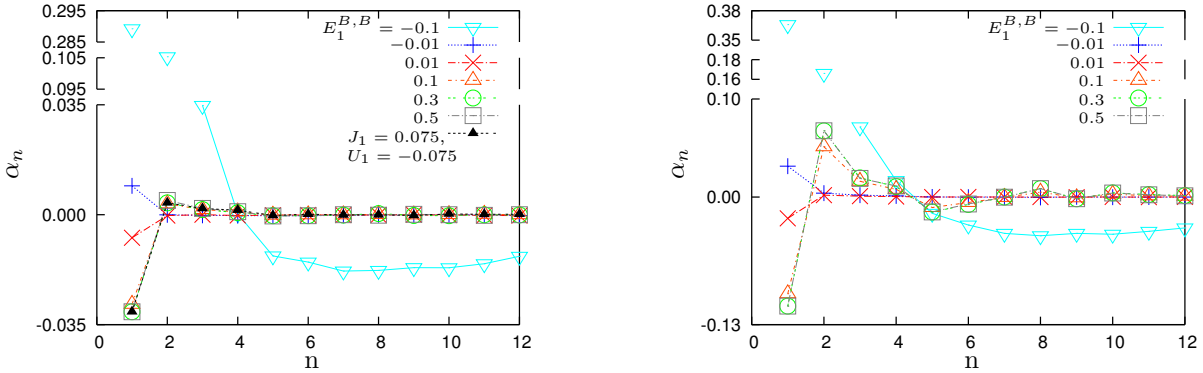

(a) 3% B-atoms solid solution

(b) 10% B-atoms solid solution

Figure 5.1.: Warren Cowley short-range order for a solid solution on an fcc lattice with pair interaction between solute atoms, where n is the shell number. The errorbars are smaller than the symbols. Lines are given to guide the eye.

system can be modeled introducing pair interactions for the solute atoms only. Simulations are undertaken using the vacancy walk Metropolis MC method with transition probabilities according to (5.5a). Time quantities are given in units of Monte Carlo step (MCS), where one MCS is defined as M attempts of particle exchange, with M the number of atoms in the system.

5.3.1. Simulation of chemical short-range order

A simulation cell of $32 \times 32 \times 32 \times 4$ atoms on an fcc type lattice was used to calculate Warren-Cowley short-range order parameters according to Section 2.2.4. After a tempering for 30 MCSs, the parameters were calculated for another 100 MCSs every tenth of a step, yielding 1000 configurations used for averaging. For each of these configurations the neighbors in the first 12 neighboring shells for each atom of type B on the lattice were counted and the average number was calculated. These numbers of neighbors were used according to (2.57) to calculate the α_n-parameters. Calculations were carried out for a temperature of 830 K. The results of simulations for a solid solution containing 3%, as well as for one containing 10% solute atoms are shown in Fig. 5.1. As $E_1^{B,B} = 100\,\text{meV}$ corresponds to ABV potentials of $J_1 = 0.075$ and $U_1 = -0.075$, Fig. 5.1a shows the short-range order parameters calculated with these potentials in addition for comparison.

As a general trend, it can be seen that a repulsive force between the solute atoms leads to a saturation in chemical short-range order, meaning that increasing the repulsive potential does not change the short-range order after a certain point is reached. This saturation potential can be estimated to be 300 meV. It can also be seen that the ABV model yields results in good agreement with the classical pair potentials. Attractive potentials, on the other hand, yield a clustering behavior which has a much stronger influence on chemical short-range order.

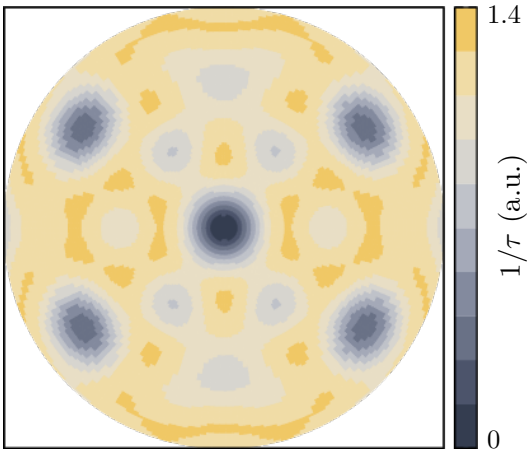

(a) Inverse correlation times calculated according to the encounter model with no atomic interaction ($1/\tau_S$).

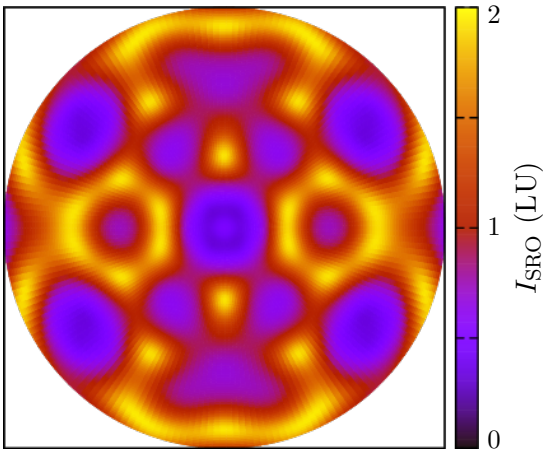

(b) Calculated short-range order intensity using parameter from Fig. 5.1b for 300 meV repulsion between solute atoms.

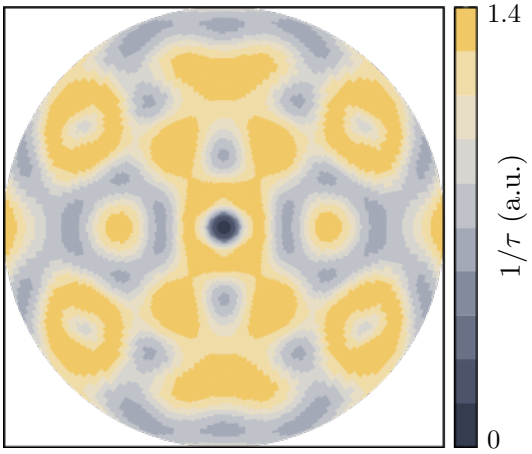

(c) Inverse correlation times calculated according to the encounter model with 300 meV repulsive force between solute atoms.

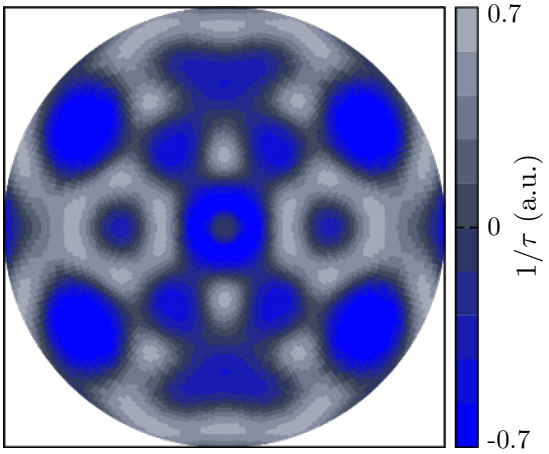

(d) Difference between Fig. 5.2a and Fig. 5.2c.

Figure 5.2.: Calculated inverse correlation times for a random vacancy walk and short-range order intensity. Calculations were made for an fcc sample with 10% B-atoms, oriented in $\langle 110 \rangle$ direction and 8 keV radiation up to $2\Theta_{max} = 90°$.

5.3.2. Computer experiment on a random walk using correlations in reciprocal space

A computer experiment was carried out to determine the influence of short-range order on a solid-solution system. Two cases are compared: no interaction between the atoms leading to a classical random walk problem and interacting atoms with a strong repulsive force of 300 meV between the solute atoms. The atomic jump probabilities for jumps to different neighboring shells where calculated in the frame of the encounter model, as discussed in Section 3.3.1. The influence of the short-range order calculated in Section 5.3.1 on the theoretical model can be seen in Fig. 5.2.

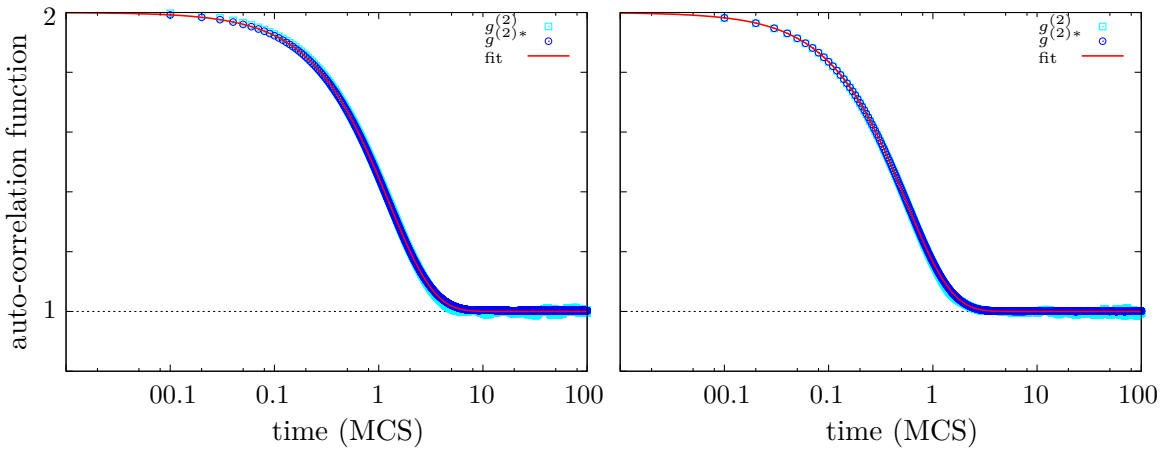

(a) $2\Theta = 11°$, $\varphi = 61°$ (b) $2\Theta = 61°$, $\varphi = 61°$

Figure 5.3.: Intensity-correlation functions calculated for two different scattering angles by Fourier transformation of different configurations in a MC simulation.

The classical approach would be to follow the atoms in real space. It is, however, also possible to simulate an aXPCS experiment to determine the jump model. In this case, after a certain time interval (a fraction of a MCS) the real space configuration is Fourier transformed[1]. From the intensities computed from the real and complex part of the amplitudes the intensity-correlation function $g^{(2)}$ is calculated. On the other had, the amplitudes can also be utalized to calculate the amplitude-correlation function, which yields the same result when applying the Siegert relation:

$$g^{(2)*} = 1 + \left(g_{\mathrm{re}}^{(1)}\, g_{\mathrm{re}}^{(1)} + g_{\mathrm{im}}^{(1)}\, g_{\mathrm{im}}^{(1)} \right) \tag{5.21}$$

Fig. 5.3 shows a comparison of $g^{(2)}$ and $g^{(2)*}$ for a small and a large scattering angle 2Θ.

Correlation functions were calculated for a number of points in reciprocal space. These points were chosen according to the parametrization introduced in Section 2.1.1.

As aXPCS is incapable of detecting vacancy jump circles, which lead to a return of a certain atom to its starting position, the values given in Table 3.1 have to be renormalized appropriately, yielding $\bar{p}_1 = 0.9229$, $\bar{p}_2 = 0.0475$, $\bar{p}_3 = 0.0194$, $\bar{p}_4 = 0.0081$, $\bar{p}_5 = 0.0010$ and $\bar{p}_6 = 0.0007$. Jumps to higher shells with a summed up probability of $\sum_i \bar{p}_i = 0.0003\ \forall i > 6$ are neglected. This can be used to calculate the $\vec{q}$-dependent inverse correlation times for this model. Fig. 5.2a gives a representation using a 2Θ and φ parametrization for a sample oriented in $\langle 110 \rangle$ direction.

A Metropolis MC vacancy walk simulation was carried out on a fcc lattice, consisting of $M = 32^3 \times 4$ atoms, where one atom is substituted for a vacancy (scattering length 0) and 10% of the atoms of type A (scattering length 28^2) were substituted for atoms of type B (scattering length 78^2) at random. The vacancy was only allowed to perform nearest-neighbor jumps. After every 0.01 MCS a Fourier transformation was carried out. The total runtime of the simulation was 1000 MCSs. The auto-correlation functions (ACFs) were averaged over $3 \times 3 \times 3$ voxels of reciprocal space for each evaluated pair of $(2\Theta, \varphi)$. In the case of repulsive force, the system was tempered for 500 MCSs before starting the calculation of the ACFs.

[1]The FFTW package http://www.fftw.org/ was used

The inverse correlation time values gained by this computer experiment for pairs of $(2\Theta, \varphi)$ were compared with an analytical model according to the encounter jump probabilities. This approach is the same as in an actual aXPCS experiment, as will be discussed in Chapter 6.

Fig. 5.4 shows the comparison of the analytical model with inverse correlation times gained from the MC experiment. The data is shown as a 2Θ-scan as well as a φ-scan. The short–range order intensity used for correcting the analytical model is also shown.

As can be seen from this computer experiment, the encounter model in combination with De Gennes narrowing describes well the chemical diffusion of solute atoms in a binary solid solution. As this model agrees very well with simulation data even for concentrations as high as 10% solute (B-type) atoms, it can be assumed to describe diffusion in solid solution over a wide range of composition, where no long-range ordering takes place.

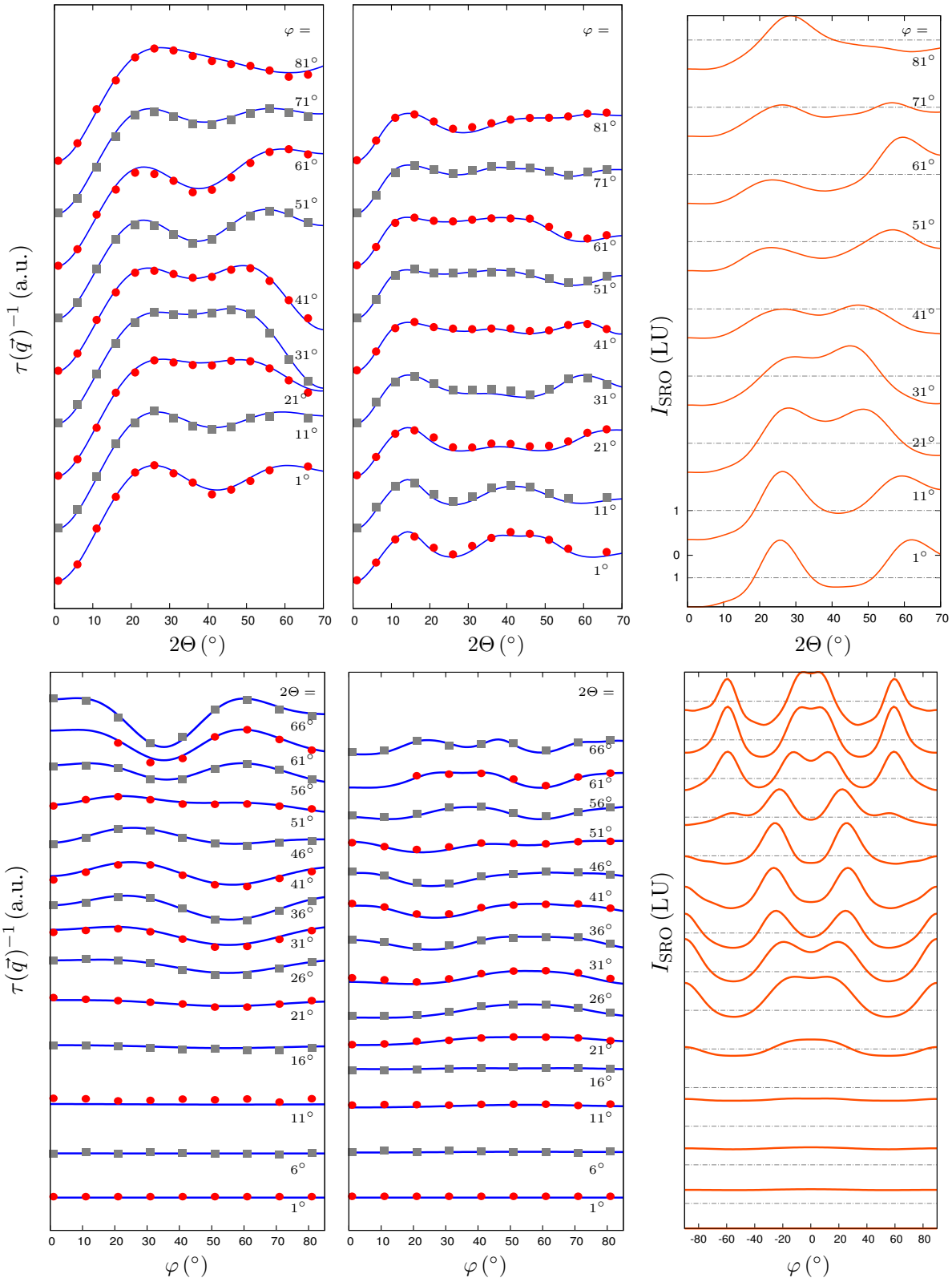

(a) No interaction between atoms, leading to a precise random walk diffusion.

(b) Repulsive force between type B atoms.

(c) Short-range order intensity for a repulsive force between type B atoms.

Figure 5.4.: Comparison of results from Monte Carlo (MC) simulation (points, errors smaller than symbols) with jump probabilities as given by the encounter model (lines) for a system with no interaction between the atoms and for a system with strong B-atom repulsion including short-range order correction. The solid solution consists of 10 at-% B-atoms and one vacancy.

6. An aXPCS experiment

The requirements for the execution of an aXPCS experiment are described in [Leit 12a] and [Ross 15]. Here only an overview of the most important keystones is given.

When coherent radiation with the appropriate wavelength λ is scattered on a number of atoms, these atoms emit spherical waves leading to an interference pattern. Coherent means that the electromagnetic waves scattered by the atoms have a fixed phase relation. One defines transversal and longitudinal coherence. The former is related to the extent and distance of the source of the electromagnetic field as it refers to the parallelism of wave fronts arriving at the sample. The best case scenario is a point source at infinite distance. By the time the wavefront reaches the localized sample its relevant section has the form of a plane wave. The transversal coherence length is defined as $\xi_t \approx \frac{\lambda R}{2\delta}$, where R is the distance between sample and source and δ is the extent of the source. The longitudinal coherence length is a measure for the monochromaticity of the electromagnetic wave, as scattering involving a spectrum of frequencies can only feature a limited acuity in the phase space. At the point where two waves from each side of the spectrum (longest and shortest wave length) are shifted by halve a wavelength, coherence is lost. The longitudinal coherence time is defined as $\tau_l = 1/\Delta\nu$, where $\Delta\nu$ is the bandwidth of the spectrum (see e.g. [Grub 08]). With this, the longitudinal coherence length is therefore defined as $\xi_l \approx c\tau_l/2 = \frac{\lambda}{2(\Delta\lambda/\lambda)}$. For a more thorough treatment of the matter see e.g. [Aber 98, Sand 99].

If a certain type of lattice is completely filled with one type of scatterers (with one particular scattering length) the scattering pattern features the well known Bragg reflection. The more perfect the lattice, the sharper the peaks. If different types of sub-lattices, e.g. α and β as in a B2 system, are occupied by a different kind of atoms each with corresponding scattering length f_A and f_B, the scattering pattern features so called super structure peaks. If perfect long-range order does not exist, either because the atomic concentration does not allow for stoichiometry or because some of the atoms occupy "wrong" places, additional intensity features appear in between these peaks in the so-called diffuse regime. As the disturbances in the lattice are not strictly periodical, a reduction of the lattice to a unit cell is not feasible any longer. Rather, the whole lattice has to be considered as one large unit cell and the scattering intensity is calculated by

$$I_{\text{interf}}(\vec{q}) \propto \sum_{i,j} f_i f_j \exp\left(\mathrm{i}\,\vec{q}\cdot(\vec{r}_i - \vec{r}_j)\right) . \tag{6.1}$$

Most X-ray sources provide only a partly coherent beam. Therefore the recorded scattering pattern is an average over different patterns corresponding to different atomic configurations, each found in a different regions of the sample. The same averaging takes place using a coherent source and measuring for a period of time much larger then the timescale where an exchange of the scatterers positions takes place, leading to different configurations. Assertions are made for average lattice properties, e.g. the average atom position and long-range order reflected in the

scattering peaks or the chemical short-range order as presented in the diffuse scattering regime. On small timescales, however, different configurations of real space yield different intensity patterns in the diffuse regime as discussed in Chapter 4. Because of the phase problem, i.e. the loss of phase information in a scattering experiment , there is no bijective function between real space configuration and scattering image. Different real space configurations can actually yield the same scattering image. Therefore, correlation comes into play when studying diffusion with coherent scattering as discussed in section Section 2.2.

The section of reciprocal space that is created by the interference of spherical waves emitted by the atoms with different scattering lengths sitting at different lattice positions is detected in an experiment as a function of the sample orientation. The resolution of such a section is limited by a physical principle called speckle phenomenon. The speckle contrast is an important parameter in aXPCS experiments, as it decreases when averaging over a section of space in case of partly coherent scattering or over time, in accordance with an averaging over a set of reciprocal spaces corresponding to different atomic configurations.

6.1. Speckle patterns

The orientation of the sample is not the only real-space feature that is reflected in reciprocal space. What is also important is the volume of the sample that is illuminated as it determines the granularity or resolution of features in reciprocal space. To put it a little differently, the Fourier transform of the illuminated area gives the smallest feature of reciprocal space, a so called speckle. Therefore, the smaller the illuminated area in real space, the bigger the speckles.

Speckles are well known from laser experiments and were first observed for X-rays almost a quarter of a century ago [Sutt 91]. There exists a manifold of approaches to the topic. Here an approach in the Fraunhofer regime was chosen.

To start with, let us consider a beam with a rectangle spot ($a \times b$) of constant brightness I_0. This means that for a scatterer of thickness d a cuboid of $V_{\mathrm{ill}} = a \times b \times d$ is illuminated with a sharp step function profile as shown in Fig. 6.1a. This can be used to calculate the form of the speckle in the Fraunhofer regime,

$$E_{\mathrm{speck}}(\vec{q}) \propto \int \mathrm{d}\vec{r}\, V_{\mathrm{ill}} \exp\left(\mathrm{i}\,\vec{q}\cdot\vec{r}\right) \tag{6.2}$$

$$\begin{aligned} &= \int \mathrm{d}r_x \left(\Theta(r_x + \frac{a}{2}) - \Theta(r_x - \frac{a}{2})\right) \exp\left(\mathrm{i}\, q_x\, r_x\right) \\ &\quad \times \int \mathrm{d}r_y \left(\Theta(r_y + \frac{b}{2}) - \Theta(r_y - \frac{b}{2})\right) \exp\left(\mathrm{i}\, q_y\, r_y\right) \\ &\quad \times \int \mathrm{d}r_z \left(\Theta(r_z + \frac{d}{2}) - \Theta(r_z - \frac{d}{2})\right) \exp\left(\mathrm{i}\, q_z\, r_z\right) , \end{aligned} \tag{6.3}$$

where $\Theta(x)$ is the Heaviside step function. And further

$$I_{\mathrm{speck}}(\vec{q}) \propto E_{\mathrm{speck}}(\vec{q}) E^*_{\mathrm{speck}}(\vec{q}) = \frac{8}{\pi^3} \frac{\sin(q_x a/2)^2}{q_x^2} \frac{\sin(q_y b/2)^2}{q_y^2} \frac{\sin(q_z d/2)^2}{q_z^2} . \tag{6.4}$$

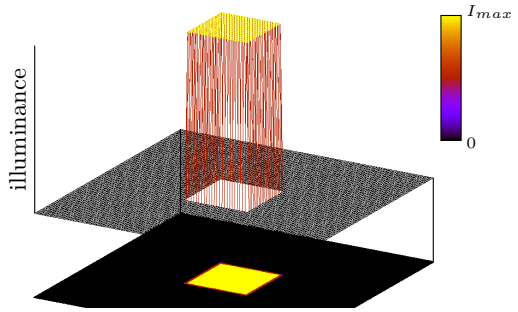

(a) Cuboid beam shape.

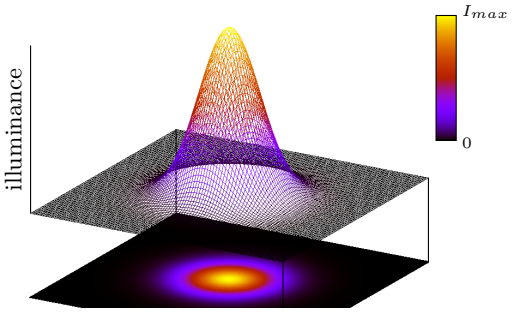

(b) Gaussian beam shape.

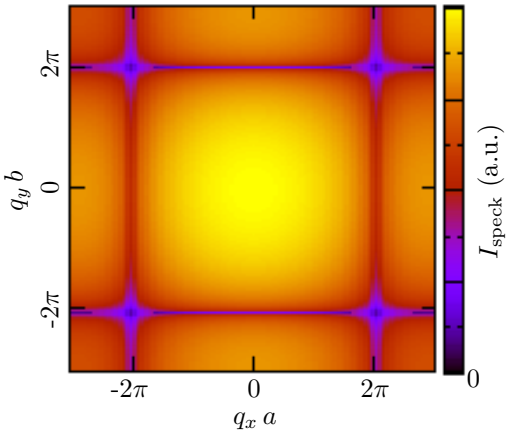

(c) Speckle pattern for (001)-plane at $q_z\, d = \pi/2$ for cuboid-shaped beam.

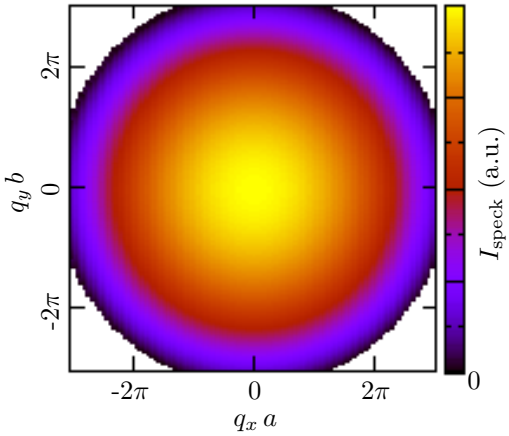

(d) Speckle pattern for (001)-plane at $q_z\, d = \pi/2$ for Gaussian-shaped beam.

Figure 6.1.: Beam profiles and corresponding speckle patterns for scattering on a completely homogeneous scattering medium with no discrete scatterers (vacuum).

The highest intensity can be found for $I_{\max} = \lim_{|\vec{q}|\to 0} I(\vec{q})$ and the first minimum at $I_{\min} = I(2\pi/a) = I(2\pi/b) = I(2\pi/d)$.

In reality the spot size is more like an ellipse and the profile of brightness can be of Gaussian form as shown in Fig. 6.1b. Therefore the amplitude of the electromagnetic field is modulated by a Gaussian. If we assume the full width at half maximum (FWHM) in r_x direction to be a and in r_y direction to be b, the illuminated area in the sample assuming constant scattering ability can be written as

$$\begin{aligned} V_{\mathrm{ill}}(r_x, r_y, r_z) = & \frac{1}{\sigma_x\sqrt{2\pi}} \exp\left(-\frac{r_x^2}{2\sigma_x^2}\right) \\ & \times \frac{1}{\sigma_y\sqrt{2\pi}} \exp\left(-\frac{r_y^2}{2\sigma_y^2}\right) \\ & \times \left(\Theta(r_z + d) - \Theta(r_z - d)\right) . \end{aligned} \tag{6.5}$$

Lets consider the Fourier transform of the r_x-term with $\sigma_x = a/(2\sqrt{2\ln(2)})$:

$$\mathscr{F}_{r_x \to q_x}\left(\left(\frac{\sqrt{2\pi}\,a}{2\sqrt{2\ln(2)}}\right)^{-1}\exp\left(-\frac{r_x^2}{2\frac{a^2}{2\ln(2)}}\right)\right) = \frac{1}{\sqrt{2\pi}}\exp\left(-\frac{a^2 q_x^2}{16\ln(2)}\right) \tag{6.6}$$

Inserting (6.6) into (6.2),

$$I_{\text{speck}} = \frac{1}{2\pi^3}\exp\left(-\frac{a^2 q_x^2 + b^2 q_y^2}{\ln(256)}\right)\frac{\sin(d\,q_z)^2}{q_z^2}\,. \tag{6.7}$$

As this function does not have a minimum, it is convenient to define the size of a speckle as the FWHM of the first scattering peak. In order to specify a speckle size that is independent on additional experimental parameters, like sample-detector distance, it will be given in units of angle. In case of a step-function profile as in (6.4), the speckle size in radian is given by $s_x \approx 5.56623/(k_{\text{in}}a)$, $s_y \approx 5.56623/(k_{\text{in}}b)$ and $s_z \approx 5.56623/(k_{\text{in}}d)$. In the case of a Gaussian beam shape (6.7), the speckle size is given as $s_x \approx 3.92103/(k_{\text{in}}a)$, $s_y \approx 3.92103/(k_{\text{in}}b)$ and $s_z \approx 5.56623/(k_{\text{in}}d)$.

As the scattering pattern is a product of a infinitely large crystal lattice and the illuminated volume, the resulting intensity pattern $I_{\text{res}}(\vec{q})$ can be seen as a convolution of a scattering pattern resulting from a crystal of infinite size, which is proportional to the structure factor $S(\vec{q})$, and the Speckle intensity:

$$I_{\text{interf}}(\vec{q}) \propto S(\vec{q}) \otimes I_{\text{speck}}(\vec{q}) \tag{6.8}$$

6.1.1. Speckles and contrast

When a speckle is illuminated by a completely coherent source, the speckle size can be calculated from the illuminated volume of the sample as described above. According to (2.67) the contrast in this case is equal to one. As already discussed, perfectly coherent X-rays are only a theoretical concept. The source is extended, which leads to a tilting of the wavefronts and the fact that the wavelength distribution is not a δ-function leads to a reduction of the longitudinal coherence length.

The effect on the speckle contrast can be discussed in the frame of statistical mechanics as was shown by Sutton (see e.g. [Sutt 06]). Here a different approach is chosen with the aim to provide useful criteria for practical experimental applications such as aXPCS. Each wavelength of each well in an extended source can be seen as an independent, perfectly coherent source. Each of these sources produces a scattering pattern on a sphere in the Fraunhofer regime, which can be detected. However, it is not possible to detect all these separate scattering patterns independently. Only the sum of them is accessible. Fig. 6.2 gives a schematic representation of the superposition of scattering spheres produced by individual sources. Therefore, information about the intensity contrast can be gained by analyzing how the scattering patterns sum up to one measurable but smeared pattern.

The dependence of the contrast on transversal coherence can be determined by analyzing the fringes of a scattering pattern produced by a slit [Grub 08]. In three dimensions the intensity

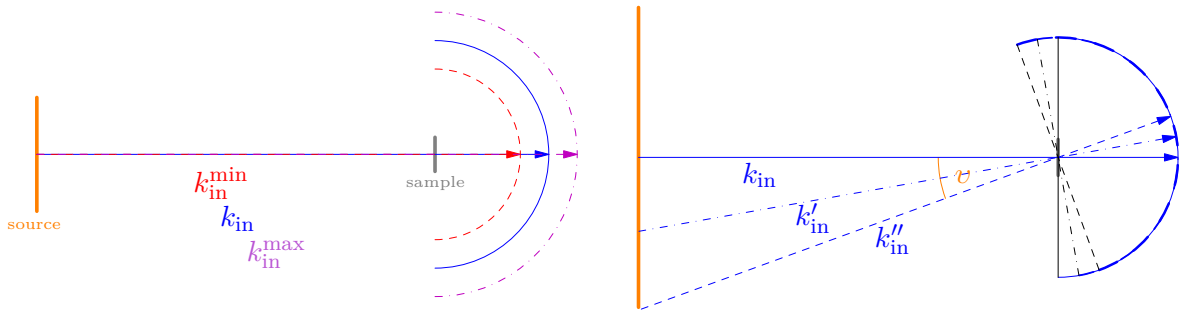

(a) A spectrum of X-rays hitting the sample leads to different $\vec{k}_{\mathrm{in}}$-vectors and therefore to different spherical wave fronts, which are summed up by a detector.

(b) An extensive source can be seen as a set of coherent sources, of which each has a corresponding vector $\vec{k}_{\mathrm{in}}$. As these vectors are twisted by an angle υ, the resulting scattering spheres are skewed by the same angle. This leads to a smearing out of scattering features.

Figure 6.2.: Schematic representation of the superposition of scattering spheres produced by individual sources leading to a reduction of longitudinal coherence as shown in (a) and transversal coherence as shown in (b).

pattern is given, similar to (6.4), by

$$I_{\mathrm{fringes}}(q_x, q_y, q_z) \propto \frac{\sin(q_x a/2)^2}{q_x^2} \frac{\sin(q_y a/2)^2}{q_y^2} \frac{\sin(q_z d/2)^2}{q_z^2} \,. \tag{6.9}$$

Using $q_x = 2k \sin\left(\frac{2\Theta}{2}\right) \cos\left(\frac{2\Theta}{2}\right) \cos(\varphi)$, $q_y = 2k \sin\left(\frac{2\Theta}{2}\right) \cos\left(\frac{2\Theta}{2}\right) \sin(\varphi)$ and $q_z = 2k \sin\left(\frac{2\Theta}{2}\right)^2$ the intensity can be written as a function of angles as

$$\begin{aligned} I_{\mathrm{fringes}}(2\Theta, \varphi) \propto & \frac{1}{k^6} \csc\left(\frac{2\Theta}{2}\right)^4 \csc(2\Theta)^4 \csc(2\varphi)^2 \sin\left(\frac{ak}{2} \sin(2\Theta) \cos(\varphi)\right)^2 \\ & \sin\left(\frac{bk}{2} \sin(2\Theta) \sin(\varphi)\right)^2 \sin\left(dk \sin(2\Theta)^2\right)^2 \,. \end{aligned} \tag{6.10}$$

As for $\varphi = 0$ this yields exactly the same pattern of fringes as plugging $q = 2k \sin(2\Theta/2)$ into a one dimensional representation of a cuboid beam form

$$I_{\mathrm{f}}(2\Theta) \propto \frac{\sin(qa/2)^2}{q^2} = \frac{\sin(k \sin(2\Theta/2) a)^2}{(2k \sin(2\Theta/2))^2} \,, \tag{6.11}$$

which is of course is the Fraunhofer approximation for single-slit diffraction. This less complicated expression will be used from now on. For azimuthal angles φ other than 0, only the slit width has to be scaled.

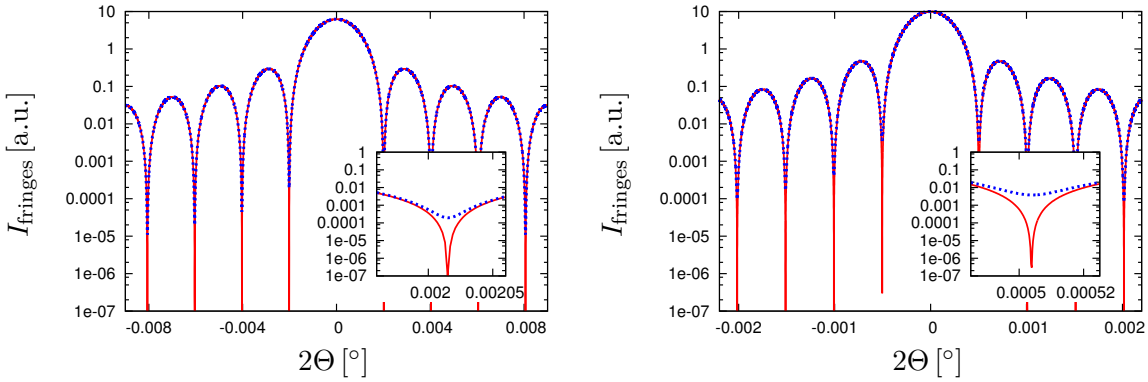

(a) Fringes for a slit size of 5 µm yielding a contrast of $\beta^{\text{tr}} = 0.997$ in the first minimum.

(b) Fringes for a slit size of 20 µm yielding a contrast of $\beta^{\text{tr}} = 0.962$ in the first minimum.

Figure 6.3.: Fringes calculated according to (6.11) and (6.12) for a 7.05 keV beam for two different slit sizes. The red, solid line shows the case of an infinitely small source and the blue, broken line the case of a source of diameter $l_s = 928\,\mu\text{m}$ and a source to sample distance of $D = 60.4\,\text{m}$.

Now let us consider an extended source where the individual scattering spheres are tilted by an angle υ as shown in Fig. 6.2b. The total intensity in this case is given by

$$I_{\text{sum-f}}(2\Theta, \upsilon_{max}) = \frac{1}{N+1}\left(I_{\text{f}}(2\Theta) + \sum_{n=1}^{N/2} I_{\text{f}}(2\Theta - \upsilon_{max}/n) + I_{\text{f}}(2\Theta + \upsilon_{max}/n)\right), \tag{6.12}$$

with $\upsilon_{max} = \tan\left(\frac{l_s/2}{D}\right)$, l_s the diameter of the source, D the source to sample distance and $N+1$ the number of scatterers in the appropriate dimension. As the number of electrons in a bunch is between 10^8 and 10^{11} [Wied 03], N is chosen to be 5000 for a crude approximation. It shall also be mentioned, that due to relativistic effects the electrons emit cones of light rather than a sphere. As these cones are not parallel, this leads to an additional tilt of the scattering spheres which further reduces the contrast.

The contrast can be calculated, according to (2.67) as

$$\beta^{\text{tr}} = \frac{I_{\text{sum-f}}(2\Theta_{\text{max}}) - I_{\text{sum-f}}(2\Theta_{\text{min}})}{I_{\text{sum-f}}(2\Theta_{\text{max}}) + I_{\text{sum-f}}(2\Theta_{\text{min}})}. \tag{6.13}$$

As $I_{\text{sum-f}}(2\Theta_{\text{min}}, 0) = 0$ for a totally coherent beam, the contrast is $\beta^{\text{tr}} = 1$ in this case. The overlap of speckle patterns increases the minimum intensity, as shown in Fig. 6.3 for two different spot-sizes. It can be seen that increasing the speckle size by reducing the spot size increases the contrast.

In order to determine the dependence of contrast on longitudinal coherence, it is important to know the maximal distance between two wavefronts. This distance is usually referred to as

maximum path-length difference (PLD) [Grub 08]. For a transmission geometry, it is given by

$$\begin{aligned}\mathrm{PLD} &\approx l_1 + l_2 - l_3 \\ &\approx d + \sin(2\Theta)(a + \tan(2\Theta)d) - \frac{d}{\cos(2\Theta)} \\ \mathrm{PLD}(2\Theta) &\approx 2d\sin(2\Theta)^2 + a\sin(2\Theta)\,.\end{aligned} \tag{6.14}$$

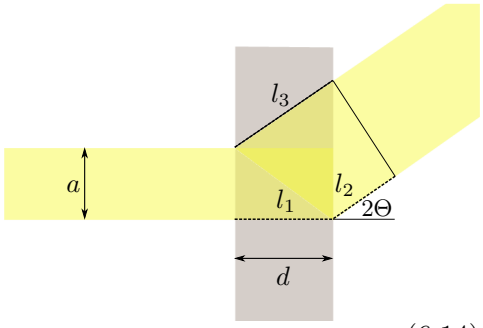

This leads to a shift in time of $\Delta t = (d + \mathrm{PLD})/c$, with c the speed of light. The summed intensity of two electromagnetic waves originating from two points in space, z and $z + \Delta z$, can be written as

$$I \propto |E_0|^2 \int \mathrm{d}z \exp(\mathrm{i}kz) \exp(\mathrm{i}k(z + \Delta z)) \tag{6.15}$$

and according to (2.64), the correlation factor is given as

$$\mathscr{G}_{ii}(\Delta t) = \lim_{t_0 \to \infty} \int_{-t_0/2}^{t_0/2} \mathrm{d}t\, E_0\, \mathrm{e}^{\mathrm{i}\,\omega t}\, E_0^*\, \mathrm{e}^{-\mathrm{i}\,\omega(t+\Delta t)} = |E_0|^2\, \mathrm{e}^{-\mathrm{i}\,\omega\Delta t} = I_0 \mathrm{e}^{-\mathrm{i}\,\omega\Delta t}\,. \tag{6.16}$$

The intensity of a monochromatic beam in dependence on PLD can therefore be written using $\Delta z = (d + \mathrm{PLD})$ as

$$I_{\mathrm{mono}}(\omega, \Delta t) = I_0 + 2\mathrm{Re}\left(\mathscr{G}_{ii}(\Delta t)\right) = 2I_0\left(1 + \cos(\omega\Delta t)\right) \tag{6.17}$$

$$I_{\mathrm{mono}}(k, \Delta z) = 2I_0\left(1 + \cos(k\Delta z)\right) \tag{6.18}$$

In case where the beam is not monochromatic, but features a spectrum that is characterized by a spectral function $g(k)$ (usually a Darwin curve when Bragg geoemetry is used), the total intensity is given by

$$I_{\mathrm{spectrum}}(\Delta z) = \frac{2I_0}{C} \int_{-\infty}^{\infty} \mathrm{d}k'\, g(k')\, \left(1 + \cos(k'\Delta z)\right)\,, \tag{6.19}$$

where C is a normalization factor. This leads to a blur of the speckle pattern in reciprocal space, which reduces the maximum intensity and increases the minimum intensity as a function of spacing Δz, as is shown in Fig. 6.4.

For a spectral function with a step-function shape, a numerical approximation can be made by

$$\begin{aligned}I_{\mathrm{spectrum}}(k, \Delta z) \approx &\frac{2I_0}{2N+1}\Big(\left(1 + \cos(k\Delta z)\right) + \\ &\sum_{i=1}^{N}\left(1 + \cos\left(k\left(1 - \frac{i\Delta k/k}{2N}\right)\Delta z\right)\right) + \left(\left(1 + \cos\left(k\left(\frac{i\Delta k/k}{2N}\right)\Delta z\right)\right)\right),\end{aligned} \tag{6.20}$$

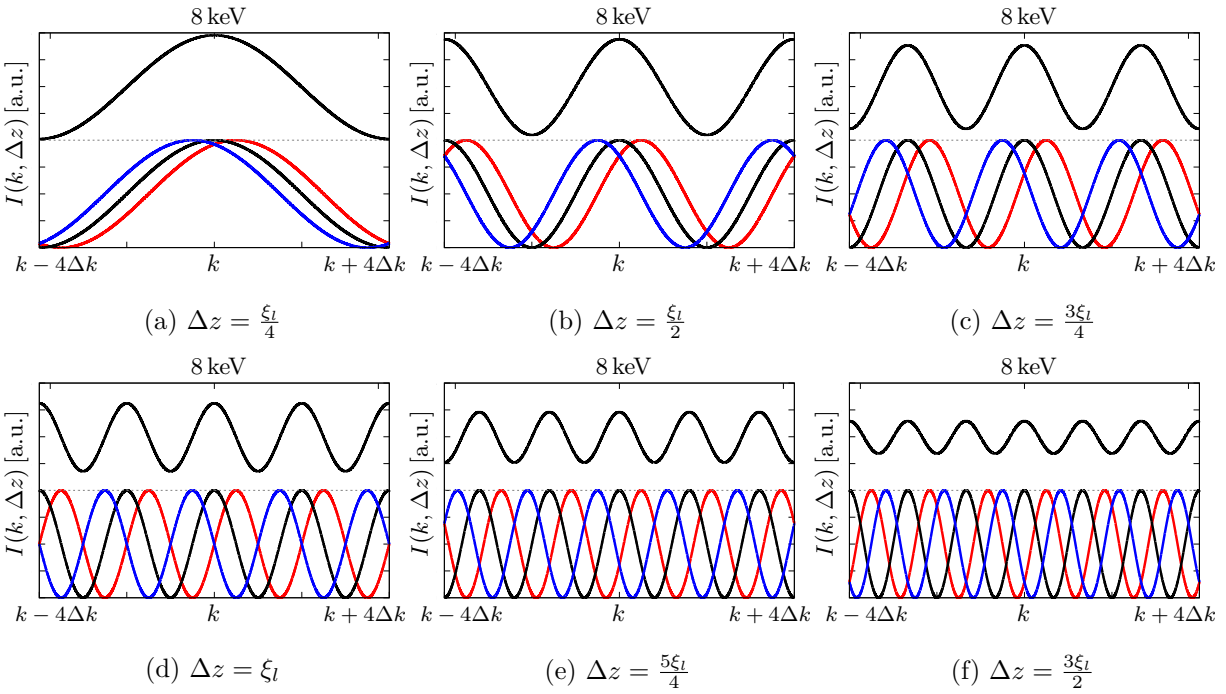

(a) $\Delta z = \frac{\xi_l}{4}$ (b) $\Delta z = \frac{\xi_l}{2}$ (c) $\Delta z = \frac{3\xi_l}{4}$

(d) $\Delta z = \xi_l$ (e) $\Delta z = \frac{5\xi_l}{4}$ (f) $\Delta z = \frac{3\xi_l}{2}$

Figure 6.4.: Intensity resulting from interference of two points spaced by Δz calculated around the scattering vector corresponding to 8 keV X-rays for $\Delta k/k = 10^{-4}$. The lower part shows the individual patterns corresponding to $\lambda_{\max}$ (red), $\bar{\lambda}$ (black) and $\lambda_{\min}$ (blue). The upper part shows the summed intensity which is decisive for the contrast, according to (6.20) with $N = 100$. The value of Δz in relation to the longitudinal coherence length ξ_l is given for each image.

where Δk gives the width of the spectrum around k. The smaller Δz is, the larger is the detail in reciprocal space (compare (6.7) with $d = \Delta z$).

An analytical solution can also be found (see Appendix A.4), yielding

$$I_{\text{spectrum}^{+/-}}(\Delta k, \Delta z) = 2I_0 \left(1 \pm \frac{\sin\left(\frac{\Delta k}{2}\Delta z\right) - \sin\left(-\frac{\Delta k}{2}\Delta z\right)}{\Delta k \Delta z} \right). \tag{6.21}$$

This can again be used to define a contrast in the form

$$\beta^{\text{l}}(\Delta k, \Delta z) = \left| \frac{I_{\text{spectrum}^{+}}(\Delta k, \Delta z) - I_{\text{spectrum}^{-}}(\Delta k, \Delta z)}{I_{\text{spectrum}^{+}}(\Delta k, \Delta z) - I_{\text{spectrum}^{-}}(\Delta k, \Delta z)} \right| \tag{6.22a}$$

$$= \left| \frac{2 \sin\left(\frac{\Delta k \Delta z}{2}\right)}{\Delta k \Delta z} \right|. \tag{6.22b}$$

As (6.22b) refers to a contrast for one specific spacing Δz, it does not account for the fact, that not only the scatterers furthest apart, but also those in-between contribute to the scattering pattern. Therefore plugging in the maximum distance as Δz only gives a lower bound of the contrast factor. The effective contrast results from a mean of all the individual contrasts of the differently spaced sources. Assuming that scatterers are separated by distances up to the longitudinal coherence length lead to interference, an upper bound of the contrast can be

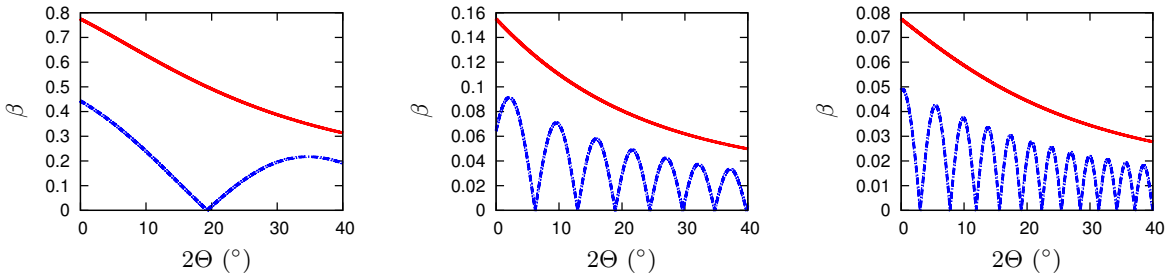

(a) $a = 1\,\mu\text{m}$ and $d = 1\,\mu\text{m}$ (b) $a = 10\,\mu\text{m}$ and $d = 5\,\mu\text{m}$ (c) $a = 15\,\mu\text{m}$ and $d = 10\,\mu\text{m}$

Figure 6.5.: Estimations for upper bound of contrast according to (6.23) (red) and lower bound of contrast according to (6.22b) (blue) for different spot-sizes and sample thicknesses.

estimated by

$$\beta^{\text{l}^*}(2\Theta) = \frac{\xi^l}{\Delta z}\,. \tag{6.23}$$

Due to the geometry of the beam, it is also possible that the PLD has a φ-dependence. Assuming a beam in form of a square with edge length a_0, the azimuthal angle-dependent width of the sample can be defined as:

$$a(\varphi) = \begin{cases} \frac{a_0}{\cos(\varphi)} & \text{if } \ 0° \leq \varphi \bmod 90° < 45° \\ \frac{a_0}{\cos(90°-|\varphi|)} & \text{if } 45° \leq \varphi \bmod 90° < 90° \end{cases} \tag{6.24}$$

This leads to $\Delta z(2\Theta, \varphi) = d(1 + 2\sin(2\Theta)^2) + a(\varphi)\sin(2\Theta)$.

6.2. Signal-to-noise ratio

According to [Falu 04, Mads 16] the signal-to-noise ratio (SNR) is linear in intensity and experimental contrast:

$$SNR \propto \langle I \rangle \beta_{\text{exp}} \tag{6.25}$$

If the transversal coherence length is sufficiently large it would therefore be in favor of the SNR to increases the spot-size on the sample, if this increases the intensity (which would not be the case for a focused beam). Doing so also reduces the speckle size. As will be discussed below, more than one ACF is usually recorded for a particular scattering-vector in order to increase statistics. Therefore, the larger the spot size, the higher the resolution in reciprocal space, the more ACFs can be recorded for a section of reciprocal space assigned to a particular $\vec{q}$-vector, which clearly is in favor of SNR.

It was also shown [Falu 06] that

$$SNR = I_{\text{coh}} \sqrt{t_{\text{tot}} \tau n_x n_y}\,, \tag{6.26}$$

where n_x and n_z are the number of detector pixels in each direction, t_{tot} is the total time for recording an ACF, I_{coh} the average coherent flux and τ is the shortest correlation time in the experiment. The relation between coherent flux and shortest correlation time can be understood

intuitively when considering the following [Shpy 14]: XPCS measures the correlation between pairs of photons rather than individual photons. In a given time window, the probability of detecting a photon in a particular pixels scales with the coherent flux. The probability of detecting a pair of photons in the same pixel, however, is the square of this value.

6.3. Experimental requirements

X-rays with sufficient coherence and the intensity required to get a signal at timescales of atomic diffusion are very difficult to come by. While optical light with excellent coherent properties can be generated by light amplification by stimulated emission of radiation (LASER), this concept is not applicable for X-rays. This has two reasons. Firstly the excited states of electrons leading to the emission of optical light have a much longer lifetime than those leading to the emission of photons with wavelength in the Angstrom regime. For example, the radiative decay rates of helium are in the order of $10^7\,\mathrm{s}^{-1}$ (see e.g. [Hero 56]). Stimulated X-ray emission, in comparison, is limited by the lifetimes of core-excited states which are in the femtosecond regime [Beye 13], creating the need to raise the excitation rate by a factor of $10^7 - 10^8$. Secondly, the reflectivity of X-ray mirrors is only good for grazing incidence angles and far below the reflectivity of optical mirrors (see table III in [Henk 93]). As each light-source partly produces coherent light of a certain wavelength, one can filter out a part of the spectrum with the desired properties. This means, however, a loss of most of the intensity.

In the early days of particle acceleration, it was realized that the parasitic bremsstrahlung produced at the bending magnets could be used for scattering experiments. This led to the construction of synchrotron light sources, serving only the purpose of creating highly intense, high energy X-rays. Wigglers and undulators, which are devices constructed as a periodical array of dipoles to laterally deflect accelerated particles [Wini 81], were introduced later. As a result, the spectrum of bremsstrahlung can exhibit peaks in a harmonica relation, yielding higher intensities for certain wavelength. A part of this spectrum (usually a harmonic beam of first order) can be extracted by filters (usually mirrors), which leads to a spectrum called pink beam that can be further monochromatized by single crystals or multilayer mirrors. More details can be found in [Ross 15] and [Mill 02, Wied 03, Ezqu 09].

It is, however, important to note that the synchrotron radiation is not produced by isolated, single charged particles such as an electron or proton. If only one charged particle would transit the udulator at a certain time, the intensity of the resulting bremsstrahlung would be far to low for application. Therefore, electrons are bundled to bunches producing higher intensities. As these charged, relativistic particles are independent, they constitute a chaotic source, which strongly limits the coherence of the produced X-ray beam.

The available sources providing X-ray with sufficient coherence have a flux of $10^7\,\mathrm{s}^{-1}\mu\mathrm{m}^{-2}$. The scattered intensity, especially for angles outside the SAXS regime is therefore very low. Let us consider the idealized case of a non-absorbing sample with a thickness so that it scatters $I_{\mathrm{scat}} = (1 - 1/e)I_0$ and spot-size of $10 \times 10\mu\mathrm{m}^2$. The total initial intensity is given by $I_0 = 10^9\,\mathrm{s}^{-1}$ and the scattering flux per steradian by $F_{\mathrm{scat}} = (1 - 1/e)10^9/(4\pi) = 5 \times 10^7\,\mathrm{s}^{-1}\mathrm{sr}^{-1}$. Assuming a step-function profile of the beam of 8 keV, the speckle size can be approximated by

$A_{\text{speck}} \approx s_x^2 \approx (5.56623/(10^{-5} \times 4.05419 \times 10^{10}))^2 \approx 1.89 \times 10^{-10}\,\text{sr}$. Therefore, the dependence on scattering angle 2Θ of the photon flux for a pixel matching a speckle can be approximated as $F_{\text{speck}}(2\Theta) \approx F_{\text{scat}} A_{\text{speck}}/\cos(2\Theta) \approx 9.5 \times 10^{-3}/\cos(2\Theta)\,\text{s}^{-1}$. Using a point detector to record the $\vec{q}$-dependent intensity, the ACF would only present a sufficient statistic if the correlation time $\tau(\vec{q})$, as defined in (2.42), would be orders of magnitude higher than those in the order of a few hundred seconds measured so far. As there is no such thing as a non-absorbing sample the flux even is orders of magnitude smaller. To improve statistics, an ensemble average over a set of neighboring speckles corresponding to a particular $\vec{q}$-vector is taken

$$g^{(2)}(\vec{q}, \Delta t) = \frac{\langle \langle I(\vec{q}_i, t)\, I(\vec{q}_i, t + \Delta t) \rangle_t \rangle_i}{\left\langle \langle I(\vec{q}_i, t) \rangle_t^2 \right\rangle_i}\,, \tag{6.27}$$

where $i = 1$ to 10^6 is the number of detector pixel. This is often referred to as multi-speckle detection scheme. It is only applicable if the gradient of $\tau(\vec{q})$ is negligible for the particular set of $\vec{q}_i$, which is usually the case. In order to record such a set of corresponding intensity-correlation functions a charge-coupled device (CCD) camera is used.

6.4. Experimental setup

Experiments have been carried out at the soft interfaces and coherent scattering beamline ID10 at the European Synchrotron Facility (ESRF) in Grenoble, France and at the Coherence applications Beamline beamline P10 at the PETRA III synchrotron at DESY, Hamburg, Germany. The characteristics important for aXPCS experiments of each beamline are given in Table 6.1. Detailed information about the optics can be found at the sources cited in the table.

	Mono-chromator	$\Delta\lambda/\lambda$	ξ_l [µm]	ξ_t [µm^2]	Flux (coh) [s^{-1}µm^{-2}]	Source size [µm^2]	S. divergence [µrad^2]	D [m]
ID10	[a]Si(111)	[a]1.4×10^{-4}	[d]1.0	[d]4×10	[a]2.6×10^7	[a]928×23	[a]25×17	[a]60.4
P10	[b]Si(111)	[b]1.0×10^{-4}	[b]1.5		[b]2.3×10^7	[b]36×6		[b]87.8

Table 6.1.: Beamline Specifications for ID10 at the ESRF and P10 at PETRA III for a 8 keV beam. Units are given in (H×V, FWHM). Sources:
[a]...http://www.esrf.eu/UsersAndScience/Experiments/SoftMatter/ID10/, April 2015
[b]...http://photon-science.desy.de/sites/site_photonscience/content/e58/e176720/e177229/e178737/e179091/e179098/e219987/P10_User_Guide_v01102013_eng.pdf, April 2015
[d]...Private communication with B. Ruta

In order to keep air scattering to a minimum, the beam is guided in vacuum with a gap between the furnace and the primary beam guide, which is closed by a silicon carbide window, as small as possible. The silicon carbide window is degenerated by the beam, which is visible in the dynamics of the speckle pattern. Therefore the position of the beam has to be slightly modified from time to time. The entrance and exit windows of the furnace are made from Kapton foil, which also shows degeneration. Due to the small beam size, however, very small

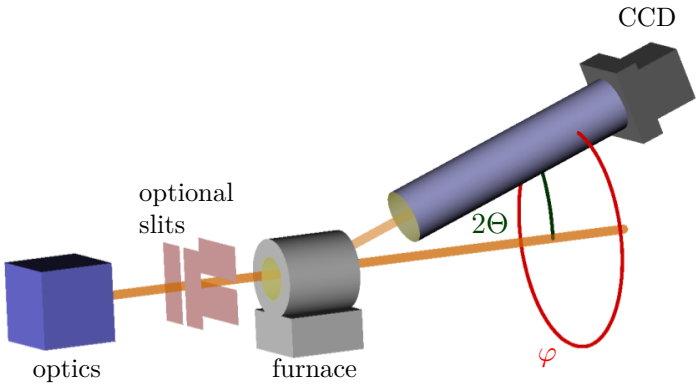

(a) Schematic representation of experimental setup.

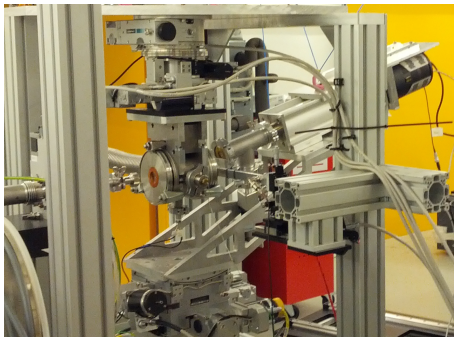

(b) Picture of experimental setup at P10, Petra III, Hamburg.

Figure 6.6.: Schematic representation and a photo of experimental setup for an aXPCS experiment. The beam-size on the sample in the furnace is either determined by focusing or by scatterless slits.

displacements of the furnace are sufficient to counteract. Behind the furnace, a flight tube is mounted to reduce air scattering between the exit window of the furnace and the CCD camera. The furnace and flight tube are evacuated to $\approx 10^{-1}$ mbar. The distance between flight tube an furnace is again chosen as small a possible. The specification of the furnace and the sample-holder within are well documented in [Ross 15]. Heating is done by thermal radiation providing a stability of temperature within 0.1 K. A diode can be used to check the stability of the beam flux.

6.4.1. Detection of scattering intensity

The data evaluation process is well described in [Leit 12a]. Here I will only treat some specific aspects.

As discussed in Section 6.1 the resolution of reciprocal space is determined by the speckle size. Measurements of scattering intensities can not be carried out in arbitrarily small time intervals. The minimal required exposure time must allow for a statistically significant number of scattered photons to be collected by the detector. By using an area detector like a CCD and averaging over all pixels (see (6.27)), the minimal required exposure time can be reduced significantly. A schematic representation of a dynamic scattering movie taken by a CCD camera for a particular set of scattering angle and azimuthal angle $(2\Theta, \varphi)$ is shown in Fig. 6.7. In order to increase statistics, a droplet algorithm [Live 00, Chus 12, Leit 12a] is used. Such an algorithm does identify all the analog to digital unit (ADU) events recorded by the chip, corresponding to photons of the energy of elastic scattering and sums them to photon events. This also reduces the amount of data that has to be processed, as 99% of the detector area does not see a photon in the time interval of one frame. The frame rate is determined by the exposure time t_{exp} and the readout time t_{out} of the detector. It can be reduced to the larger of the two $(max(t_{\mathrm{exp}}, t_{\mathrm{out}}))$, if the camera can be operated in kinetic mode. While until a couple of years ago the low intensity of the X-ray source limited the time resolution by creating the need for longer exposure times, with modern synchrotron sources becoming brighter and brighter the limiting factor increasingly

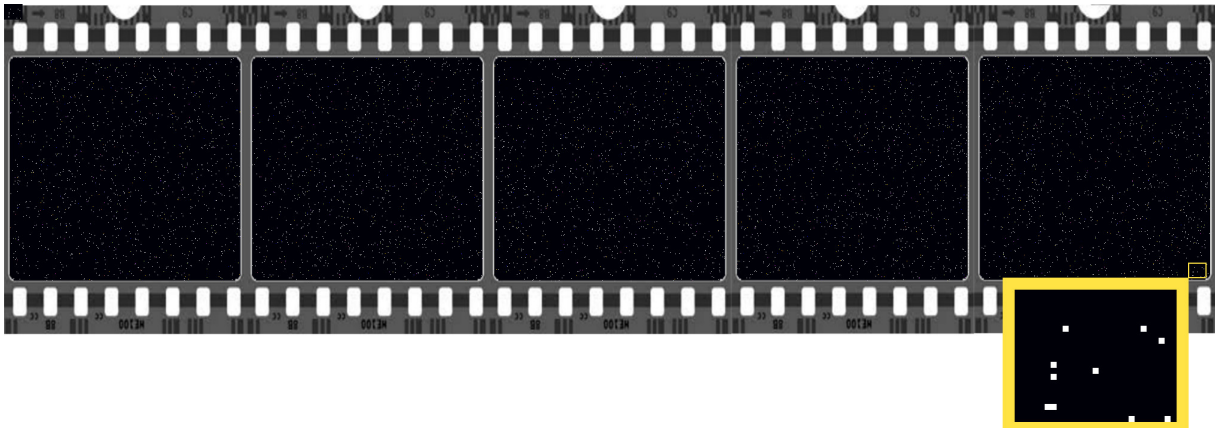

Figure 6.7.: Schematic representation of frames taken with Princeton Instruments Pixis detector at P10, Petra III.

Table 6.2.

camera	developer	number of pixels	pixel size [μm^2]	readout time [s]	beamline	cooling Peltier
iKon-M	Andor	1024×1024	13×13	0.61	ID10	Peltier
PI-LCX	Princeton Instr.	1340×1300	20×20	2.29	P10	

becomes the readout time.

In order to allow for a proper dark current correction, the temperature of the chip has to be fairly stable at temperatures around -50 °C. The distance between sample and CCD is chosen depending on the pixel size of the detector in such a way that the size of a speckle fits the size of a pixel. In order to minimize sample-to-detector distance and weight of the detector, small pixel sizes are desirable. An overview over the cameras used for aXPCS experiments at the beamlines ID10 and P10 is given in Table 6.2.

6.4.2. Projection of the Ewald sphere

As demonstrated in Section 2.1.1 for elastic scattering the multitude of possible scattering vectors span a sphere. It is, however, usually not possible to have a detection device which exactly fits this sphere. This leads to a projection of the sphere onto the detector surface. In the extreme case the detection surface is flat. Defining the position of the direct beam ($\vec{k}_{\mathrm{in}}$) as the origin on the detector, the distance on the sphere to a certain point at position $\vec{q}$ is given by $b_s = k_{\mathrm{in}}\, 2\Theta$ with the angle given in radian, while the length on the detector resulting from the central projection is given by $b_f = k_{\mathrm{in}} \tan(2\Theta)$. The distortion on a flat detector in dependence of the scattering angle is therefore given by $b_f/b_s = \tan(2\Theta)/2\Theta$ for angles in radian. From this it can be easily seen that detection with a flat detector is limited to angles of $2\Theta \in (-\pi/2, \pi/2)$ and that for angles up to $2\Theta = \pi/6$ the distortion is less than 10%.

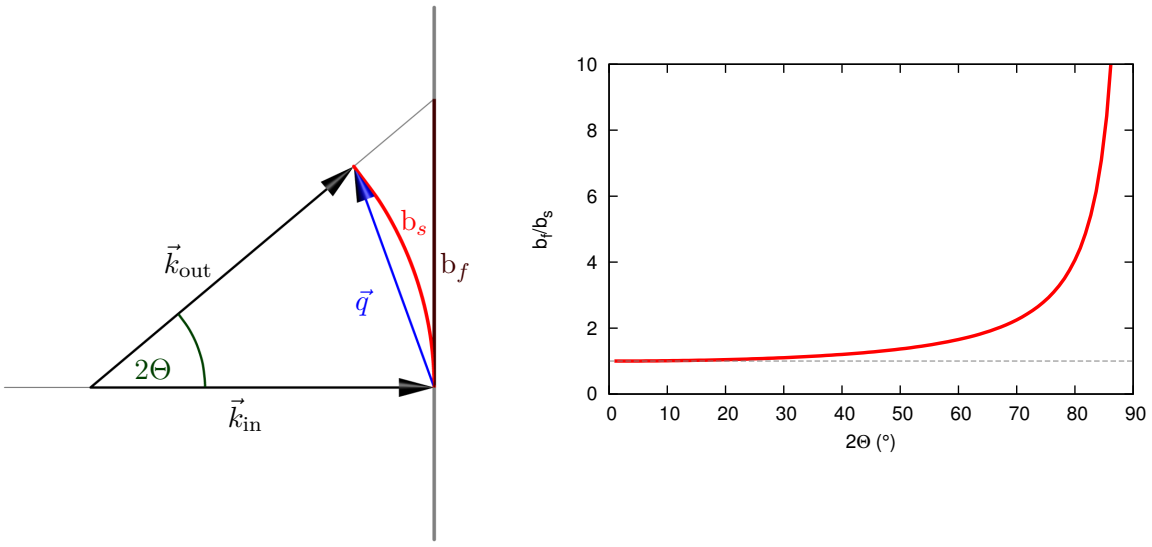

(a) Distance between the source and point corresponding to certain $\vec{q}$-value on Ewaldsphere (b_s) and corresponding projection on a flat detector (b_f).

(b) Ratio of length on Ewald sphere (b_s) and length of projection on flat detector (b_f) depending on scattering angle 2Θ.

Figure 6.8.

6.5. Sample preparation

To study atomic-scale diffusion in binary alloys, it is desirable to have single crystalline samples. For such samples an azimuthal dependence in q-space is given, as described in Section 2.1.1.

The relation between the initial intensity I_0 and the transmitted intensity I_{tr} as a function of the scattering angle 2Θ is given by

$$I_{\text{tr}}(2\Theta) = I_0 \int_0^d \mathrm{d}x\, \exp(-\mu_\lambda x) s \exp\left(\frac{-\mu_\lambda (d-x)}{\cos(2\Theta)}\right) = I_0 s \frac{\exp\left(\frac{-\mu_\lambda d}{\cos(2\Theta)}\right) - \exp(-\mu_\lambda d)}{\mu_\lambda \left(1 - \frac{1}{\cos(2\Theta)}\right)}, \quad (6.28)$$

where d is the sample thickness, μ_λ the wavelength dependent attenuation coefficient, and s the isotropic scattering factor. Maximization of this function with respect to d yields the sample thickness, where the transmitted energy has a minimum. Assuming a small reflective intensity, which is independent of the sample thickness, this means that the intensity scattered by the sample has a maximum. The optimal scattering thickness is therefore given by

$$d_{\text{opti}}(2\Theta) = \frac{\ln(\cos(2\Theta))}{\mu_\lambda \left(1 - \frac{1}{\cos(2\Theta)}\right)}. \quad (6.29)$$

6.5.1. Exemplary model $Ni_{0.90}Pt_{0.10}$

Here the steps to manufacturing a sample fit for aXPCS measurements are discussed. As a model system, a $Ni_{0.90}Pt_{0.10}$ single crystal sample was chosen.

Flakes from a rolled platinum sheet with a purity of 99.997% (provided by Johnson Matthey)

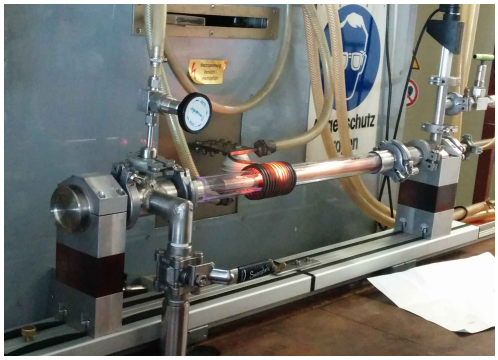

(a) Cold boat at the Technical University Vienna

(b) A lump of a $Ni_{75at.\%}Pd_{25at.\%}$ solid solution after cold boat melting.

Figure 6.9.

were cut and weighted with a precision balance. They were mixed with nickel flakes of a purity of 99,98% (by Goodfellow) in a weight-ratio of m_{Ni}/m_{Pt}=2.70776. Unities of about 4 g were melted in a cold boat at the Institute of Solid State Physics at the Technical University of Vienna. This was done in the following way: The metal flakes were positioned in one of the copper boats. The sample environment, consisting of the cold boat and a surrounding tubular quartz glass was sealed and flushed with argon several times. The induction coil was placed over the appropriate cold boat and the electrical current was increased until the sample was melted, as shown in Fig. 6.9a. The sample was turned upside down and the induction melting process was repeated. This was done several times to achieve a homogeneous solid solution. A lump produced in this way is shown in Fig. 6.9b.

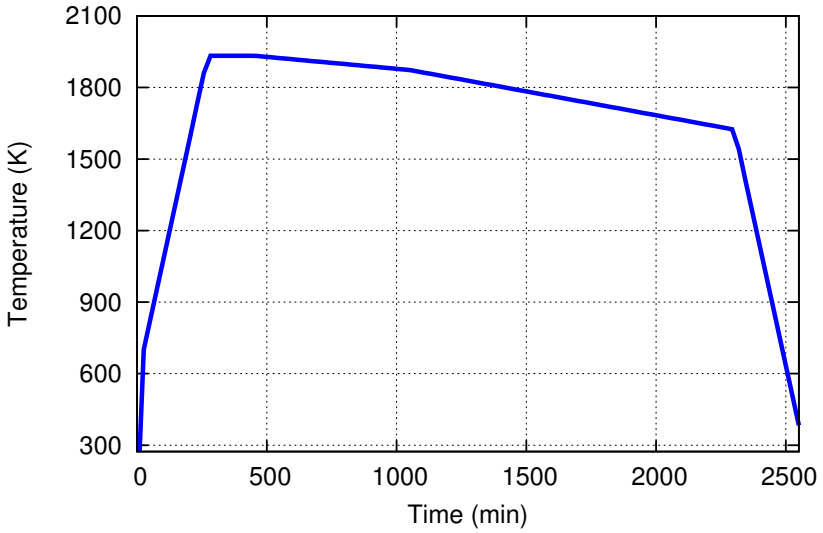

Figure 6.10.: Temperature curve for growing a $Ni_{0.90}Pt_{0.10}$ single crystal in a Tammann-Stöber furnace. The Maximum temperature was 1933.15 K, where the sample was held for 3 h.

Single crystal growth was performed in a Tammann-Stöber furnace by HTM Reetz GmbH[1].

[1]For information about the furnace, pleas visit http://www.htm-reetz.de/en/devices/special-furnace,

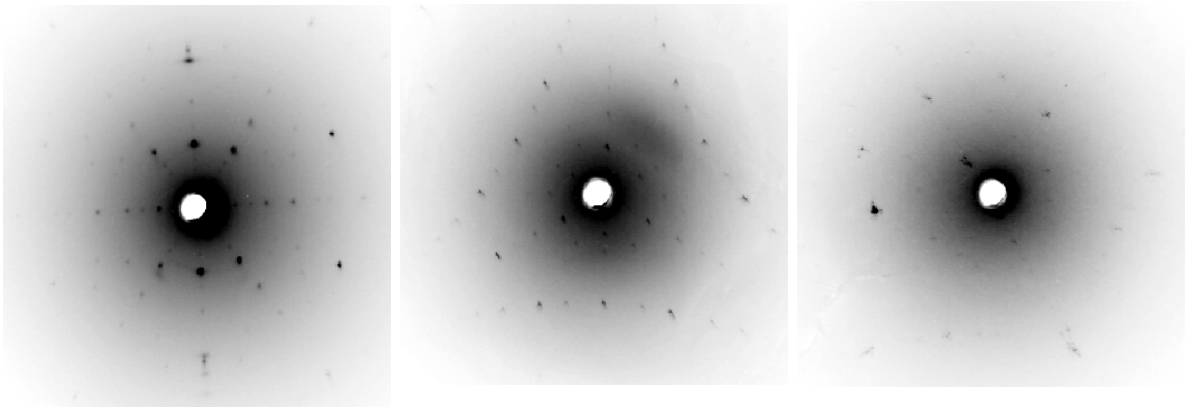

(a) $Ag_{0.58}Mg_{0.42}$ single crystal oriented in $\langle 110 \rangle$ direction. (b) $Fe_{0.54}Al_{0.46}$ single crystal oriented in $\langle 111 \rangle$ direction. (c) $Ni_{0.90}Pt_{0.10}$ single crystal oriented in $\langle 110 \rangle$ direction.

Figure 6.11.: Laue measurements in back scattering geometry of the oriented samples.

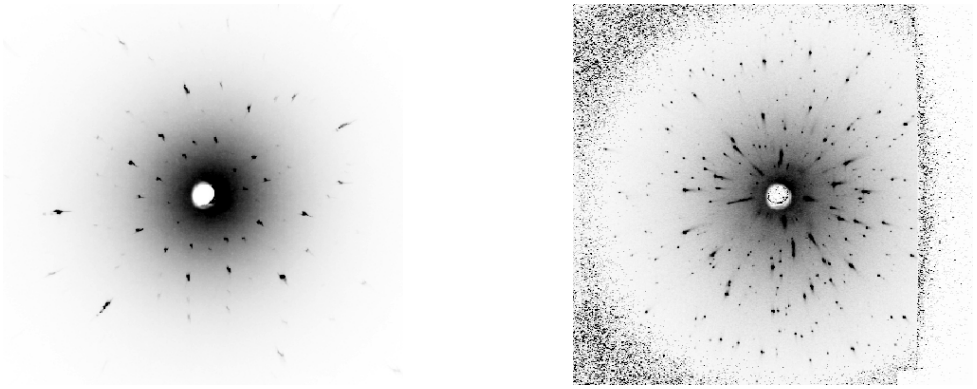

(a) $Fe_{0.54}Al_{0.46}$ single crystal oriented in $\langle 111 \rangle$ direction. (b) $Ni_{0.90}Pt_{0.10}$ single crystal oriented in $\langle 110 \rangle$ direction.

Figure 6.12.: Transmission Laue measurements of samples dimpled to scattering thickness.

This system is similar to the vertical Bridgman crystal growth method as it is also based on vertical gradient freezing. Instead of providing a changing temperature gradient by slowly moving the sample out of the hot area of the furnace, the furnace has a fixed steep temperature gradient in its heating element and a calandria is gradually cooled down. This way the sample does not have to be moved, which reduces the risk of defects due to vibrations. The lump was put into a tubular crucible made of aluminum-oxide of 99.7% purity, with a diameter of 13.4 mm and a round tip at the bottom. The temperature profile for melting is shown in Fig. 6.10. The specimen was grown in argon with a pressure slightly above one bar. Fig. 6.13a shows the final product. The surface of the sample is covered with aluminum oxide, which is of blue color due to nickel impurities. The sample was cut using a precision wire saw[2] and oriented using the Laue technique. For a cubic lattice an orientation in $\langle 110 \rangle$ direction is preferred as the orthogonal part of the reciprocal space vector is parallel to a large number of crystallographic main directions (see Section 2.1.1) yielding the most information. A recorded Laue pattern for this orientation

(April 2015).

[2]For information about the wire saw, pleas visit http://www.kdunipress.pl/pily.htm, (April 2015).

is shown in Fig. 6.11.

(a) Single crystalline sample of $Ni_{0.90}Pt_{0.10}$ with surfaces cut in (110) orientation (top) and (100) orientation (side). The surface shows residues of aluminum oxide colored blue by nickel impurity.

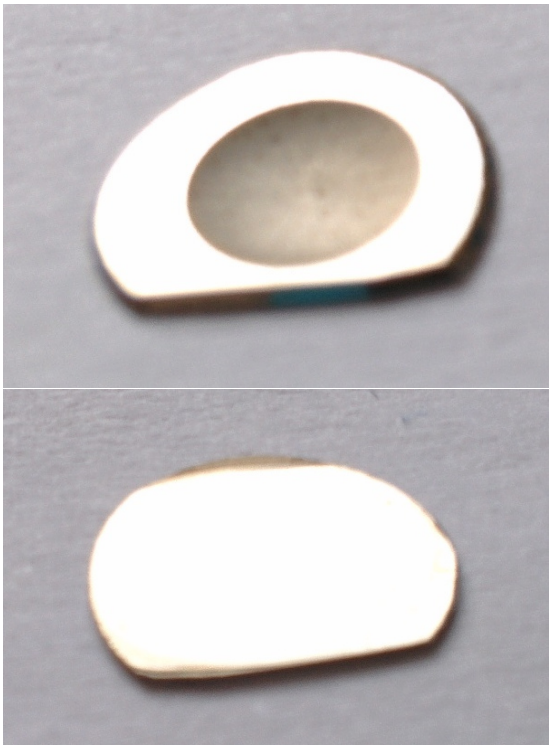

(b) Single crystalline sample ready for measurement. The top image shows the side that faces the beam.

Figure 6.13.: Single crystalline samples of $Ni_{0.90}Pt_{0.10}$.

The oriented plan-parallel slice is ground to a thickness of about 500 µm and polished on both sides. As a thin single crystal tends to twist, only part of the sample is ground to the ideal scattering thickness. This can be achieved using a dimpling grinder, which removes material such that a negative spherical surface is engraved. Such a profile, however, has a geometry unfavorable for scattering experiments, as the sample thickness increases with the scattering vector by more than a factor of $1/\cos(2\Theta)$ as would be the case for a flat sample. Therefore, only one side, which faces the beam source, is dimpled while the other one is left plane. The sample quality can be checked by means of a transmission Laue measurement, see Fig. 6.12.

The composition of the samples was checked by energy-dispersive X-ray spectroscopy (EDX) on the electron-microscope Zeiss Supra 55 VP, Faculty Center for Nano Structure Research, University of Vienna. Different areas of the sample were examined, as shown in Fig. 6.14. Measurements were taken at three different sites of the sample as can be seen in Fig. 6.14, yielding concentrations in atom-percent of $c^1_{\mathrm{Ni}} = 0.899$, $c^1_{\mathrm{Pt}} = 0.101$, $c^2_{\mathrm{Ni}} = 0.901$, $c^1_{\mathrm{Pt}} = 0.099$ and $c^3_{\mathrm{Ni}} = 0.901$, $c^3_{\mathrm{Pt}} = 0.099$. The average concentrations of $c^1_{\mathrm{Ni}} = 0.9003(12)$, $c^1_{\mathrm{Pt}} = 0.0987(11)$ are in very good agreement with the projected ratio of 90:10. The amount of Ni diffusing into the crucible can therefore be neglected and the amount of impurities is very low.

The lattice constant can be determined from WAXS measurements. Debye-Scherer rings were found at 44.00° for the (111) reflex as shown in Fig. 4.1b and at 51.27° for the (200) reflex. This

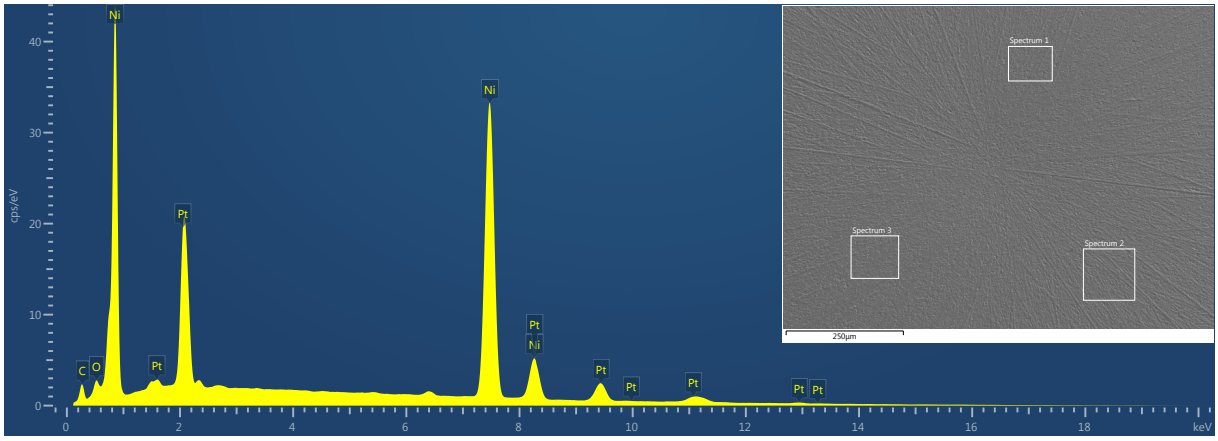

Figure 6.14.: Energy-dispersive X-ray spectroscopy spectrum of the $Ni_{0.90}Pt_{0.10}$ sample. Three different locations in the dimpled areal of the sample were scanned, as indicated by the smaller image.

gives a lattice constant of 3.5643(5) Å. The thickness of the sample was determined by X-ray absorption measurement to 23(1) µm.

A sample ready for an aXPCS experiment can be seen in Fig. 6.13b.

6.5.2. B2 - samples

$Fe_{0.54}Al_{0.46}$

The sample was prepared for Mössbauer measurements and details can be found elsewhere [Feld 95]. As a dimpling grinder was not available at the time, the entire sample was ground to a thin foil. The orientation in ⟨111⟩ direction was checked by Laue measurement (see Fig. 6.11b and Fig. 6.12a). The composition was examined by EDX to $c_{Fe} = 0.539(7)$ and $c_{Fe} = 0.460(7)$. The lattice constant for this composition was found to be 2.929 Å according to previous experimental investigations [Tayl 58].

$Ag_{0.58}Mg_{0.42}$

The sample was grown using an old Brigman furnace in a graphite crucible. An EDX analysis yielded $c_{Ag} = 0.58(1)$ and $c_{Mg} = 0.42(1)$ at the position of measurement. It should be noted, that the magnesium concentration dropped to a lower value of about $c_{Mg} = 0.24(1)$ at the outer rim of the sample. The lattice constant can be determined from the Debye-Scherer rings (the (110) at 38.2° and the (200) at 55.4°) shwon in Fig. 4.1a. This yields 3.325(11) Å, which is in agreement with the literature value of 3.3 Å [Naye 84].

6.5.3. Polycrystalline samples

Sometimes it is impossible to grow single crystals, because the composition dependent ordering does not allow for it. An attempt to grow a $Ni_{0.70}Pt_{0.30}$ single crystal has proven unsuccessful. In such a case different approaches have to be taken. As we could show [Stan 13], polycrystalline samples also yield usable information for discriminating diffusion mechanisms. It is, however,

of vital importance to have good control of grain size in such a sample. As grain growth is an issue at temperatures where aXPCS experiments are conducted, a favorable approach would be to use powder samples where the maximum grain size can be controlled by the granulation of the powder.

7. Diffusion in a solid solution

The feasibility of an aXPCS experiment was demonstrated on the example of a $Cu_{0.90}Au_{0.10}$ single crystal [Leit 09]. We followed up by studying the diffusive motion of platinum atoms in a $Ni_{0.97}Pt_{0.03}$ solid solution.

This system was chosen with three goals in mind:

- To investigate whether the correlation of vacancy jumps in a solid solution with a low concentration of solute atoms follows the same principle as in a pure metal. It was shown that the encounter model yields appropriate jump rates to the corresponding neighboring positions if De Gennes narrowing and thus the short-range order intensity is taken into account. It is assumed that short-range order does not influence the probabilities of these jumps. It does, however, influence the correlation time according to (2.44). In order to check the validity of this assumption, Monte Carlo simulations were carried out as discussed in Section 5.3.2.

- To demonstrate the applicability of aXPCS to polycrystalline samples. It could be shown, that polycrystalline samples also yield useful information about jump length. However, the grain size and their growth must be carefully controlled for such experiments, as discussed in Section 6.5.3.

- To test the low contrast limit which is to show that aXPCS also works for for very low concentrations far from the stoichiometry. As the diffuse intensity is proportional to a Laue unit, $c_A c_B (f_A - f_B)^2$, it is strongest for a binary system of 50:50 composition. We could show, that concentrations as small as 3 at.% still yield a high enough signal, if the scattering contrast $(f_A - f_B)$ is large as in case of Ni and Pt.

The results of this work were published in [Stan 13].

8. Diffusion in intermetallic B2-systems

Intermetallic alloys are of great technical interest as structural materials or due to their magnetic and thermoelectric properties. Therefore, a lot of time and effort has been spent on the study of such systems. Still, there is an ongoing debate about the diffusion mechanisms in binary alloys, especially in the interesting class of B2 systems. It is the aim of this chapter to use experimental results gained from aXPCS experiments to shine some light on the matter. At the beginning an overview over some selected results from previous works will be given. One should notice, that information about point defects is of vital importance for understanding microscopic diffusion mechanisms.

Originally B2 alloys were either considered to be of the anti structure type, where constitutional defects are formed as A_β antisites for an excess of A-atoms and vice versa, or to be of the triple defect type, where antisites only exist on one sublattice and vacancies only on the other (e.g. A_β and V_α) [Chan 82]. In the latter case, an excess of A-type atoms would be compensated by the formation of A_β while an excess of B-type atoms would be compensated by the formation of additional cells, half filled with V_α-type vacancies. It has, however, become apparent, that this view is too simplistic and it was shown that hybrid behavior is possible. A good overview of the topic is given e.g. in [Koga 01, Leit 15].

Following this review the results of the studies on two systems, $Fe_{0.54}Al_{0.46}$ and $Ag_{0.58}Mg_{0.42}$, are shown. First, short-range order in the systems is discussed, as it is needed to account for De Gennes narrowing as shown in (2.44). Then the results from the aXPCS experiments at the synchrotron facilities will be shown and discussed. To conclude, the results will be compared with the vacancy diffusion models introduced in Section 3.3.

8.1. Status of research

8.1.1. Transition metal - aluminides

This class of alloys has received special attention due to the technical applicability for high-temperature structural applications. Materials of this type show a good combination of mechanical properties, have a low weight-to-strength ratio (specific strength), good corrosion and oxidation resistance and low raw material cost [Deev 96]. Prominent members in this respect are Ni-Al and Fe-Al. Here the discussion will be restricted to the latter.

The major drawback in the application of Fe-Al alloys is their poor ductility at low temperatures [Kim 15]. With increasing vacancy concentration the hardness increases while the ductility decreases [Jord 03]. Due to the low formation enthalpy for vacancies in Fe-Al with Fe excess compared to pure metals (see Table 8.1), large concentrations of vacancies can be formed at temperatures far from the melting point. This allows to tailor manufacturing and application properties by controlling vacancies. Therefore, understanding atomic motion at such temperatures is of great interest. Previous atomistic diffusion studies, however, were unable to reach

temperatures below about 1200 K due to a limited energy resolution [Vogl 05]. This restriction does not hold for aXPCS, which makes it the method of choice for such an investigation.

In these alloys, the vehicles of diffusion are vacancies. Their availability and mobility therefore determines the hopping mechanisms.

Investigation of vacancy concentration has shown to be difficult in Fe-Al at lower temperatures, as vacancies seem to be frozen-in below 1000 K [Chan 82] and cannot be eliminated even with slow cooling in a furnace [Jord 03], yielding varying results that depend on sample preparation (see e.g. Fig. 11 in [Jord 03]). Annealing for several tenth of hours at low temperatures (400 °C) will reduce the number of vacancies significantly [Jord 03]. The vacancy concentration for 45-at.% Al was given as c_V=0.0017(11) for annealing at 773 K for 120h [Koga 97], which is in good agreement with values found elsewhere [Hehe 01, Hara 01]. However, Wolff et al. [Wolf 99] found a vacancy concentration of $c_V \sim 10^{-5}$ for $Fe_{0.57}Al_{0.43}$ annealed at 650 K.

System	$\epsilon_V^{\mathrm{f}}[eV]$	ϵ_V^{m} [eV]	technique	source
$Fe_{0.50}Al_{0.50}$	0.30		Differential dilatometry (ht)	[Kerl 99]
$Fe_{0.50}Al_{0.50}$	0.85		Differential dilatometry (lt)	[Kerl 99]
$Fe_{0.54}Al_{0.46}$	0.50			[Pari 78]
$Fe_{0.55}Al_{0.45}$	1.5(2)	1.0(1)	Time-differential length change	[Scha 99]
$Fe_{0.67}Al_{0.43}$	0.51		Differentail dilatometry (ht)	[Kerl 99]
$Fe_{0.67}Al_{0.43}$	0.92		Differentail dilatometry (lt)	[Kerl 99]
$Fe_{0.67}Al_{0.43}$	0.70	1.6	Hardness measurement	[Morr 98]
$Fe_{0.60}Al_{0.40}$	0.94(1)	1.64		[Pari 78]
$Fe_{0.60}Al_{0.40}$	0.38		Lattice parameter	[Ho 78]
$Fe_{0.60}Al_{0.40}$	0.91		Resistance	[Rivi 74]
$Fe_{0.60}Al_{0.40}$	0.98(6)		Positron lifetime	[Wolf 97]
$Fe_{0.60}Al_{0.40}$	1.13(6)		Doppler broadening	[Wolf 97]
$Fe_{0.61}Al_{0.39}$	0.98(7)	1.7(2)	Positron lifetime	[Wurs 95]
$Fe_{0.63}Al_{0.37}$	1.04(7)	1.7(2)	Positron lifetime	[Wurs 95]
$Fe_{0.65}Al_{0.35}$	1.04(6)		Doppler broadening	[Wolf 97]

Table 8.1.: Experimentally found formation (ϵ_V^{f}) and migration (ϵ_V^{m}) enthalpies for vacancies in Fe-Al systems. (lt) indicates measurement at low and (ht) at high temperature.

Fe-Al is well investigated in terms of formation and migration energies of vacancies. An overview over experimental results can be found in Table 8.1. An overview is also given in Wolff et al. [Wolf 99], where a variation in migration enthalpy (0.5-1.8 eV) is argued to point towards different defect types operating as diffusion vehicles in different phases. Simulation techniques found a formation enthalpy of $\epsilon_{\mathrm{V}}^{\mathrm{f}} = 1.05\,\mathrm{eV}$ [Jord 03]. The activation enthalpy for vacancy clustering was found to be 1.27(15) eV [Hara 05]. According to calculations using the grandcanonical formalism [Fahn 99a], the effective formation energy for an Al atom on the Fe-sublattice is 1.98 eV, for a vacancy on the Fe-sublattice (α) it is 1.56 eV and for a vacancy on the Al-sublattice (β) it is 2.96 eV which is higher than the experimentally measured migration enthalpies.

A number of investigations have been undertaken to find the dominant defects in Fe-Al. According to Chang and Neumann [Chan 82], the constitutional defect for the Fe-rich side

from the stoichiometric composition are Fe atoms on the Al-sublattice (Fe_{Al}) and for the Al-rich side Fe vacancies (V_{Fe}). Such a system is known as a triple defect systems. In later studies [Maye 95, Athe 97, Koga 98] it was found that the thermal defects Fe_{Al}, V_{Al}, Al_{Fe} and V_{Fe} coexist in the vicinity of stoichiometry, leading to a hybrid behavior. Bakker at all [Bakk 97, Jord 03] claim, that there is a transition from the triple defect to the hybrid state when the temperature of the system exceeds 1100 °C.

Other works (see [Fahn 02] and literature cited therein) suggest, that the dominant thermal defect for Fe rich B2 Fe-Al systems is the triple defect. In this context the term triple defect refers to a defect composed of an antisite atom on one and two vacancies on an other sublattice. For slight deviation from stoichiometry ($Fe_{0.505}Al_{0.495}$) a concentration of $c(Fe_{Al}) = 0.0336(40)$ and $c(Al_{Fe}) = 0.0084(40)$ was found [Krac 95]. For a higher Fe concentration, the ratio $c(Fe_{Al})/c(Al_{Fe})$ can be expected to be much higher. The same tendency can be expected when the temperature decreases, as the concentration of constitutional Fe_{Al} defect has a much weaker temperature dependency than the concentration of thermal defects.

Positron annihilation studies suggest, that single vacancies, as well as vacancy clusters like divacancies and clusters consisting of vacancies and antisite atoms are present in Fe-Al [Hara 01]. Numerical results suggest, that at least at high temperatures ($T/T_{melt} = 0.84$) almost all of the vacancies are to be found on the Fe-sublattice for a Fe-excess of more than 1% [Koga 01]. It was concluded from ab initio studies, that no V_{Al}-V_{Fe} nearest-neighbor pairs exist and that vacancies tend to form next-nearest-neighbor pairs [Fahn 99b, Amar 10]. This is in contradiction with experimental results [Wolf 99], claiming that the vacancies are nearest neighbors. Furthermore it was shown that including magnetism in the ab initio calculations has a strong effect. The local-spin-density approximation (LSDA) yields a magnetic ground state for B2 FeAl, while experimental results show that it is nonmagnetic [Bogn 98]. Also calculations using a generalized-gradient-expansion approximation (GGA) show a strong spin dependence. These effects are discussed in [Bess 06]. Unfortunately no assertion of formations of threefold defects such as the triple defect were made for Fe-Al in this work. Detailed studies using EAM potentials were undertaken to find defect complexes for stoichiometric B2 FeAl [Nogu 05]. These studies found a $V_{Al} - V_{Fe} - Fe_{Al}$ complex to be stable and the classical triple defect ($V_{Fe} - Fe_{Al} - V_{Fe}$) to be metastable with a low activation barrier for formation. Similar formations were also found in Ni-Al for $c_{Ni} > 0.55$ (see [Xu 09] Fig. 7). These recent results are in disagreement with previous calculations, e.g. [Fu 97].

Self diffusion studies aided by the Darken-Manning equation show, that the self-diffusion coefficient of Al is estimated to be a factor of 0.6 smaller that that of Fe in $Fe_{0.48}Al_{0.52}$ [Naka 03]. This indicates that Fe and Al diffuse via a similar mechanism. Investigations in frame of transition state theory [Fahn 99a] gave a migration energy of 2.16 eV for direct next-nearest neighbor jumps and 6.0 eV for direct third-nearest neighbor jumps. Comparing this with the migration enthalpies given above, only direct ⟨100⟩-jumps can be considered to be possible while any further direct jumps can be ruled out due to their high energy barrier. The same investigation showed, that the experimentally determined activation energy of Fe self diffusion (effective vacancy formation energy of about 1 eV plus vacancy migration energy of about 1.7 eV) is about 2.7 eV [Fahn 99a], which is in very good agreement with results of time-differential length change

experiments for $Fe_{0.55}Al_{0.45}$ [Scha 99]. Fähnle et al. also found, that the energy difference in the six jump cycle (6JC) between initial and intermediate configuration is about 3 eV, which leads to a migration energy much larger than 1.7 eV. For the three jump cycle (3JC) the calculated upper limit of the migration enthalpy is 3.1 eV, which could be reduced due to polarization effects [Fahn 99a].

Weinkamer et al. [Wein 98, Wein 99] used a Monte Carlo approach to determine the dominant diffusion mechanism in Fe-Al. As they employed the ABV method where only one vacancy is allowed in the system, interaction between vacancies could not be accounted for. It was demonstrated [Lech 00] that vacancies have an influence on the phase diagram. Therefore, it is also plausible to assume, that they influence chemical short-range order. Furthermore, treating only one vacancy naturally eliminates di-vacancy mechanisms from the consideration.

8.1.2. Magnesium alloys

Magnesium alloys have a variety of possible technical applications as light weight materials due to their low density. However, as they have relative low strength and creep resistance, the actual area of technical application is rather small. Silver-magnesium alloys only have application as low heat resistive compounds. Understanding the diffusion mechanism in this class of systems could again help to provide a remedy.

Contrary to Fe rich Fe-Al, Ag rich Ag-Mg is an antisite defect type, which means that the same number of antisite atoms, A_B and B_A will be predominantly formed with A or B excess respectively [Koga 01].

The diffusion process suggested for this system is the classical 6JC [Domi 65, Belo 04]. This is why this system was chosen in comparison to Fe-Al.

8.2. The samples

8.2.1. Fe-Al samples

Microscopic diffusion studies in Fe-Al systems have a long tradition in our group [Vogl 05]. Therefore, in addition to the above mentioned characteristics of this material class, they posed an interesting candidate for aXPCS studies. Especially so, since former studies hinted towards the presence of effective $\langle 111 \rangle$-jumps [Wein 99], which can not be explained by the 6JC or 3JC.

Two samples already measured by QMS were chosen, a sample close to the stoichiometry ($Fe_{0.54}Al_{0.46}$) and one with an iron content slightly higher than in the Fe_3Al phase ($Fe_{0.83}Al_{0.17}$). As can be seen from Fig. 8.1 however, the fluorescence peak at 6 keV is higher than the elastic peak at 7.05 keV for the second sample. This fluorescence could be due to Mn impurities introduced in the manufacturing process. As such high fluorescence strongly reduces the signal-to-noise ratio (SNR) only the first sample was investigated.

8.2.2. $Ag_{0.58}Mg_{0.42}$ sample

Because only a Bridgman furnace with a maximum temperature of 1100 °C was available for crystal growth at the time, a low melting Ag-Mg B2 system was chosen as a candidate for

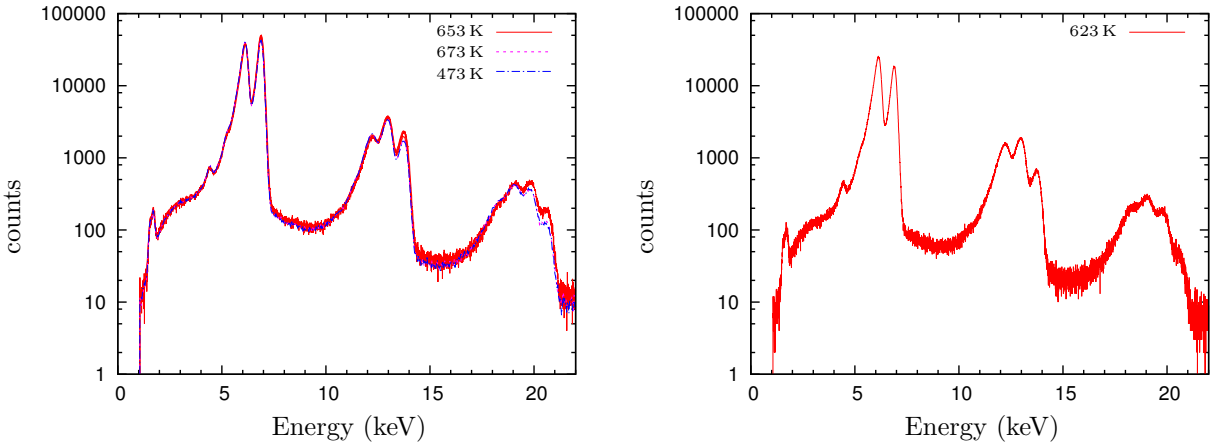

(a) $Fe_{0.54}Al_{0.46}$ (b) $Fe_{0.83}Al_{0.17}$

Figure 8.1.: Energy histograms measured with a 7.05 keV synchrotron beam at beamline P10, Petra III for two different Fe-Al samples. At 5.9 keV the fluorescence peak is visible, the elastic peak lies at 7.05 keV. At 14.10 keV and at 21.15 keV there are peaks corresponding to a cumulation of two and three elastically scattered photons. The escape peak is around 5.45 keV. The other peaks are pile ups of the mentioned photons, e.g. 13.05 keV corresponds to one elastically scattered plus one fluorescence photon.

a 6JC diffusion in comparison to the $Fe_{0.54}Al_{0.46}$ sample. The manufacturing as well as the characterization process is described in Section 6.5. The sample concentration of 42 at.% Mg is less then aimed for, but should be within the limit of the 6JC.

8.3. Chemical short-range order

Even though some short-range order parameters are published for selected solid solution systems, information about short-range order in intermetallics is very scarce. In fact at least for the systems Ag-Mg and Fe-Al no information about short-range order on the sublattices could be found in the literature. As this information is vital in the evaluation of aXPCS data, effort was taken to find the missing short-range order information.

8.3.1. Determining I_{SRO} by scattering techniques

An intensity map of the $Ag_{0.58}Mg_{0.42}$ sample collected using the Bruker Nanostar for SAXS is shown in Fig. 4.1a. It can be seen from comparison with Fig. 4.1b, that the short-range order intensity is much less distinct than for the solid solution sample.

As the Nanostar is only equipped with a Cu anode it could not be used to map diffuse scattering for Fe-containing samples because of iron fluorescence. A Bruker D8, which is used for WAXS measurements could be equipped with a Co anode, but very long exposure times for each angle are required for mapping short-range order intensity in this way. The patched up intensity map from such an attempt can be seen in Fig. 8.2a. Each point represents an intensity integrated over an area of one angular degree. Unfortunately, as can be seen, the data quality

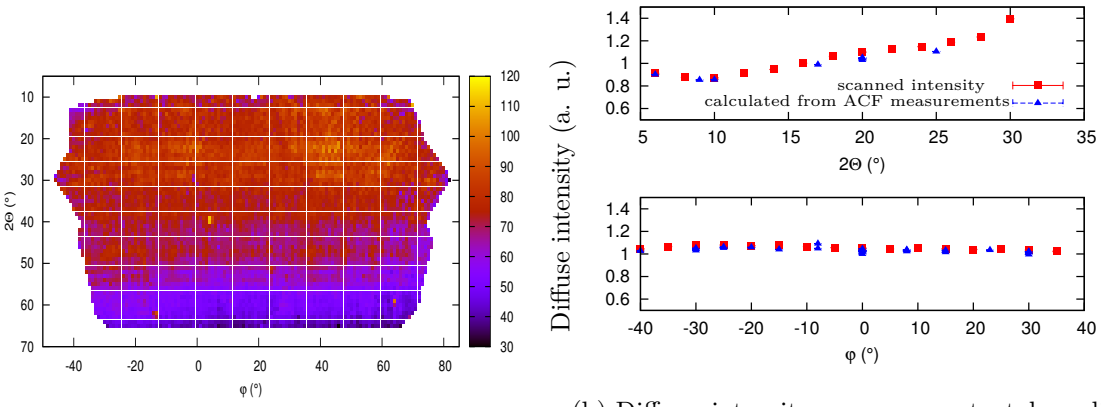

(a) Attempted map using a Bruker D8. Intensities were summed up to pixels corresponding to one square-degree.

(b) Diffuse intensity measurements taken directly at the beamline P10, Petra III in experimental setup for aXPCS experiment. The intensity was normalized by its mean value.

Figure 8.2.: Measurements of diffuse intensity for the $Fe_{0.54}Al_{0.46}$ sample.

is insufficient to draw any quantitative conclusions about short-range order. Therefore, other means of finding short-range order information were sought out.

At the synchrotron a scan of 2Θ and φ was carried out. The intensity was integrated over the whole detector area. These intensities were corrected for the increase of the sample thickness with increasing scattering angle $(1/\cos(2\theta))$. As Petra III operates in a top-up mode, the intensity of the beam has a good stability over time. It is therefore possible to average the intensities of all frames collected when measuring the ACFs in an aXPCS experiment for certain sets of $(2\Theta, \varphi)$ and use them for an evaluation of diffuse intensity. As can be seen in Fig. 8.2b, the angular variation of the measured diffuse intensity is very low.

This can mean two things. Either short-range order and displacement effects are both very small, or the effects cancel each other out. In order to clarify what is the case simulation techniques were used.

8.3.2. Determining I_{SRO} by simulation techniques

Different approaches were undertakten to find short-range order in the systems by means of simulation. As order is usually temperature dependent, simulations should be undertaken at virtual temperatures corresponding to the temperature where the actual experiment was performed. The long-range order parameter, defined as $\eta_A = \frac{A_\beta - A_\alpha}{N_A}$ with $N_A = A_\beta + A_\alpha$, can be used to calibrate the temperature scale using the order-disorder transition temperature T_C.

Using pair potentials

On the basis of a Bethe–Bragg–Williams approximation [Will 35, Alln 93], Semenova et al. determined pair interaction parameters as an input for calculations of defect correlations. With this, long-range order as well as short-range order parameters were determined. Parameters

were published for Fe-Al systems [Seme 08]

$$E_1^{\mathrm{FeFe}} = 0.010(2)\,\mathrm{eV}, \qquad E_1^{\mathrm{AlAl}} = -0.055(10)\,\mathrm{eV}, \qquad E_1^{\mathrm{FeAl}} = -0.210(40)\,\mathrm{eV},$$
$$E_1^{\mathrm{FeV}} = -0.210(25)\,\mathrm{eV}, \qquad E_1^{\mathrm{AlV}} = -0.013(2)\,\mathrm{eV}, \qquad E_1^{\mathrm{VV}} = 0.068(10)\,\mathrm{eV}\,,$$

as well es for an Ag-Mg system [Seme 12]

$$E_1^{\mathrm{AgAg}} = 0.010(2)\,\mathrm{eV}, \qquad E_1^{\mathrm{MgMg}} = -0.055(10)\,\mathrm{eV}, \qquad E_1^{\mathrm{AgMg}} = -0.287(40)\,\mathrm{eV},$$
$$E_1^{\mathrm{AgV}} = -0.395(25)\,\mathrm{eV}, \qquad E_1^{\mathrm{MgV}} = -0.013(2)\,\mathrm{eV}, \qquad E_1^{\mathrm{VV}} = 0.068(10)\,\mathrm{eV}\,.$$

The subscript indicates, that the pair interactions are defined for nearest-neighbor atoms ($n = 1$). In order to find the virtual critical temperature, simulations using these potentials were undertaken on lattices of $16^3 \times 2$ atoms. The temperature was increased in steps of 50 K. For each temperature, 500 MCSs were calculate. The dependence of long-range order on temperature is shown in Fig. 8.3a. As can be seen from this figure, the virtual transition temperature for $Fe_{0.54}Al_{0.46}$ was found to be $T_C = 3170(50)\,K$ and for $Ag_{0.58}Mg_{0.42}$ to be $T_C = 4560(50)\,K$. According to the phase diagram[1] the transition temperature for 54-at% Fe lies at 1583 K. For $Ag_{0.58}Mg_{0.42}$ it can be found at 1083 K. This was used to calculated the virtual temperatures corresponding to the temperatures of 653 K and 423 K for the Fe-Al system and the Ag-Mg system respectively, where aXPCS measurements were undertaken. For those temperatures the Warren-Cowley short-range order parameters were calculated.

As can be seen from Fig. 8.3b, Fig. 8.3c and Fig. 8.3d, the short-range order parameters have a very strong dependence on the vacancy concentration. Increasing the vacancy concentration increases the short-range order intensity. Furthermore, the fluctuations in the short-range order parameters, especially for high vacancy concentrations, are strong even after a large number of MCSs. This does not allow for a quantitative estimation of $\alpha_{\tilde{n}}$, even if the exact vacancy concentration would be known. However, it is apparent that the parameters for chemical short-range order on the Al-sublattice and Mg-sublattice respectively are very small $|\alpha_{\tilde{n}}| \leq 0.01$ for a vacancy concentration of 0.2% and are even an order of magnitude lower for a vanishingly small vacancy concentration. As the number of antisites on the other sublattice is very small, the short-range order parameters fluctuate even more strongly. According to (2.60) the sublattice predominantly occupied by one species does not have an influence on the short-range order intensity. Due to the small parameters also the total short-range order intensity is weak, which is in accordance with the experimental findings.

It can be concluded, that when interaction parameters are defined for only one neighboring shell and the interactions do not follow a very simplistic model as in Section 5.3.1, no quantitative information about short-range order parameters for different neighboring shells can be gained. It appears only to be possible to define an effective short-range order parameter α, according to

[1] Ortrud Kubaschewski, Rainer Schmid-Fetzer, updated by Lazar Rokhlin, Lesley Cornish, Olga Fabrichnaya and MSIT® ; Effenberg, G. (Ed.); MSI Eureka in SpringerMaterials; sm_msi_r_10_011481_02_full_LnkDia1 (MSI Materials Science International Services GmbH, Stuttgart, 2007), http://materials.springer.com/msi/phase-diagram/docs/sm_msi_r_10_011481_02_full_LnkDia1; accessed: 27-05-2015, 18:09:13 GMT+0200 (CEST)

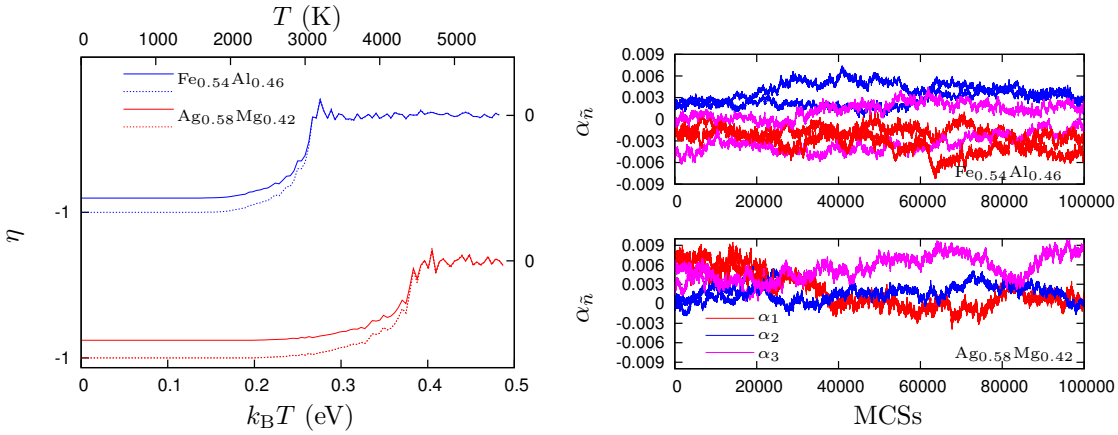

(a) Long-range order parameter η as a function of temperature for Fe-Al and for Ag-Mg for minority atoms (solid line) and majority atoms (broken line).

(b) First three short-range order parameters calculated for a $32^2 \times 2$ lattice with a 0.1984% vacancy concentration.

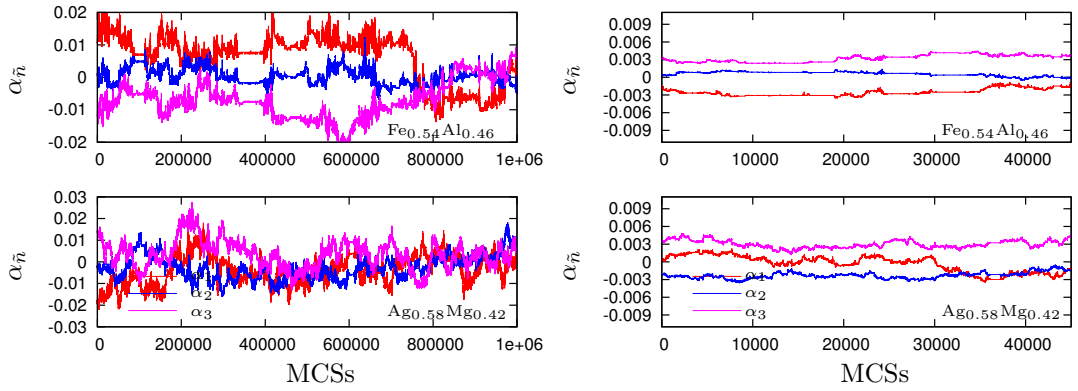

(c) First three short-range order parameters calculated for a $16^2 \times 2$ lattice with a 0.0122% vacancy concentration.

(d) First three short-range order parameters calculated for a $32^2 \times 2$ lattice with a 0.0015% vacancy concentration.

Figure 8.3.: Long-range order parameter and Warren-Cowley short-range order parameters $\alpha_{\tilde{n}}$ of simple cubic Al/Mg-sublattice as a function of MCS for nearest-neighbor shell ($\tilde{n} = 1$), next-nearest-neighbor shell ($\tilde{n} = 2$) and third-nearest neighbor shell ($\tilde{n} = 3$) calculated for $Fe_{0.54}Al_{0.46}$ and $Ag_{0.58}Mg_{0.42}$ using pair potentials provided by Semenova et al. [Seme 08, Seme 12].

[Gang 68]:

$$V(1-\alpha) = \frac{1}{Z_1} \sum_n Z_n V_n (1-\alpha_n), \tag{8.1}$$

with V_n the specific interaction energy and Z_n the coordination number for the nth neighboring shell. Unfortunately, no short-range order intensity can be calculated from such a parameter.

Using the ABV model

Schmid and Binder have introduced ABV parameters, which provided reasonable long-range order parameters and allowed to reproduce the phase diagram of the Fe-Al system [Schm 92]. The formalism was introduced in Section 5.2.1. In the notation of (5.13) interaction parameters

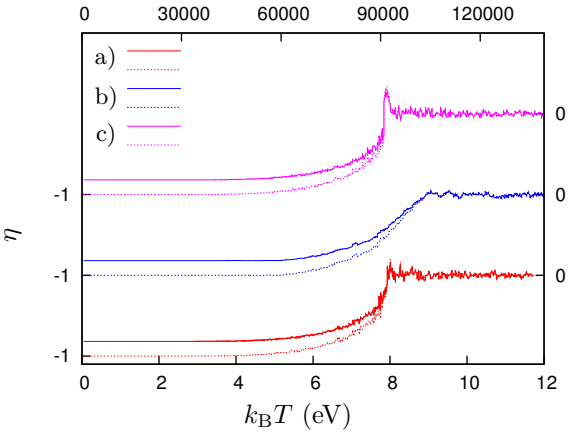

(a) Long-range order parameter for Fe-sublattice (broken line) and Al-sublattice (solid line) as function of temperature.

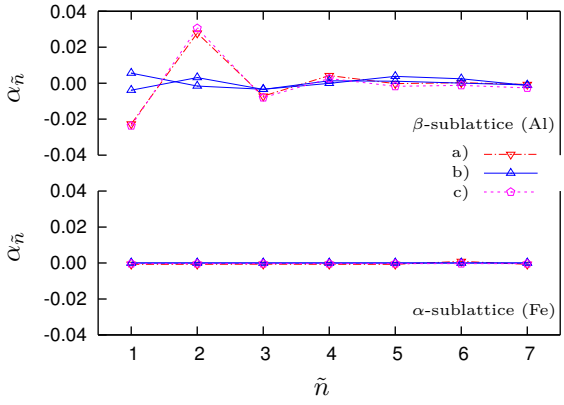

(b) Short-range order parameters for a temperature corresponding to 653 K.

Figure 8.4.: The following ABV-potentials (in units of eV) were used to calculate long-range and short-range order parameters of a $Fe_{0.54}Al_{0.46}$ system:
a) $J_1 = 1$, $J_2 = 0.167$, $J_3 = -0.208$ and $U_i = 0.0$
b) $J_1 = 1$, $J_2 = 0.167$, $J_3 = -0.208$, $U_1 = 0.0$, $U_2 = 8.0$ and $U_3 = -4.0$
c) $J_1 = 1$, $J_2 = 0.167$, $J_3 = -0.208$, $U_1 = 0.0$, $U_2 = 0.8$ and $U_3 = -0.4$

are given as $J_1 = 1$, $J_2 = 0.167$ and $J_3 = -0.208$. Weinkamer et al. [Wein 99] extended these potentials by introducing interactions between the atoms and the vacancy in the system, $U_1 = 0$, $U_2 = 8$ and $U_3 = -4$. The parameter U_n accounts for interaction of the vacancy with atoms of type A or B and is necessary to explain the results of a Mössbauer experiment [Vogl 94]. The very high interaction potentials introduced by Weinkamer et al. lead to frozen states after only few MCSs, where no further change in ensemble takes place. In the original work this was managed by introducing a waiting time algorithm, where a change of state is forced upon the system in every step and the probability is used to scale the time [Ferd 07, Bibo 14]. In order to omit this, the potentials were modified to $U_1 = 0$, $U_2 = 0.8$ and $U_3 = -0.4$, which should lead to a similar, but less distinct behavior without frozen states.

Simulations giving the temperature dependence of η for all three cases using a simulation cell of $M = 16^3 \times 2$ for the concentrations $c_A = 0.54$ and $c_B = 0.46$ are given in Fig. 8.4. At each temperature 200 MCSs were calculated.

In case of the potentials introduced by Schmid and Binder, the transition temperature was found to be $T_C = 7.9(1)$ eV. A temperature of $T_\mathrm{exp} = 653$ K, therefore, corresponds to 3.3 eV. For the potentials introduced by Weinkamer et al. it was found to be $T_C = 8.5(1)$ eV ($T_\mathrm{exp} = 3.5$ eV), and for the modified potentials to be $T_C = 7.8(1)$ eV ($T_\mathrm{exp} = 3.2$ eV). Short-range order parameters are expacted not to vary significantly within a temperature range of $0.1 \times J_1$, so this precision of temperature determination is satisfactory.

The short-range order parameters for the two sublattices calculated from simulations using the appropriate interaction parameters at the temperatures corresponding to 653 K are shown in Fig. 8.4b.

Using embedded atom method (EAM) potentials

The EAM is a powerful tool for simulating thermodynamic and physical properties. The parameters of a work by Ouyang et al. [Ouya 12] were chosen in order to find chemical short-range order parameters in $Fe_{0.54}Al_{0.46}$. Other properties of the Fe-Al system, like the elastic constants, self diffusion constants and phonons are well reproduced by this potential. The parameters used are shown in Table A.1.

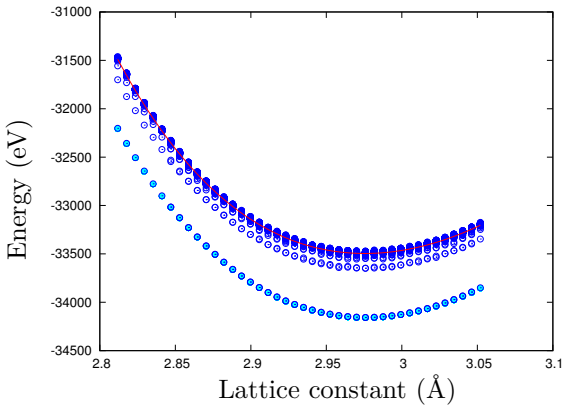

(a) Lattice constant calculations. The light blue, full symbols give the system energy for the un-relaxed state. The blue, open cycles indicate values after each MCS for relaxing for 100 MCSs. The red line gives the fit of a polynomial of fourth order, which has its minimum at 2.975 Å.

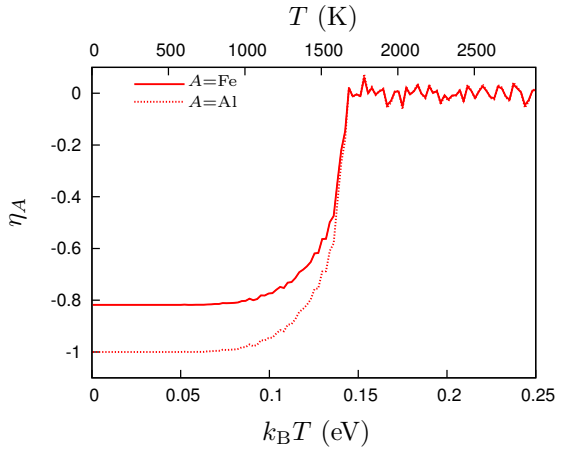

(b) Long-range order parameter η as a function of temperature calculated for a lattice of $16^3 \times 2$ atoms. The transition temperature is in agreement with the literature value of 1583 K.

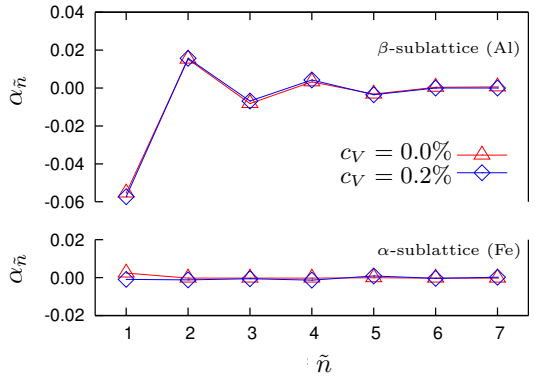

(c) Short-range order parameters calculated for a lattice of $16^3 \times 2$ atoms using the on-lattice approach. The vacancy concentration only slightly influences the short-range order parameters.

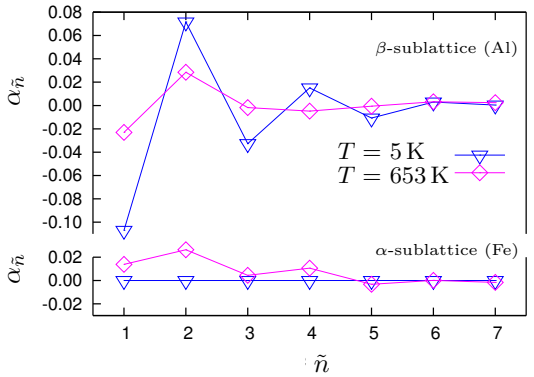

(d) Short-range order parameters calculated for a lattice of $16^3 \times 2$ atoms using the off-lattice approach. The vacancy concentration was 0.0%. Parameters for two temperatures are given.

Figure 8.5.: Properties calculated from simulations using EAM potentials by Ouyang et al. [Ouya 12].

Two approaches were undertaken: in the first, the inter-atomic distances were fixed, leading to discrete lattice sites. This is usually called an on-lattice approach. In the second case the atoms were allowed to relax freely due to local variations in the potential. The probability

for relaxation of a certain increment was again decided by the Boltzmann factor. This will be referred to as the off-lattice approach. Exchanges on the lattice were carried out in accordance with the classical Metropolis rules, as discussed in Section 5.1.

In the first step the equilibrium lattice constant was found by a variation of the inter-atomic distances. For each distance, the total energy was calculated for the unrelaxed state and after each MCS for relaxing the atoms for 100 MCSs. The resulting curve was fitted by a polynomial of forth order, as shown in Fig. 8.5a. This yielded a lattice constant of 2.975 Å, which is only slightly larger than experimentally determined value [Tayl 58].

In order to check the order-disorder transition temperature, an on-lattice simulation using $M = 16^3 \times 2$ atoms was carried out, as shown in Fig. 8.5b. The transition temperature is in good agreement with experimental values.

To determine, if the number of vacancies influences short-range order, simulations with a vacancy concentration of 0.2% as well as simulations for a binary system with no vacancies were carried out. As can be seen from Table 8.2, the number of vacancies does not play an important role for short-range order in this case.

Simulations following the off-lattice approach are very time consuming due to the relaxation process after each exchange on the lattice. At temperatures close to zero the same short-range order parameters are found as with the on-lattice approach. At elevated temperatures, where the atoms do not occupy the minima positions in the energy landscape, chemical short-range order is reduced. As can be seen from comparison of Fig. 8.5c and Fig. 8.5d, α_1 is reduced by a factor of 3, while α_2 is enhanced when using the off-lattice approach. Apart from that the first three parameters have similar character, while α_4 changes its sign. As can be seen from Fig. 8.6d the short-range order intensity in the region of small 2Θ values is enhanced for the parameters gained from the off-lattice approach.

8.3.3. Comparison of results

From the results shown in Section 8.3.2 it can be concluded, that potentials reaching further than the first neighbor shell allow the system to converge much faster to an equilibrium state, allowing to draw conclusions about chemical short-range order.

A comparison of all the short-range order parameters calculated, as well as concentrations of antisites an vacancies on the two sublattices for the potentials discussed above is given in Table 8.2.

	ABV Schmid & Binder [Schm 92]	ABV Weinkamer et al. [Wein 99] mod ($U_n/10$)	Pair Pot Semenova et al. [Seme 08] c_V=0.19%	EAM Ouyang et al. [Ouya 12] c_V = 0.20% on-latt	EAM Ouyang et al. [Ouya 12] c_V = 0.20% off-latt
c_V on μ =Fe	0.000002	0.000002	0.000000	0.003894	-
c_V on μ =Al	0.000029	0.000029	0.003967	0.000012	-
$c(\mathrm{Al_{Fe}})$	0.0007	0.0004	0.0004	0.0003	0.0508
$c(\mathrm{Fe_{Al}})$	0.8993	0.8996	0.9178	0.0821	0.1309
α_1^{Al}	-0.0227	-0.0237	-	-0.0573	-0.0230
α_2^{Al}	0.0279	0.0306	-	0.0157	0.0285
α_3^{Al}	-0.0072	-0.0080	-	-0.0069	-0.0017
α_4^{Al}	0.0043	0.0026	-	0.0042	-0.0048
α_5^{Al}	-0.0002	-0.0017	-	-0.0036	-0.0006

Table 8.2.: Comparison of parameters calculated from simulations using different interaction potentials for $\mathrm{Fe_{0.54}Al_{0.46}}$.

All, but the EAM potentials lead to the majority of the vacancies occupying the Al-sublattice. Experimental findings as well as calculations using the grandcanonical formalism [Fahn 99a], however, suggest that the vacancies reside manly on the Fe-sublattice, as discussed in Section 8.1.1.

Short-range order intensity is calculated for all simulations yielding appropriate parameters according to (2.60). As the concentration of minority atoms on the majority sublattice is negligible, only the simple-cubic Al-sublattice has to be considered. The calculated short-range order intensity maps for a sample oriented in $\langle 111 \rangle$ direction are shown in Fig. 8.6.

As can already be seen from the short-range order parameters, the short-range order intensity is fairly similar for all four simulations shown. Furthermore, it can be seen that it is weak in the area where measurements were made, which is in accordance with the experimental findings. As the EAM potentials reproduce many physical parameter, it is assumed that the chemical short-range order gained from this simulations gives the best representation of reality.

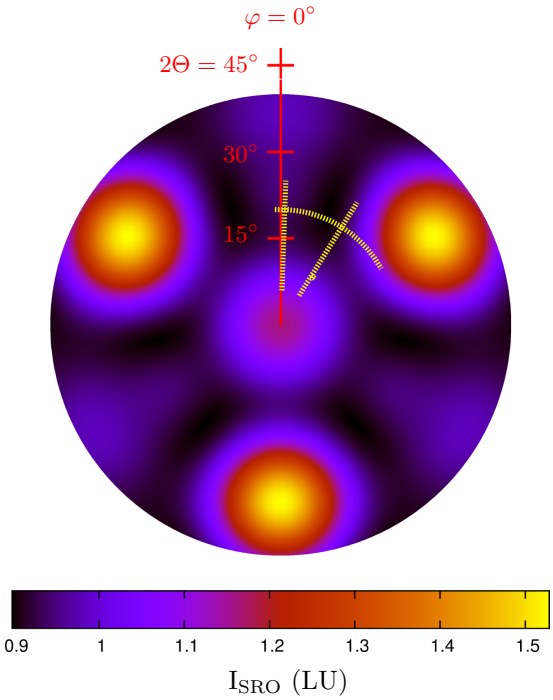

(a) Short-range order intensity from ABV potential by Schmid & Binder [Schm 92].

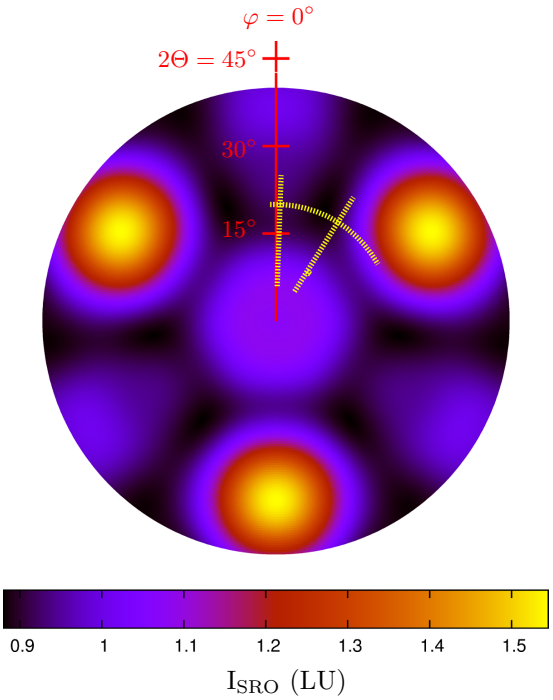

(b) Short-range order intensity from modification of ABV potential by Weinkamer et al. [Wein 99].

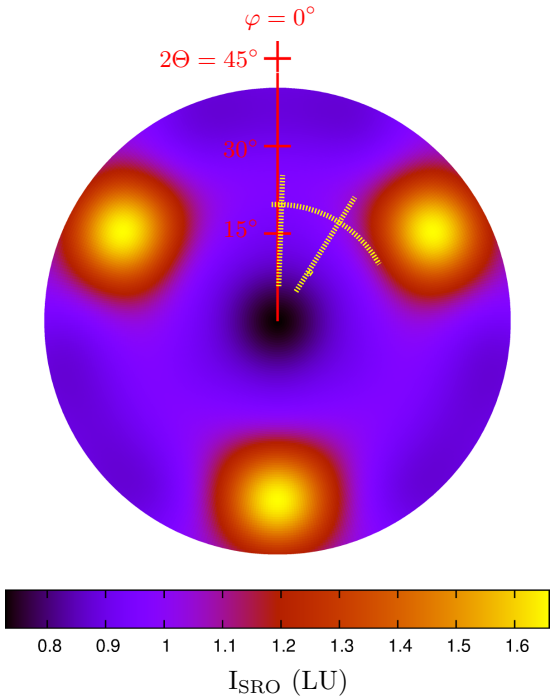

(c) Short-range order intensity from EAM potential by [Ouya 12] with on-lattice approach and 0.2% vacancies.

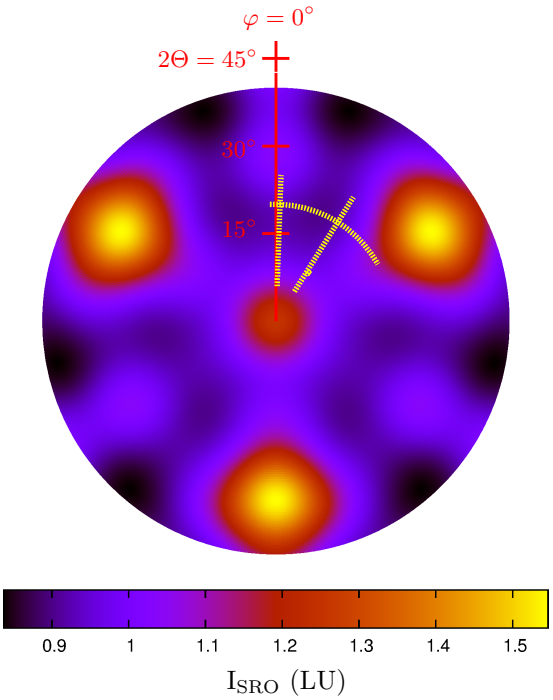

(d) Short-range order intensity from EAM potential by [Ouya 12] with off-lattice approach and 0.0% vacancies.

Figure 8.6.: Map of short-range order intensity calculated for $Fe_{0.54}Al_{0.46}$ single crystal oriented in ⟨111⟩ direction using different potentials for atomic interaction. The red line indicates $\varphi = 0°$. The yellow, broken line indicates the regions of reciprocal space, where aXPCS measurements were carried out.

8.4. Measurements of atomic jump length distribution by aXPCS in $Fe_{0.54}Al_{0.46}$

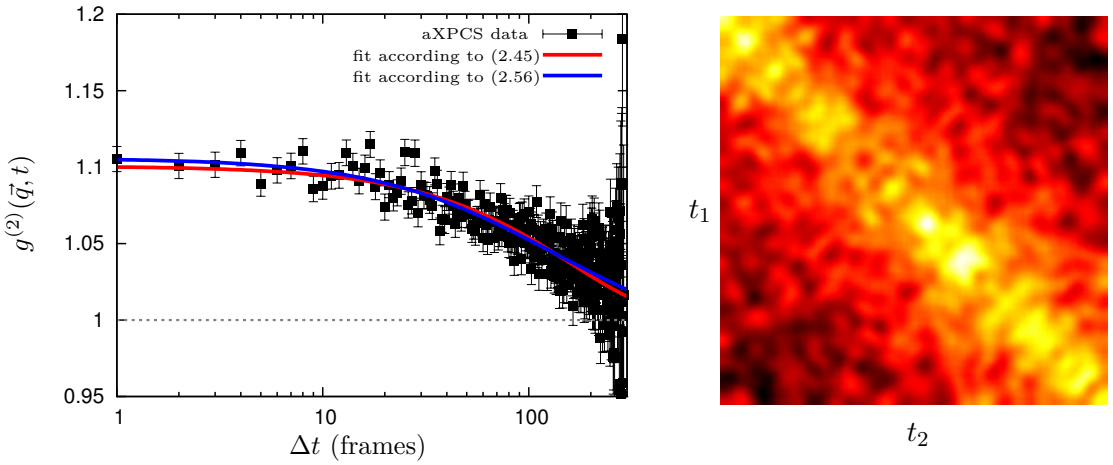

(a) Intensity-autocorrelation function measured and fitted with a single exponential decay (red) and a combination of two exponential decays (blue) accounting for different sublattices.

(b) Two dimensional representation of two-times correlation function $\Gamma(\vec{q}, t_1, t_2)$ according to (2.26).

Figure 8.7.: Autocorrelation function and two-times autocorrelation function measured for the $Fe_{0.54}Al_{0.46}$ sample at $2\Theta = 6°$ and $\varphi = 2°$.

8.4.1. Technical details

Both Fe-Al samples were measured during the beamtime I-20110131EC at the beamline P10, Petra III in April 2012. Due to the strong fluorescence in the $Fe_{0.83}Al_{0.17}$ sample, only the $Fe_{0.54}Al_{0.46}$ was thoroughly investigated. This sample was oriented in $\langle 111 \rangle$ direction (see Section 6.5.2 for details). The energy of the X-ray beam was set to 7.05 keV in order to stay below the iron K-absorption edge, which is 7.112 keV[2]. The sample to detector distance was 83 cm. The CCD camera PIXIS-XB with a CCD array of 1340×1300 pixel of 20×20 µm^2 was used. The readout time of the detector was 2.29 s/frame. All frames were taken with an exposure time of 3 s. The beam size was defined by beam focusing to approximately 3 µm(horizontal)×2 µm(vertical). Measurements were undertaken at temperatures between 573 K and 723 K. The $[\bar{1}\bar{1}2]$-direction ($\varphi = 0°$) was tilted by 32° with respect to the vertical axis of the laboratory system.

A measured intensity-autocorrelation function is shown in Fig. 8.7a. The stability of the equilibrium state as well as of the experimental setup can be monitored by calculating the two-times correlation function as shown in Fig. 8.7b.

[2] http://www.kayelaby.npl.co.uk/atomic_and_nuclear_physics/4_2/4_2_1.html 06.2015

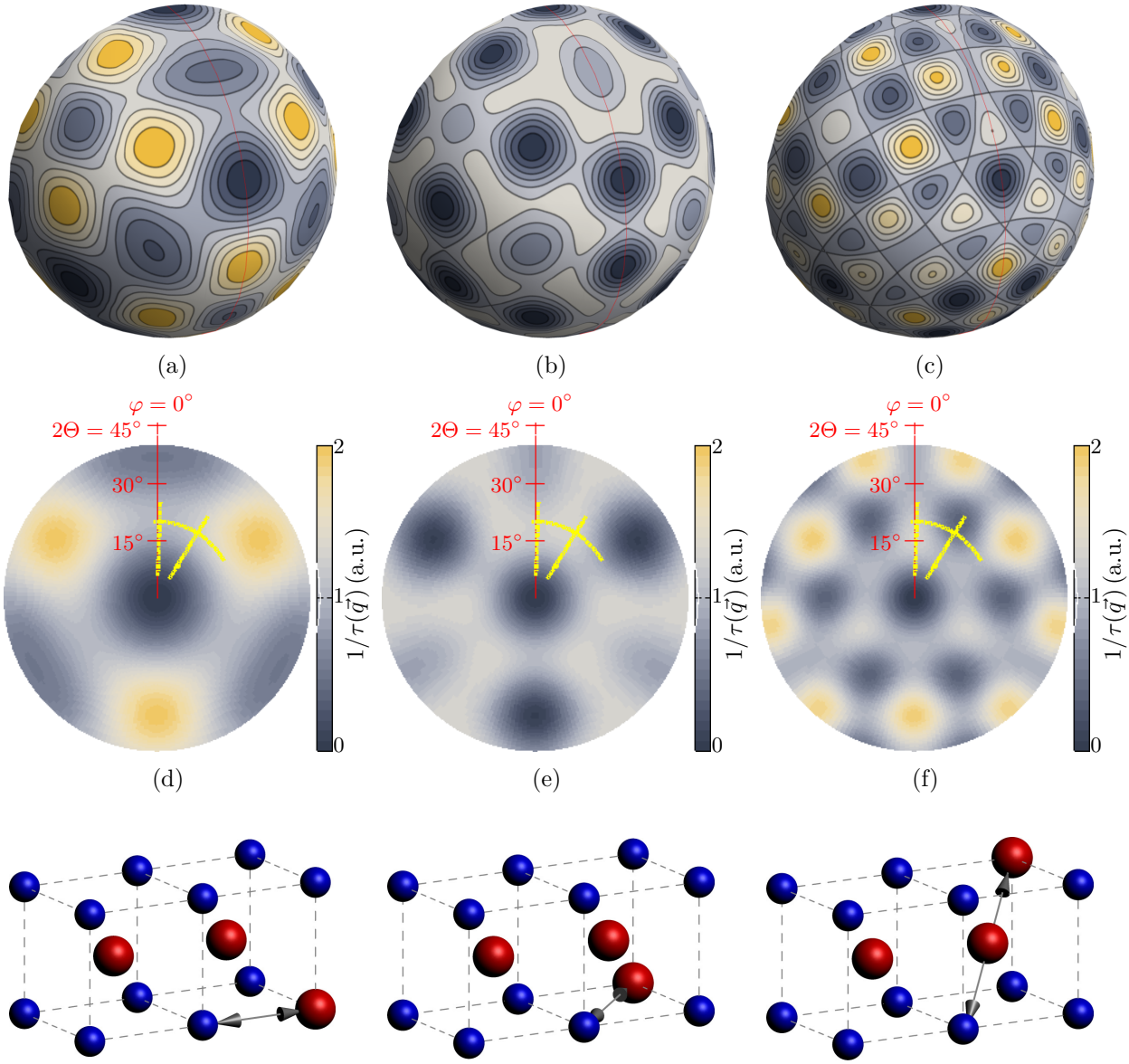

Figure 8.8.: Different jump models for effective jumps exclusive to a certain neighboring shell within the simple cubic sublattice of a in a B2 system. Calculations were done for a beam energy of 7.05 keV, a lattice constant of 2.929 Å and $\vec{k}_{\text{in}} \parallel \langle 111 \rangle$. The top pictures show inverse correlation times on a half scattering sphere with the origin in the north pole. Middle images show a projection of the section relevant for the aXPCS experiment. The yellow lines mark the regions of reciprocal space, where measurements were carried out. The lower images show the corresponding exchange of atoms on the lattice.

8.4.2. Single-sublattice approach

As discussed in Section 8.1.1 for Fe-Al close to stoichiometry, it can be assumed that Al-atoms occupy only one sublattice, while the second sublattice is almost exclusively occupied by Fe-atoms and vacancies. In this case, only the sublattice occupied by both types of atoms is visible in the aXPCS experiment. In order to solve the jump matrix for such an approach, the

occupation probability for one sublattice is set to zero ($W_\beta = 0$) and the appropriate residence time on the lattice becomes very large, leading to $\kappa_\beta = 0$. Plugging this into (3.13) leads to following correlation times:

$$\tau_1(\vec{q}) = \frac{\tau_0}{\kappa_\alpha(1 - S_{\alpha\alpha'}(\vec{q}))} , \qquad \tau_2(\vec{q}) = \infty \tag{8.2}$$

The first correlation time (τ_1) is in accordance with (2.34), with $S_{\alpha\alpha'}(\vec{q})$ being the sum over cosine terms corresponding to the jump vectors within the sublattice. Therefore, jumps take place exclusively on this simple cubic Bravais lattice. For the sublattice, possible jumps are $\langle 100 \rangle$, $\langle 110 \rangle$ and $\langle 111 \rangle$. The appropriate jump models calculated according to (2.34) with only one probability being nonzero and Table 2.2 with the experimental parameters for exclusive jumps to these shells are shown in Fig. 8.8. The second correlation time (τ_2) leads to a contribution of the exponential decay of zero. The measured intensity-correlation function can therefore be fitted by a single exponential decay. Such a fit for an ACF measured at $2\Theta = 6°$ and $\varphi = 2°$ is shown in Fig. 8.7a in comparison to a fit with a sum of exponential decays.

Fig. 8.9 shows the fitted correlation time as a function of 2Θ and φ and three exclusive jump models with no short-range order correction, as shown in Fig. 8.8. At some combinations of angles $(2\Theta, \varphi)$, several ACFs were measured. Their weighted sum was used to calculate an average ACF.

As can be seen from Fig. 8.9, the $\langle 111 \rangle$ jump mechanism appears to be the dominant mechanism. It shall be noted, that the data points collected for $\varphi = 32°$ lie exactly in the vertical plane of the synchrotron beam, where polarization effects can play a significant role. However, as no estimation as to how strong this effect really is could be made, they are treated like the rest of the data.

In order to find a more quantitative estimate, a model including all three jump processes with weights $p_{100} = \bar{p}_1$, $p_{110} = \bar{p}_2$ and $p_{111} = \bar{p}_3$ according to (2.34) and (2.44) is fitted to the whole dataset simultaneously. Chemical short-range order is accounted for using (2.58) and the chemical short-range order parameters for the Al-sublattice calculated from different simulation potentials as shown in Table 8.2. Table 8.3 gives an overview of the best fit of a weighted jump mechanism corrected with different short-range order parameters according to Section 8.3.2.

I_{SRO} (from parameters by)	p_{100}	p_{110}	p_{111}	τ_0 (s)	red. χ^2
no short-range order ($\alpha_{\tilde{n}>0} = 0$)	0.05	0.34	0.61	672(21)	1.814
Schmid & Binder	0.18	0.12	0.70	678(21)	1.819
Weinkamer et al. modified	0.17	0.10	0.73	677(21)	1.822
Ouyang et al. c_V=0.0%, on-lattice	0.32	0.11	0.57	679(22)	1.880
Ouyang et al. c_V=0.2%, on-lattice	0.33	0.11	0.56	679(21)	1.853
Ouyang et al. c_V=0.0%, off-lattice	0.19	0.11	0.70	676(21)	1.792

Table 8.3.: Probabilities for jumps to certain neighboring shell within the Al-sublattice and average residence time fitted with short-range order correction using parameters from Table 8.2 for different interaction potentials.

Fig. 8.11 features the result of such a fit using I_{SRO} according to the off-lattice approach with EAM potentials by Ouyang et al. [Ouya 12] , as shown in Fig. 8.10.

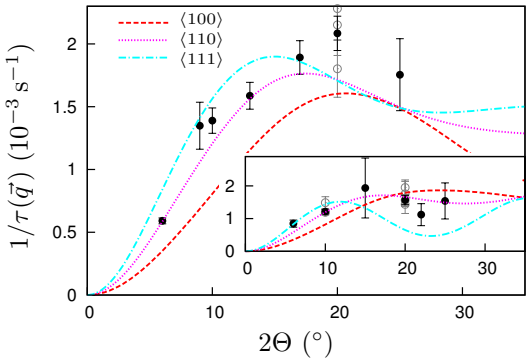

(a) Inverse correlation time as a function of scattering angle for $\varphi = 2°$ and $\varphi = 32°$ (insert).

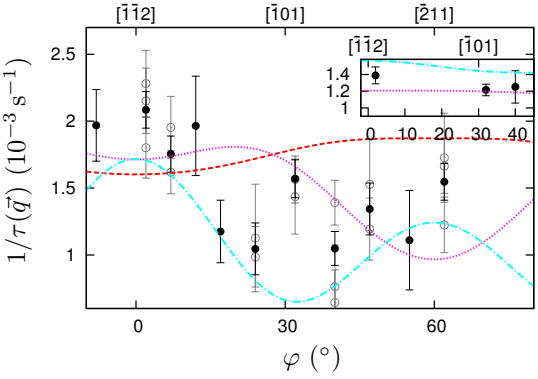

(b) Inverse correlation time as a function of azimuthal angle for $2\Theta = 20°$ and $2\Theta = 10°$ (insert).

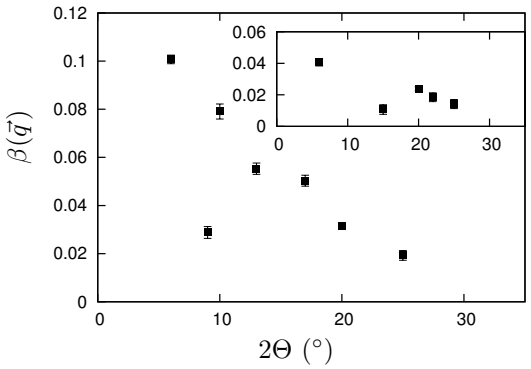

(c) Fitted contrast factor $\beta(\vec{q})$ corresponding to sub-figure (a).

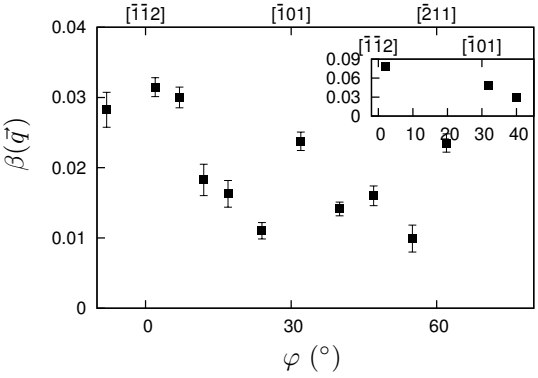

(d) Fitted contrast factor $\beta(\vec{q})$ corresponding to sub-figure (b).

Figure 8.9.: (a) and (b): Symbols with error represent inverse correlation times, $1/\tau(\vec{q})$, gained by fitting measured intensity-correlation functions with single exponential decay for different sets of $(2\Theta, \varphi)$ for $Fe_{0.54}Al_{0.46}$ oriented in the ⟨111⟩ direction at a temperature of 653 K. In the cases where more than one measurement was carried out at a certain point, the individual measurements are represented by the open, gray symbols and the weighted sum is represented by a full, black symbol. The lines represent models for distinct sets of jump vectors (exclusively ⟨100⟩, ⟨110⟩ or ⟨111⟩ jumps) without short-range order correction as shown in Fig. 8.8.
(c) and (d): Contrast factor $\beta(\vec{q})$ as a function of scattering angle and azimuthal angle. The correlation between large error bars in $\tau(\vec{q})$ and low contrast is noticeable.

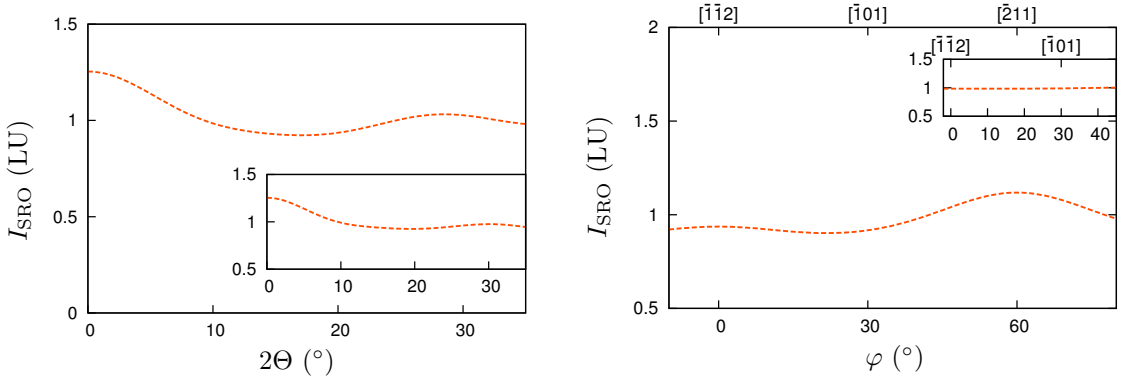

(a) 2Θ-scan of short-range order intensity for $\varphi = 2°$ and $\varphi = 32°$ (insert).

(b) φ-scan of short-range order intensity for $2\Theta = 20°$ and $2\Theta = 10°$ (insert).

Figure 8.10.: Short-range order intensity for sections of reciprocal space corresponding to the region where the aXPCS experiment was carried out, calculated from EAM with potentials by Ouyang et al. [Ouya 12] using the off-lattice approach. The increase of intensity towards small angles 2Θ reproduces the tendency in the experimental data as shown in Fig. 8.2b

The results given in Table 8.3 can be used to calculate the effective chemical diffusion constant, $\tilde{D}$, according to (3.1):

$$\tilde{D}(T) = \frac{\left\langle \tilde{R}^2 \right\rangle}{6\tau_0} = \frac{p_{100}\, d^2 + p_{110}\, (\sqrt{2}d)^2 + p_{111}\, (\sqrt{3}d)^2}{6\tau_0} \tag{8.3}$$

When correcting for chemical short-range order according to different simulation results this yields slightly different diffusion constants, as can be seen in Table 8.4.

	$\tilde{D}_{\mathrm{Fe_{0.54}Al_{0.46}}}(653\,\mathrm{K})$ $(\times 10^{-23}\,\mathrm{m^2 s^{-1}})$
no short-range order	5.46(18)
Schmid & Binder	5.32(17)
Weinkamer et al. modified	5.40(17)
Ouyang et al. c_V=0.0%, on-lattice	4.73(16)
Ouyang et al. c_V=0.2%, on-lattice	4.71(15)
Ouyang et al. c_V=0.0%, off-lattice	5.30(17)

Table 8.4.: Diffusivities for $\mathrm{Fe_{0.54}Al_{0.46}}$ at 653 K when correcting aXPCS data with different short-range order intensities.

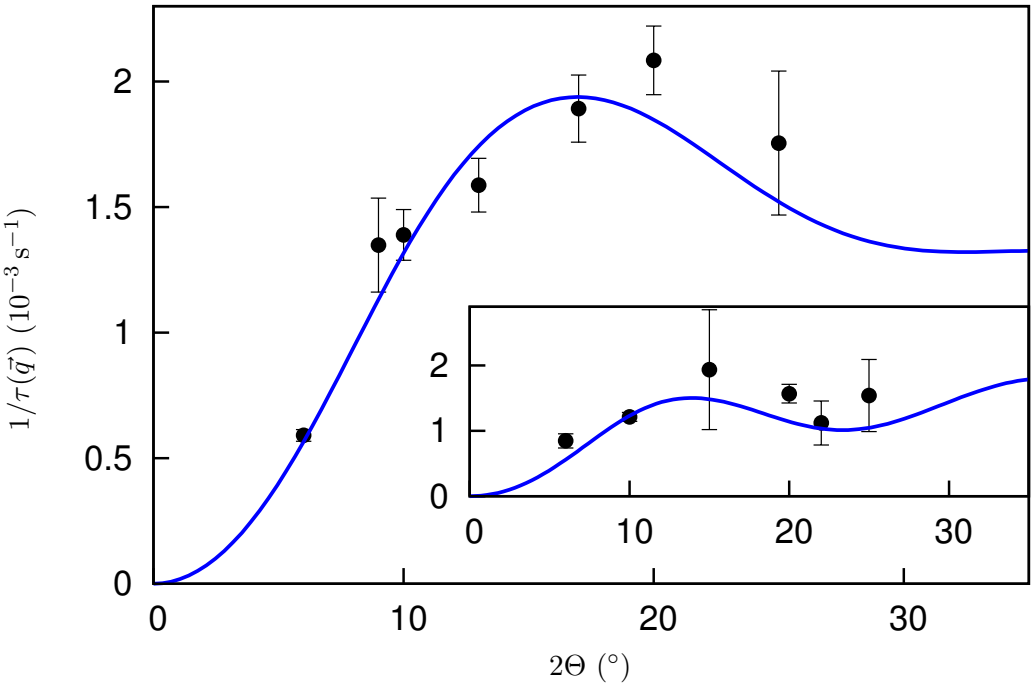

(a) 2Θ-scan, $\varphi = 2°$ and $\varphi = 32°$ (insert).

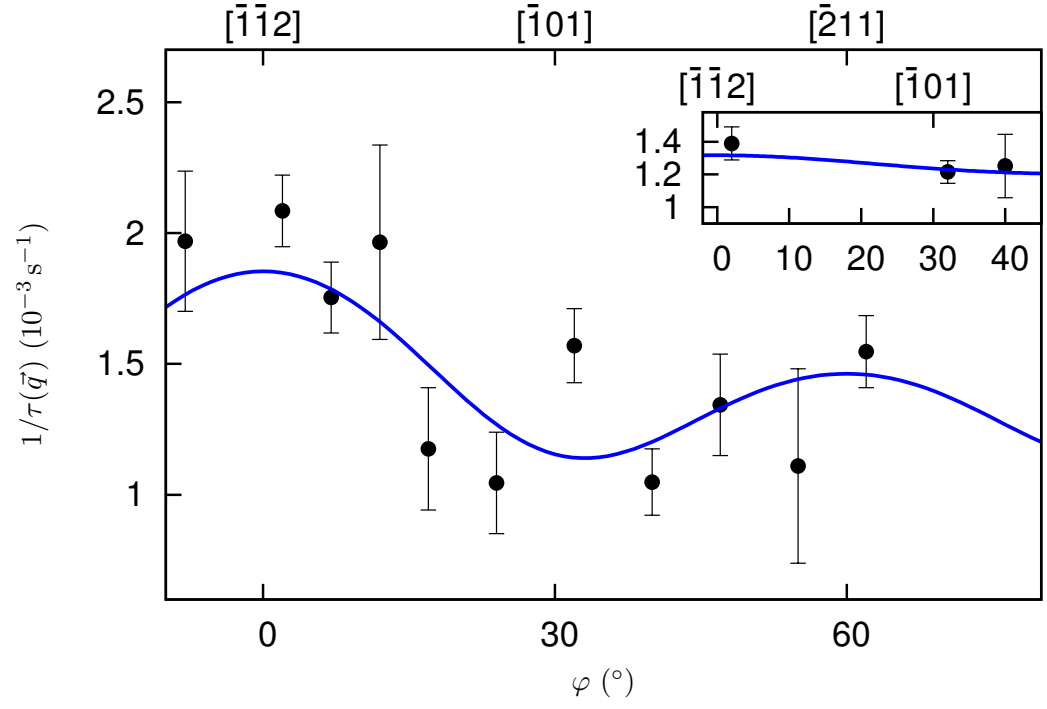

(b) φ-scan, $2\Theta = 20°$ and $2\Theta = 10°$ (insert).

Figure 8.11.: A model with ⟨100⟩, ⟨110⟩ as well as ⟨111⟩ jumps was simultaneously fitted to all experimental data. In order to correct for short-range order, intensity calculated from a EAM off-lattice simulation was used. The best fit was found for the jump probabilities $p_{100} = 0.19$, $p_{110} = 0.11$ and $p_{111} = 0.70$ and an average residence time $\tau_0 = 676(21)\,s$. This fit is represented by the blue line.

8.4.3. Arrhenius theory

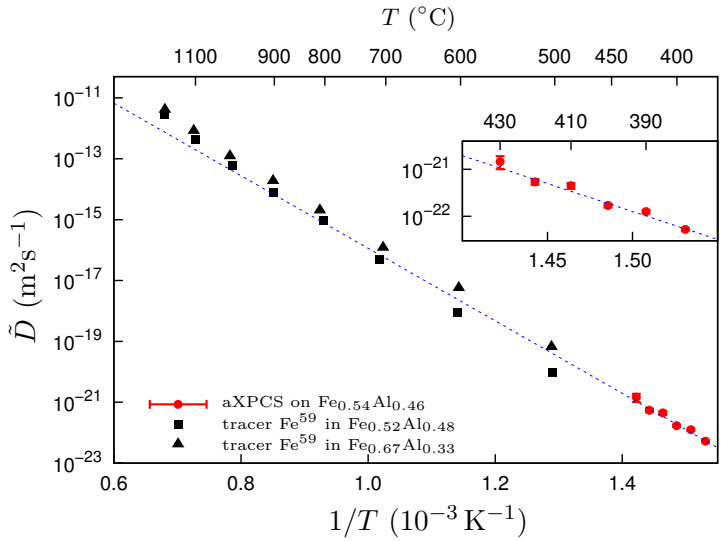

Figure 8.12.: Temperature dependence of diffusivities for chemical diffusion in $Fe_{0.54}Al_{0.46}$ from aXPCS measurements compared with data measured by tracer experiments for similar Fe-Al compositions [Egge 00].

Additionally to the measured ACFs for different pairs of $(2\Theta, \varphi)$ at 653 K, measurements at different temperatures were taken at $(10°, 32°)$. When a model is found, it can be used to calculate the average waiting time τ_0 for measurements of $\tau(\vec{q})$ according to

$$\tau_0 = \tau(\vec{q}) \frac{\sum_n \bar{p}_n (1 - C_n(\vec{q}))}{I_{\mathrm{SRO}}(\vec{q})} \,. \tag{8.4}$$

In combination with (8.3) and (3.4b), this can be used to calculate the activation energy $\tilde{E}_\mathrm{a}$ and the pre-exponential factor $\tilde{D}_0$ for chemical diffusion.

Short-range order information from the EAM simulation with parameters by Ouyang et al. and the off-lattice approach was used in the model. Diffusivities calculated this way from ACFs at different temperatures along with a fit according to (3.4b) are shown in Fig. 8.12. An activation energy of $\tilde{E}_\mathrm{a} = 2.36(19)\,\mathrm{eV}$ with a pre-exponential factor $\tilde{D}_0 \approx 9 \times 10^{-5}\,\mathrm{m^2 s^{-1}}$ was found. This is in good agreement with the activation energy of $E_\mathrm{a} = 2.5(3)\,\mathrm{eV}$ found by Schaefer et al. [Scha 99].

8.4.4. Superstructure approach

When no assumptions about lattice occupancy are made, the intensity-correlation function has to be fitted with the square of the weighted sum of two exponential decays, see (2.56). This increases the number of free parameters to 5. Furthermore, for a dataset that can be described by a single exponential decay and does not have very good SNR, discrimination of the two correlation times in the fitting process is difficult. Fig. 8.7a shows one possible fit for a weighted sum of two exponential decays, however, the fit very much depends on the choice of starting values. This leads to large error bars in the fitted parameters, as can be seen in Fig. 8.13. As the weighting factors w_i scale with the Siegert factor $\beta(\vec{q})$, their ratio is given.

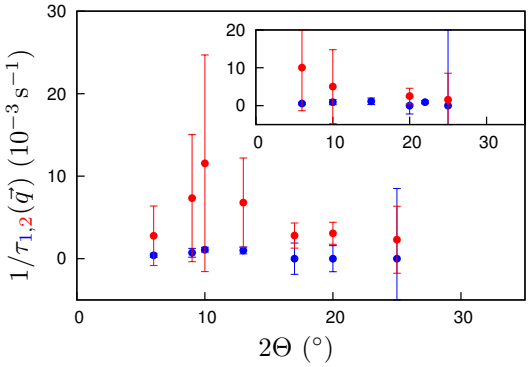

(a) Scan of scattering angle for $\varphi = 2°$ and $\varphi = 32°$ (insert).

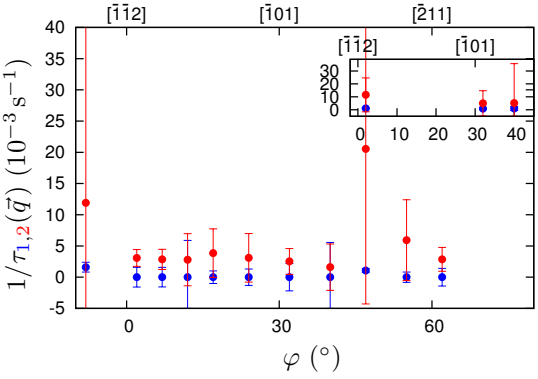

(b) Scan of azimuthal angle for $2\Theta = 20°$ and $2\Theta = 10°$ (insert).

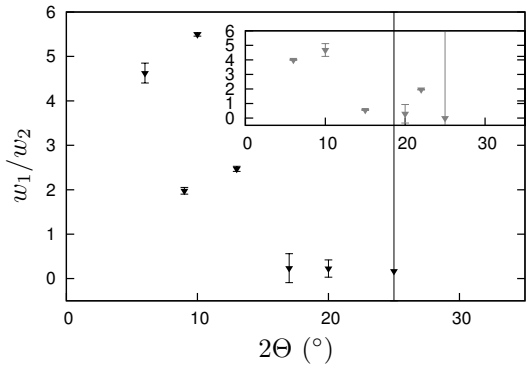

(c) Fitted ratio of weighting factors w_1 and w_2 corresponding to sub-figure (a).

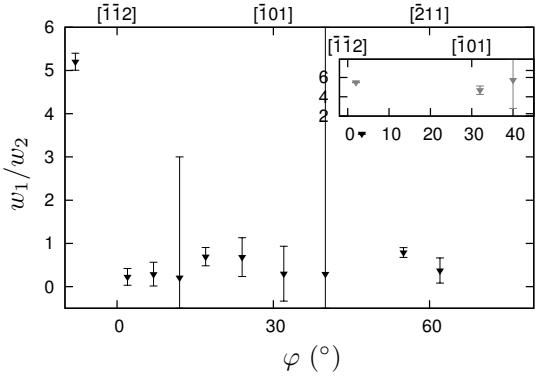

(d) Fitted ratio of weighting factors w_1 and w_2 corresponding to sub-figure (b).

Figure 8.13.: (a) and (b): Plot of inverse of correlation times $\tau_1(\vec{q})$ and $\tau_2(\vec{q})$ gained by fitting the intensity-correlation functions with a squared sum of two exponential decays according to (2.56) for different sets of $(2\Theta, \varphi)$ for $Fe_{0.54}Al_{0.46}$ oriented in the $\langle 111 \rangle$ direction.
(c) and (d): Plot of ratio of weighting factors w_1 and w_2.

Fitting a model with up to 8 free parameters (τ_0, κ_α, κ_β, W_α, $W_\beta = 1 - W_\alpha$, $\bar{p}_1^{\alpha\alpha'}$, $\bar{p}_2^{\alpha\alpha'}$, $\bar{p}_3^{\alpha\alpha'} = 1 - \bar{p}_1^{\alpha\alpha'} - \bar{p}_2^{\alpha\alpha'}$, $\bar{p}_1^{\beta\beta'}$, $\bar{p}_2^{\beta\beta'}$, $\bar{p}_3^{\beta\beta'} = 1 - \bar{p}_1^{\beta\beta'} - \bar{p}_2^{\beta\beta'}$) to such data does not give reasonable results.

Alternatively, a different approach must be taken, where all intensity-correlation functions are fitted simultaneously according to (3.9) - (3.13). A gnuplot fit routine for this approach can be found in Section A.5. Due to the large number of dimensions in the fit, the starting values must be chosen carefully. As a fit result with a reduced χ^2 of 1.0326, the following parameters were gained. The average residence time was found to be $\tau_0 = 18.1(2.8)\,s$. The lattice occupation was $W^\alpha = 0.99956$, yielding $W^\beta = 0.00044$. Further, $\kappa^\alpha = 0.0175$ and $\kappa^\beta = 0.0310$, from which the residence times for jumps within a sublattice can be calculated as $\tau^{\alpha\alpha'} = \tau_0/\kappa^\alpha = 1034(160)\,s$ and $\tau^{\beta\beta'} = \tau_0/\kappa^\beta = 584(91)\,s$. The residence time on the minority sublattice (α) found by this approach is therefore much larger than the one found by the single sublattice approach. The jump probabilities were found to be $p_{100}^{\alpha\alpha'} = 0.05$, $p_{110}^{\alpha\alpha'} = 0.31$, $p_{111}^{\alpha\alpha'} = 0.64$, $p_{100}^{\beta\beta'} = 0.00$,

$p_{110}^{\beta\beta'} = 0.00$ and $p_{111}^{\beta\beta'} = 1.00$. This is in good agreement with the results from the single sublattice approach.

However, this approach does not account for short-range order. In order to gain more quantitative results for jump probabilities as well as occupation probabilities from this approach, additional theoretical development has to be undertaken.

8.4.5. Interpretation of results

As can be seen from Table 8.3, all short-range order configurations gained from the applied potentials yield a probability for effective $\langle 111 \rangle$ jump of more than 50%. Furthermore it was shown in Section 8.4.3, that the model quite well reproduces the activation energy measured by other techniques. Therefore, it is plausible to assume that $\langle 111 \rangle$ jumps are the dominant jump mechanism in this system. Such jumps can, however, not be described by the well established diffusion mechanisms, like e.g. the 6JC. Direct $\langle 111 \rangle$ jumps can be ruled out as the migration barrier would be to high. Correlated single vacancy jump cycles like the 10-jump cycle are unlikely to explain this behavior, as longer jump sequences would have to be more probable than a 6JC.

As discussed in Section 3.3 the percolation threshold for B2 systems lies close to 55 at.%. The system studied here is therefore only slightly below this limit. For systems where the threshold is reached, diffusion takes place primarily via the ASB, as discussed in Section 3.3.2, which does not lead to chemical diffusion and is therefore invisible for aXPCS. In such a system chemical diffusion can take place via a different mechanism on a much slower rate than tracer diffusion. As it can not be expected that the percolated area remains completely invariable, the percolation pathways change. This local rearrangement of pathways, for example, leads to chemical diffusion.

For a system slightly below the percolation threshold, sub-regions where percolation already exists are likely to be formed. To cross a gap between such regions, it is proposed that two vacancies perform a correlated jump described by the linear triple-defect mechanism (lTDM) as shown in Fig. 3.5. The $\langle 100 \rangle$ and $\langle 110 \rangle$ jumps can be explained by the 3JC or by different divacancy mechanisms [Leit 15].

Bakker et al. stated [Bakk 97], that “When atoms are accommodated on wrong sublattices where they do not fit, strain will develop, accompanied by the storage of elastic enthalpy in the compound. A considerable part of the strain energy is caused by anti-site atoms (and vacancies)”. This could play a role especially at low temperatures. It can be speculated that this could be in favor of forming a lTD rather than a triangle-arrangement of the antisite atom and the two vacancies. Furthermore, the lTDM yields a higher diffusion constant than other triple-defect mechanisms.

As the gaps between the percolated areas represent a bottleneck for diffusive motion, it is clear that the responsible mechanism is the controlling one. The fact that the activation energy is comparable to those found by other experimental techniques is in favor of this argument.

8.5. Measurements of atomic jump length distribution by aXPCS in $Ag_{0.58}Mg_{0.42}$

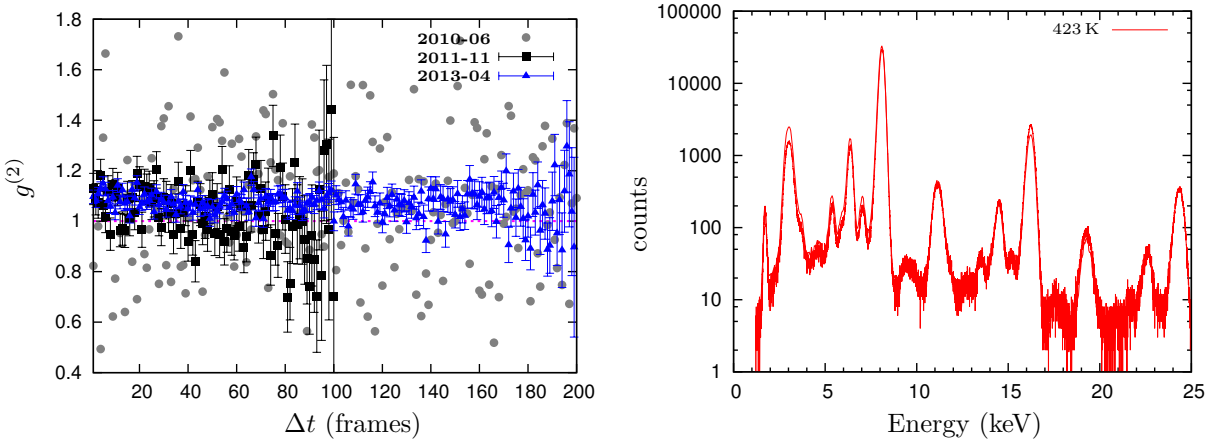

(a) Indication of SNR for three intensity autocorrelation functions measured during different beamtimes at ID10, ESRF for an $Ag_{0.58}Mg_{0.42}$ sample.

(b) Energy histograms measured at beamline ID10 at the ESRF for $Ag_{0.58}Mg_{0.42}$.

Figure 8.14.

8.5.1. Technical details

The details about the sample, which was oriented in ⟨110⟩ direction, can be found in Section 6.5.2. During beamtime HS-4083, which took place in June 2010 at beamline ID10 of the ESRF, a series of frames was collected at $2\Theta = 5.0°$ and room temperature in order to determine whether the sample would yield a sufficient contrast. As the scattering intensity was a factor of three lower than that of a $Ni_{0.48}Al_{0.52}$ sample, no further measurements were taken. During beamtime HS-4357 in November 2011 the room temperature measurement was repeated at $2\Theta = 10.0°$, yielding a contrast of $\beta = 1\%$. It was decided that this contrast is not sufficient for further measurements. During beamtime HC-885 in April 2013 the sample was taken up again. A measurement at a temperature of 353 K was made at $2\Theta = 6.0°$. Again a contrast of 1% was found and it was decided to increase the temperature to 423 K and to undertake measurements. Fig. 8.14a shows the improvement in SNR due to the improvement of the synchrotron beam over time.

All measurements were done using the iKon-M CCD chip. Readout time was determined to be 0.61 s/frame. Exposure times were between 4 s for small angles and 8 s for angles larger than $2\Theta = 8°$. Sample-to-detector distance at HC-885 was 67 cm. The illuminated area on the sample was determined by slits of $10 \times 10\,\mu m^2$. Measurements were taken at 423 K. The [001]-direction ($\varphi = 0°$) was tilted by 36.6° with respect to the horizontal axis. The beam energy was 8.1 keV.

An energy histogram of the sample is shown in Fig. 8.14b. At 8.1 keV the elastic photon peak is visible. At 16.2 keV and 24.3 keV the elastic two and three photon peaks can be seen. The

escape peak is found at 5.45 keV. There is the Mg K_α line visible at 1.25 keV and the Ag $L_\beta 3$ line at 3.23 keV. Other peaks are superpositions.

8.5.2. Single-sublattice approach

Even though the number of minority atoms on the majority sublattice might be larger than in the case of Fe-Al, the dominant part of the diffuse intensity comes from the minority sublattice. Therefore, in a first step the investigation can be limited to this sublattice, i.e. the Mg sublattice.

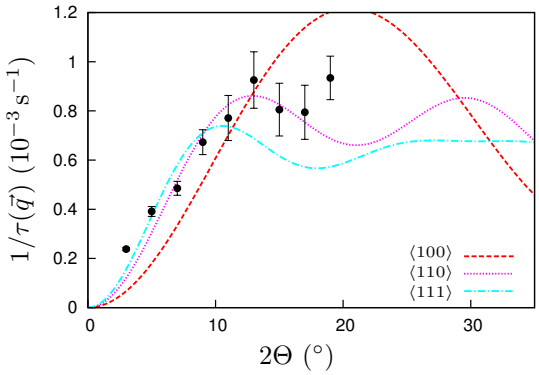

(a) Inverse correlation time as a function of scattering angle for $\varphi = 36.6°$.

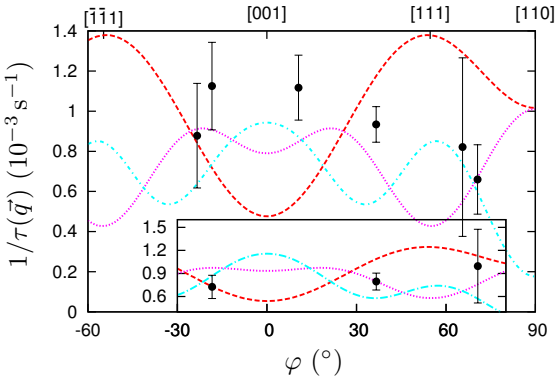

(b) Inverse correlation time as a function of azimuthal angle for $2\Theta = 19°$ and $2\Theta = 17°$ (insert).

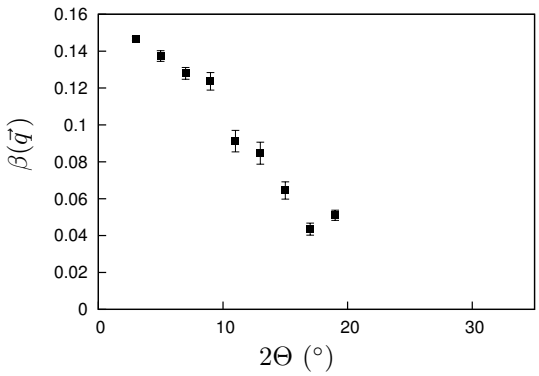

(c) Fitted contrast factor $\beta(\vec{q})$ corresponding to sub-figure (a).

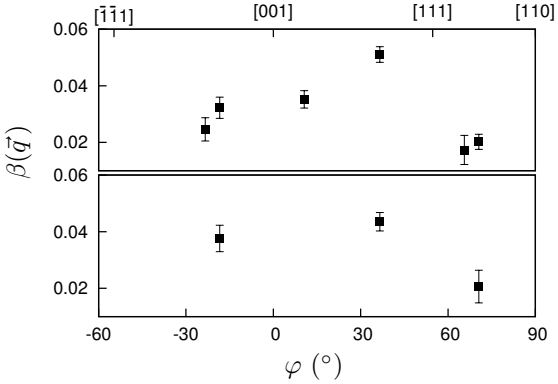

(d) Fitted contrast factor $\beta(\vec{q})$ corresponding to sub-figure (b), $2\Theta = 19°$ (top) and $2\Theta = 17°$ (bottom).

Figure 8.15.: (a) and (b): Plot of inverse of correlation times $\tau(\vec{q})$ gained by fitting measured intensity-correlation functions with single exponential decay for different sets of $(2\Theta, \varphi)$ for $Ag_{0.58}Mg_{0.42}$ oriented in the $\langle 110 \rangle$ direction, measured with 8.1 keV at a temperature of 423 K. The lines represent models for distinct set of jump vectors (exclusively $\langle 100 \rangle$, $\langle 110 \rangle$ or $\langle 111 \rangle$ jumps) with no short-range order correction. (c) and (d): Contrast factor (Siegert factor) $\beta(\vec{q})$.

As can be seen from Fig. 8.15a and Fig. 8.15b jumps to the next-nearest-neighbor shell appear to be a promising candidate for describing diffusion in this system. In order to be able to make more quantitative assertions, the data was fitted according to (2.34) and (2.44). As the

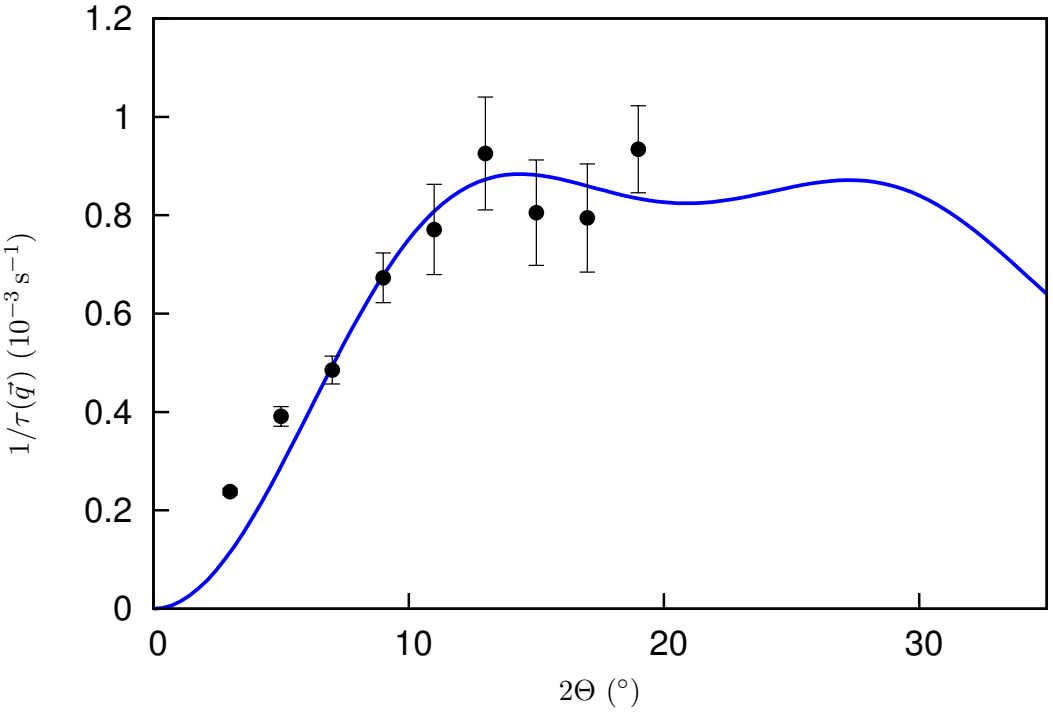

(a) 2Θ-scan, $\varphi = 36.6°$.

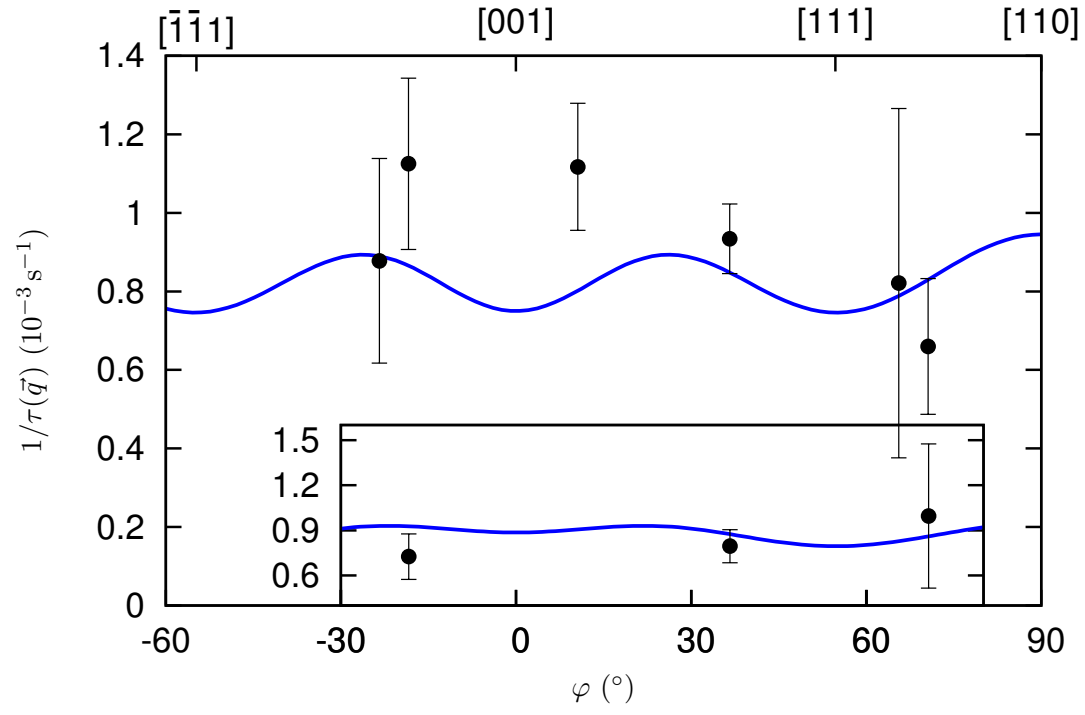

(b) φ-scan, $2\Theta = 19°$ and $2\Theta = 17°$ (insert).

Figure 8.16.: A model with ⟨100⟩, ⟨110⟩ and ⟨111⟩ jumps was simultaneously fitted to all experimental data, except the point at $2\Theta = 4°$, which is assumed to be to high due to instabilities in the setup. The best fit was found for the jump probabilities $p_{100} = 0.28$, $p_{110} = 0.63$ and $p_{111} = 0.09$ and an average residence time $\tau_0 = 1268(41)\,s$. This fit is represented by the blue line.

experimental findings suggest that chemical short-range order is weak in this system and because no potentials that would yield more information in a simulation could be found, the short-range order intensity was assumed to be constant ($I_{\mathrm{SRO}}(\vec{q}) = 1$).

The best fit was achieved yielding $p_{100} = 0.28$, $p_{110} = 0.63$ and $p_{111} = 0.09$ and an average residence time of $\tau_0 = 1268(41)$ with reduced $\chi^2 = 0.9662$. This fit can be seen in Fig. 8.16. For comparison also a fit was carried out, where p_{111} was set to zero. The best fit was achieved with jump probabilities $p_{100} = 0.26$ and $p_{110} = 0.74$, yielding $\tau_0 = 1264(41)$ with reduced $\chi^2 = 0.975$.

Calculating the effective chemical diffusion constant according to (8.3) yields

$$\tilde{D}_{\mathrm{Ag_{0.58}Mg_{0.42}}}(423\,\mathrm{K}) = 2.62(9) \times 10^{-23}\,\mathrm{m^2 s^{-1}} \text{ including } \langle 111\rangle \text{ jumps and}$$
$$\tilde{D}_{\mathrm{Ag_{0.58}Mg_{0.42}}}(423\,\mathrm{K}) = 2.54(9) \times 10^{-23}\,\mathrm{m^2 s^{-1}} \text{ with only } \langle 100\rangle \text{ and } \langle 110\rangle \text{ jumps.}$$

It can be concluded, that $\langle 110\rangle$ jumps are dominant in this system with and addition of $\langle 100\rangle$ jumps. The presence of $\langle 111\rangle$ jumps is doubtful.

8.5.3. Superstructure approach

As in the case of Fe-Al, fitting individual ACFs according to (2.56) yields arbitrary results for $\tau_{1,2}(\vec{q})$, depending on the initial parameters set in the fit routine. In order to make such an approach possible, measurements with a much higher Siegert factor and better SNR of the ACFs are necessary.

8.5.4. Interpretation of results

A number of diffusion mechanisms introduced in Section 3.3 can account for the $\langle 100\rangle$ and $\langle 110\rangle$ jumps. In order to find out which is in place, formation enthalpies of defects have to be considered [Leit 15]. It is, however, even at this premature state of research possible to say, that a different mechanism than the lTDM, which was proposed for Fe-Al, operates in Mg-Ag alloys.

8.6. Conclusion

The investigation of two intermetallic compounds, one of a hybride-triple defect type ($Fe_{0.54}Al_{0.46}$) and one of the antisite type ($Ag_{0.58}Mg_{0.42}$) by aXPCS showed, that different effective atomic exchanges dominate chemical diffusion in both systems. For the $Fe_{0.54}Al_{0.46}$ the linear triple-defect mechanism (lTDM) is proposed resulting in effective $\langle 111 \rangle$ jumps bridging gaps between percolated areas, where the antistructure-bridge mechanism (ASB) operates.

In ordered intermetallics the chemical short-range order on the sublattices appears to be less pronounced than in solid solutions. Simulations using a few available potentials for the Fe-Al system yielded slightly different results. It was shown, that an on-lattice and an off-lattice approach can yield similar, but different short-range order parameters, which has an influence on the resulting jump probabilities. The dominating jump length could, however, be clearly distinguished. For a more quantitative inquiry, the exact chemical short-range order of the system under investigation has to be determined, which is probably only possible by spending much time and effort on reciprocal space mapping techniques performed at a synchrotron.

In general, short-range order parameters can be used to compare simulation results with experimental findings. It would be good, if the computational community would publish such parameters more frequently, as they unfortunately seem to be considered irrelevant today.

9. Outlook

The scope where aXPCS can be applied to the investigation of atomic scale diffusion is already broad, reaching from intermetallics and solid solutions at temperatures of a few hundred degree Celsius [Leit 09, Stan 13] to glassy systems at intermediate [Leit 12b, Ross 14] and low temperatures of a few tens of Kelvin [Ross 15]. However there are still some limitations to this technique which are expected to be unmade by technical developments in the near future.

As discussed in Section 6.4.1, the readout time of area detectors is a limiting factor towards the investigation of fast processes. This is especially true for detectors with a large number of pixels, as the standard readout mechanism scans the ADU values row by row. Detectors based on the principle, where each pixel is built like a separate detector and can be read out independently, like the Pilatus and more recently the Eiger family have of course much faster readout times. Other concepts like Charge Integrating systems have very fast readout times, even though they are allegedly somewhat difficult to handle. Hybrid systems like the ePix series, AGIPD or are probably more user friendly. The problem with those detectors at the moment is, however, that they are in general very bulky and heavy, making them difficult to maneuver. Especially so if the detector has to be moved by large angles over wide areas of the scattering sphere, as is the case in an aXPCS experiment. With decreasing pixel size for these types of detector, such limitations will be overcome, which will allow for much faster detection rates. A particularly interesting candidate that already exists is the LAMBDA-detector.

On the end of the beam source, as seen from (6.26) an increase in coherent flux allows either for a decrease of the smallest accessible correlation time or for a reduction of number of pixels in the multi-speckle detection scheme as described by (6.27). This will make fast diffusion processes corresponding to high temperatures accessible and thereby allow for a direct comparison of aXPCS with results from other atomistic techniques under equal sample conditions and open up a large crowd of new candidates for investigation. Higher intensities, however, mean that more energy will be deposited on the sample. Maybe when this is imminent, works regarding the influence of photon energy on dynamics in the sample will not be considered to be data recycling. On the other hand of the time spectrum synchrotron sources get ever more stable supplying the user with constant intensities (top up mode) and a locally very stable beam (very little jitter). This allows for measurements over long time periods corresponding to very low temperatures. The timescale of dynamics accessible to aXPCS measurements will therefore grow in a way unmatched by any other atomistic technique. This will allow for a systematic investigation of concentration as well as temperature dependence of diffusion mechanisms in alloys. As boarders between different phases are only sharp in theory and the interaction between the atoms exist over the whole range of concentration, it is not clear at which point the jump mechanism changes and how it changes. Furthermore for systems with a vacancy mechanism, interactions between atoms and vacancies plays a role. There are very few experimental methods capable of making assertions about such interactions. They are, however, likely to be important for material

properties. It is therefore of great interest, how effective atomic jumps change within the phase diagram. Such knowledge would certainly have a large impact on material tailoring.

The increase of coherent intensity available will be carried by two major developments. The first is known as diffraction limited storage ring. The emittance of an electron beam, which is a measure of the compactness of the electron cloud in phase space is proportional to the square of the electron beam energy and inversely proportional to the bending radius and the third power of the number of bending magnets [Eber 15]. As reducing the beam energy obviously has its drawbacks and increasing the bending radius is limited by constructional features, the idea is to increase the number of bending magnets per supercell, which is why one also talks about a multi-bend achromat (MBA) lattice design [Eber 15]. Such a design yields total transversal coherence of the beam for energies below the diffraction limit, which extends to about 1 keV for MBA rings. For aXPCS experiments this allows for increasing the spot size which leads to smaller speckles and less dependence on the gradient of correlation time with $\vec{q}$. However, care has to be taken that the sample is homogeneous when increasing the spot size. Furthermore the increase in intensity will allow for using higher order crystallographic reflexes for monochromatization, yielding a much higher longitudinal coherence. This will in turn increase the Siegert factor and allow to have samples of a thickness close to the ideal scattering length. The second approach is that of a linear accelerator, which has even lower emittance, especially in the high energy region [Eber 15]. The main advantage of this concept, additionally to an increase in photon flux, is self-amplified spontaneous emission or self-seeding [Aman 12], where the interaction of the magnetic field of the electrons in the bunch with the magnetic field of a long undulator leads to sinusoidal density profile in the bunch, so called microbunching. As the emission of the electrons in a bunch is incoherent for wavelength shorter than the bunchlength [Eber 15], this microbunching drastically increases the coherence length.

Another experimental challenge will remain in the form of fluorescence for some samples. Choosing very small exposure times in a time window, so that only scattered light is collected and the slightly delayed light coming from fluorescence is shut off (as is done for some optical light applications) will not work for X-rays, as fluorescence processes take place at much faster timescales. Once intense, coherent light in the high energy regime (above 10 keV) will become available it will, however, be possible to reduce fluorescence by using filters like aluminum foils between sample and detector. Additionally, structures and structural changes below one angstrom can be accessed by such high energy X-rays.

These technical improvements will allow for much better SNR in aXPCS experiments which will allow for much more quantitative assertions for a large number of parameters within the jump matrix approach in the future. With increased coherent scattering intensity, also less scattering contrast in elements under investigation is needed, which will allow for all combinations of elements to be studied. Someday maybe even systems like Cu-Fe. Also for studies of impurity diffusion, the amount of impurity needed can be reduced. Here an interesting field in the investigation of carbon diffusion in steel will open up. Maybe someday it will even be possible to directly investigate the jumps of vacancies in very pure and perfect crystals like for example in silicon wavers.

A. Appendix

A.1. Abbreviations

ACF auto-correlation function

ADU analog to digital unit

ASB antistructure-bridge mechanism

aXPCS atomic-scale X-ray Photon Correlation Spectroscopy

CCD charge-coupled device

CE canonical ensemble

DLS Dynamic Light Scattering

DP dynamic pair mechanism

EDX energy-dispersive X-ray spectroscopy

EAM embedded atom method

LF leap frog mechanism

FWHM full width at half maximum

LASER light amplification by stimulated emission of radiation

ITD linear triple-defect

ITDM linear triple-defect mechanism

LU Laue unit

MBA multi-bend achromat

MC Monte Carlo

MCS Monte Carlo step

NMR Nuclear Magnetic Resonance

PLD path-length difference

QNS Quasi-elastic Neutron Scattering

QMS Quasi-elastic Mößbauer Spectroscopy

SAXS small-angle X-ray scattering

6JC six jump cycle

SNR signal-to-noise ratio

TDM triple-defect mechanism

3JC three jump cycle

XPCS X-ray Photon Correlation Spectroscopy

WAXS wide-angle X-ray scattering

WS waltzing-step mechanism

A.2. Definition of the rotation matrix

The rotation matrix is defined as:

$$R(\varphi, u_x, u_y, u_z) = \begin{pmatrix} u_x^2 + \left(u_y^2 + u_z^2\right)\cos(\varphi) & u_x u_y - u_x u_y \cos(\varphi) - u_z u^2 \sin(\varphi) & 2\sin(\varphi/2)\left(u_x u_z \sin(\varphi/2) + u_y u^2 \cos(\varphi/2)\right) \\ u_x u_y - u_x u_y \cos(\varphi) + u_z u^2 \sin(\varphi) & u_y^2 + \left(u_x^2 + u_z^2\right)\cos(\varphi) & 2\sin(\varphi/2)\left(u_y u_z \sin(\varphi/2) - u_x u^2 \cos(\varphi/2)\right) \\ 2\sin(\varphi/2)\left(u_x u_z \sin(\varphi/2) - u_y u^2 \cos(\varphi/2)\right) & 2\sin(\varphi/2)\left(u_y u_z \sin(\varphi/2) + u_x u^2 \cos(\varphi/2)\right) & u_z^2 + \left(u_x^2 + u_y^2\right)\cos(\varphi) \end{pmatrix} \Big/ u^2 \tag{A.1}$$

For clarity, the squared absolute value $u^2 = u_x^2 + u_y^2 + u_z^2$ of the rotation vector $\vec{u}$ was extracted. φ refers to the rotational angle, which is the azimuthal angle in Section 2.1.1.

A.3. Parameters for LEAM potentials for a Fe–Al system according to Ouyang et al. [Ouya 12]

	Fe	Al			Fe	Al
F_{10}	-2.29717e+00	-2.68705e+00		α	8.341805	10.168835
F_{11}	-8.90017e-02	-1.45138e-01		δ	5.888118	8.020946
F_{12}	1.35477e-01	1.49820e-01		λ_0	-2.96535372734070e-01	-2.84844450652599e-02
F_{13}	6.51888e-02	8.58974e-02		λ_1	-6.86818702765834e-01	2.26253814593105e-01
F_{14}	1.21338e-02	1.25671e-02		λ_2	9.21433631811882e+00	-7.73232595256378e-01
F_{20}	-2.32000e+00	-2.74000e+00		λ_3	-2.31791124636865e+01	3.86949752665298e+00
F_{21}	0.00000e+00	0.00000e+00		λ_4	2.55435422978587e+01	-1.35649697682291e+01
F_{22}	1.51240e-02	3.60093e-02		λ_5	-1.32408993096583e+01	2.04540388369782e+01
F_{23}	0.00000e+00	0.00000e+00		λ_6	2.64175146115575e+00	-1.06908995952681e+01
F_{24}	3.09105e-02	1.96952e-02		κ_0	1.90272772078082e-03	-1.42235717555228e-04
F_{30}	-2.32000e+00	-2.74000e+00		κ_1	-1.91654105383744e-03	9.78171751734746e-03
F_{31}	0.00000e+00	0.00000e+00		κ_2	2.08761078809353e-02	-3.51750745765951e-04
F_{32}	1.51240e-02	3.60093e-02		κ_3	-4.16458964131414e-01	-2.62491637456329e-01
F_{33}	7.79914e-05	1.02339e-02		κ_4	1.44223338080658e+00	7.60178831190332e-01
F_{34}	0.00000e+00	0.00000e+00		κ_5	-1.43995150930854e+00	-6.20000344131861e-01
f_e	9.935526e-03	5.045380e-03		ϕ_e	2.950690e-01	1.097910e-01
β	2.640265	1.952672		r_1	2.482419	2.863570
ρ_1	4.564865	5.561137		r_b	2.487585	3.894877
ρ_2	5.370429	6.542514		r_c	5.732900	6.403138
				r_e	6.118688	6.861309

Table A.1.: Parameters for Long-range analytical embedded atom method potentials as ascertained by Ouyang et al. [Ouya 12] for Fe–Al alloys.

A.4. Analytical form of contrast dependent on longitudinal coherence

$$
\begin{aligned}
& I_{\text{spectrum}}(\Delta z) \\
=& \frac{2I_0}{C} \int_{-\infty}^{\infty} \mathrm{d}k' \left(\theta\left(k' - \frac{\Delta k}{2}\right) - \theta\left(k' + \frac{\Delta k}{2}\right) \right) \left(1 + \cos(k'\Delta z)\right) && \text{(A.2a)} \\
=& \frac{2I_0}{\Delta k} \int_{-\Delta k/2}^{\Delta k/2} \mathrm{d}k' \left(1 + \cos(k'\Delta z)\right) && \text{(A.2b)} \\
=& 2I_0 \left(1 + \frac{1}{\Delta k} \int_{-\Delta k/2}^{\Delta k/2} \mathrm{d}k' \cos(k'\Delta z) \right) && \text{(A.2c)} \\
=& 2I_0 \left(1 + \frac{1}{\Delta k} \frac{\sin(k'\Delta z)}{\Delta z} \Bigg|_{k' \to -\Delta k/2}^{\Delta k/2} \right) && \text{(A.2d)} \\
=& 2I_0 \left(1 + \frac{\sin\left(\frac{\Delta k}{2}\Delta z\right) - \sin\left(-\frac{\Delta k}{2}\Delta z\right)}{\Delta k \Delta z} \right) && \text{(A.2e)} \\
& && \text{(A.2f)}
\end{aligned}
$$

A.5. Fit routine for fitting all intensity-correlation functions simultaneously according to jump matrix approach

$	1	2	3	4	5	6
	time t	exposure time	2Θ	φ	$g^{(2)}$	$\Delta g^{(2)}$

Table A.2.: Columns in datafile

```
########
#
#       x = 2theta
#       y = phi
#       z = t
#
# ___________________________________________________________________________________________________________

FIT_LIMIT = 1e-10

pi=3.14159265358979323846

d=3.3

En = 8.1                # in eV
k=2.0*pi/(12.3984/En)

# ~~~~~~~~~~~~~~~~~~~~~~~~~~~~~~~~~~~~~~~~~~~~~~~~~~~~~~~~~~~~~~~~~~~~~~~~~~~~~~~~~~~~~~~~~~~~~~~~~~~~~~~~~~~~~~~~

readout =  0.61
phicorr = 23.6

####________ 1 1 0 ________####
#
q1(x,y) = 2*k*sin(x/2*pi/180) * (1./sqrt(2.)* (sin(x/2.*pi/180.) + cos(x/2.*pi/180.)*sin(y*pi/180.) ) )
q2(x,y) = 2*k*sin(x/2*pi/180) * (-1./sqrt(2.)* (sin(x/2.*pi/180.) - cos(x/2.*pi/180.)*sin(y*pi/180.) ))
q3(x,y) = 2*k*sin(x/2*pi/180) * (cos(x/2.*pi/180.)*cos(y*pi/180.) )

C(x,y) = cos(q1(x,y)*d/2.)*cos(q2(x,y)*d/2.)*cos(q3(x,y)*d/2.)
Sa(x,y) = abs(pa1)*1./3*( cos(q1(x,y)*d) + cos(q2(x,y)*d) + cos(q3(x,y)*d) )\
              + abs(pa2)*1./3*( cos(q1(x,y)*d)*cos(q2(x,y)*d) + cos(q1(x,y)*d)*cos(q3(x,y)*d) + cos(
                  q2(x,y)*d)*cos(q3(x,y)*d) )\
              + abs(pa3)*cos(q1(x,y)*d)*cos(q2(x,y)*d)*cos(q3(x,y)*d)
Sb(x,y) = abs(pb1)*1./3*( cos(q1(x,y)*d) + cos(q2(x,y)*d) + cos(q3(x,y)*d) )\
              + abs(pb2)*1./3*( cos(q1(x,y)*d)*cos(q2(x,y)*d) + cos(q1(x,y)*d)*cos(q3(x,y)*d) + cos(
                  q2(x,y)*d)*cos(q3(x,y)*d) )\
              + abs(pb3)*cos(q1(x,y)*d)*cos(q2(x,y)*d)*cos(q3(x,y)*d)

Omega(x,y) = sqrt(  4*abs(Wa)*abs(1.0 - Wa)* C(x,y)**2 - abs(Wa)**2 * ( abs(ka)*(1 - Sa(x,y)) - abs(kb)
    *(1 - Sb(x,y)) )**2  )

ba1(x,y) = sqrt(1./abs(Wa))*sqrt(1./abs(1.0 - Wa))* ( abs(Wa)* (abs(ka)*(Sa(x,y)-1) - abs(kb)*(Sb(x,y)
    -1) ) - Omega(x,y) ) / ( 2*C(x,y) )
bb1(x,y) = 1.
ba2(x,y) = sqrt(1./abs(Wa))*sqrt(1./abs(1.0 - Wa))* ( abs(Wa)* (abs(ka)*(Sa(x,y)-1) - abs(kb)*(Sb(x,y)
    -1) ) + Omega(x,y) ) / ( 2*C(x,y) )
bb2(x,y) = 1.

w1(x,y) = abs( sqrt(abs(Wa))*ba1(x,y) + sqrt(abs(1.0 - Wa))*bb1(x,y) )**2
w2(x,y) = abs( sqrt(abs(Wa))*ba2(x,y) + sqrt(abs(1.0 - Wa))*bb2(x,y) )**2

tau1(x,y) = 2*abs(Wa)*tau0 / (  abs(Wa)*( abs(ka)*(1-Sa(x,y)) + abs(kb)*(1-Sb(x,y)) ) - Omega(x,y)  )
tau2(x,y) = 2*abs(Wa)*tau0 / (  abs(Wa)*( abs(ka)*(1-Sa(x,y)) + abs(kb)*(1-Sb(x,y)) ) + Omega(x,y)  )

beta(x,y) = (x == 15 && y == (0 + phicorr)) ? beta_15_0 : \
                        (x == 6 && y == (0 + phicorr)) ? beta_6_0 : \
                        (x == 25 && y == (0 + phicorr)) ? beta_25_0 : \
                        (x == 22 && y == (0 + phicorr)) ? beta_22_0 : \
                        (x == 20 && y == (0 + phicorr)) ? beta_20_0 : \
                        (x == 20 && y == (-15 + phicorr)) ? beta_20_m15 : \
                        (x == 20 && y == (-40 + phicorr)) ? beta_20_m40 : \
```

```
                (x == 20 && y == (-20 + phicorr)) ? beta_20_m20 : \
                (x == 20 && y == (23 + phicorr)) ? beta_20_23 : \
                (x == 20 && y == (-25 + phicorr)) ? beta_20_m25 : \
                (x == 20 && y == (8 + phicorr)) ? beta_20_8 : \
                (x == 20 && y == (-8 + phicorr)) ? beta_20_m8 : \
                (x == 20 && y == (15 + phicorr)) ? beta_20_15 : \
                (x == 20 && y == (30 + phicorr)) ? beta_20_30 : \
                (x == 20 && y == (-30 + phicorr)) ? beta_20_m30 : \
                (x == 25 && y == (-30 + phicorr)) ? beta_25_m30 : \
                (x == 17 && y == (-30 + phicorr)) ? beta_17_m30 : \
                (x == 13 && y == (-30 + phicorr)) ? beta_13_m30 : \
                (x == 9 && y == (-30 + phicorr)) ? beta_9_m30 : \
                (x == 6 && y == (-30 + phicorr)) ? beta_6_m30 : \
                (x == 10 && y == (-30 + phicorr)) ? beta_10_m30 : \
                (x == 10 && y == (8 + phicorr)) ? beta_10_8 : \
                (x == 10 && y == (0 + phicorr)) ? beta_10_0 : 0.01

g2(x,y,t,u) = 1.0 + beta(x,y) *( w1(x,y)**2 * exp( -2*t/tau1(x,y) ) + 2*w1(x,y)*w2(x,y) * exp( -t*(tau1
    (x,y)+tau2(x,y))/(tau1(x,y)*tau2(x,y)) ) + w2(x,y)**2 * exp( -2*t/tau2(x,y) ) )

#-------------------------------------------------------------------------------

fit [*:*] [*:*] [*:*] g2(x,y,t,u) "./allacf.dat" u 3:($4+phicorr):($1*($2+readout)):5:6 via tau0, ka,
    kb, Wa, pa1, pa2, pa3, pb1, pb2, pb3
```

Bibliography

[Aber 98] D. L. Abernathy, G. Grübel, S. Brauer, I. McNulty, G. B. Stephenson, S. G. J. Mochrie, A. R. Sandy, N. Mulders, and M. Sutton. "Small-Angle X-ray Scattering Using Coherent Undulator Radiation at the ESRF". *J Synchrotron Radiat*, Vol. 5, No. 1, pp. 37–47, Jan 1998. doi: 10.1107/s0909049597015835.

[Alln 93] A. R. Allnatt and A. B. Lidiard. *Atomic transport in solids*. Cambridge Univ. Press, Cambridge [u.a.], 1. publ. Ed., 1993. doi: 10.1017/CBO9780511563904.

[Aman 12] J. Amann, W. Berg, V. Blank, F.-J. Decker, Y. Ding, P. Emma, Y. Feng, J. Frisch, D. Fritz, J. Hastings, and et al. "Demonstration of self-seeding in a hard-X-ray free-electron laser". *Nature Photon*, Vol. 6, No. 10, pp. 693–698, Aug 2012. doi: 10.1038/nphoton.2012.180.

[Amar 10] H. Amara, C. C. Fu, F. Soisson, and P. Maugis. "Aluminum and vacancies in α-iron: Dissolution, diffusion, and clustering". *Phys. Rev. B*, Vol. 81, No. 17, p. 174101, May 2010. doi: 10.1103/physrevb.81.174101.

[Ande 84] I. Anderson, A. Heidemann, J. Bonnet, D. Ross, S. Wilson, and M. McKergow. "Proton residence times in the solid solution phase of the Y–H system studied by quasi-elastic neutron scattering". *Journal of the Less Common Metals*, Vol. 101, pp. 405–418, Aug 1984. doi: 10.1016/0022-5088(84)90116-4.

[Arit 89] M. Arita, M. Koiwa, and S. Ishioka. "Diffusion mechanisms in ordered alloys – a detailed analysis of six-jump vacancy cycle in the B2 type lattice". *Acta Metallurgica*, Vol. 37, No. 5, pp. 1363–1374, May 1989. doi: 10.1016/0001-6160(89)90167-3.

[Arrh 89] S. Arrhenius. "Über die Reaktionsgeschwindigkeit bei der Inversion von Rohrzucker durch Säuren". *Zeitschrift für physikalische Chemie*, Vol. 4, pp. 226–248, 1889.

[Athe 97] M. Athènes, P. Bellon, and G. Martin. "Identification of novel diffusion cycles in B2 ordered phases by Monte Carlo simulation". *Philosophical Magazine A*, Vol. 76, No. 3, pp. 565–585, Sep 1997. doi: 10.1080/01418619708214023.

[Bakk 97] H. Bakker, I. Modder, and M. Kuin. "Extension of Miedema's semiempirical model to estimates of the formation enthalpies of point defects in intermetallic compounds with the B2 structure". *Intermetallics*, Vol. 5, No. 7, pp. 535–546, Jan 1997. doi: 10.1016/s0966-9795(97)00032-0.

[Belo 04] I. V. Belova and G. E. Murch. "Calculation of Tracer and Chemical Diffusion Coefficients in the Intermetallic Compound β-AgMg". *Defect and Diffusion Forum*, Vol. 224-225, pp. 45–52, 2004. doi: 10.4028/www.scientific.net/ddf.224-225.45.

[Belo 98] I. Belova and G. Murch. "The anti-structural bridge mechanism for diffusion in ordered alloys of the B2 type". *Intermetallics*, Vol. 6, No. 2, pp. 115–119, Jan 1998. doi: 10.1016/s0966-9795(97)00053-8.

[Bend 79] O. Bender and K. Schroeder. "Theory of Mössbauer line broadening due to diffusion of Mössbauer atoms via vacancies". *Phys. Rev. B*, Vol. 19, No. 7, pp. 3399–3413, Apr 1979. doi: 10.1103/physrevb.19.3399.

[Bess 06] R. Besson, A. Legris, and J. Morillo. "Influence of complex point defects in ordered alloys: An ab initio study of B2 Fe-Al-B". *Phys. Rev. B*, Vol. 74, No. 9, p. 094103, Sep 2006. doi: 10.1103/physrevb.74.094103.

[Beye 13] M. Beye, S. Schreck, F. Sorgenfrei, C. Trabant, N. Pontius, C. Schüßler-Langeheine, W. Wurth, and A. Föhlisch. "Stimulated X-ray emission for materials science". *Nature*, Vol. 501, No. 7466, pp. 191–194, Aug 2013. doi: 10.1038/nature12449.

[Bibo 14] A. Biborski, R. Kozubski, and V. Pierron-Bohnes. ""Order-Order" Kinetics in Triple-Defect B2-Ordered Binary Intermetallics: Kinetic Monte Carlo Simulation". *Diffusion Foundations*, Vol. 2, pp. 191–220, Sep 2014. doi: 10.4028/www.scientific.net/df.2.191.

[Bocq 96] J. Bocquet, G. Brebec, and Y. Limoge. *Chapter 7 - Diffusion in Metals and Alloys*, pp. 535 – 668. North-Holland, Oxford, fourth edition Ed., 1996. doi: 10.1016/B978-044489875-3/50012-0.

[Bogn 98] J. Bogner, W. Steiner, M. Reissner, P. Mohn, P. Blaha, K. Schwarz, R. Krachler, H. Ipser, and B. Sepiol. "Magnetic order and defect structure of Fe_x Al_{1-x} alloys around x = 0.5: An experimental and theoretical study". *Physical Review B*, Vol. 58, No. 22, pp. 14922–14933, Dec 1998. doi: 10.1103/physrevb.58.14922.

[Bori 71] B. Borie and C. J. Sparks. "The interpretation of intensity distributions from disordered binary alloys". *Acta Crystallogr Sect A Cryst Phys Diffr Theor Gen Crystallogr*, Vol. 27, No. 3, pp. 198–201, May 1971. doi: 10.1107/s0567739471000469.

[Brau 95] S. Brauer, G. Stephenson, M. Sutton, R. Brüning, E. Dufresne, S. Mochrie, G. Grübel, J. Als-Nielsen, and D. Abernathy. "X-Ray Intensity Fluctuation Spectroscopy Observations of Critical Dynamics in Fe_3Al". *Physical Review Letters*, Vol. 74, No. 11, pp. 2010–2013, Mar 1995. doi: 10.1103/physrevlett.74.2010.

[Chan 82] Y. Chang and J. P. Neumann. "Thermodynamics and defect structure of intermetallic phases with the B2 (CsCl) structure". *Progress in Solid State Chemistry*, Vol. 14, No. 4, pp. 221–301, Jan 1982. doi: 10.1016/0079-6786(82)90004-8.

[Chud 61] C. T. Chudley and R. J. Elliott. "Neutron Scattering from a Liquid on a Jump Diffusion Model". *Proceedings of the Physical Society*, Vol. 77, No. 2, pp. 353–361, Feb 1961. doi: 10.1088/0370-1328/77/2/319.

[Chus 12] Y. Chushkin, C. Caronna, and A. Madsen. "A novel event correlation scheme for X-ray photon correlation spectroscopy". *J Appl Cryst*, Vol. 45, No. 4, pp. 807–813, Jun 2012. doi: 10.1107/s0021889812023321.

[Cipe 10] L. Cipelletti and E. R. Weeks. *Glassy dynamics and dynamical heterogeneity in colloids*, Chap. Glassy dynamics and dynamical heterogeneity in colloids, pp. 110–151. Oxford University Press, 2010. doi: 10.1093/acprof:oso/9780199691470.003.0004.

[Clap 66] P. C. Clapp and S. C. Moss. "Correlation Functions of Disordered Binary Alloys. I". *Phys. Rev.*, Vol. 142, No. 2, pp. 418–427, Feb 1966. doi: 10.1103/physrev.142.418.

[Cowl 50] J. M. Cowley. "An Approximate Theory of Order in Alloys". *Phys. Rev.*, Vol. 77, No. 5, pp. 669–675, Mar 1950. doi: 10.1103/physrev.77.669.

[Cowl 60] J. Cowley. "Short- and Long-Range Order Parameters in Disordered Solid Solutions". *Phys. Rev.*, Vol. 120, No. 5, pp. 1648–1657, Dec 1960. doi: 10.1103/physrev.120.1648.

[De G 59] P. De Gennes. "Liquid dynamics and inelastic scattering of neutrons". *Physica*, Vol. 25, No. 7-12, pp. 825–839, Jan 1959. doi: 10.1016/0031-8914(59)90006-0.

[Deev 96] S. Deevi and V. Sikka. "Nickel and iron aluminides: an overview on properties, processing, and applications". *Intermetallics*, Vol. 4, No. 5, pp. 357–375, Jan 1996. doi: 10.1016/0966-9795(95)00056-9.

[Divi 00] S. Divinski and C. Herzig. "On the six-jump cycle mechanism of self-diffusion in NiAl". *Intermetallics*, Vol. 8, No. 12, pp. 1357–1368, Dec 2000. doi: 10.1016/s0966-9795(00)00062-5.

[Divi 97] S. V. Divinski and L. N. Larikov. "Diffusion by anti-structure defects in non-stoichiometric intermetallic compounds with B2 and $L1_2$ structures". *J. Phys.: Condens. Matter*, Vol. 9, No. 37, pp. 7873–7883, Sep 1997. doi: 10.1088/0953-8984/9/37/018.

[Domi 65] H. Domian and H. Aaronson. "Diffusion in Body Centered Cubic Metals". *American Society for Metals*, p. 209, 1965.

[Drau 99] R. Drautz and M. Fähnle. "The six-jump diffusion cycles in B2 compounds revisited". *Acta Materialia*, Vol. 47, No. 8, pp. 2437–2447, Jun 1999. doi: 10.1016/s1359-6454(99)00106-8.

[Duca 91] F. Ducastelle. *Order and phase stability in alloys. Cohesion and structure ; 3*, North-Holland, Amsterdam [u.a.], 1991.

[Eber 15] W. Eberhardt. "Synchrotron radiation: A continuing revolution in X-ray science—Diffraction limited storage rings and beyond". *Journal of Electron Spectroscopy and Related Phenomena*, Jun 2015. doi: 10.1016/j.elspec.2015.06.009.

[Egge 00] M. Eggersmann and H. Mehrer. "Diffusion in intermetallic phases of the Fe-Al system". *Philosophical Magazine A*, Vol. 80, No. 5, pp. 1219–1244, May 2000. doi: 10.1080/01418610008212112.

[Eins 05] A. Einstein. "Über die von der molekularkinetischen Theorie der Wärme geforderte Bewegung von in ruhenden Flüssigkeiten suspendierten Teilchen". *Annalen der Physik*, Vol. 322, No. 8, pp. 549–560, 1905. doi: 10.1002/andp.19053220806.

[Elco 58] E. W. Elcock and C. W. McCombie. "Vacancy Diffusion in Binary Ordered Alloys". *Phys. Rev.*, Vol. 109, pp. 605–606, Jan 1958. doi: 10.1103/PhysRev.109.605.

[Elco 59] E. W. Elcock. "Vacancy Diffusion in Ordered Alloys". *Proceedings of the Physical Society*, Vol. 73, No. 2, pp. 250–264, Feb 1959. doi: 10.1088/0370-1328/73/2/314.

[Evan 35] M. G. Evans and M. Polanyi. "Some applications of the transition state method to the calculation of reaction velocities, especially in solution". *Trans. Faraday Soc.*, Vol. 31, p. 875, 1935. doi: 10.1039/tf9353100875.

[Eyri 35] H. Eyring. "The Activated Complex in Chemical Reactions". *The Journal of Chemical Physics*, Vol. 3, No. 2, p. 107, 1935. doi: 10.1063/1.1749604.

[Ezqu 09] T. Ezquerra, M. Garcia-Gutierrez, A. Nogales, and M. Gomez. *Applications of Synchrotron Light to Scattering and Diffraction in Materials and Life Sciences*. Springer Berlin Heidelberg, 2009. doi: 10.1007/978-3-540-95968-7.

[Fahn 02] M. Fähnle. "Atomic Defects and Diffusion in Intermetallic Compounds: The Impact of the ab initio Electron Theory". *Defect and Diffusion Forum*, Vol. 203, pp. 37–46, 2002. doi: 10.4028/www.scientific.net/DDF.203-205.37.

[Fahn 99a] M. Fähnle, J. Mayer, and B. Meyer. "Theory of atomic defects and diffusion in ordered compounds, and application to B2-FeAl". *Intermetallics*, Vol. 7, No. 3–4, pp. 315 – 323, 1999. doi: 10.1016/S0966-9795(98)00116-2.

[Fahn 99b] M. Fähnle, J. Mayer, and B. Meyer. "Theory of atomic defects and diffusion in ordered compounds, and application to B2-FeAl". *Intermetallics*, Vol. 7, No. 3-4, pp. 315–323, Mar 1999. doi: 10.1016/s0966-9795(98)00116-2.

[Falu 04] P. Falus, M. A. Borthwick, and S. G. J. Mochrie. "Fast CCD camera for x-ray photon correlation spectroscopy and time-resolved x-ray scattering and imaging". *Review of Scientific Instruments*, Vol. 75, No. 11, p. 4383, 2004. doi: 10.1063/1.1808913.

[Falu 06] P. Falus, L. B. Lurio, and S. G. J. Mochrie. "Optimizing the signal-to-noise ratio for X-ray photon correlation spectroscopy". *J Synchrotron Rad*, Vol. 13, No. 3, pp. 253–259, Apr 2006. doi: 10.1107/s0909049506006789.

[Feld 95] R. Feldwisch, B. Sepiol, and G. Vogl. "Elementary diffusion jump of iron atoms in intermetallic phases studied by Mössbauer spectroscopy–II. From order to disorder".

Acta Metallurgica et Materialia, Vol. 43, No. 5, pp. 2033–2039, May 1995. doi: 10.1016/0956-7151(94)00382-r.

[Ferd 07] R. K. Ferdinand Haider and T. Abinandanan. *Alloy physics; a comprehensive reference*, Chap. Simulation Techniques, pp. 653–706. Wiley-VCH, Weinheim, 2007.

[Fran 01] S. Frank, S. Divinski, U. Södervall, and C. Herzig. "Ni tracer diffusion in the B2-compound NiAl: influence of temperature and composition". *Acta Materialia*, Vol. 49, No. 8, pp. 1399–1411, May 2001. doi: 10.1016/s1359-6454(01)00037-4.

[Fu 93] C. Fu, Y.-Y. Ye, M. Yoo, and K. Ho. "Equilibrium point defects in intermetallics with the B2 structure: NiAl and FeAl". *Phys. Rev. B*, Vol. 48, No. 9, pp. 6712–6715, Sep 1993. doi: 10.1103/physrevb.48.6712.

[Fu 97] C. Fu and X. Wang. "The effect of electronic structure on the defect properties of FeAl". *Materials Science and Engineering: A*, Vol. 239-240, pp. 761–768, Dec 1997. doi: 10.1016/s0921-5093(97)00664-3.

[Ganc 00] M. G. Ganchenkova and A. V. Nazarov. "Simulation of defect complex migration in ordered intermetallic structures". *Computational Materials Science*, Vol. 17, No. 2–4, pp. 319 – 323, 2000. doi: 10.1016/S0927-0256(00)00045-8.

[Gang 68] A. Gangulee and M. Bever. "The Silver-Rich Solid Solution in the System Silver-Magnesium: I) Short-Range Order". *TRANS MET SOC AIME*, Vol. 242, No. 2, pp. 272–277, 1968.

[Gitt 06] A. S. Gittings and D. J. Durian. "Gaussian and non-Gaussian speckle fluctuations in the diffusing-wave spectroscopy signal of a coarsening foam". *Appl. Opt.*, Vol. 45, No. 10, p. 2199, 2006. doi: 10.1364/ao.45.002199.

[Glau 63] R. J. Glauber. "Time-Dependent Statistics of the Ising Model". *Journal of Mathematical Physics*, Vol. 4, No. 2, p. 294, 1963. doi: 10.1063/1.1703954.

[Grub 08] G. Grübel, A. Madsen, and A. Robert. *Soft Matter Characterization*, Chap. X-Ray Photon Correlation Spectroscopy (XPCS), pp. 953–995. Springer Netherland, 2008. doi: 10.1007/978-1-4020-4465-6_18.

[Gyor 83] B. L. Gyorffy and G. M. Stocks. "Concentration Waves and Fermi Surfaces in Random Metallic Alloys". *Physical Review Letters*, Vol. 50, No. 5, pp. 374–377, Jan 1983. doi: 10.1103/physrevlett.50.374.

[Hara 01] T. Haraguchi, F. Hori, R. Oshima, and M. Kogachi. "A study of vacancy-type defects in the B2-phase region of the Fe–Al system by positron annihilation method". *Intermetallics*, Vol. 9, No. 9, pp. 763–770, Sep 2001. doi: 10.1016/s0966-9795(01)00061-9.

[Hara 05] T. Haraguchi, K. Yoshimi, M. Yoo, H. Kato, S. Hanada, and A. Inoue. "Vacancy clustering and relaxation behavior in rapidly solidified B2 FeAl ribbons". *Acta Materialia*, Vol. 53, No. 13, pp. 3751–3764, Aug 2005. doi: 10.1016/j.actamat.2005.04.027.

[Haus 87] J. Haus and K. Kehr. "Diffusion in regular and disordered lattices". *Physics Reports*, Vol. 150, No. 5-6, pp. 263–406, Jun 1987. doi: 10.1016/0370-1573(87)90005-6.

[Hehe 01] T. Hehenkamp, P. Scholz, B. Köhler, and R. Kerl. "Vacancy Formation and Diffusion in FeAl-Alloys". *Defect and Diffusion Forum*, Vol. 194-199, pp. 389–396, 2001. doi: 10.4028/www.scientific.net/ddf.194-199.389.

[Hemp 00] R. Hempelmann. *Quasielastic Neutron Scattering and Solid State Diffusion*. Oxford University Press, Nov 2000. doi: 10.1093/acprof:oso/9780198517436.001.0001.

[Henk 93] B. Henke, E. Gullikson, and J. Davis. "X-Ray Interactions: Photoabsorption, Scattering, Transmission, and Reflection at E = 50-30,000 eV, Z = 1-92". *Atomic Data and Nuclear Data Tables*, Vol. 54, No. 2, pp. 181–342, Jul 1993. doi: 10.1006/adnd.1993.1013.

[Hero 56] S. Heron, R. W. P. McWhirter, and E. H. Rhoderick. "Measurements of Lifetimes of Excited States of Helium Atoms". *Proceedings of the Royal Society A: Mathematical, Physical and Engineering Sciences*, Vol. 234, No. 1199, pp. 565–583, Mar 1956. doi: 10.1098/rspa.1956.0058.

[Ho 78] K. Ho and R. Dodd. "Point defects in FeAl". *Scripta Metallurgica*, Vol. 12, No. 11, pp. 1055–1058, Nov 1978. doi: 10.1016/0036-9748(78)90024-8.

[Hunt] H. B. Huntington. private communication to Dr. Slifkin.

[Hunt 61] H. Huntington, N. Miller, and V. Nerses. "Self-diffusion in 50-50 Gold-Cadmium". *Acta Metallurgica*, Vol. 9, No. 8, pp. 749–754, Aug 1961. doi: 10.1016/0001-6160(61)90105-5.

[Jord 03] J. Jordan and S. Deevi. "Vacancy formation and effects in FeAl". *Intermetallics*, Vol. 11, No. 6, pp. 507–528, Jun 2003. doi: 10.1016/s0966-9795(03)00027-x.

[Kao 93] C. Kao and Y. Chang. "On the composition dependencies of self-diffusion coefficients in B2 intermetallic compounds". *Intermetallics*, Vol. 1, No. 4, pp. 237–250, Jan 1993. doi: 10.1016/0966-9795(93)90035-t.

[Keen 01] D. A. Keen. "A comparison of various commonly used correlation functions for describing total scattering". *J Appl Cryst*, Vol. 34, No. 2, pp. 172–177, Apr 2001. doi: 10.1107/s0021889800019993.

[Kerl 99] R. Kerl, J. Wolff, and T. Hehenkamp. "Equilibrium vacancy concentrations in FeAl and FeSi investigated with an absolute technique". *Intermetallics*, Vol. 7, No. 3-4, pp. 301–308, Mar 1999. doi: 10.1016/s0966-9795(98)00118-6.

[Kim 15] S.-H. Kim, H. Kim, and N. J. Kim. "Brittle intermetallic compound makes ultra-strong low-density steel with large ductility". *Nature*, Vol. 518, No. 7537, pp. 77–79, Feb 2015. doi: 10.1038/nature14144.

[Koga 01] M. Kogachi and T. Haraguchi. "Point defects in B2-type intermetallic compounds". *Materials Science and Engineering: A*, Vol. 312, No. 1-2, pp. 189–195, Aug 2001. doi: 10.1016/s0921-5093(00)01892-x.

[Koga 97] M. Kogachi and T. Haraguchi. "Quenched-in vacancies in B2-structured intermetallic compound FeAl". *Materials Science and Engineering: A*, Vol. 230, No. 1-2, pp. 124–131, Jul 1997. doi: 10.1016/s0921-5093(97)00016-6.

[Koga 98] M. Kogachi, T. Haraguchi, and S. Kim. "Point defect behavior in high temperature region in the B2-type intermetallic compound FeAl". *Intermetallics*, Vol. 6, No. 6, pp. 499–510, Jan 1998. doi: 10.1016/s0966-9795(97)00097-6.

[Koiw 92] M. Koiwa. *Ordered Intermetallics – Physical Metallurgy and Mechanical Behaviour*, Chap. 4. Kinetic Processes and Creep Behavior – Diffusion Mechanisms in the B2 Type Intermetallic Compounds, pp. 449–464. Vol. 213 of *NATO ASI Series, Series E*, Springer Netherlands, 1992. doi: 10.1007/978-94-011-2534-5_28.

[Krac 95] R. Krachler, H. Ipser, B. Sepiol, and G. Vogl. "Diffusion mechanism and defect concentrations in β'-FeAl, an intermetallic compound with B2 structure". *Intermetallics*, Vol. 3, No. 1, pp. 83–88, Jan 1995. doi: 10.1016/0966-9795(94)p3690-p.

[Kriv 69] M. A. Krivoglaz. *Theory of X-ray and thermal-neutron scattering by real crystals*. Plenum Press, 1969.

[Kriv 96] M. A. Krivoglaz. *Diffuse Scattering of X-Rays and Neutrons by Fluctuations*. Springer-Verlag Berlin Heidelberg, 1996.

[Kurz 12] Å. Kurzawski and K. Malarz. "Simple Cubic Random-Site Percolation Thresholds for Complex Neighbourhoods". *Reports on Mathematical Physics*, Vol. 70, No. 2, pp. 163–169, Oct 2012. doi: 10.1016/s0034-4877(12)60036-6.

[Kutn 77] R. Kutner and I. Sosnowska. "Thermal neutron scattering from a hydrogen-metal system in terms of a general multi-sublattice jump diffusion model–I". *Journal of Physics and Chemistry of Solids*, Vol. 38, No. 7, pp. 741–746, Jan 1977. doi: 10.1016/0022-3697(77)90067-1.

[Laut 93] W. Lauterborn, T. Kurz, and M. Wiesenfeldt. *Kohärente Optik*. Springer Science + Business Media, 1993. doi: 10.1007/978-3-642-78264-0.

[Lech 00] F. Lechermann and M. Fähnle. "Ab initio statistical mechanics for alloy phase diagrams and ordering phenomena including the effect of vacancies". *Phys. Rev. B*, Vol. 63, No. 1, p. 012104, Dec 2000. doi: 10.1103/physrevb.63.012104.

[Leit 09] M. Leitner, B. Sepiol, L.-M. Stadler, B. Pfau, and G. Vogl. "Atomic diffusion studied with coherent X-rays". *Nature Materials*, Vol. 8, No. 9, pp. 717–720, Jul 2009. doi: 10.1038/nmat2506.

[Leit 11] M. Leitner and G. Vogl. "Quasi-elastic scattering under short-range order: the linear regime and beyond". *J. Phys.: Condens. Matter*, Vol. 23, No. 25, p. 254206, Jun 2011. doi: 10.1088/0953-8984/23/25/254206.

[Leit 12a] M. Leitner. *Studying Atomic Dynamics with Coherent X-rays*. Springer Berlin Heidelberg, 2012. doi: 10.1007/978-3-642-24121-5.

[Leit 12b] M. Leitner, B. Sepiol, L.-M. Stadler, and B. Pfau. "Time-resolved study of the crystallization dynamics in a metallic glass". *Physical Review B*, Vol. 86, No. 6, Aug 2012. doi: 10.1103/physrevb.86.064202.

[Leit 15] M. Leitner. "Thermodynamics of point defects and diffusion mechanisms in B2-ordered compounds". 2015. arXiv:1503.03798v1.

[Lemi 99] P.-A. Lemieux and D. J. Durian. "Investigating non-Gaussian scattering processes by using nth-order intensity correlation functions". *Journal of the Optical Society of America A*, Vol. 16, No. 7, p. 1651, 1999. doi: 10.1364/josaa.16.001651.

[Lerc 09] D. Lerch, O. Wieckhorst, G. L. W. Hart, R. W. Forcade, and S. Müller. "UNCLE: a code for constructing cluster expansions for arbitrary lattices with minimal user-input". *Modelling Simul. Mater. Sci. Eng.*, Vol. 17, No. 5, p. 055003, Jun 2009. doi: 10.1088/0965-0393/17/5/055003.

[Live 00] F. Livet, F. Bley, J. Mainville, R. Caudron, S. Mochrie, E. Geissler, G. Dolino, D. Abernathy, G. Grübel, and M. Sutton. "Using direct illumination CCDs as high-resolution area detectors for X-ray scattering". *Nuclear Instruments and Methods in Physics Research Section A: Accelerators, Spectrometers, Detectors and Associated Equipment*, Vol. 451, No. 3, pp. 596–609, Sep 2000. doi: 10.1016/s0168-9002(00)00333-8.

[Mads 16] A. Madsen, A. Fluerasu, and B. Ruta. *Synchrotron Light Sources and Free-Electron Lasers*, Chap. Structural Dynamics of Materials Probed by X-Ray Photon Correlation Spectroscopy. Springer Science + Business Media, 1 Ed., 2016. doi: 10.1007/978-3-319-04507-8.

[Maie 79] K. Maier, H. Mehrer, and G. Rein. "Self-diffusion in molybdenum". *Zeitschrift fur Metallkunde*, Vol. 70, No. 4, pp. 271–276, 1979.

[Mann 59] J. R. Manning. "Correlation Effects in Impurity Diffusion". *Phys. Rev.*, Vol. 116, No. 4, pp. 819–827, Nov 1959. doi: 10.1103/physrev.116.819.

[Mant 08] M. Mantina, Y. Wang, R. Arroyave, L. Q. Chen, Z. K. Liu, and C. Wolverton. "First-Principles Calculation of Self-Diffusion Coefficients". *Physical Review Letters*, Vol. 100, No. 21, p. 215901, May 2008. doi: 10.1103/physrevlett.100.215901.

[Maye 95] J. Mayer, C. Elsässer, and M. Fähnle. "Concentrations of Atomic Defects in B2–Fe_xAl_{1-x}. An Ab-Initio Study". *phys. stat. sol. (b)*, Vol. 191, No. 2, pp. 283–298, Oct 1995. doi: 10.1002/pssb.2221910205.

[Mehr 07] H. Mehrer. *Diffusion in Solids*. Springer Berlin Heidelberg, 2007. doi: 10.1007/978-3-540-71488-0.

[Metr 53] N. Metropolis, A. W. Rosenbluth, M. N. Rosenbluth, A. H. Teller, and E. Teller. "Equation of State Calculations by Fast Computing Machines". *The Journal of Chemical Physics*, Vol. 21, No. 6, p. 1087, 1953. doi: 10.1063/1.1699114.

[Mich 09] J. V. Michalowicz, J. M. Nichols, F. Bucholtz, and C. C. Olson. "An Isserlis' Theorem for Mixed Gaussian Variables: Application to the Auto-Bispectral Density". *J Stat Phys*, Vol. 136, No. 1, pp. 89–102, Jun 2009. doi: 10.1007/s10955-009-9768-3.

[Mill 02] D. M. Mills. *Third-generation hard X-ray synchrotron radiation sources: source properties, optics, and experimental techniques*. Vol. 1, Wiley-VCH, 2002.

[Mish 03] Y. Mishin, A. Y. Lozovoi, and A. Alavi. "Evaluation of diffusion mechanisms in NiAl by embedded-atom and first-principles calculations". *Phys. Rev. B*, Vol. 67, p. 014201, Jan 2003. doi: 10.1103/PhysRevB.67.014201.

[Morr 98] M. Morris, O. George, and D. Morris. "Vacancies, vacancy aggregates and hardening in FeAl". *Materials Science and Engineering: A*, Vol. 258, No. 1-2, pp. 99–107, Dec 1998. doi: 10.1016/s0921-5093(98)00922-8.

[Mull 03] S. Müller. "Bulk and surface ordering phenomena in binary metal alloys". *J. Phys.: Condens. Matter*, Vol. 15, No. 34, pp. R1429–R1500, Aug 2003. doi: 10.1088/0953-8984/15/34/201.

[Mund 78] J. Mundy, S. Rothman, N. Lam, H. Hoff, and L. Nowicki. "Self-diffusion in tungsten". *Phys. Rev. B*, Vol. 18, No. 12, pp. 6566–6575, Dec 1978. doi: 10.1103/physrevb.18.6566.

[Murc 01] G. E. Murch. *Diffusion Kinetics in Solids*, Chap. 3, pp. 171–238. Wiley-Blackwell, Aug 2001. doi: 10.1002/352760264x.ch3.

[Naka 03] R. Nakamura and Y. Iijima. "Self-diffusion of aluminium in the intermetallic compound Fe-48 at. *Philosophical Magazine*, Vol. 83, No. 4, pp. 477–483, Jan 2003. doi: 10.1080/0141861021000055655.

[Naye 84] A. A. Nayeb-Hashemi and J. B. Clark. "The Ag-Mg (Silver-Magnesium) system". *Bulletin of Alloy Phase Diagrams*, Vol. 5, No. 4, pp. 348–358, Aug 1984. doi: 10.1007/bf02872949.

[Niel 00] V. M. Nield and D. A. Keen. *Diffuse neutron scattering from crystalline materials*. Clarendon Press, 2000.

[Nogu 05] R. N. Nogueira and C. G. Schön. "Embedded atom method study of the interactions between point defects in iron aluminides: Double defects". *Intermetallics*, Vol. 13, No. 11, pp. 1233–1244, Nov 2005. doi: 10.1016/j.intermet.2005.04.007.

[Ouya 12] Y. Ouyang, X. Tong, C. Li, H. Chen, X. Tao, T. Hickel, and Y. Du. "Thermodynamic and physical properties of FeAl and Fe_3Al: an atomistic study by EAM simulation". *Physica B: Condensed Matter*, Vol. 407, No. 23, pp. 4530–4536, Dec 2012. doi: 10.1016/j.physb.2012.08.025.

[Pari 78] D. Paris and P. Lesbats. "Vacancies in Ee-Al alloys". *Journal of Nuclear Materials*, Vol. 69-70, pp. 628–632, Feb 1978. doi: 10.1016/0022-3115(78)90297-0.

[Peco 85] R. Pecora. *Dynamic light scattering: applications of photon correlation spectroscopy*. Springer, 1985. doi: 10.1007/978-1-4613-2389-1.

[Pete 78] N. Peterson. "Self-diffusion in pure metals". *Journal of Nuclear Materials*, Vol. 69-70, pp. 3–37, Feb 1978. doi: 10.1016/0022-3115(78)90234-9.

[Prof 97] T. Proffen and R. B. Neder. "DISCUS: a program for diffuse scattering and defect-structure simulation". *J Appl Cryst*, Vol. 30, No. 2, pp. 171–175, Apr 1997. doi: 10.1107/s002188989600934x.

[Rand 94] O. G. Randl, B. Sepiol, G. Vogl, R. Feldwisch, and K. Schroeder. "Quasielastic Mössbauer spectroscopy and quasielastic neutron scattering from non-Bravais lattices with differently occupied sublattices". *Phys. Rev. B*, Vol. 49, No. 13, pp. 8768–8773, Apr 1994. doi: 10.1103/physrevb.49.8768.

[Rivi 74] J. P. Rivière and J. Grilhé. "Influence de la concentration en aluminium sur l'énergie de migration des lacunes de trempe dans les alliages ordonnés Fe–Al". *Phys. Stat. Sol. (a)*, Vol. 25, No. 2, pp. 429–436, Oct 1974. doi: 10.1002/pssa.2210250208.

[Ross 14] M. Ross, M. Stana, M. Leitner, and B. Sepiol. "Direct observation of atomic network migration in glass". *New Journal of Physics*, Vol. 16, No. 9, p. 093042, Sep 2014. doi: 10.1088/1367-2630/16/9/093042.

[Ross 15] M. Ross. *Atomic Diffusion in Glasses Studied with Coherent X-rays*. PhD thesis, University of Vienna, 2015.

[Rowe 71] J. Rowe, K. Sköld, H. Flotow, and J. Rush. "Quasielastic neutron scattering by hydrogen in the α and β phases of vanadium hydride". *Journal of Physics and Chemistry of Solids*, Vol. 32, No. 1, pp. 41–54, Jan 1971. doi: 10.1016/s0022-3697(71)80006-9.

[Sanc 84] J. Sanchez, F. Ducastelle, and D. Gratias. "Generalized cluster description of multi-component systems". *Physica A: Statistical Mechanics and its Applications*, Vol. 128, No. 1-2, pp. 334–350, Nov 1984. doi: 10.1016/0378-4371(84)90096-7.

[Sand 99] A. R. Sandy, L. B. Lurio, S. G. J. Mochrie, A. Malik, G. B. Stephenson, J. F. Pelletier, and M. Sutton. "Design and characterization of an undulator beamline optimized for small-angle coherent X-ray scattering at the Advanced Photon Source". *J Synchrotron Radiat*, Vol. 6, No. 6, pp. 1174–1184, Nov 1999. doi: 10.1107/s0909049599009590.

[Scha 99] H.-E. Schaefer, K. Frenner, and R. Würschum. "Time-Differential Length Change Measurements for Thermal Defect Investigations: Intermetallic B2-FeAl and B2-NiAl Compounds, a Case Study". *Physical Review Letters*, Vol. 82, No. 5, pp. 948–951, Feb 1999. doi: 10.1103/physrevlett.82.948.

[Schm 92] F. Schmid and K. Binder. "Modelling order-disorder and magnetic transitions in iron-aluminium alloys". *J. Phys.: Condens. Matter*, Vol. 4, No. 13, pp. 3569–3588, Mar 1992. doi: 10.1088/0953-8984/4/13/019.

[Scho 03] A. Schöps. *Diffuse Röntgenstreuung an binären Legierungen*. PhD thesis, Fakultät Mathematik und Physik der Universität Stuttgart, 2003.

[Scho 99] B. Schönfeld. "Local atomic arrangements in binary alloys". *Progress in Materials Science*, Vol. 44, No. 5, pp. 435–543, Dec 1999. doi: 10.1016/s0079-6425(99)00005-5.

[Schw 77] L. H. Schwarz and J. B. Cohen. *Diffraction from Materials. Material Science Series*, Academic Press INC, 1977.

[Schw 98] W. Schweika. *Disordered Alloys*. Springer Berlin Heidelberg, 1998. doi: 10.1007/bfb0110656.

[Seme 08] O. Semenova, R. Krachler, and H. Ipser. "A generalized defect correlation model for B2 compounds". *Solid State Sciences*, Vol. 10, No. 9, pp. 1236–1244, Sep 2008. doi: 10.1016/j.solidstatesciences.2007.11.041.

[Seme 12] O. Semenova and R. Krachler. "Quasi chemical and defect correlation models for intermetallic compounds with B2-structure: new applications". *J Mater Sci*, Vol. 47, No. 10, pp. 4439–4448, Feb 2012. doi: 10.1007/s10853-012-6302-9.

[Sepi 93] B. Sepiol and G. Vogl. "Experimental Arguments Against Six-Jump Cycle Model of Diffusion in FeAl, an Intermetallic Compound with B2 Structure". *Defect and Diffusion Forum*, Vol. 95-98, pp. 831–838, 1993. doi: 10.4028/www.scientific.net/ddf.95-98.831.

[Shol 81] C. A. Sholl. "Diffusion correlation factors and atomic displacements for the vacancy mechanism". *Journal of Physics C: Solid State Physics*, Vol. 14, No. 20, pp. 2723–2729, Jul 1981. doi: 10.1088/0022-3719/14/20/011.

[Shpy 14] O. G. Shpyrko. "X-ray photon correlation spectroscopy". *J Synchrotron Rad*, Vol. 21, No. 5, pp. 1057–1064, Aug 2014. doi: 10.1107/s1600577514018232.

[Sinh 88] S. Sinha and D. Ross. “Self-consistent density response function method for dynamics of light interstitials in crystals”. *Physica B+C*, Vol. 149, No. 1-3, pp. 51–56, Mar 1988. doi: 10.1016/0378-4363(88)90218-5.

[Stan 13] M. Stana, M. Leitner, M. Ross, and B. Sepiol. “Studies of atomic diffusion in Ni–Pt solid solution by x-ray photon correlation spectroscopy”. *J. Phys.: Condens. Matter*, Vol. 25, No. 6, p. 065401, Jan 2013. doi: 10.1088/0953-8984/25/6/065401.

[Stol 80] N. A. Stolwijk, M. v. Gend, and H. Bakker. “Self-diffusion in the intermetallic compound CoGa”. *Philosophical Magazine A*, Vol. 42, No. 6, pp. 783–808, Dec 1980. doi: 10.1080/01418618008239385.

[Surr 12] A. Surrey, D. Pohl, L. Schultz, and B. Rellinghaus. “Quantitative Measurement of the Surface Self-Diffusion on Au Nanoparticles by Aberration-Corrected Transmission Electron Microscopy”. *Nano Lett.*, Vol. 12, No. 12, pp. 6071–6077, Dec 2012. doi: 10.1021/nl302280x.

[Sutt 06] M. Sutton. *Neutron and X-ray Spectroscopy*, Chap. X-Ray Intensity Fluctuation Spectroscopy, pp. 297–318. Springer-Verlag, 2006. doi: 10.1007/1-4020-3337-0_9.

[Sutt 91] M. Sutton, S. G. J. Mochrie, T. Greytak, S. E. Nagler, L. E. Berman, G. A. Held, and G. B. Stephenson. “Observation of speckle by diffraction with coherent X-rays”. *Nature*, Vol. 352, No. 6336, pp. 608–610, Aug 1991. doi: 10.1038/352608a0.

[Tayl 58] A. Taylor and R. Jones. “Constitution and magnetic properties of iron-rich iron-aluminum alloys”. *Journal of Physics and Chemistry of Solids*, Vol. 6, No. 1, pp. 16–37, Jul 1958. doi: 10.1016/0022-3697(58)90213-0.

[Van 54] L. Van Hove. “Correlations in Space and Time and Born Approximation Scattering in Systems of Interacting Particles”. *Phys. Rev.*, Vol. 95, No. 1, pp. 249–262, Jul 1954. doi: 10.1103/physrev.95.249.

[Vine 57] G. H. Vineyard. “Frequency factors and isotope effects in solid state rate processes”. *Journal of Physics and Chemistry of Solids*, Vol. 3, No. 1–2, pp. 121 – 127, 1957. doi: 10.1016/0022-3697(57)90059-8.

[Vive 93] E. Vives and A. Planes. “Ordering Kinetics by Vacancies”. *International Journal of Modern Physics C*, Vol. 04, No. 03, pp. 701–720, Jun 1993. doi: 10.1142/s0129183193000604.

[Vogl 05] G. Vogl and B. Sepiol. *Diffusion in condensed matter; methods, materials, models*, Chap. 2 The Elementary Diffusion Step in Metals Studied by the Interference of Gamma-Rays, X-Rays and Neutrons, pp. 65–91. Springer-Verlag, 2005. doi: 10.1007/3-540-30970-5_2.

[Vogl 94] G. Vogl and B. Sepiol. "Elementary diffusion jump of iron atoms in intermetallic phases studied by Mössbauer spectroscopy—I. Fe–Al close to equiatomic stoichiometry". *Acta Metallurgica et Materialia*, Vol. 42, No. 9, pp. 3175–3181, Sep 1994. doi: 10.1016/0956-7151(94)90416-2.

[Warr 51] B. E. Warren, B. L. Averbach, and B. W. Roberts. "Atomic Size Effect in the X-Ray Scattering by Alloys". *Journal of Applied Physics*, Vol. 22, No. 12, p. 1493, 1951. doi: 10.1063/1.1699898.

[Wasi 68] R. Wasilewski. "Structure defects in CsCl intermetallic compounds – I. Theory". *Journal of Physics and Chemistry of Solids*, Vol. 29, No. 1, pp. 39 – 49, 1968. doi: 10.1016/0022-3697(68)90252-7.

[Wein 00] R. Weinkamer. *Diffusion und diffusive Phasenumwandlungen in binären Legierungen*. PhD thesis, University of Vienna, 2000.

[Wein 98] R. Weinkamer, P. Fratzl, B. Sepiol, and G. Vogl. "Monte Carlo simulation of diffusion in a B 2-ordered model alloy". *Phys. Rev. B*, Vol. 58, No. 6, pp. 3082–3088, Aug 1998. doi: 10.1103/physrevb.58.3082.

[Wein 99] R. Weinkamer, P. Fratzl, B. Sepiol, and G. Vogl. "Monte Carlo simulations of Mössbauer spectra in diffusion investigations". *Phys. Rev. B*, Vol. 59, No. 13, pp. 8622–8625, Apr 1999. doi: 10.1103/physrevb.59.8622.

[Welb 94] T. R. Welberry and B. D. Butler. "Interpretation of diffuse X-ray scattering via models of disorder". *J Appl Cryst*, Vol. 27, No. 3, pp. 205–231, Jun 1994. doi: 10.1107/s0021889893011392.

[Welb 95] T. R. Welberry and B. D. Butler. "Diffuse X-ray Scattering from Disordered Crystals". *Chemical Reviews*, Vol. 95, No. 7, pp. 2369–2403, Nov 1995. doi: 10.1021/cr00039a005.

[Wied 03] H. Wiedemann. *Synchrotron Radiation. Advanced Texts in Physics*, Springer-Verlag Berlin Heidelberg, 2003. doi: 10.1007/978-3-662-05312-6.

[Will 35] E. Williams. "The effect of thermal agitation on atomic arrangement in alloys. III". *Proceedings of the Royal Society of London. Series A, Mathematical and Physical Sciences*, Vol. 152, No. 875, pp. 231–252, 1935. doi: 10.1098/rspa.1935.0188.

[Wini 81] H. Winick, G. Brown, K. Halbach, and J. Harris. "Wiggler and undulator magnets". *Phys. Today*, Vol. 34, No. 5, p. 50, 1981. doi: 10.1063/1.2914568.

[Wolf 77] D. Wolf. "Theory of Mössbauer line broadening due to correlated diffusion in crystals". *Appl. Phys. Lett.*, Vol. 30, No. 12, p. 617, 1977. doi: 10.1063/1.89281.

[Wolf 97] J. Wolff, M. Franz, A. Broska, and T. Hehenkamp. "Defect Types and Diffusion Mechanism in FeAl Compounds-A Positron Annihilation Study". *Defect and Diffusion Forum*, Vol. 143, pp. 239–244, 1997. doi: 10.4028/www.scientific.net/DDF.143-147.239.

[Wolf 99] J. Wolff, M. Franz, A. Broska, R. Kerl, M. Weinhagen, B. Köhler, M. Brauer, F. Faupel, and T. Hehenkamp. "Point defects and their properties in FeAl and FeSi alloys". *Intermetallics*, Vol. 7, No. 3-4, pp. 289–300, Mar 1999. doi: 10.1016/s0966-9795(98)00105-8.

[Wurs 95] R. Würschum, C. Grupp, and H.-E. Schaefer. "Simultaneous Study of Vacancy Formation and Migration at High Temperatures in B2-Type Fe Aluminides". *Physical Review Letters*, Vol. 75, No. 1, pp. 97–100, Jul 1995. doi: 10.1103/physrevlett.75.97.

[Wynb 67] P. Wynblatt. "Diffusion mechanisms in ordered body-centered cubic alloys". *Acta Metallurgica*, Vol. 15, No. 9, pp. 1453–1460, Sep 1967. doi: 10.1016/0001-6160(67)90176-9.

[Xu 09] Q. Xu and A. V. der Ven. "First-principles investigation of migration barriers and point defect complexes in B2–NiAl". *Intermetallics*, Vol. 17, No. 5, pp. 319 – 329, 2009. doi: 10.1016/j.intermet.2008.11.007.

[Xu 10] Q. Xu and A. Van der Ven. "Atomic transport in ordered compounds mediated by local disorder: Diffusion in B 2–Ni_xAl_{1-x}". *Phys. Rev. B*, Vol. 81, No. 6, p. 064303, Feb 2010. doi: 10.1103/physrevb.81.064303.

[Yald 91] K. Yaldram and K. Binder. "Monte Carlo simulation of phase separation and clustering in the ABV model". *J Stat Phys*, Vol. 62, No. 1-2, pp. 161–175, Jan 1991. doi: 10.1007/bf01020864.

[Youn 66] W. M. Young and E. W. Elcock. "Monte Carlo studies of vacancy migration in binary ordered alloys: I". *Proceedings of the Physical Society*, Vol. 89, No. 3, pp. 735–746, Nov 1966. doi: 10.1088/0370-1328/89/3/329.

[Zern 27] F. Zernike and J. A. Prins. "Die Beugung von Röntgenstrahlen in Flüssigkeiten als Effekt der Molekülanordnung". *Zeitschrift für Physik*, Vol. 41, No. 2, pp. 184–194, Jun 1927. doi: 10.1007/bf01391926.

B. Curriculum Vitae

Education

09/1996 – 06/2004	Bundesrealgymnasium, Bad Ischl
07/2004 – 06/2005	Compulsory community service, Bad Ischl
09/2005 – 08/2006	Round-the-world trip
10/2006 – 06/2011	Undergraduate studies in physics, University of Vienna
06/2011	Diploma thesis "Studies of atomic diffusion in NiPt by X-ray photon correlation spectroscopy", supervisor Ao. Univ. Prof. Dr. B. Sepiol
10/2011 – 08/2015	Doctroial program in physics, University of Vienna
08/2015	Doctorial thesis "Studies of atomic diffusion in binary alloys by X-ray Photon Correlation Spectroscopy with particular attention to B2 phases", supervisor Ao. Univ. Prof. Dr. B. Sepiol
since 10/2011	Research assistant at the group Dynamics of Condensed Systems, Faculty of Physics, University of Vienna

Peer-reviewed publications

2014	M. Stana, M. Ross and B. Sepiol, *Atomic Migration Studies with X-Ray Photon Correlation Spectroscopy in Recent Progress in Diffusion Thermodynamics and Kinetics in Intermetallic Compounds*, Diffusion Foundations (Volume 2), TTP.
2014	M. Ross, M. Stana, M. Leitner and B. Sepiol, New J. Phys. 16, 093042.
2013	M. Stana, M. Leitner, M. Ross and B. Sepiol, J. Phys.: Condens. Matter 25, 065401.

Prices and awards

09/2013	*"Best Poster Award"*, DyProSo XXXIV, Vienna, Austria
08/2013	*"Second Prize, Best Poster Award"*, Diffusion Fundamentals V, 2013, Leipzig, Germany
02/2013	*"Young Scientist Best Lecture Prize"*, 8th European NESY Winter-School & Symposium on Neutron and Synchrotron Radiation, 2013, Planneralm, Austria

Conference contributions

Talks

03/2015 "Following atomic jumps with aXPCS - how fluctuations of coherently scattered intensities yield information on atomic-scale diffusion", 9th European NESY Winter-School & Symposium on Neutron and Synchrotron Radiation, Altaussee, Austria.

08/2014 "Using coherent X-rays to measure atomic-scale diffusion", DIMAT 2014, Münster, Germany.

04/2014 "Studying spatially resolved atomic diffusion processes using X-rays - atomic-scale X-ray photon correlation spectroscopy and its application to metallic alloys", DPG-Frühjahrstagung, Dresden, Germany.

02/2013 "How to Measure Atomic Scale Diffusion? - From Randomly Distributed Slits to Dynamic X-Ray Speckle Patterns", 8th European NESY Winter-School & Symposium on Neutron and Synchrotron Radiation, Planneralm, Austria.

03/2012 "Studies of atomic diffusion in crystalline alloys by XPCS", 76. Jahrestagung der DPG und DPG-Frühjahrstagung, Berlin, Germany.

Posters

09/2014 "Studies of atomic scale diffusion by X-ray photon correlation spectroscopy", HERCULES Specialised Course HSC-17, Greonble, France.

03/2014 "Studies of atomic scale diffusion by X-ray photon correlation spectroscopy", XIII. Research Coures on X-ray Science, DESY, Hamburg, Germany.

09/2013 "Studies of atomic scale diffusion by x-ray photon correlation spectroscopy", DyProSo XXXIV, Vienna, Austria.

09/2013 "Studies of atomic scale diffusion by quasielastic Mößbauer spectroscopy and x-ray photon correlation spectroscopy", ICAME, Opatija, Croatia.

08/2013 "Studies of atomic scale diffusion by x-ray photon correlation spectroscopy", Diffusion Fundamentals V, Leipzig, Germany.

09/2012 "Studies of atomic diffusion in crystalline alloys by XPCS", The 11th Biennial Conference on High Resolution X-Ray Diffraction and Imaging, St. Petersuburg, Russia.

Synchrotron experience

Beamtimes

01/2014	I-20130061 EC	Advanced studies on atomic dynamics in superionic conducting glasses with aXPCS, PETRA III, Hamburg
04/2013	HC-885	Atomic dynamics in superionic conducting glasses, ESRF, Grenoble
02/2013	I-20120485 EC	Atomic dynamics in superionic conducting glasses, PETRA III, Hamburg
04/2012	I-20110131 EC	Atomic Diffusion in B2-FeAl, PETRA III, Hamburg
11/2011	HS-4357	Atomic diffusion in B2-AuMg measured by XPCS, ESRF, Grenoble
05/2011	I-20100274 EC	Atomic Diffusion in B2-NiAl, PETRA III, Hamburg
11/2010	HS-4228	Atomic diffusion in the noble metal binary alloys, ESRF, Grenoble
06/2010	HS-4082	Mechanism of diffusion in NiAl measured by XPCS, ESRF, Grenoble

Courses

09/2014	HERCULES Specialised Course HSC-17: *Dynamical properties investigated by neutrons and synchrotron X-rays*, Greonble, France.
03/2014	XIII. Research Coures on X-ray Science: *Correlation Functions in the Time Domain: Trends in Coherent X-ray Scattering*, DESY, Hamburg, Germany.
03/2013	XII. Research Coures on X-ray Science: *Theoretical Foundations of Research with X-ray Free Electron Lasers and Synchrotron Radiation Sources* , DESY, Hamburg. Germany.

Teaching experinece

At the University of Vienna, Austria:

03/2015 - 06/2015	Physics Laboratory II
03/2015 - 06/2015	Laboratory Solid State Physics: Advanced Materials
03/2015 - 06/2015	Solid State Physics II - Exercises
10/2014 - 01/2015	Physics laboratory I - for beginners
10/2014 - 01/2015	Laboratory Solid State Physics: Advanced Materials
10/2014 - 01/2015	Solid State Physics I - Exercises
03/2014 - 06/2014	Solid State Physics II - Exercises
10/2013 - 01/2014	Laboratory Solid State Physics: Advanced Materials
10/2013 - 01/2014	Solid State Physics I - Exercises
03/2013 - 06/2013	Seminar Structure and Dynamics of Condensed Systems
03/2013 - 06/2013	Seminar on advanced materials
03/2013 - 06/2013	Laboratory Solid State Physics: Advanced Materials - Advanced lab course in solid state physics
03/2013 - 06/2013	Solid State Physics II - Exercises
10/2012 - 01/2013	Solid State Physics I - Exercises